



Transition Metal-Radical Complexes and Their Catalytic Reactivity

Dissertation for the degree of **Doktor der Naturwissenschaft**
in the Fakultät für Naturwissenschaften
(Department Chemie)
at the **Universität Paderborn**

Presented by

Chandan Mukherjee

Mülheim an der Ruhr, 2006

To my parents and Debanjali

"If we knew what it was we were doing, it would not be called research, would it?"

- Albert Einstein

Acknowledgements:

I would like to mention that submission of this Thesis would not have been possible at all had I not been bestowed with the benign association of the scientific elite of the Max-Planck-Institut für Bioanorganische Chemie, Mülheim an der Ruhr, Germany.

- First of all, I humbly offer my deepest respect to **Prof. Dr. P. Chaudhuri**, who offered me the scope to be a Research scholar under him. His constant guidance, perpetual inspiration with occasional reformatory thrashings always acted as motivating factors to my research work.
- **Prof. Dr. K. Wieghardt**, for the opportunity of working in his research group and providing me with all needed laboratory facilities.
- **Dr. T. Weyhermüller** and **Mrs. H. Schucht** for their excellent work with the X-ray crystallography.
- **Dr. E. Bothe**, **Mrs. P. Höfer** and **Mr. H. Schmidt** for their help during electrochemical measurements.
- **Prof. Dr. E. Rentschler** for assistance with the fitting of some magnetochemical data.
- **Dr. E. Bill**, **Mr. A. Göbels**, **Mr. F. Reikowski**, **Mr. J. Bitter**, **Mrs. Sand** and **Mr. B. Mienert** for discussions and measurements of EPR, SQUID, NMR and Mössbauer spectroscopy.
- **Mr. U. Pieper** and **Mrs. R. Wagner** for their help in the laboratory.
- **Mrs. U. Westhoff**, **Mrs. G. Schmidt** and **Mrs. M. Trinoga** for skilful GC and LC analyses.
- **Mrs. J. Theurich**, **Mrs. T. Montenbruck** and **Mrs. B. Deckers** for their helpfulness in general.
- **Dr. J. F. Berry** and **Dr. P. L. Larsen**, for careful revision of the manuscript.
- **Dr. K. Ray**, **Mr. N. Roy**, **Mr. B. Biswas**, **Dr. A. Patra**, **Dr. K. Chlopek**, **Dr. S. Khanra**, **Mr. S. Presow**, **Dr. K. Merz**, **Dr. T. Petrenko**, **Dr. R. Kapre**, **Dr. S. Kinge**, **Mr. B. Pluijmaekers**, **Dr. S. Kokatam**, **Dr. S. Blanchard**, **Dr. L. Benisvy**, **Dr. Y. Song**, **Dr. N. Aliaga-Alcade**, **Dr. K. S. Min**, **Mr. F. Benidito**, **Dr. N. Muresan**, **Dr. J. Sandor**, and all the other members of the institute for their help to my work and friendly life inside and outside the laboratory.

- Family **Mukherjee** and Family **Ghosh** for constant inspiration and encouragement.
- Family **Basak** for their help in general.
- My **parents** for their constant inspiration and encouragement.
- I am highly indebted to my girlfriend **Debanjali** for her understanding, inspiration, invaluable support and having faith in me.
- My elder **Brother** and elder **Sister** for their encouragement.
- Deutsche Forschungsgemeinschaft (DFG) and Max-Planck-Gesellschaft (MPG) for financial support.

This work was carried out between August 2003 and June 2005 at the **Max-Planck-Institut für Bioanorganische Chemie**, Mülheim an der Ruhr, Germany.

Papers published:

1. A review article: Biomimetic metal-radical reactivity: aerial oxidation of alcohols, amines, aminophenols and catechols catalyzed by transition metal complexes

Phalguni Chaudhuri, Karl Wieghardt, Thomas Weyhermüller, Tapan K. Paine, Soumen Mukherjee and Chandan Mukherjee. Biol. Chem. **2005**, 386, 1023-1033.

2. A trinuclear complex containing $Mn^{II}Mn^{III}Mn^{IV}$, radicals, quinone and chloride ligands potentially relevant to PS II

Chandan Mukherjee, Thomas Weyhermüller, Karl Wieghardt and Phalguni Chaudhuri, Dalton Trans., **2006**, 2169-2171.

Examination Committee:

Prof. Dr. W. Bremser

Prof. Dr. K. Huber

Prof. Dr. G. Henkel

Prof. Dr. P. Chaudhuri

Examination: 7th August, 2006.

Contents:

Chapter 1:

Introduction, Background and Objectives

1.1	Introduction	3-4
1.2	Background	5-16
1.3	Objectives	17-20
1.4	References	21-23

Chapter 2:

Synthesis, Characterization and Catalytic Reactivity of Transition Metal Complexes formed with N, N'-bis (2-hydroxy-3,5-di-tert-butylphenyl)-2,2'-diaminobiphenyl amine, (H₄L)

2.1	Synthesis and characterization of the ligand (H₄L)	27-28
2.2	Methoxide bridged dinuclear non-oxovanadium (V) complex (1)	29-33
2.3	Five coordinate square pyramidal high-spin Fe(III) complex(2)	34-40
2.4	Distorted square planar Ni(II) and Pd(II) complexes(3 and 4)	41-50
2.5	Distorted square planar Cu(II) complex(5) and its catalytic reactivity	
	2.5.1 Synthesis and characterization of the complex (5)	51-56
	2.5.2 Catalytic reactivity, Aerial oxidation of benzylalcohol; mimicking the function of Galactose Oxidase	57-63
2.6	References	64-67

Chapter 3:

Synthesis, Characterization and Catalytic Reactivities of the Tetracoordinate Cu(II)-Complexes formed with the Ligands, N(2-hydroxy-3,5-di-tert-butylphenyl)-3,5-di-substituted-aniline, H_2L^X ($X = -CF_3, -F, -Cl, -OMe, -tBu$)

3.1 Introduction	72-73
3.2 Synthesis and characterization of ligands and complexes	73-85
3.3 Catalytic reactivities, aerial oxidation of benzyl alcohol, ethanol and methanol; mimicking the function of Galactose Oxidase	86-90
3.4 References	91-91

Chapter 4:

Synthesis, Characterization and Catalytic Reactivity of Polynuclear Transition Metal Complexes formed with N (2-hydroxy-3,5-di-tert-butylphenyl)-2-aminobenzylalcohol, $H_3L^{CH_2OH}$

4.1 Synthesis and characterization of the ligand ($H_3L^{CH_2OH}$)	94-96
4.2 Alkoxide bridged dinuclear oxovanadium (V) complex (1)	97-102
4.3 A trinuclear Mn-cluster(2)	103-109
4.4 A Cu_4O_4 cubane complex (3)	
4.4.1 Synthesis and characterization of the complex (3)	110-121
4.4.2 Catalytic reactivity, Aerial oxidation of 2-aminophenol; mimicking the function of Phenoxazinone Synthase	122-125
4.5 References	126-127

Chapter 5:

Synthesis, Characterization and Catalytic Reactivities of a Monoradical-Containing Mononuclear Mn(IV) complex

5.1 Synthesis and characterization of the ligand ($\text{H}_3\text{L}^{\text{COOH}}$)	130-131
5.2 Synthesis and characterization of the complex (1)	132-138
5.3 Catalytic reactivities,	
5.3.1 Aerial oxidation of primary amines; mimicking the function of Amine Oxidases	139-142
5.3.2 Aerial oxidation of 2-aminophenol; mimicking the function of Phenoxazinone Synthase	143-146
5.4 References	147-148

Chapter 6:

Conclusions and Perspectives

6.1 Conclusions	154-156
6.2 Perspectives	157-158

Chapter 7:

Equipment and Experimental work

7.1 Methods and equipments	162-164
7.2 Experimental works	
7.2.1 Synthesis of ligands	165-168
(i) Synthesis of N, N'-bis(2-hydroxy-3, 5-di- <i>tert</i> -butylphenyl)- 2,2'-diaminobiphenyl compound (H_4L)	
(ii) Synthesis of N(2-hydroxy-3,5-di- <i>tert</i> -butylphenyl)- benzylalcohol compound ($\text{H}_3\text{L}^{\text{CH}_2\text{OH}}$)	
(iii) Synthesis of N(2-hydroxy-3,5-di- <i>tert</i> -butylphenyl)- anthanilic acid compound ($\text{H}_3\text{L}^{\text{COOH}}$)	

7.2.2 Synthesis of complexes **169-179**

- (i) Synthesis of $[\text{V}(\text{L})(\mu_2\text{OMe})_2(\text{L})\text{V}]^0$
- (ii) Synthesis of $[\text{Fe}(\text{HL}^\bullet)\text{Cl}]^0$
- (iii) Synthesis of $[\text{Ni}(\text{L}^{\bullet\bullet})]^0$
- (iv) Synthesis of $[\text{Pd}(\text{L}^{\bullet\bullet})]^0$
- (v) Synthesis of $[\text{Cu}(\text{L}^{\bullet\bullet})]^0$
- (vi) Synthesis of $[\text{Cu}(\text{L}^\bullet)][\text{PF}_6]$
- (vii) General method for the Synthesis of Cu(II) complexes
 , $[\text{Cu}(\text{L}^{\text{X}\bullet})_2]$ formed with $\text{H}_2\text{L}^{\text{X}}$ ligands
- (viii) Synthesis of $[\text{V}_2\text{O}_2(\text{L}_{\text{Cat}}^{\text{CH}_2\text{OH}})_2]^0$
- (ix) Synthesis of $[\text{Mn}_3(\text{L}_{\text{SQ}}^{\text{CH}_2\text{OH}\bullet})_2(\text{L}_{\text{Cat}}^{\text{CH}_2\text{OH}})(\text{L}_{\text{BQ}}^{\text{CH}_2\text{OH}})\text{Cl}]^0$
- (x) Synthesis of $[\text{Cu}_4(\text{L}_{\text{SQ}}^{\text{CH}_2\text{OH}\bullet})_4]^0$
- (xi) Synthesis of $[\text{Mn}(\text{L}_{\text{SQ}}^{\text{COOH}\bullet})(\text{L}_{\text{Cat}}^{\text{COOH}})][\text{HNEt}_3]$

7.2.3 Reactivity studies **170-182**

Appendices: **186-202**

- (1) Crystallographic data
- (2) Magnetochemical data
- (3) Curriculum Vitae

Abbreviations:

Technical terms:

AF : antiferromagnetic
Ag / AgNO₃ : reference electrode
av. : average
B : magnetic field
CT : charge transfer
D : zero-field splitting
deg. : degree (°)
e- : electron
E : total energy
exp. : experimental
Fc⁺/Fc : internal electrochemical standard
H : Hamiltonian
J : coupling constant (cm⁻¹)
m/z : mass per charge
RT : room temperature (298 K)
S : electron spin
sim. : simulated
TIP : temperature independent paramagnetism

Units:

Å : angstrom (10⁻¹⁰ m)
cm : centimeter
emu : electromagnetic unit
G : gauss
h : hour
K : Kelvin
m : meter
M : molar
min. : minute
mm : millimeter

nm : nanometer (10^{-9} m)

s : second

T : tesla

V : volts

μ_B : bohr magnetron

Symbols:

λ : wavelength (nm)

ε : extinction coefficient ($M^{-1}cm^{-1}$)

μ_{eff} : magnetic moment (μ_B)

δ : Isomer shift (mm/s)

ΔE_Q : quadrupole splitting (mm/s)

Solvents and reagents:

TBAPF₆ : tetrabutylammonium hexafluorophosphate, supporting electrolyte

Cat.: catechol

SQ : iminosemiquinone

BQ : iminobenzoquinone

CH₂Cl₂ : dichloromethane

CHCl₃ : chloroform

Et₂O : diethylether

Et₃N : triethylamine

EtOH : ethanol

HCl : hydrogen chloride

KBr : potassium bromide

MeOH : methanol

MeCN : acetonitrile

Techniques:

CV : cyclic voltammetry

EA : elemental analysis

EI : electron ionisation

EPR : electron paramagnetic resonance

ESI : electrospray ionisation

IR : infrared spectroscopy

MS: mass spectroscopy

SQUID : superconducting quantum interface device

SWV : square wave voltammetry

UV-VIS/NIR : ultraviolet-visible/ near infrared spectroscopy

p.i : Paramagnetic impurity

Latin expressions:

ca. : around

et al. : and co-workers

e.g. : for example

i.e. : namely

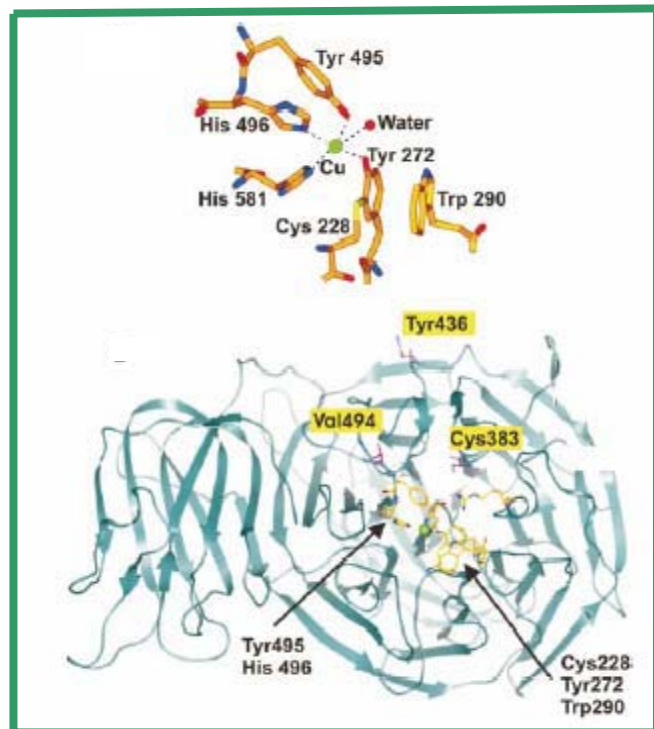
tert- : tertiary

vs. : versus, against

via : through

Chapter 1

Introduction, Background and Objectives



1.1 Introduction

Bioinorganic chemistry constitutes the discipline at the interface of the more classical areas of inorganic chemistry and biology.¹ Although biology is generally associated with organic chemistry, inorganic elements and especially metal ions are essential to life processes. Bioinorganic chemists study these inorganic species, with special emphasis on how they function *in vivo*. Inorganic elements have also been artificially introduced into biological systems as probes of structure and function. Bioinorganic chemistry thus has two major components namely the study of the naturally occurring inorganic elements in biology and the introduction of metals into biological systems as probes and drugs. Metalloenzymes are a subclass of metalloproteins that perform specific catalytic functions. Many metalloenzymes catalyze reactions that involve either oxidation or reduction of substrates. In most of these enzymatic catalytic processes aerial oxygen plays a crucial role to bring the enzyme to its initial active form.

Widespread occurrence of amino-acid radicals in enzyme catalysis is now well documented.²⁻⁶ Enzymes containing amino-acid radicals are generally associated with transition metal ions typically iron, manganese, cobalt or copper. In some instances the metal is absent; it is apparently replaced by redox-active organic cofactors such as *S*-adenosylmethionine or flavins. Functionally, their role is analogous to that of the metal ion in metalloproteins. The metal ion containing active sites help to generate and stabilize the amino-acid radical and the radical, in turn, initiates catalysis by abstracting a hydrogen atom from the substrate. There are embellishments to this principle. Nevertheless, leaving aside Photosystem II, the general scheme of ‘metal generates radical that initiates catalysis by hydrogen-atom abstraction’ remains the underlying principle. Tyrosine-based radical enzymes are among the best characterized.⁶⁻⁷ The tyrosine residue functions as a redox-active cofactor by interconverting between the oxidized phenoxyl radical and the normal phenol or phenolate states. The fungal enzymes galactose oxidase, amine oxidases, cytochrome c oxidase, etc. are examples of the enzymes that use both tyrosine residues and metals as partners in affecting redox chemistry.

The field of biomimetic chemistry covers a large area, quite as large as biochemistry itself. Non-exhaustively, we can emphasize the following topics: (i) abiotic models for the active sites of enzymes, (ii) models for biological processes.

Abiotic models may serve: (i) to elucidate structures of biomolecules (enzymes) not known or partially known to date, (ii) to elucidate biological mechanisms which remain black boxes (still unknown), (iii) to prepare authentic reagents (catalysts) usable for chemical

syntheses. The applied fields that ensue may be: (i) new catalysts (syntheses), (ii) new drugs (medicinal chemistry), (iii) new nutrients (agrochemistry), (iv) tools for biological studies. It should also be emphasized that biomimetic chemistry not only serves biology, but may also be a conceptual approach for chemical problems. As an example, organic syntheses may be inspired by known biosynthetic pathways.

Two types of models for the active sites in metalloenzymes can be envisaged: structural models and functional models (of course, ideal models are relevant to both types!). Structural models for the active sites in metalloenzymes can be used to help the determination of the active site molecular structure. The design of these models starts from partial spectroscopic data concerning the enzyme itself and from the ensuing hypothesis for the molecular formula of the active site. The comparison of the spectroscopic data obtained from the model and from the enzyme respectively, confirms or invalidates the hypothesis. So, step by step, the hypothesis for the active site structure is improved. A lot of structures have been established by this approach, which has been further confirmed by crystallographic structural determinations. Structural models may also be functional models. Mimicking the known (crystallographic data) structure of the active site of the enzyme can lead to models that exhibit the catalytic function of the enzyme. These models may be valuable catalysts for syntheses. They are also tools for studies concerning the enzymatic mechanism: some transient species are often involved for a given enzymatic catalytic cycle, which are more or less characterized. Good models for these reaction intermediates may be key steps for the understanding of the enzymatic processes.

The design of functional models for redox metalloenzymes can start from the known, partially known or unknown structure of the active site of the enzyme. The stoichiometry of the catalyzed reaction and the products of the reaction are the only properties which have to be known.

Thus, the study and modeling of the active site of metalloproteins is a field of great interest within the scientific community. Indeed, proteins containing iron, manganese, cobalt or copper ions at the active sites are mainly involved as redox catalysts in the range of biological processes, such as electron transfer, dioxygen transport, Photosystem II and oxidation of various bio-substrates. New and very effective bio-inspired homogeneous catalysts for common reactions under mild conditions may be discovered.⁸

1.2 Background

Galactose Oxidase (GO_{ase}) from filamentous *heat-rot* fungus *Fusarium ssp.* was first isolated in 1959,⁹ that selectively catalyzes the aerial oxidation of primary alcohols to the corresponding aldehydes with concomitant reduction of molecular oxygen to hydrogen peroxide (eq 1).¹⁰



GO_{ase} is a single polypeptide with a molecular mass of 68.5 kDa, and is unusual because, in contrast to most copper proteins that affect multi-electron redox reactions by using multinuclear active sites, GO_{ase} uses an isolated single copper center to carry out the required two-electron redox chemistry.

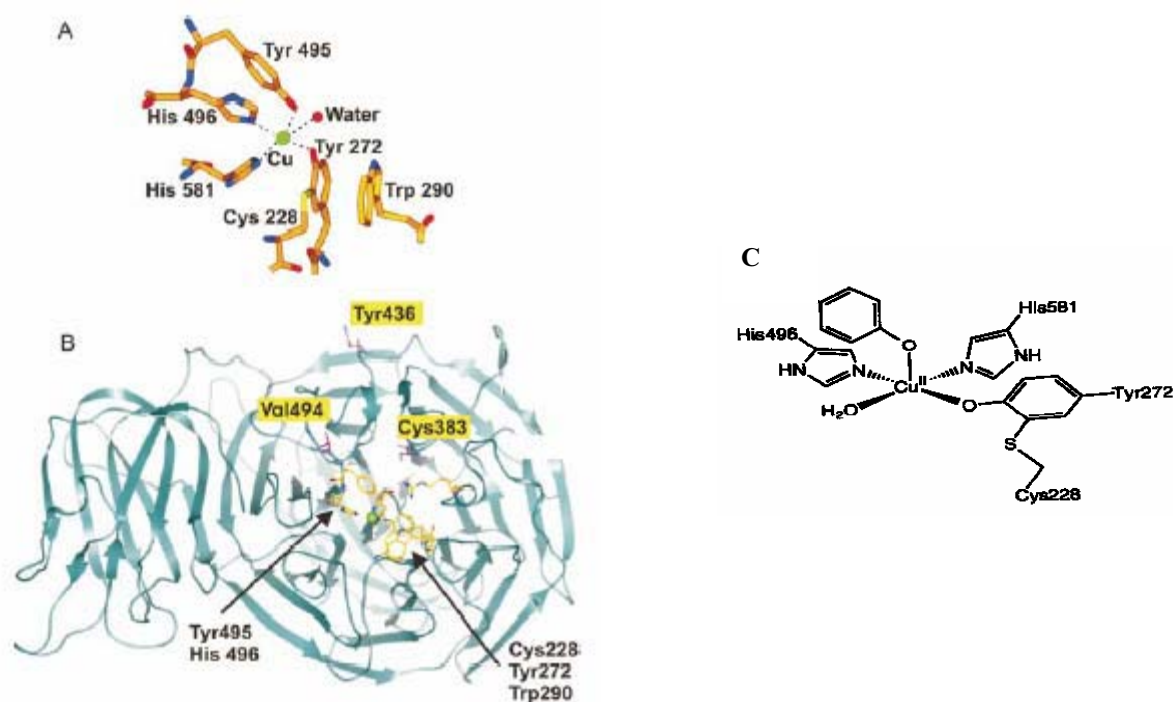


Figure 1.1. Structure of GO_{ase} . (A) The active site showing the copper ligands, the thioether bond between Tyr272 and Cys228, and the stacking interaction with Trp290. (B) An overview of the GO_{ase} monomer showing domains 1 and 2 and showing the locations of the residues Cys383, Tyr436 and Val 494 (shown in mauve and highlighted by yellow labels), which form the basis of the present study. The active site residues are shown in atom colouring and are labelled by arrows. Non-covalent bond interactions are shown as dotted lines.¹¹⁻¹² (C) Schematic diagram of GO_{ase} .

The copper ion is square pyramidal, with the tyrosinate ligand (or protonated form) weakly bound in the axial position and two histidine imidazole ligands, a second tyrosinate, and either water (pH 7) or acetate (from buffer, pH 4.5)¹²⁻¹³ in the equatorial sites, the latter being the binding site of the substrate to the copper center. Interestingly, the equatorial tyrosinate is linked to a nearby cysteine via an *ortho* C–S bond to afford a thioether-modified phenolate ligand (Y272-C228), which is within π -stacking distance of a tryptophan residue (Figure 1.1). The active site of GO_{ase} contains one copper (II) ion and a tyrosine 272 radical. Hence, two redox sites are present in the active form of this mononuclear metalloenzyme. The mechanism of GO_{ase} is now well established (Figure 1.2).¹⁴⁻¹⁶ As a first step of the catalytic process, an alcoholate is formed through the deprotonation of the substrate by the axial tyrosinate ligand. In the next reaction step, a hydrogen atom

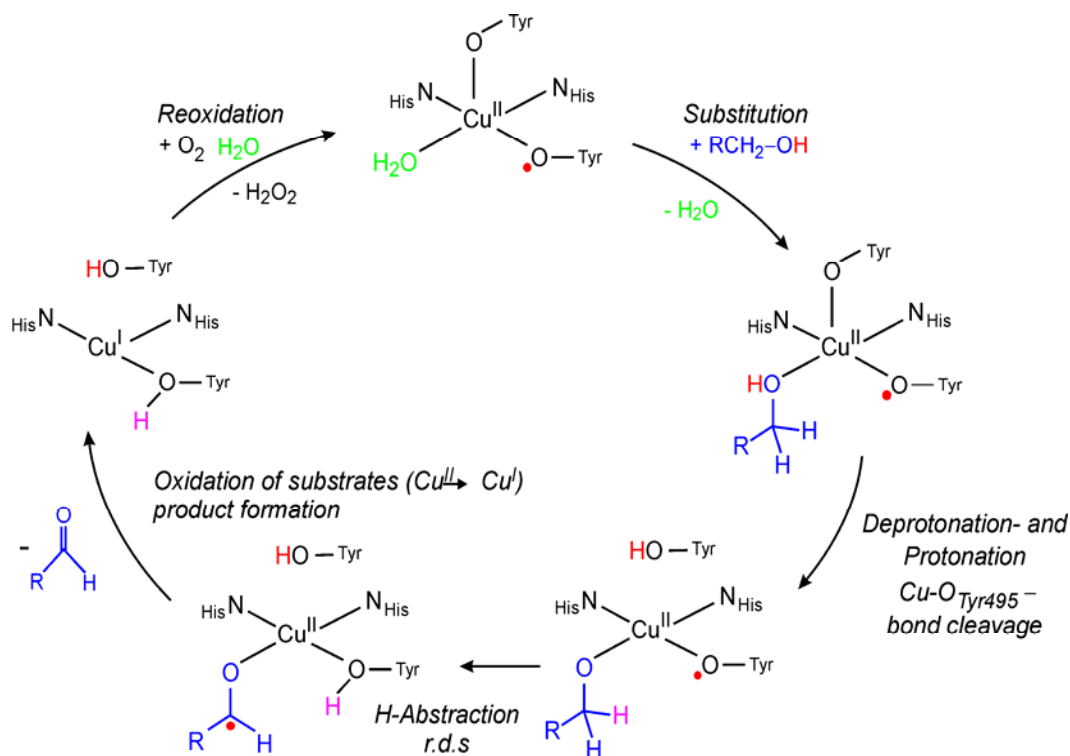
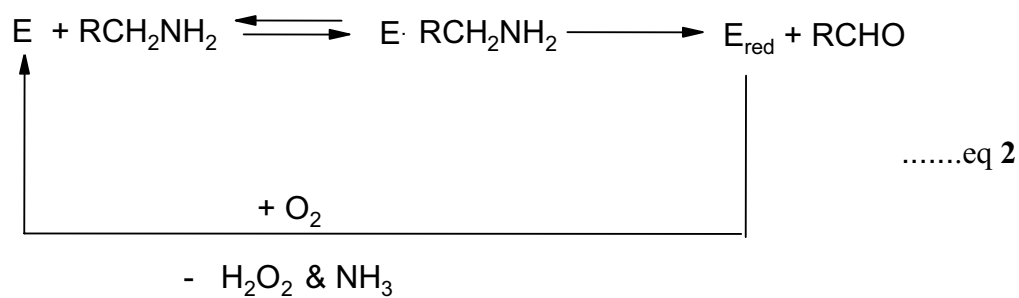


Figure 1.2. The proposed mechanism for Galactose Oxidase.¹⁴

is abstracted from the substrate to the equatorial tyrosine 272 radical and subsequently or simultaneously the copper center is reduced to Cu(I) by the single electron transfer from the ketyl radical. The catalytic cycle is closed by recovering the initial copper oxidation state under concomitant reduction of molecular oxygen to hydrogen peroxide. Measurement of the

kinetic isotope effect (KIE) reveals that the H-atom abstraction from the α -C atom of the coordinated substrate is rate limiting for this catalytic process.

Another copper-containing mononuclear metalloenzyme is Amine Oxidase (AOs), which catalyzes the oxidative deamination of amines to the corresponding aldehydes, with subsequent reduction of molecular oxygen to hydrogen peroxide (eq 2).¹⁵



Amine Oxidases can be divided into two groups based on the cofactors they utilize, quinone and copper containing Amine Oxidases (CuAOs) (Figure 1.3, 1.4) and flavin-dependent mono Amine Oxidases (MAOs). MAOs can oxidize primary, secondary, and tertiary amines either by concerted covalent catalysis or by a single electron transfer mechanism, both requiring flavin adenine dinucleotide (FAD) as a cofactor.¹⁷⁻¹⁸ Quinone copper containing Amine Oxidases generally oxidize primary amines and can be subdivided based on the cofactor present in the active site. The first group contains 2,4,5-trihydroxyphenylalanine quinone (TPQ) or topa-quinone, which is produced by post-translational modification of an invariant tyrosine residue (Figure 1.5.i).²¹ The second class of quinone copper-containing amine oxidases uses lysyl tyrosyl quinone (LTQ) as their cofactor and are referred to as lysyl oxidases (Figure 1.5.ii).

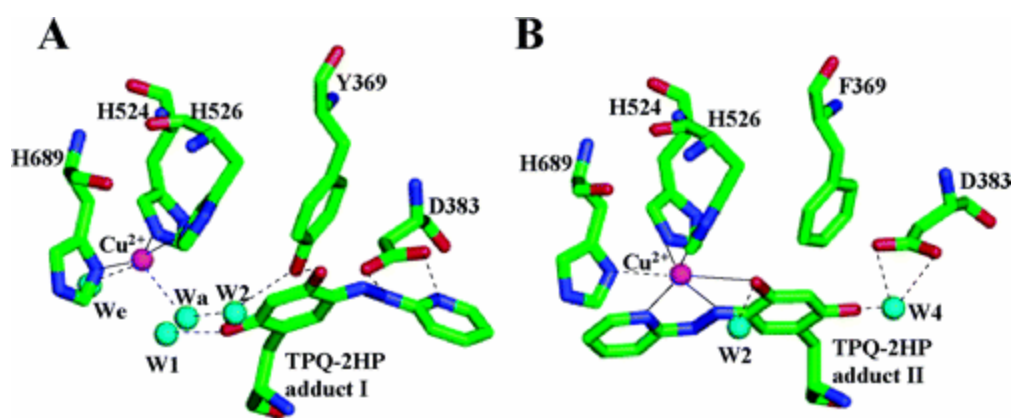


Figure 1. 3. Crystal structures of WT-ECAO adduct I (A) and Y369F adduct II (B) (magenta sphere, copper; blue spheres, water).²⁰

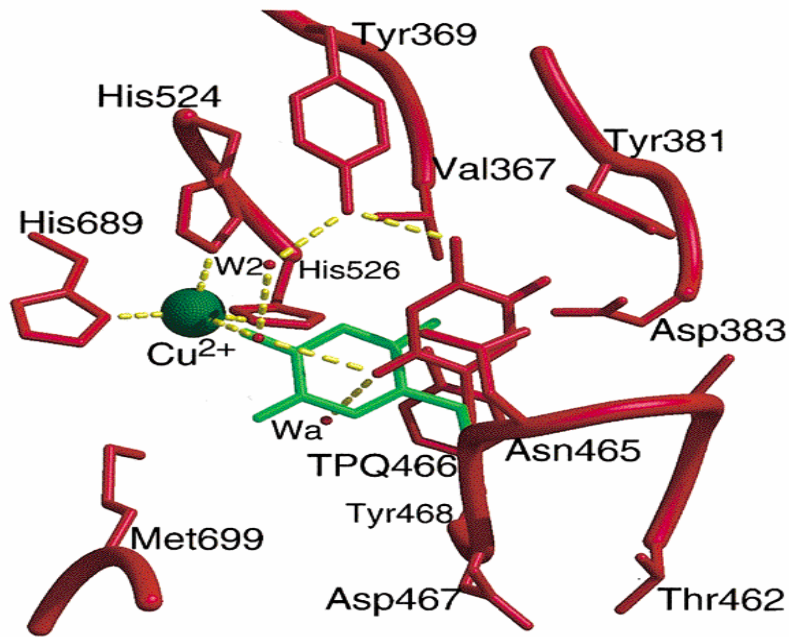


Figure 1. 4. Active site of *E. coli* copper Amine Oxidase.¹⁹

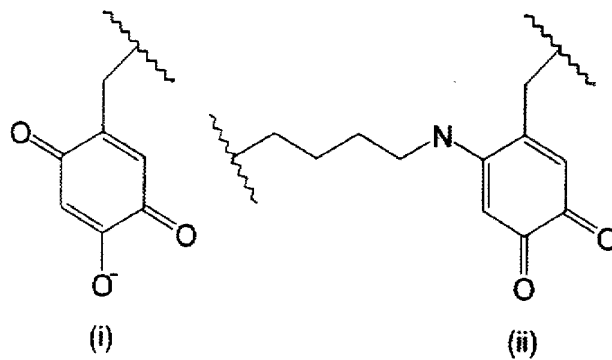


Figure 1.5. (i) 2,4,5-trihydroxy-phenylalanine quinone (TPQ) (ii) lysyl tyrosyl quinone (LTQ).

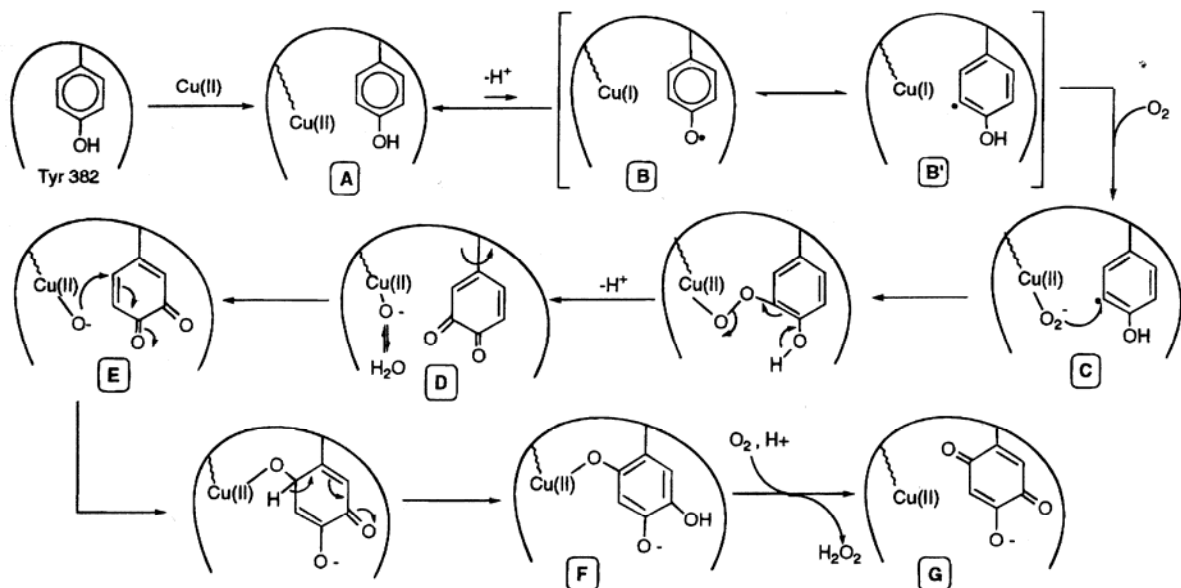


Figure 1.6. Mechanism for the biogenesis of the TPQ cofactor in Phenylethylamine Oxidase (PEAO).

For the biogenesis of the TPQ cofactor from tyrosine residue (Figure 1.6), copper (II) initially binds to the apoprotein to give a copper (II)-enzyme complex (A). The complex exists in equilibrium with a copper (I)-tyrosine radical (B). In the next step copper (I) ion reacts with dioxygen to produce an activated oxygen complex, which is copper (II)-superoxide (C). This activated complex attacks the tyrosine radical to yield dopa quinone (D). This copper oxide/ hydroxide species may be in rapid exchange with solvent water, allowing solvent oxygen incorporation in TPQ. Rotation about the β -carbon would move the C2 ring near the copper bound oxidase (E). Nucleophilic attacks by the copper oxide on the dopa quinone would yield topa (F). In presence of dioxygen, topa would then rapidly be oxidized to TOQ (G).

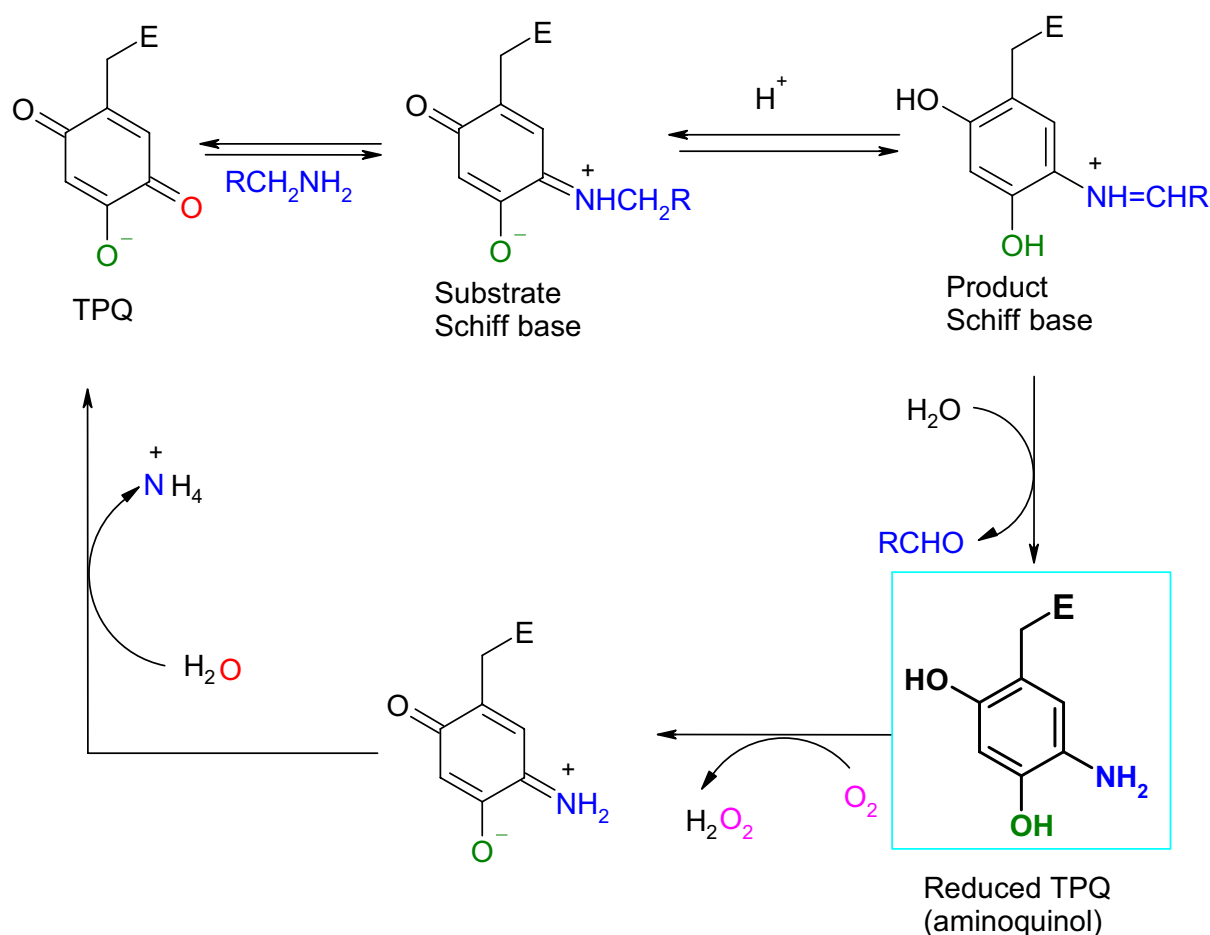
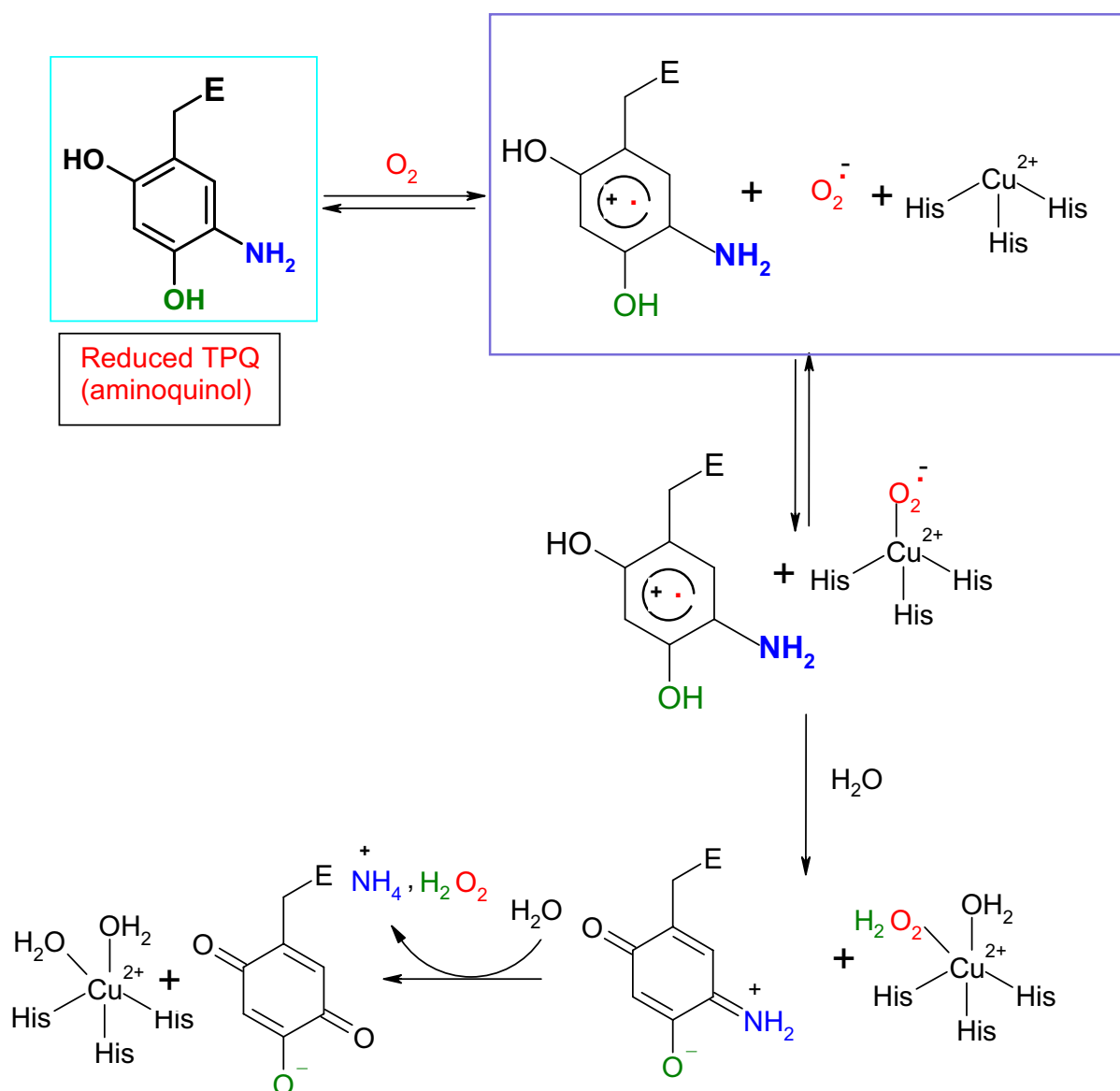


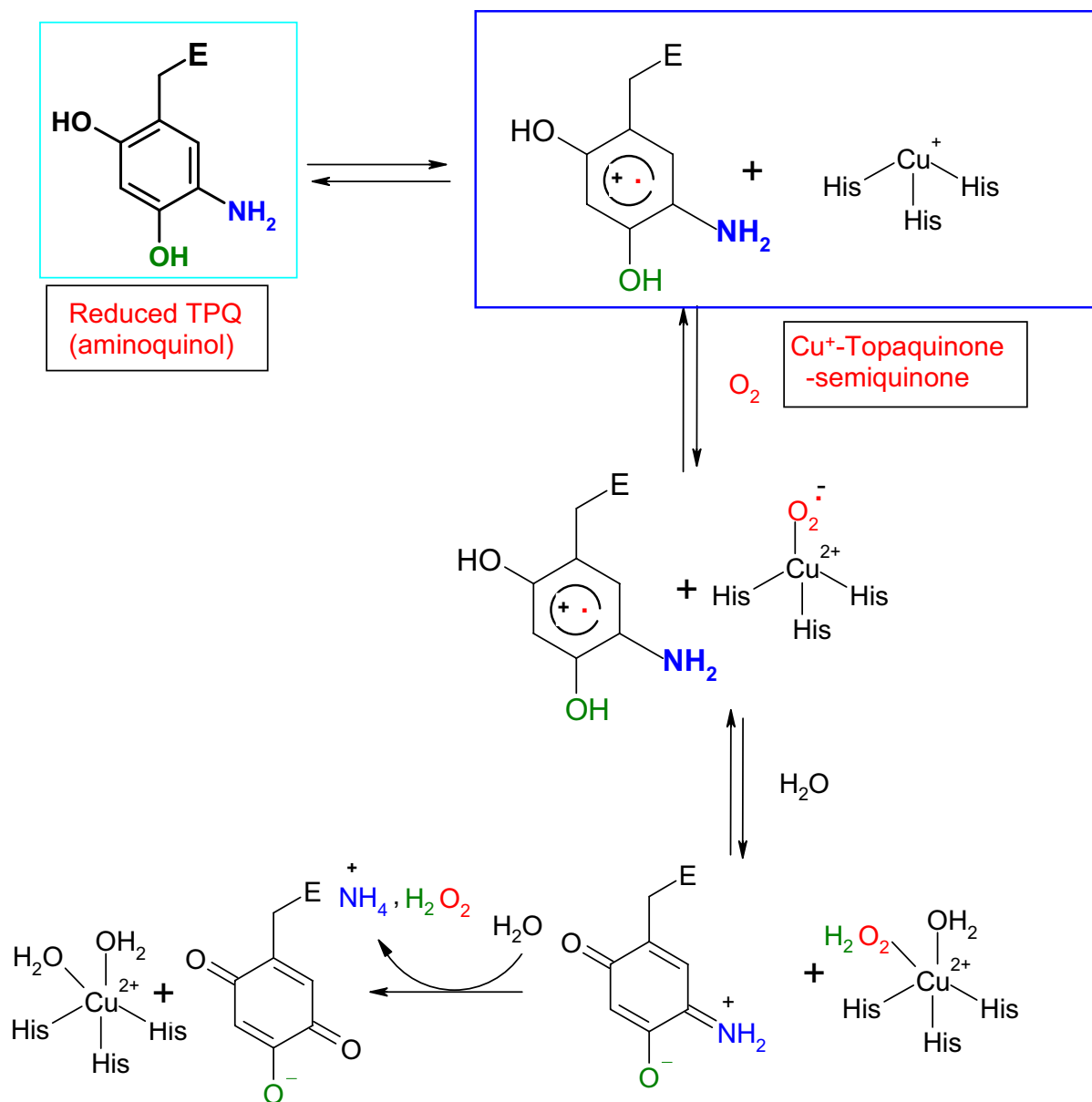
Figure 1.7. The proposed mechanism for Amine Oxidases.¹⁴

The role of the TPQ cofactor in amine oxidation is well understood. To start the reductive half reaction, TPQ reacts with the substrate amine to form the substrate schiff base, activating the C-1 proton of the substrate for abstraction. Proton abstraction results in the product schiff base (PSB), with reduction of the cofactor. Hydrolysis of this intermediate releases the aldehyde product, leaving the enzyme in aminoquinol form (TPQ_{red}). In the oxidative half-reaction, oxygen interacts with TPQ_{red} to produce hydrogen peroxide and iminoquinone.



Scheme A. The proposed mechanism for the oxidative half reaction viz. direct involvement of oxygen.

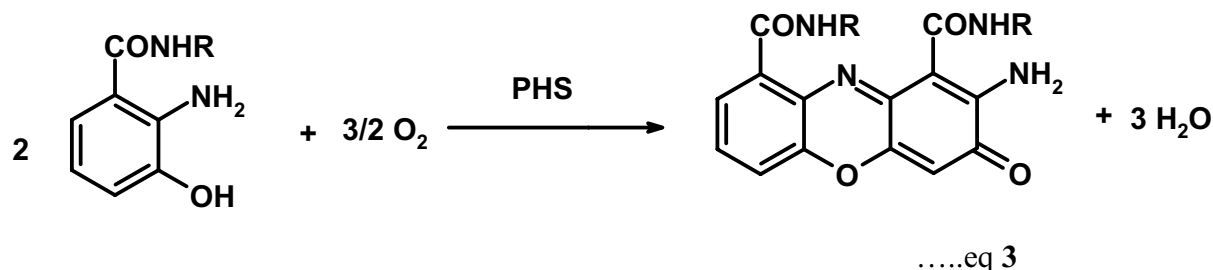
Finally, hydrolysis of the iminoquinone releases ammonia and regenerates TPQ_{ox} (Figure 1.7). Detailed spectroscopic and kinetic studies show that only TPQ cofactor takes part in the reductive half-reaction.²²⁻³⁰ The mechanism of the oxidative half-reaction is less well understood. During this half reaction it has been proposed that the TPQ_{red} cofactor is either oxidized directly by oxygen (Scheme A), or oxidised indirectly via the active site copper (Scheme B).



Scheme B. The proposed mechanism for the oxidative half reaction viz. the active site copper(II).

In the first scenario, oxygen is bound in a non-metal site prior to reaction with reduced cofactor, whereas in the second proposal the copper (II) takes one electron from aminoquinol to produce copper (I) and TPQ-semiquinone form. The evidence for the later proposal consists of direct observation of the copper (I)-semiquinone species by EPR spectroscopy in anaerobic conditions, in the substrate-reduced enzyme from various sources. Support for the former hypothesis includes extensive kinetic experiments with bovine serum amino oxidase (BSAO). It is quite clear the copper (II) center in the active site of amine oxidases not only converts the tyrosine residue to topa quinone (TPQ) but also plays a crucial role for the oxidative half-reaction.

Phenoxazinone synthase (PHS), an oligomeric multicopper oxidase produced by *streptomyces antibioticus*, is responsible for the six-electron oxidative coupling of two molecules of 4-methyl 3-hydroxy anthraniloyl petapeptide to form antineoplastic agent actinomycin D (eq 3).^{31a}



PHS exists in two different forms. One is a dimeric form and the other is a hexameric form. The dimers and hexamers are distinct stable molecular forms and are not related by a simple equilibrium-aggregation phenomenon. The regulation and structural differences between these two oligomeric forms is currently unknown. The hexameric form is much more catalytically active than that of the dimeric form, probably due to the accessibility of the active site, geometry of the copper centers, and the availability of the proper solvent channels. Recently, J. P. Allen, W. A. Francisco and co-workers^{31b} have published an incomplete but conclusive crystal structure of the hexameric form of PHS.

The hexameric form consists of six equivalent subunits which are not crystallographically related but follows an approximate 6-fold rotation about the center. Figure 1.8 shows the structure of the hexameric form.

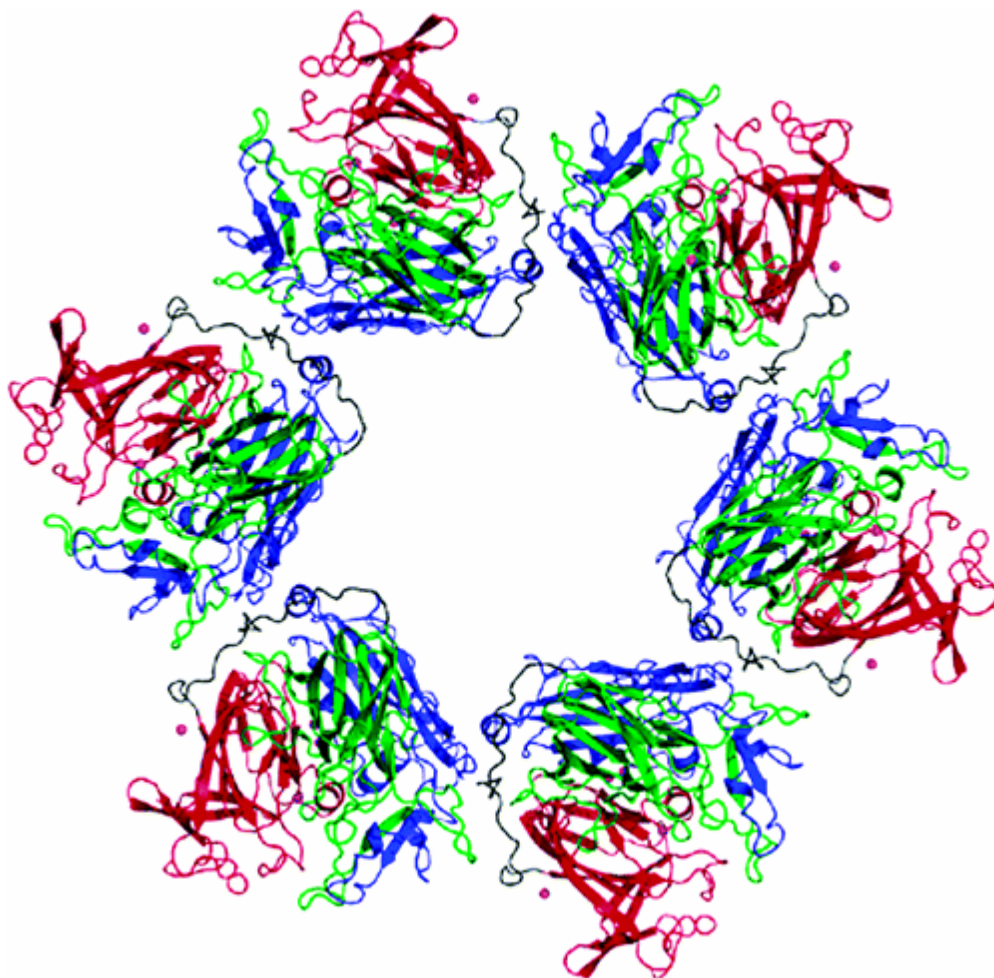


Figure 1.8. Hexameric structure of PHS. The cross-sectional diameter is 185 Å with a 50 Å inner cavity that is unoccupied. The exterior of the hexamer is formed by domain 3 (red), with domain 1 (blue) largely forming the interior as well as the protein-protein contact region with domain 2 (green). The copper cofactors (purple) as well as the coordinating ion or molecule *X* and water molecule (red) are shown as spheres. Note that the loop extending from domain 1 to 2 (black) contributes to the binding site between the subunits.

Each subunit of the hexamer contains five copper atoms as speculated earlier by spectroscopic studies.³²⁻³³ These copper atoms form one mononuclear type 1 center, two mononuclear type 2 centers, and one binuclear type 3 center.

The type 1 center, identified as Cu1, has distorted square pyramidal geometry with His524, His608, Cys603, Met613 and a missing axial ligand common to type 1 copper centers. Among these residues, only axial methionine ligand is not conserved among the multicopper oxidases. The type 1 copper center is ~12.5 Å away from Cu2 of the type 3 center and depicted in Figure 1.9. The type 1 copper center is connected to type 3 center through the HCH motif that facilitates the transfer of electrons between these two centers.

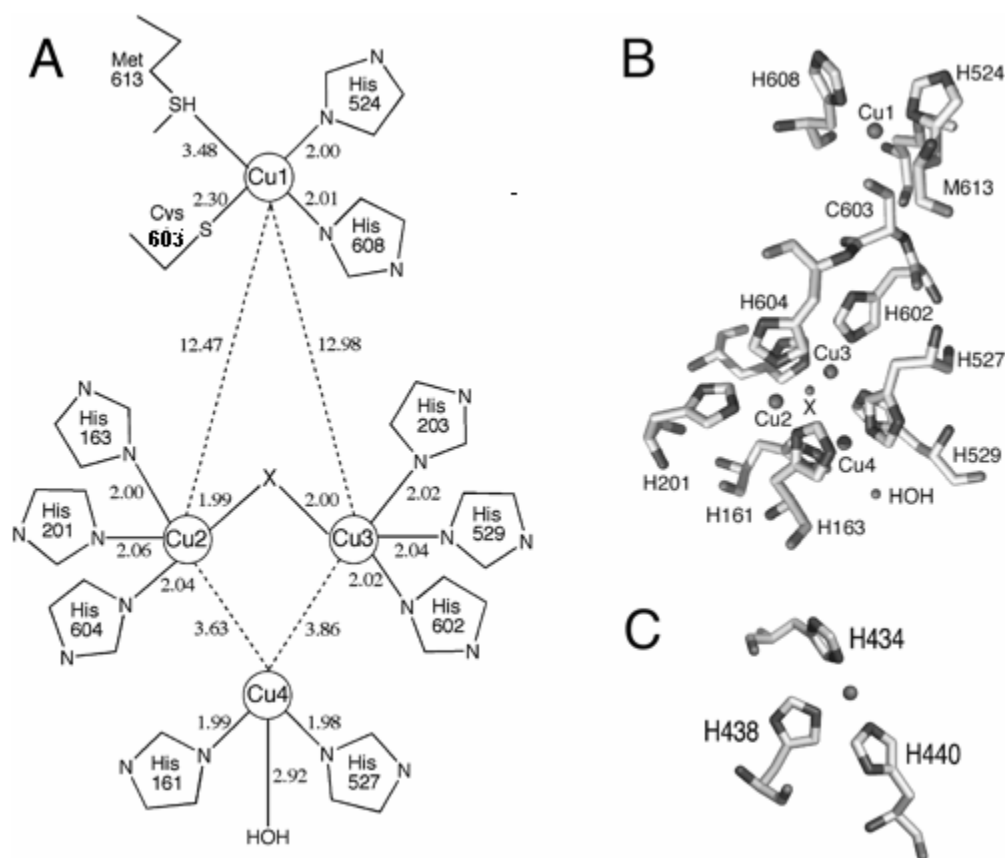


Figure 1.9. Copper centers including the coordinating ligands. (A) Diagram of the arrangement of the four conserved copper atoms, the distances to the ligating atoms, and the distances between the copper atoms. (B) Four conserved copper atoms and their surrounding ligands (shaded by atom type). (C) New type 2 copper atom and the three histidine ligands (shaded by atom type). X represents an unidentified bridging ligand such as OH.

The distance between two copper centers in the binuclear type 3 copper center is 3.88 Å. Two copper atoms of the unit are identified as Cu2 and Cu3 and are linked with each other via an unidentified molecule or group denoted by X. The Cu2-X-Cu3 bond angle is 153.13°. His163, His201 and His604 act as ligands to Cu2 center and His929, His203 and His602 are the ligands attached to the Cu3 center.

The copper atom of one of the type 2 centers, identified as Cu4, is 3.63 and 3.86 Å away from Cu2 and Cu3 centers, respectively. The Cu4 center is surrounded by His161, His527 and a water molecule.

The fifth copper atom, identified as Cu5, is part of type 2 center and bound at a loop that establishes interactions between the subunits of the hexamer and stabilises the form. The Cu5 center has T-shape coordination with three histidines and depicted in Figure 1.10. The distance between the Cu5 and both Cu1 and Cu4 centers is ~ 25 Å and is unlikely to play a role in the transfer of electrons to the substrates.

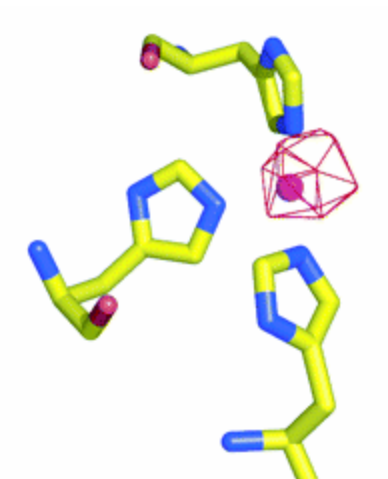
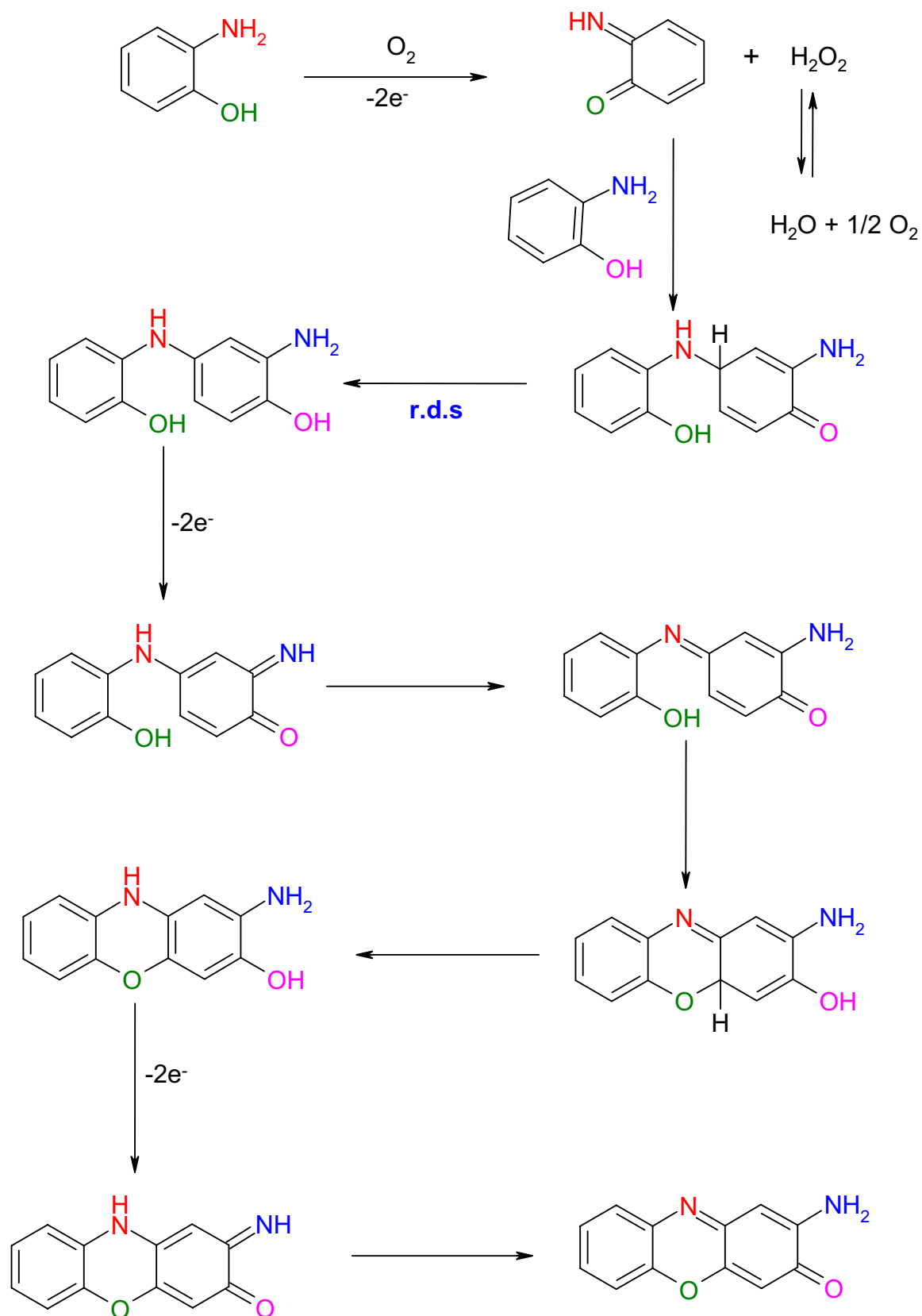


Figure 1.10. Stereoview; the three histidines, 434, 438, and 440, and the Cu5 center.

The type 2 centers seem to be involved in catalytic activity, and can be reduced by substrate under anaerobic conditions. The mechanism for the formation of the phenoxazinone chromophore is studied using isolated enzyme and the proposed mechanism is illustrated in Scheme C.³³⁻³⁴



Scheme C. The proposed mechanism for the formation of phenoxazinone chromophore by 6-electron oxidation of 2 molecules of 2-aminophenol.

1.3 Objectives

In 1991 Ito and co-workers characterized Galactose Oxidase crystallographically. Since then, structural and functional model compounds of Galactose Oxidase have drawn attention from bioinorganic chemists. The search for low molecular weight phenoxyl Cu(II) complexes as functional models for GO which would mimic this reactivity had a promising start in 1996 when Tolman and co-workers³⁵ reported a stoichiometric oxidation of benzyl alcohol to benzaldehyde by a phenoxyl radical complex. In the same year Wang and Stack³⁶ reported the first truly catalytic system, which in presence of a base and an oxidizing agent oxidizes benzyl alcohol to benzaldehyde with up to 10 turnovers. A different system was described by Pierre and co-workers in 1998.³⁷ They showed that the electrochemically one-electron oxidized phenoxyl radical complex electrocatalyzes, in the presence of KOH, the oxidation of primary alcohols to the corresponding aldehydes (where > 30 turnovers were observed).

In 1998 Stack³⁸ et al. and Chaudhuri, Wieghardt and co-workers³⁹ described the first biomimetic catalytic systems for the aerial oxidation of primary alcohols. Among the structural models of the active site of GO_{ase} described³⁵⁻⁴⁹ only a few contain two phenolic arms and involve the [N2O2] copper coordination sphere of the enzyme. Some of the functional models of GO_{ase} involve salen-type ligands and exhibit interesting catalytic activity only with activated alcohols as substrates. These model complexes do true GO_{ase} chemistry but are not, strictly speaking, structural models. The best results have been obtained by Chaudhuri, Wieghardt *et al.*^{39, 45,46} with a set of complexes in which the redox chemistry during the catalytic cycle is ligand based and the proposed mechanism is similar to the mechanism proposed for GO_{ase} itself.

Very recently, a few structural and functional models of GO_{ase} have appeared in literature⁵⁰⁻⁵² which uses a phenol containing tripodal ligand. The models mimics the native enzyme structurally and also the functional aspect by oxidizing primary alcohols to the corresponding aldehydes with moderate turnover numbers.

Functional as well as structural models for Amine Oxidases are very rare in literature. LARGERON *et al.*⁵³ have used controlled-potential electrolysis with an organic cofactor, 3, 4-azaquinone, to oxidize various primary amines. A copper containing functional model complex was reported by Chaudhuri *et al.*⁵¹ Investigations of the mechanism for the catalytic oxidative deamination of amines by amine oxidases is very important as functional model compound(s) and pure proteins do not provide clear ideas yet. The ambiguity regarding the mechanism arises in the oxidative half-reaction (Figure 1.11). W. Kaim *et al.*

have shown the existence of temperature-dependent valence tautomerism between copper(I)-semiquinone and Cu(II)-quinone forms.⁵⁴ It may be a clue that amine oxidases follow different mechanistic pathways at different temperatures. Hence, it is essential to investigate the above postulation with a good quality functional model complex of amine oxidases.

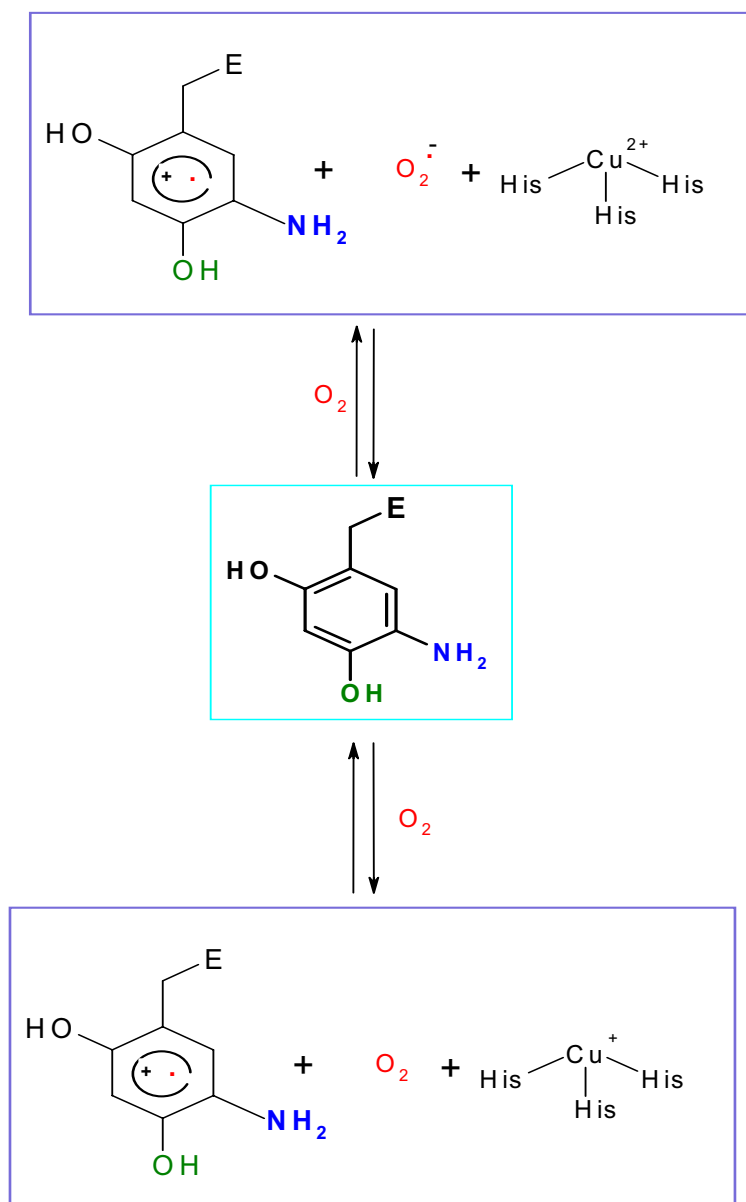


Figure 1.11. Two different mechanistic path ways for the oxidative half reaction for AOs.

Structural model compound(s) of Phenoxazinone Synthase has yet to be synthesized. A few functional models exist in the literature.⁵⁵⁻⁵⁹ In most of the cases oximatecobalt(II)⁵⁷ has been used. Oximateiron(II)⁵⁷ is also found as a good functional model for Phenoxazinone Synthase. The mechanism that has been proposed using model compounds for the formation

of the phenoxazinone chromophore from 2-aminophenol is a radical-mechanism.⁵⁵⁻⁵⁷ Though the formation of Phenoxazinone chromophore by catalytic activity of Phenoxazinone Synthase is an aerial oxidation process, molecular oxygen has been used together with functional model compounds to oxidize 2-aminophenol to 2-amino-phenoxazine-3-one.

It is important to note that the author L. I. Simándi⁵⁵⁻⁵⁶ has shown use of oximatecobalt(II), 2-aminophenol and molecular oxygen for not only catalytic activation of dioxygen but also for kinetics and mechanistic study of the catalytic oxidation of 2-aminophenol. It is quite clear that to have a functional model compound for Phenoxazinone Synthase aerial oxidation of 2-aminophenol is important. *Hence, a functional model that can have catalytic activity for aerial oxidation of 2-aminophenol to 2-amino-phenoxazine-3-one is necessary.*

The aim of this work is two fold: (i) to gain deeper insight into the electronic structure of the metal core and the ligand surrounding of these radical-containing complexes and, thereby, to better understand such metal-radical interactions in natural systems; and (ii) to explore the aerial-oxidation chemistry of well-characterized metal complexes, which is expected to provide the basis for new catalytic oxidation systems for synthetic and industrial processes.

To produce radical containing metal complexes, which will act as functional as well as structural model compounds of some radical containing metalloenzymes, e.g. Galactose Oxidase, Amine Oxidases etc. following non-innocent (which will change their redox property in the presence of metal ion and oxygen) ligands have been synthesised. These ligands are H_4L , H_2L^x , H_3L^{COOH} , $H_3L^{CH_2OH}$ (Figure 1.12).

The ligand H_4L was synthesized in order to prepare distorted square planar transition metal +II complexes. Owing to its steric constraint, radical-containing Cu(II) complex with distorted square planar geometry will be formed. The complex would be an ideal example to study the active site of GOase and also its function as a catalyst for aerial oxidation of alcohols.

Radical-containing Ni(II), Pd(II), Pt(II) complexes with distorted square planar geometry are important to find out the effect of distortion on the electronic structure to those of perfect or nearly perfect corresponding square planar complexes.

Furthermore the ligand, H_4L can be employed to prepare pentacoordinate square pyramidal or trigonal bipyramidal, or hexacoordinate-octahedral complexes with transition metals like iron, cobalt, manganese, chromium etc. These complexes are important in understanding metal-radical interactions and also as bio-inspired catalysis.

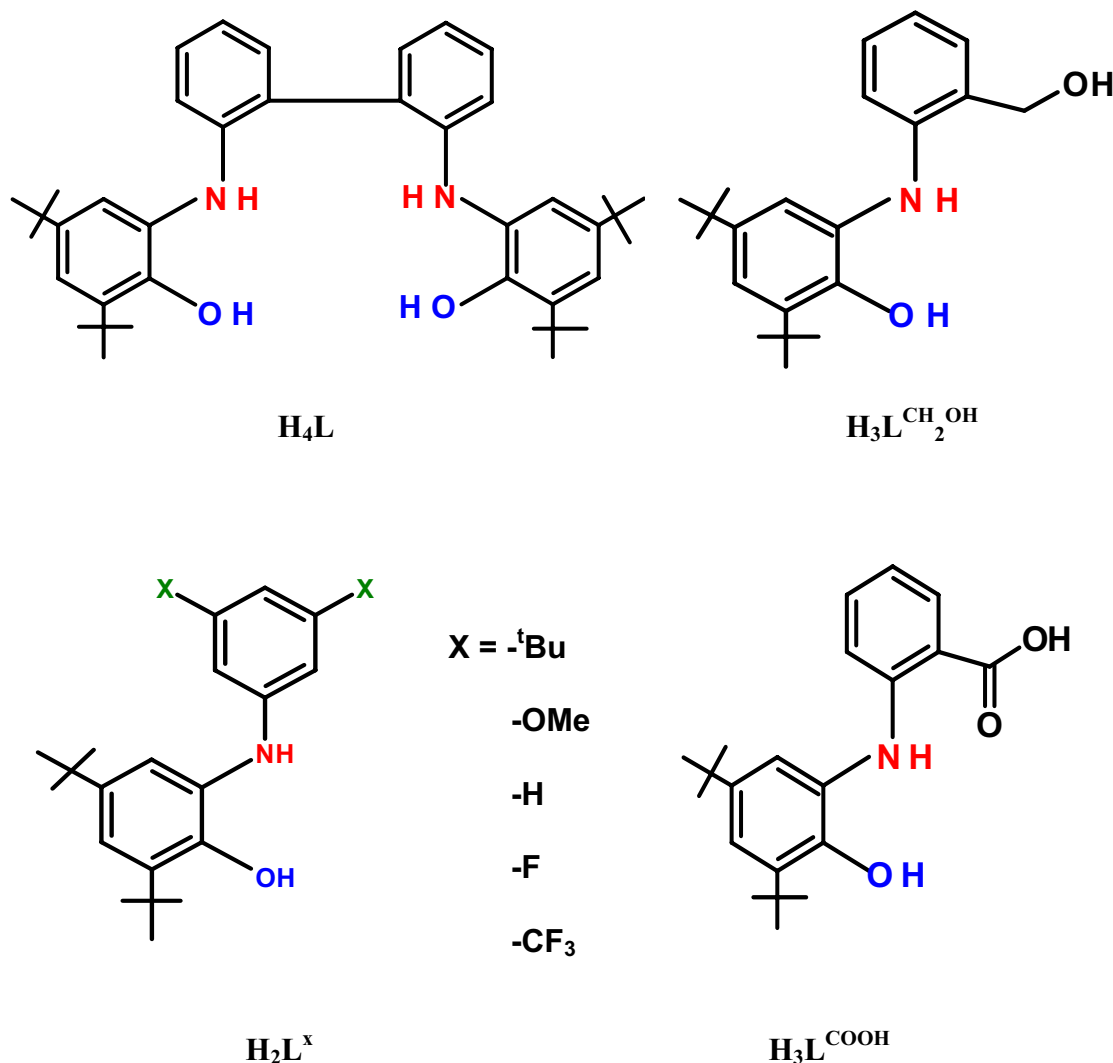


Figure 1.12. Sketch of ligands.

The ligands, $\text{H}_2\text{L}^{\text{X}}$, are bidentate ligands. These ligands may form square planar copper complexes with 2:1 ligand: metal ratio. To find out the effect of substituent on the geometry and the catalytic processes (if they catalyze aerial oxidations of alcohols or amines), a few ligands with electron donating or withdrawing groups at the 3,5-positions of the N-phenyl ring have been synthesized.

Besides synthesizing non-innocent tetradentate and bidentate ligands, tridentate ligands were synthesized, $\text{H}_3\text{L}^{\text{COOH}}$ and $\text{H}_3\text{L}^{\text{CH}_2\text{OH}}$. The ligand, $\text{H}_3\text{L}^{\text{CH}_2\text{OH}}$ may have a tendency to form polynuclear transition metal complexes in its deprotonated form containing an alcoholate group with a strong π -donor ability.

Contrary to the ligand, $\text{H}_3\text{L}^{\text{CH}_2\text{OH}}$, a weakly π -donating group (carboxylate) will be a part of the ligand, $\text{H}_3\text{L}^{\text{COOH}}$. Hence, formation of polynuclear transition metal complexes is less likely with the ligand, $\text{H}_3\text{L}^{\text{COOH}}$.

1.4 References

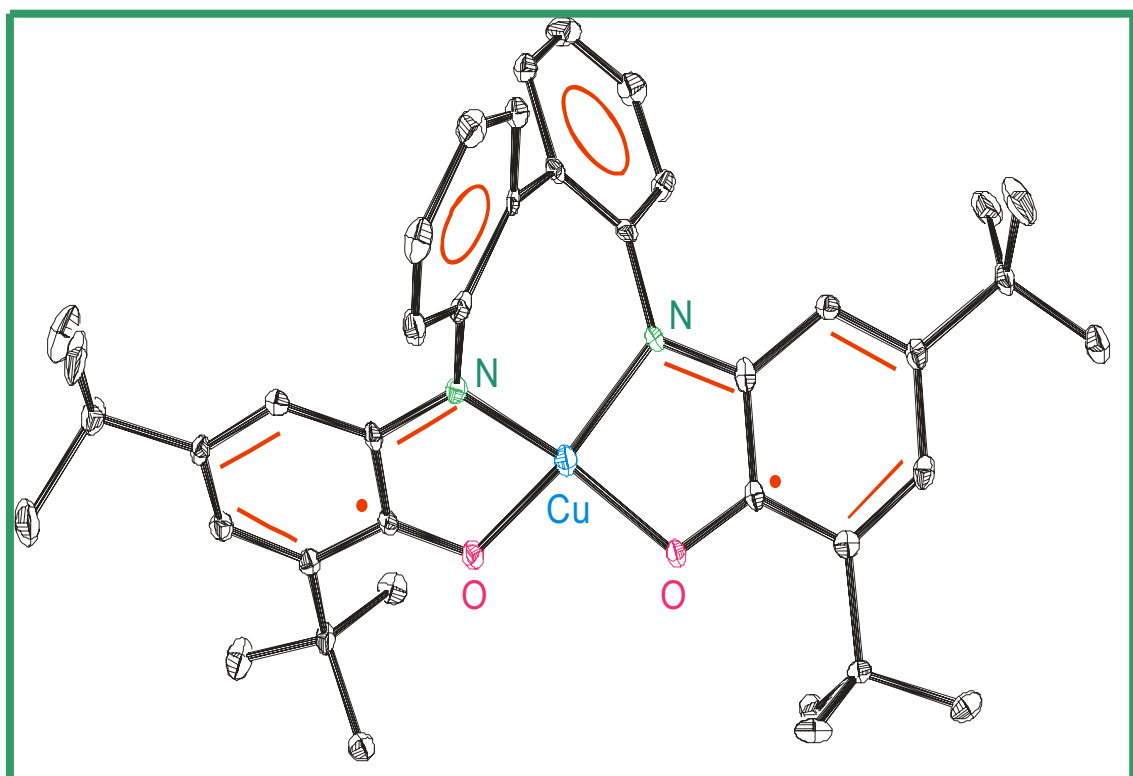
1. Lippard, J.S.; Berg, J.M.; *Principles of Bioinorganic Chemistry*; University Science Books, **1994**.
2. Sigel, H.; Sigel, A. *Metal Ions in Biological Systems*, Vol. 30, New York, Basel: Marcel Dekker. **1994**.
3. Fontecave, M.; Pierre, J.-L. *Bull. Soc. Chim. Fr.* **1996**, *133*, 653.
4. Babcock, G.T.; Espe, M.; Hoganson, C.; Lydak-Simantiris, N.; McCracken, J.; Shi, W.; Styring, S.; Thomas, C.; Warncke, K. *Acta Chem. Scand.* **1997**, *51*, 533.
5. Banerjee, R. *Chem. Rev.* **2003**, *103*, 2081.
6. Stubbe, J.; van der Donk, W. *Chem. Rev.* **1998**, *98*, 705.
7. Chaudhuri, P.; Wieghardt, K. *Prog. Inorg. Chem.* **2001**, *50*, 151.
8. Reedijk, J.; Bouwman, E.; *Bioinorganic Catalysis*, Marcel Dekker, Inc., **1999**.
9. Cooper, J. A. D.; Smith, W.; Bacila, M.; Medina, H.; *J. Biol. Chem.*, **1959**, *234*, 445.
10. Whittaker, J. W. *Chem. Rev.*, **2003**, *103*, 234.
11. Wilkinson, D.; Akumanyi, N.; Hurtado-Guerrero, R.; Dawkes, H.; Knowles, P.F.; Phillips, S.E.V.; McPherson, M.J. *Protein Engineering, Design & Selection* vol. 17 no. 2 pp. 141-148, **2004**.
12. Ito, N.; Phillips, S. E. V.; Stevens, C.; Ogel, Z.B.; McPherson, M. J.; Keen, J. N.; Yadav, K.D. S.; Knowles, P. F. *J. Mol. Biol.* **1994**, *238*, 794–814.
13. Ito, N.; Phillips, S.E.V.; Stevens, C.; Ogel, Z.B.; McPherson, M.J.; Keen, J.N.; Yadav, K.D.S.; Knowles, P.F. *Nature*, **1991**, *350*, 87.
14. Whittaker, W.; In: H. Sigel and A. Sigel, Editors, *Metalloenzymes Involving Amino Acid Residue and Related Radicals* **30**, Marcel Dekker, New York, **1994**.
15. Janes, S. M.; Mu, D.; Wemmer, D.; Smith, A. J.; Kaur, S.; Maltby, D.; Burlingame, A. L.; Klinman, J. P. *Science*, **1990**, *248*, 981.
16. Knowles, P.F.; Ito, N. *Perspectives on Bio-inorganic Chemistry*, vol. 2, Jai, London, **1993**.
17. Borman, C.D.; Saysell, A.; Sokolowski, M.B.; Twitchett, C.; Wright, A.; Sykes, A.G. *Coord. Chem. Rev.* **1999**, *190–192*, 771.
18. Binda, C.; Mattevi, A.; Edmondson, D. E. *J. Biol. Chem.* **2002**, *277*, 23973.
19. Murray, J. M.; Saysell, C. G.; Wilmot, C. M.; Tambyrajah, W. S.; Jaeger, J.; Knowles, P. F.; Phillips, S. E. V.; McPherson M. J. *Biochemistry*. **1999**, *38*, 8217.

20. Mure, M.; Kurtis, C. R.; Brown, D.E.; Rogers, M. S.; Tambyrajah, W. S.; Saysell, C.; Wilmot, C. M.; Simon E. V. Phillips, S.E. V.; Knowles, P.F.; Dooley, D. M.; McPherson, M.J. *Biochemistry*. **2005**, *44*, 1583.
21. Ruggiero, C.E.; Smith, J. A.; Tanizawa, K.; Dooley, D.M. *Biochemistry*. **1997**, *36*, 1953.
22. Schwartz, B.; Olgin, A. K.; Klinman, J.P. *Biochemistry*. **2001**, *40*, 2954
23. Hartmann, C.; Klinman, J. P. *J. Biol. Chem.* **1987**, *262*, 962.
24. Hartmann, C.; Brzovic, P.; Klinman, J. P. *Biochemistry*. **1993**, *32*, 2234.
25. Cai, D.; Dove, J.; Nakamura, N.; Sanders-Loehr, J.; Klinman, J. P. *Biochemistry*. **1997**, *36*, 11472.
26. Nakamura, N.; Moenne-Loccoz, P.; Tanizawa, K.; Mure, M.; Suzuki, S.; Klinman, J. P.; Sanders-Loehr, J. P. *Biochemistry*. **1997**, *36*, 11479.
27. Su, Q.; Klinman, J. P. *Biochemistry*. **1998**, *37*, 12513.
28. Hevel, J. M.; Mills, S. A.; Klinman, J. P. *Biochemistry*. **1999**, *38*, 3683.
29. Dooley, D. M.; McGuirl, M. A.; Brown, D. E.; Turowski, P. N.; McIntire, W. S.; Knowles, P. F. *Nature*. **1991**, *349*, 262.
30. Dooley, D. M.; Scott, R. A.; Knowles, P. F.; Colangelo, C. M.; McGuirl, M. A.; Brown, D. E. *J. Am. Chem. Soc.* **1998**, *120*, 2599.
31. (a) Hollstein, U. *Chem. Rev.* **1974**, *74*, 625. (b) Smith, A.W.; Camara-Artigas, A.; Wang, M.; Allen, J.P.; Jr. Francisco, W.A. *Biochemistry*. **2006**, *45*, 4378.
32. Smith, A.W.; Camara-Artigas, A.; Olea, C.; Jr. Francisco, W.A.; Allen, J.P. *Acta Cryst.* **2004**, *D 60*, 1453.
33. Barry, C.E.; Nayar, P.G.; Begley, T.P. *Biochemistry*. **1989**, *8*, 6323.
34. Barry, C.E.; Nayar, P.G.; Begley, T.P. *J. Am. Chem. Soc.* **1988**, *110*, 3333.
35. Halfen, J. A.; Jazdzewski, B. A.; Mahapatra, S.; Berreau, L. M.; Wilkinson, E. C.; Que, L. Jr., Tolman, W. B. *J. Am. Chem. Soc.* **1997**, *119*, 8217.
36. Wang, Y.; Stack, T. D. P. *J. Am. Chem. Soc.* **1996**, *118*, 13097.
37. Zurita, D.I.; Gautier-Luneau, S.; Menage, Piere, J. L.; Saint-Aman, E. *J. Biol. Inorg. Chem.* **1997**, *2*, 46.
38. Wang, Y.; DuBois, J.; Hedman, L B.; Hodgson, K. O.; Stack, T. D. P. *Science*, **1998**, *279*, 537.
39. Chaudhuri, P.; Hess, M. Flörke, U.; Wieghardt, K. *Angew. Chem., Int. Ed.* **1998**, *37*, 2217.
40. Pierre, J.-L. *Chem. Soc. Rev.* **2000**, *29*, 251;

41. Jazdzewski, B. A.; Tolman, W. B. *Coord. Chem. Rev.* **2000**, 200-202, 633.
42. Sokolowski, A.; Leutbecher, H.; Weyhermüller, T.; Schnepf, R.; Bothe, E.; Bill, E.; Hildenbrandt, K.; Wieghardt, K. *J. Biol. Inorg. Chem.* **1997**, 2, 444.
43. Ochs, C.; Hahn, F.; E. Fröhlich, R. *Eur. J. Inorg. Chem.* **2001**, 2427.
44. Wang, Y.; DuBois, J. L.; Hedman, B.; Hodgson, K. O.; Stack, T. D. P. *Science*, **1998**, 279, 537.
45. Chaudhuri, P.; Hess, M.; Müller, J.; Hildenbrandt, K.; Bill, E.; Weyhermüller, T.; Wieghardt, K. *J. Am. Chem. Soc.* **1999**, 121, 9599.
46. Chaudhuri, P.; Hess, M.; Weyhermüller, T.; Wieghardt, K. *Angew. Chem.* **1999**, 111, 1165; *Angew. Chem. Int. Ed.* **1999**, 38, 1095.
47. Itoh, S.; Taki, M.; Takayama, S.; Nagatomo, S.; Kitagawa, T.; Sakurada, N.; Arakawa, R.; Fukuzumi, S. *Angew. Chem.* **1999**, 111, 2944;
48. Vaidyanathan, M.; Palaniandavar, M.; Gopalan, R. S. *Inorg. Chim. Acta.* **2001**, 241.
49. Vaidyanathan, M.; Viswanathan, R.; Palaniandavar, M.; Balasubramanian, T.; Prabhakaran, P.; Muthiah, P. T. *Inorg. Chem.* **1998**, 37, 6418.
50. Thomas, F.; Gellon, G.; Luneau, I.G.; Aman, E. S.; Pierre, J.-L. *Angew. Chem. Int. Ed.* **2002**, 41, 3047.
51. Paine, T.K.; Weyhermüller, T.; Wieghardt, K.; Chaudhuri, P. *Dalton Trans.* **2004**, 2092.
52. Fabien, M.P.; Thomas, F.; Hamman, E.; Saint-Aman, C.; Bucher, Pierre, J.-L. *Chem. Eur. J.* **2004**, 10, 4114.
53. Langeron, M.; Neudorffer, A.; Fleury, M. B. *Angew Chem Int Ed Engl.* **2003**, 42, 1026.
54. Rall, J.; Wanner, M.; Albrecht, M.; Hornung, F. M.; Kaim, W. *Chem. Eur. J.* **1999**, 5, 2802.
55. Simóndi, L.I.; Simóndi, T.M.; May, Z.; Besenyi, G. *Coord. Chem. Rev.* **2003**, 245(1-2), 85.
56. Simóndi, L.I.; Barna, T.M.; Nemeth, S. *J. Chem. Soc., Dalton Trans.* **1996**, 473-78.
57. Simóndi, L.I.; Barna, T. M.; Korecz, L.; Rockenbauer, A. *Tetrahedron. Lett.*, **1993**, 34, 717.
58. Simóndi, T.M.; Simóndi, L.I.; Györ, M.; Rockenbauer, A.; Gomory, A. *J. Chem. Soc., Dalton Trans.*, **2004**, 1056.
59. Horváth, T.; Kaiser, J.; Speier, G. *Journal of molecular catalysis A: Chemical.* **2004**, 215,9.

Chapter 2

Synthesis, Characterization and Catalytic Reactivity of Transition Metal Complexes formed with N, N'-bis (2-hydroxy-3,5-di-tert-butylphenyl)-2,2'-diaminobiphenyl amine, (H_4L)



2.1 Synthesis and characterization of the ligand, *N, N'*-bis(2-hydroxy-3,5-di-*tert*-butylphenyl)-2,2'-diaminobiphenylamine, H_4L

The ligand, H_4L (shown in Figure 2.1) was synthesized by stirring 2,2'-diaminobiphenyl with 3,5-di-*tert*-butyl-catechol (1:2) in *n*-hexane, under air, with triethylamine as a base. The ligand was characterized by different spectroscopic methods by IR, NMR, GC, GC-MS and mass spectroscopy. The ligand shows characteristic peaks in IR spectrum due to –O-H and –N-H stretches at 3479 cm^{-1} and 3371 cm^{-1} respectively. The peaks at 2957 to 2868 cm^{-1} are due to the –C-H stretching of the *tert*-butyl group, a sharp band at 1595 cm^{-1} is observed due to the –C-C stretching of the aromatic rings, and bands at 1509 – 1426 cm^{-1} from skeletal vibrations. The –C-N stretching appears at 1579 cm^{-1} . The sharp peak at 753 cm^{-1} is due to the –C-H stretching of the tetra substituted aromatic rings. The ^1H NMR spectrum in CD_2Cl_2 for H_4L exhibits signals at 1.23 ppm (s, 18 *t*-Bu H), 1.40 ppm (s, 18 *t*-Bu H), 5.16 ppm (s, 2H), 7.30–6.56 ppm (12 H from aromatic ring). GC and GC-MS measurements have been performed to check the purity and the composition of the ligand. Mass-spectroscopy in EI mode confirms the composition of $\text{C}_{40}\text{H}_{52}\text{N}_2\text{O}_2$ (592 gm / mole) for H_4L . Showing its non-innocent character, the ligand can exist in the five different oxidation states depicted in Figure 2.2. The tetradentate ligand (H_4L) is able to lose both phenolic protons and amine protons thereby producing two iminosemiquinone radicals in presence of transition metal(s) ions and oxygen.¹ The *tert*-butyl groups at the 2 and 4 positions of the phenol stabilize these iminosemiquinone radicals.²

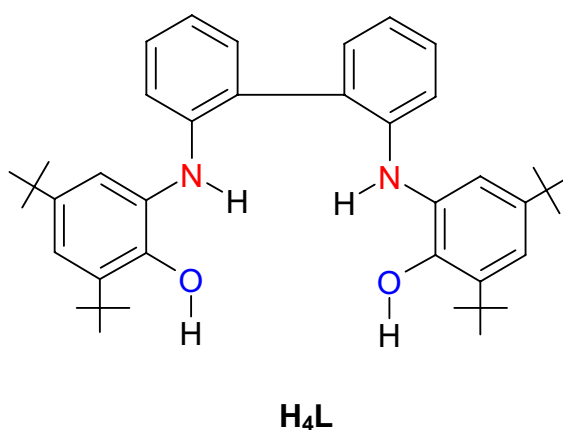


Figure 2. 1. The non-innocent ligand H_4L .

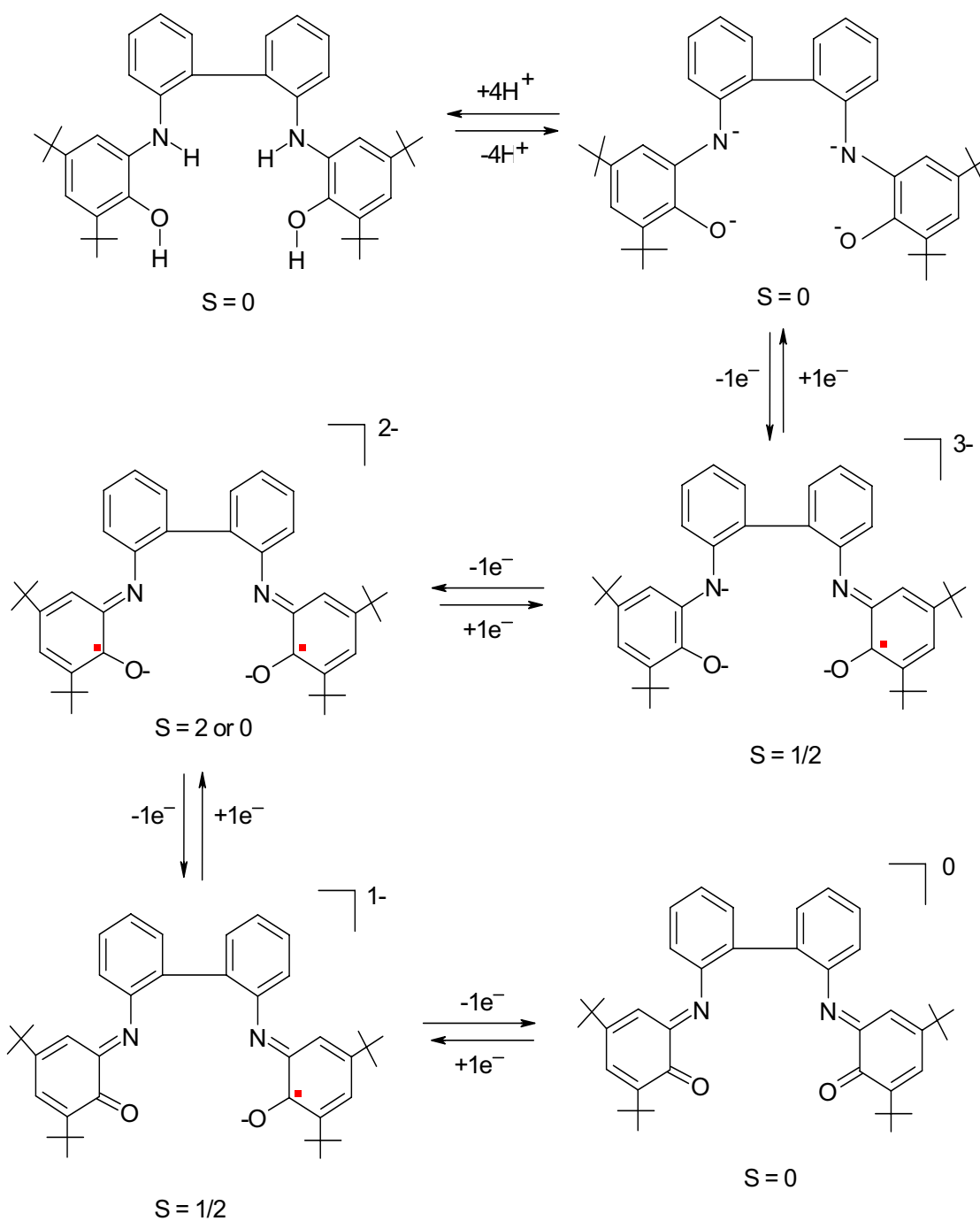


Figure 2.2. Different oxidation states of H_4L .

This chapter concerns synthesis, characterization and catalytic reactivities of the complexes formed with the first row and Pd from second row transition metals. These complexes are, $[V^V_2(\mu_2OMe)_2(L)_2]$ (1), $[Fe^{III}(HL^\bullet)Cl]$ (2), $[Pd^{II}(L^{\bullet})]$ (3), $[Ni^{II}(L^{\bullet})]$ (4) and $[Cu^{II}(L^{\bullet})]$ (5)

2.2 Methoxide bridged dinuclear non-oxovanadium (V) complex (1)

It is well established that vanadium is present at the active site of certain enzymes, including haloperoxidases in sea *algae* and *lichens*³⁻⁷ and some nitrogenases in nitrogen-fixing *azoto-bactor*.⁸⁻⁹ Furthermore, vanadium ions are bound to tyrosinate residues in vanadium-modified *transferrin*¹⁰ and *amavadin*,¹¹⁻¹³ and certain sea squirts or tunicates (polyphenol ascidians) are able to store vanadium in high concentrations. In view of the importance of the interaction of V(III), V(IV) and V(V) with tyrosinate residues,^{10,14} vanadium-phenolate chemistry is receiving considerable attention.¹⁴⁻¹⁷ There is well developed chemistry for V(IV)/V(V) “oxo” species but very few “bare” i.e. “non-oxo”, vanadium complexes with phenol or phenoxyl as chelating ligand have been prepared and fully characterized.^{18-32, 36} Hence, synthesis and full characterization of non-oxo vanadium(V) complexes with phenol bites are worth investigation.

Complex **1** was prepared by sequentially adding H₄L (2 mmol), VOSO₄·5H₂O (2 mmol) and 0.2 ml triethylamine in 30 ml methanol under air. Deep blue colored, microcrystalline solid precipitated after stirring this solution for 2h.

IR spectrum of complex **1** is different than that of the ligand IR spectrum. The peaks, in the 2952-2866 cm⁻¹ region arise due to the -C-H stretching of the *tert*-butyl group, and are seen to be present in the complex IR spectrum, and thereby clearly indicate the coordination of the ligand with the central metal. The absence of 3478 cm⁻¹ and 3370 cm⁻¹ bands, characteristic for -O-H and -N-H stretching, clearly indicates the deprotonation of the phenolic and amino protons after coordination of the ligand to the metal. However, the presence of a broad band at approximately 3400 cm⁻¹ is possibly due to the coordinated water molecule in complex **1**. Complex **1** does not exhibit any sharp band(s) in the 900-1000 cm⁻¹ region. This feature is indicative for the absence of the V=O structural unit in the complex. The elemental analysis for **1** suggests a composition of C₈₂H₁₀₂N₄O₆V₂ (1340 g/mol), in good agreement with the ESI (pos, in CH₂Cl₂) spectrum where an m/z signal at 1340.5 is attributed to M⁺.

X-ray quality single crystals of **1** were isolated from a 1:1:1 MeOH, CH₃CN and CH₂Cl₂ solution mixture. ORTEP diagram of the molecule with atom labeling scheme is shown in Figure 2.3 and Table 2.1 contains selected bond lengths and bond angles. The

binuclear vanadium complex is neutral with pseudo octahedral geometry around the both vanadium (V(1), V(2)) ions. The two vanadium ions are connected through two μ_2 methoxide bridges. Complex **1** contains a C_2 axis that passes vertically through the V(1), O(45), V(2) and O(95) atoms containing plane. The oxidation state of the vanadium ions could be assigned to +III, +IV or +V with two iminosemiquinone radicals, one iminosemiquinone radical or the amidophenolate form of the ligand respectively. The respective O(1)-C(2), C(7)-N(8), O(27)-C(28), and C(22)-N(21) bond lengths are 1.326(5), 1.369(7), 1.331(7) and 1.406(5) Å. From these bond lengths V(III) with two iminosemiquinone composition can be ruled out easily for the neutral complex **1**. The average V-phenolic oxygen bond length is 1.885(3) Å. From the V-phenolic oxygen bond length it is not possible to assign the oxidation state of the vanadium ion.³³

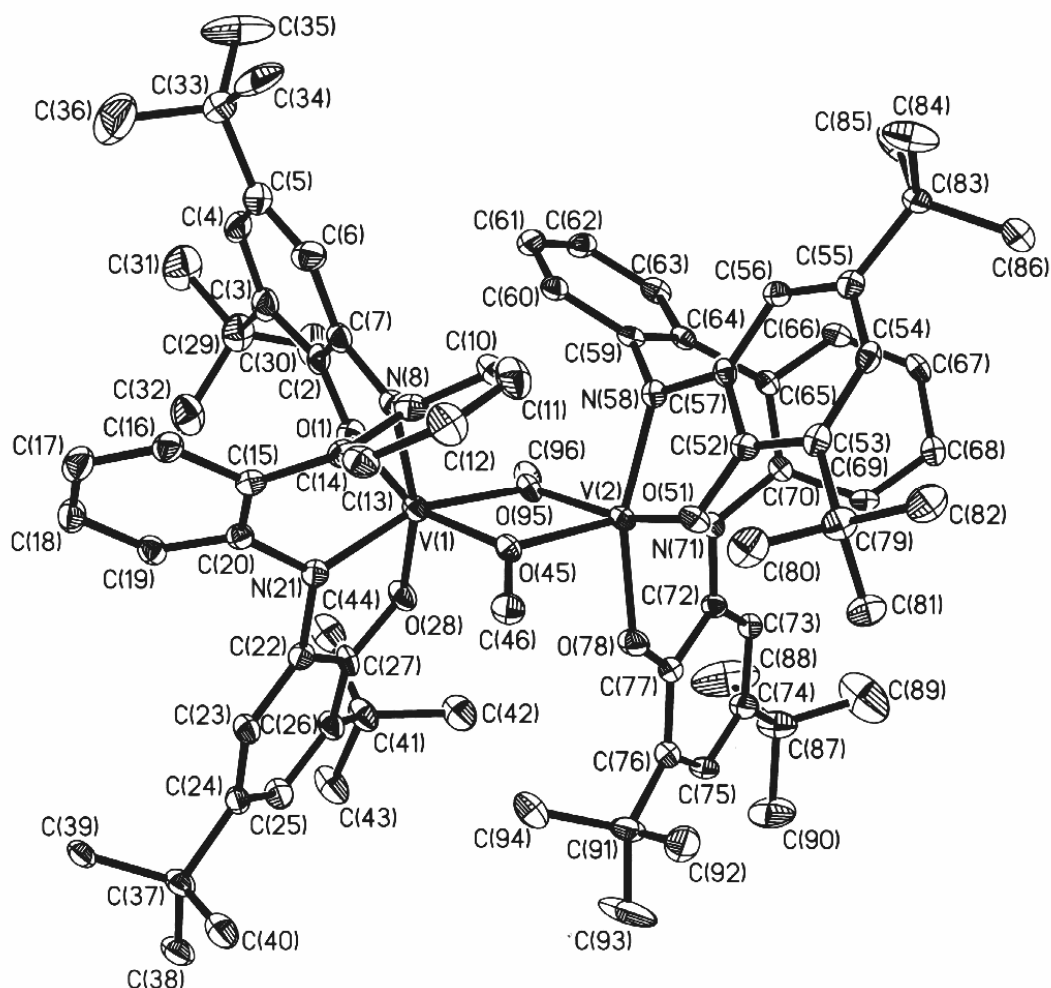


Figure 2.3. ORTEP diagram of **1**.

The average C-C bond length of the *tert*-butyl containing phenyl rings supports assignment of the amidophenolate form of the coordinating ligands.³⁴ Therefore, from a structural perspective, oxidation state of the both vanadium ions in the neutral complex **1** is assigned as V(V) and coordinated ligands are categorized as the fully reduced amidophenolate form.

Table 2.1. Selected bond distances (Å) and angles (degree) for **1**

V(1)-O(28)	1.884(3)	V(1)-N(21)	1.950(3)
V(1)-O(45)	1.908(3)	V(1)-O(95)	2.057(3)
V(1)-O(1)	1.919(3)	V(1)-V(2)	3.1195(10)
O(28)-V(1)-O(45)	106.68(13)	N(21)-V(1)-N(8)	91.84(15)
O(28)-V(1)-O(1)	88.22(13)	O(28)-V(1)-O(95)	82.24(12)
O(45)-V(1)-O(1)	159.10(13)	O(45)-V(1)-O(95)	75.82(12)
O(28)-V(1)-N(21)	81.4(2)	N(21)-V(1)-O(95)	159.32(14)
O(45)-V(1)-N(21)	96.96(13)	N(8)-V(1)-O(95)	107.29(13)
O(28)-V(1)-N(8)	162.75(15)	O(1)-V(1)-O(95)	92.23(12)
O(45)-V(1)-N(8)	89.82(14)	V(1)-O(95)-V(2)	103.85(13)
O(1)-V(1)-N(8)	77.26(14)	V(1)-O(45)-V(2)	103.99(13)

Variable temperature (2-290 K) magnetic susceptibility measurements using a SQUID magnetometer at 1 T indicate that complex **1** is diamagnetic. The diamagnetic nature of the complex was further confirmed by measuring ¹H NMR spectrum of **1** in CD₂Cl₂ solution at 300 K (see experimental section). The ⁵¹V NMR spectrum is depicted in Figure 2.4. The spectrum of complex **1** exhibits a broad peak at ~ 120 ppm (relative to VOCl₃).

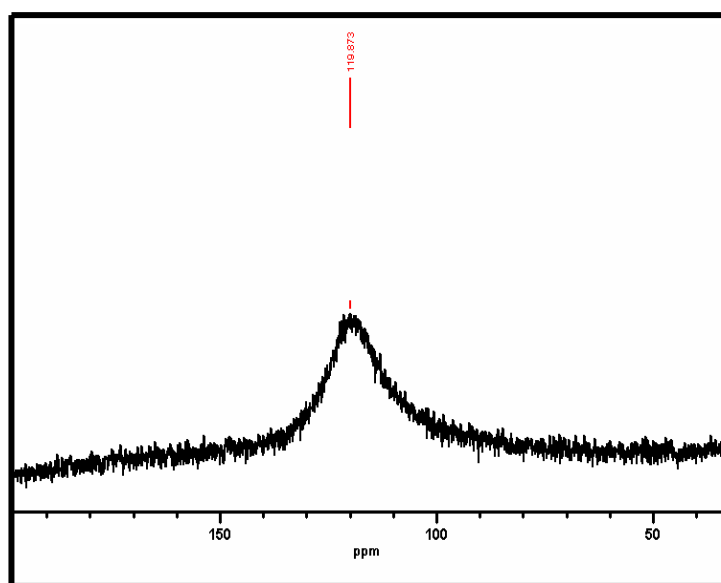


Figure 2. 4. ⁵¹V NMR in CD₂Cl₂ at room temperature.

The cyclic voltammogram (CV) of complex **1** has been recorded in CH₂Cl₂ containing 0.1M [ⁿBu₄N] PF₆ as a supporting electrolyte at a glassy carbon working electrode and a Ag/AgNO₃ reference electrode. Ferrocene was used as an internal standard, and potentials are referred versus the ferrocenium/ferrocene couple (Fc⁺/Fc). Figure 2.5 shows the CV of **1** recorded in the potential range +0.7 V to -1.2 V. Within that potential range complex **1** shows one reversible one-electron-transfer wave and one irreversible one-electron-transfer wave.

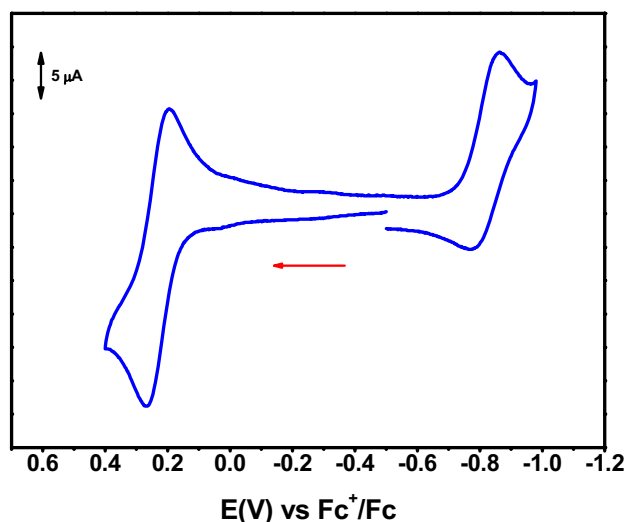


Figure 2.5. Cyclic voltammogram of **1** at room temperature under an anaerobic condition.

From coulometric measurement at an appropriately fixed potential it has been established that the wave at 0.23 V corresponds to one electron oxidation and the wave at -0.822 V corresponds to one-electron reduction.

The electronic spectra of the neutral species and electrochemically oxidized species are shown in Figure 2.6. In the neutral complex, the intense peak at 630 nm is assigned to phenolate-to-metal (V) charge transfer (LMCT)^{34, 55} which shifts to smaller wavelength, 600 nm, upon one-electron oxidation. The absorption coefficient also increases from 10700 M⁻¹cm⁻¹ to 12400 M⁻¹cm⁻¹. As both vanadium ions are in the +V oxidation state, the oxidation must be ligand centered. The new band appearing at 400 nm ($\epsilon = 7000 \text{ M}^{-1}\text{cm}^{-1}$) is presumably due to the formation of phenoxyl radical. Erasmus-Buhr et. al.³⁵ and Chaudhuri et. al.³⁶ have reported the band at 400 nm is due to the ligand to metal charge transfer.

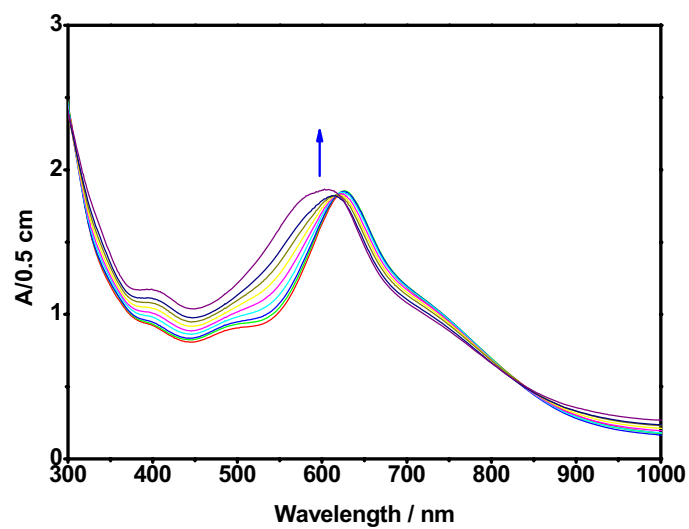
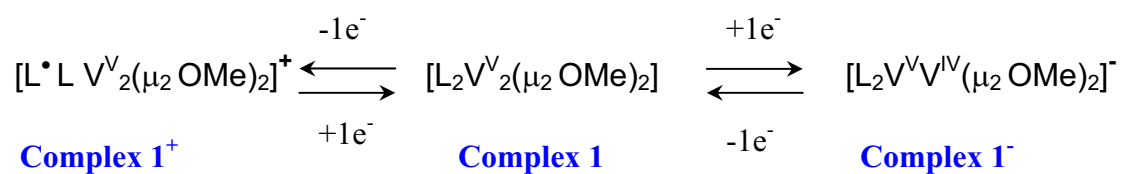


Figure 2.6. Change in UV-VIS spectrum of complex 1 during coulometric $1 e^-$ oxidation.

Thus the electrochemical behaviour of the complex can be summarized as follows.



2.3 Five coordinate square pyramidal high-spin Fe(III) complex(2)

The ligand H₄L (2 mmol), anhydrous FeCl₃(4 mmol) and 0.2 ml triethylamine were added in 30 ml CH₃CN. After stirring under air for 1 hour, deep greenish-blue microcrystalline solid was precipitated out with an yield of 75%.

The IR spectrum of complex **2** shows a sharp band at 3280 cm⁻¹ and indicates the presence of –NH group. The bands in the 2960-2870 cm⁻¹ region are due to the –C-H stretching of *tert*-butyl groups and confirm the coordination of the ligand to the metal. The IR spectrum can also serve as an important tool in understanding the oxidation state of the coordinated ligand qualitatively. The iminosemiquinone form of the ligand, i.e. one electron oxidized ligand, while chelated to the Fe(III) ion usually shows strong band for C-O• at around 1485 cm⁻¹ and a less intense band at approximately 1247 cm⁻¹ arises due to phenolic C-O stretching.³⁷⁻⁴⁵ In the IR spectrum of complex **2** both bands are observed and hence, provides qualitative evidence for the presence of mixed valence iminosemiquinone-aminophenolate form of the coordinated ligand. The mass spectrum in ESI (Pos, CH₂Cl₂) mode shows two intense peaks at 679.45 corresponding to M⁺ (C₄₀H₄₉N₂O₂FeCl) and at 644.2 corresponding to [M-Cl]⁺. Elemental analysis confirms further the composition C₄₀H₄₉N₂O₂FeCl (679.5 g/ mol) and supports the result obtained by mass spectrum analysis.

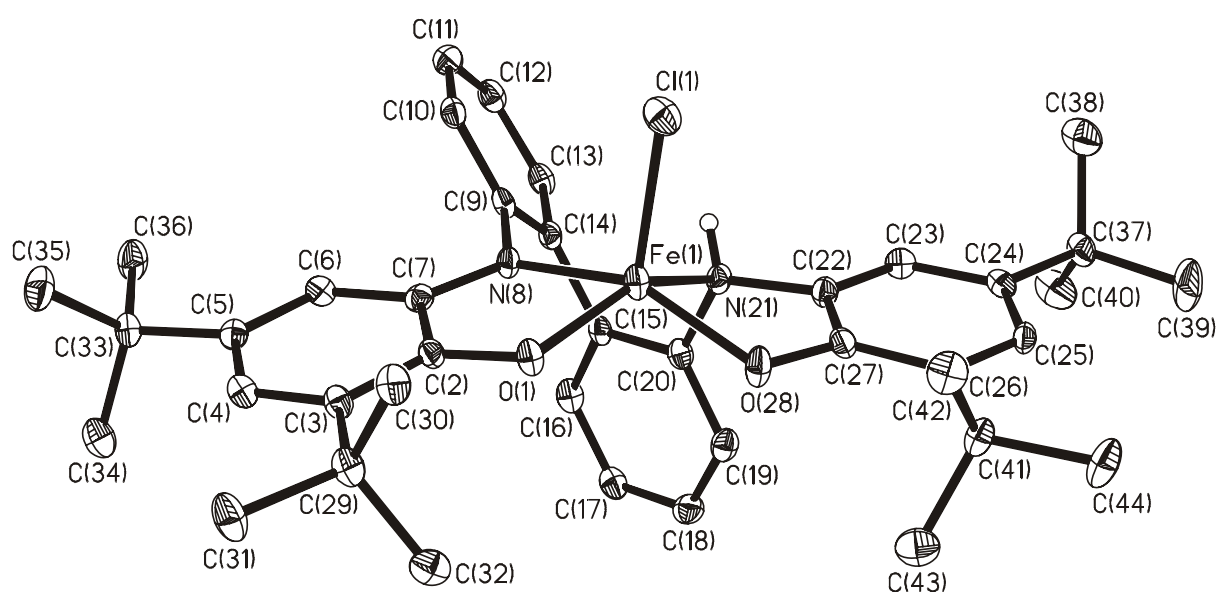


Figure 2.7. ORTEP diagram of **2**.

Dark greenish-blue crystals of complex **2** were obtained by slow evaporation of a 1:1 CH₂Cl₂ / CH₃CN solution mixture. The X-ray crystal structure has been determined at 100(2) K to minimize standard deviations as compared to the room temperature structure. ORTEP diagram of the complex molecule is shown in Figure 2.7, and important bond distances and angles appear in Table 2.2. The geometry of the central Fe ion is square-pyramidal where two N-atoms and two O-atoms occupy basal positions. The distance between the plane comprising of N(8)-N(21)-O(1)-O(28) and Fe ion is 0.55 Å. A chloride ion, which is attached to Fe ion, is at the apex position of the pyramid. The respective Fe(1)-O(1), Fe(1)-O(28), Fe(1)-N(21), Fe(1)-N(8), and Fe(1)-Cl(1) bond distances are 1.943(2), 1.905(2), 2.044(2), 2.206(3) and 2.2277(3) Å and are in accord with the pentacoordinate high-spin ferric species.⁴⁶ The C-O and C-N bond distances for the chelated ligand containing O(1), O(28), N(21), N(8) atoms are 1.305(3), 1.347(3), 1.452(4) and 1.345(4) Å respectively. These above bond distances indicate that one of the *tert*-butyl containing phenyl rings is in iminosemiquinone form and the other is in aminophenolate form. C(9)-N(8)-C(7), C(7)-N(8)-Fe(1), C(9)-N(8)-Fe(1) bond angles are 119.1(2), 113.4(2) and 126.34(18)° respectively. 114.9(2), 102.9(2) and 110.7(2)° are the respective C(22)-N(21)-C(20), C(22)-N(21)-Fe(1) and C(22)-N(21)-Fe(1) bond angles.

Table 2.2. Selected bond distances (Å) and angles (degree) for **2**.

Fe(1)-N(8)	2.044 (2)	C(4)-C(5)	1.444 (4)
Fe(1)-N(21)	2.206 (3)	C(5)-C(6)	1.364 (4)
Fe(1)-O(1)	1.943 (2)	C(6)-C(7)	1.422 (4)
Fe(1)-O(28)	1.905 (2)	C(22)-N(21)	1.424 (4)
C(2)-O(1)	1.305 (3)	C(22)-C(23)	1.381 (4)
C(7)-N(8)	1.345 (4)	C(23)-C(24)	1.393 (4)
C(2)-C(7)	1.453 (4)	C(24)-C(25)	1.398 (4)
C(2)-C(3)	1.426 (4)	C(25)-C(26)	1.402 (4)
C(3)-C(4)	1.371 (4)	C(26)-C(27)	1.411 (4)
C(9)-N(8)	1.424 (4)	C(27)-O(28)	1.347 (4)
C(9)-C(10)	1.389 (4)	C(20)-C(15)	1.398 (4)
C(10)-C(11)	1.383 (4)	C(15)-C(16)	1.392 (4)
C(11)-C(12)	1.384 (4)	C(16)-C(17)	1.393 (4)
C(12)-C(13)	1.382 (4)	C(17)-C(18)	1.383 (4)
C(13)-C(14)	1.396 (4)	C(18)-C(19)	1.387 (4)
C(14)-C(9)	1.409 (4)	C(19)-C(20)	1.386 (4)
O(1)-Fe(1)-N(8)	79.79 (9)	O(1)-Fe(1)-O(28)	99.20 (9)
N(8)-Fe(1)-N(21)	79.33 (9)	O(1)-Fe(1)-N(21)	146.61 (9)
N(21)-Fe(1)-O(28)	85.3 (11)	O(28)-Fe(1)-N(8)	148.62 (10)
C(27)-O(28)-Fe(1)	114.78 (19)	C(2)-O(1)-Fe(1)	112.21 (18)
C(22)-N(21)-C(20)	114.9 (2)	C(7)-N(8)-C(9)	119.1 (2)
Fe(1)-N(21)-C(20)	110.72 (18)	C(9)-N(8)-Fe(1)	126.34 (18)
C(22)-N(21)-Fe(1)	102.9 (17)	C(7)-N(8)-Fe(1)	113.4 (2)

From the above bond angles it is quite clear that N(8)-atom is sp^2 hybridized and supports the amido form while the N(21)-atom is sp^3 and in amino form. Moreover, from the crystal structure, the H-atom attached to N(21) atom has been observed directly. Therefore, from the crystal structure it can be concluded that the neutral pentacoordinate mononuclear iron complex is a monoradical-containing Fe(III) ion.⁴⁶

Zero-field Mössbauer spectrum of the solid sample of complex **2** has been recorded at 80 K to obtain independent spectroscopic information on the local spin and the oxidation state of the iron ion. Figure 2.8 shows this spectrum. Complex **2** exhibits a single quadrupole doublet and the simulation of the experimental results gives an isomer shift, δ , of 0.436 mm s^{-1} , and a quadruple splitting, $|\Delta E_Q|$, of 1.542 mm s^{-1} . These parameters unequivocally indicate the presence of a high-spin ferric ion in the neutral mono-radical-containing complex.⁴⁶⁻⁴⁷

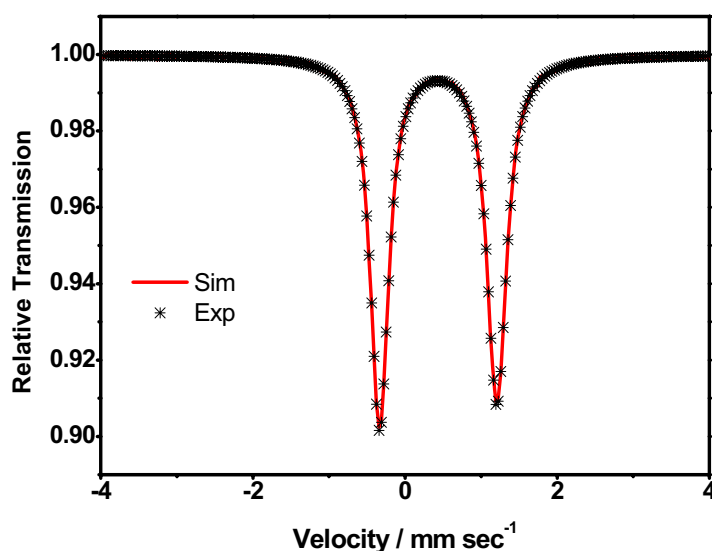


Figure 2.8. Mössbauer spectrum of **2** at 80 K and at zero-field.

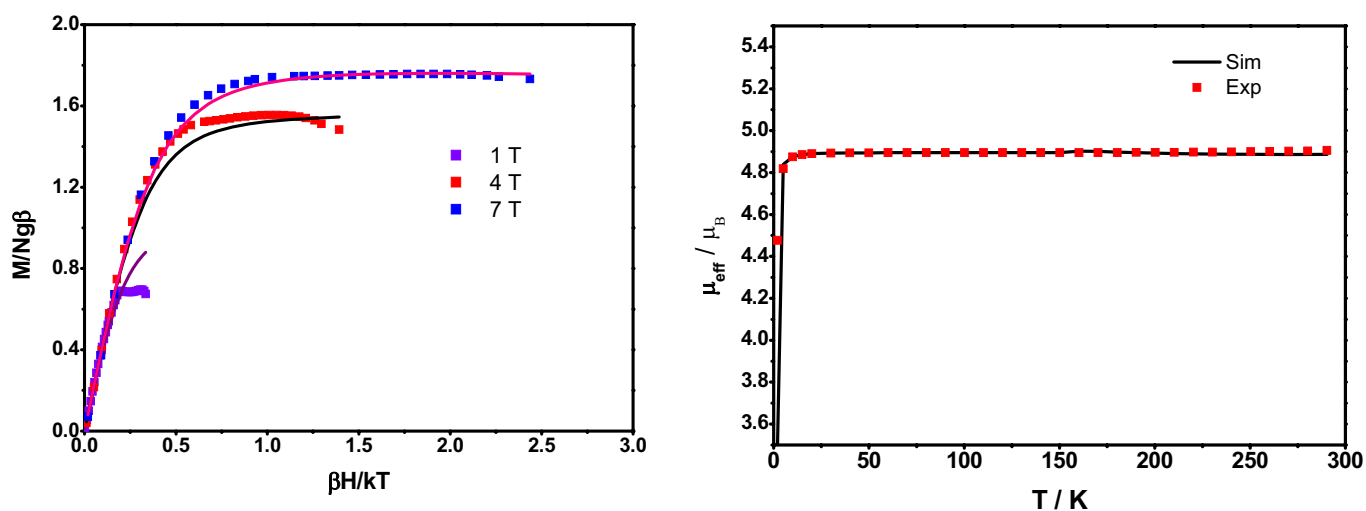


Figure 2.9. Magnetic measurements of **2** at different field and different temperature.

Variable temperature magnetic susceptibility measurements on a solid sample were performed in the range 2-290 K for complex **2** using SQUID magnetometer at external field 1 T. Figure 2.9 shows μ_{eff} vs T and field dependant magnetization measurements. At room temperature as well as 9 K the μ_{eff} value is $4.88 \mu_{\text{B}}$. This value indicates a total spin state $S_{\text{t}} = 2$ throughout 9-290 K temperature range. No change in μ_{eff} value with respect to temperature indicates two interesting features. First, a strong antiferromagnetic coupling between high spin $\text{Fe}^{\text{III}}(\text{d}^5)$ ion and the radical anion, and second, excited state with spin multiplicity more than 5 is not populated in the temperature range, i.e. the energy difference between the ground state ($S_{\text{t}} = 2$) and excited higher energy state ($S_{\text{t}}' = 3$) is more than 200 cm^{-1} ($1 \text{ cm}^{-1} = 0.69 \text{ K}$). Fit to the experimental results (magnetic moment at 1 T and VTVH measurements) were obtained using the Heisenberg spin exchange Hamiltonian $\hat{H} = -2\sum_{i<j} J_{ij} \hat{S}_i \cdot \hat{S}_j$ in which J_{ij} represents the exchange constants and the subscripts i and j number the pairwise interacting paramagnetic centres. Simulation to the experimental results provides the following fitting parameters; $g_{\text{Fe}} = 2.03$, zero field splitting, $|D|$ of 2.15 cm^{-1} .

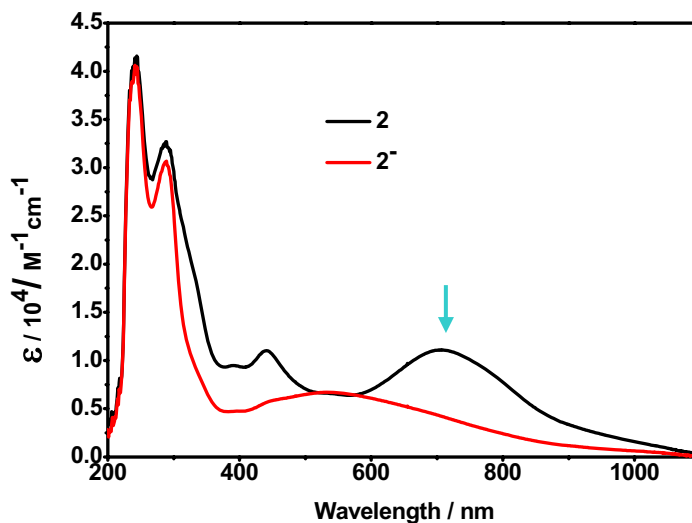


Figure 2.10. Change in electronic absorption spectra of **2** after $1e^-$ reduction.

Figure 2.10 displays the electronic spectrum of complex **2** in CH_2Cl_2 solution at ambient temperature. The spectrum displays two very intense absorption maxima ($\epsilon = 11100$

$M^{-1}cm^{-1}$ (710 nm) and $\epsilon = 11000 M^{-1}cm^{-1}$ (443 nm)) in the visible range, 400-800 nm. The intense absorption at 443 nm is presumably a ligand-to-metal charge transfer whereas that at 710 nm may be assigned to an intervalence ligand-to-ligand charge transfer.

The electrochemical activity of complex **2** has been studied by cyclic voltammetry (CV) in CH_2Cl_2 containing 0.01 M [TBA]PF₆ as a supporting electrolyte, a Pt working electrode and a Ag/AgNO₃ reference electrode. Figure 2.11 shows the cyclic voltammogram of complex **2** recorded in the potential range 0.8 to -1.6 V.

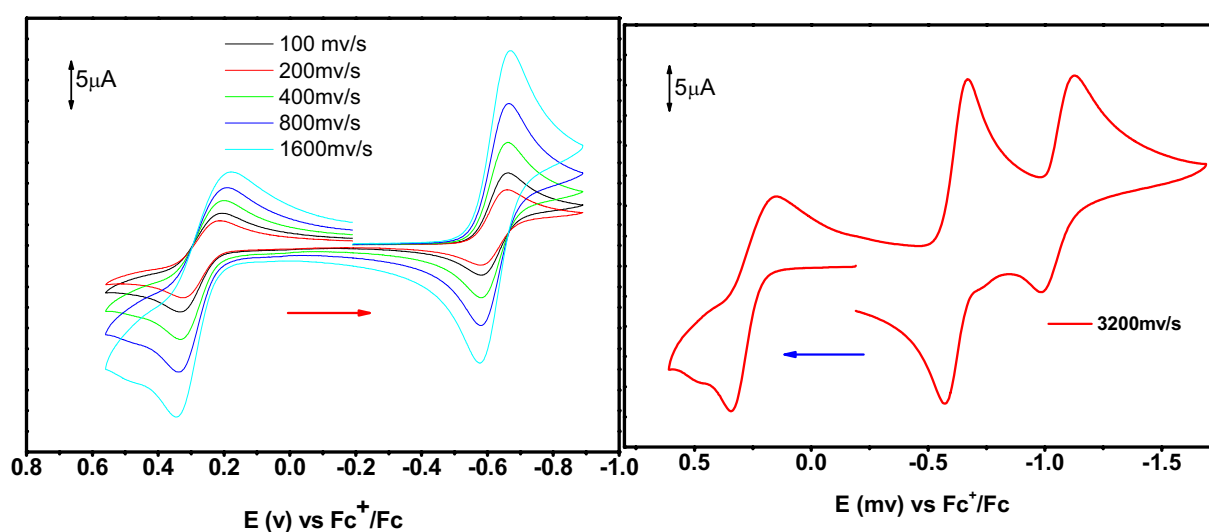


Figure 2.11. Cyclic voltammograms of **2** at different scan rates.

Complex **3** shows one one-electron quasi-reversible wave at 0.215 V and two reversible one-electron-transfer waves at -0.615 V and -1.065 V. The redox potentials are referred versus the ferrocenium/ferrocene couple. Controlled potential coulometric analysis shows that the electron-transfer at 0.215 V corresponds to one one-electron oxidation while that at -0.615 V and -1.065 V correspond to one-electron reductions. The change in UV-VIS/NIR spectrum after the coulometric one electron reduction appears in Figure 2.10. Upon one electron reduction the sharp and strong bands at 710 and 443 nm diminish and a broad band at around 530 nm ($\epsilon = 6700 M^{-1}cm^{-1}$) appears. The new band is assigned to phenolate-to-metal charge transfer band.⁴⁸

Complex **2** is X-band EPR silent, as expected for an integer spin system ($S_t = 2$) with presumably high D value. The one-electron reduced species should be a non-integer spin system and EPR active in nature. Therefore, X-band EPR spectrum of electrochemically one-

electron-reduced species of **3** in CH_2Cl_2 solution at 10 K has been measured. Figure 2.12 shows the X-band EPR spectrum of the one-electron reduced species. Clearly, an axial $S = 1/2$ signal is observed. This type of X-band EPR signal appears for low spin $\text{Fe}^{\text{III}}(\text{d}^5)$.⁴⁹⁻⁵⁰ Two types of electronic configurations, $(\text{d}_{xz}, \text{d}_{yz})^4(\text{d}_{xy})^1$ and $(\text{d}_{xy})^2(\text{d}_{xz}, \text{d}_{yz})^3$, exist in low-spin $\text{Fe}(\text{III})$ species (Figure 2.12). Major factor determining the ground state electronic configurations are; (i) type of complex i.e. octahedral, square pyramidal, and trigonal bipyramidal, (ii) the ligand field strength of the axial ligand, (iii) the deformation of the basal plane. From simulation of the experimental spectrum the following parameters were obtained, $g_x = 1.9157$, $g_y = 1.9157$ and $g_z = 2.041$, with line width, W_x , W_y , and W_z values of 0.17 mT, 0.09 mT, and 0.01 mT respectively. Thus, the reduced species of **2** possesses an $S = 1/2$ ground state and the unpaired electron predominantly resides on a metal d orbital and most probably in d_{xy} orbital as the complex is square pyramidal with an axial chloride ligand. If the reduction were metal centred, and there were no change in the spin state of metal ion, then the signal should appear as an $S = 3/2$ system and would be an $S = 5/2$ system if the reduction were ligand centred. The observed $S = 1/2$ signal may be described as follows; after one-electron reduction the iminosemiquinone part of the ligand becomes an amidophenolate and hence the ligand field strength has increased. Therefore, high-spin $\text{Fe}^{\text{III}}(\text{d}^5)$ shifts to low-spin $\text{Fe}^{\text{III}}(\text{d}^5)$.

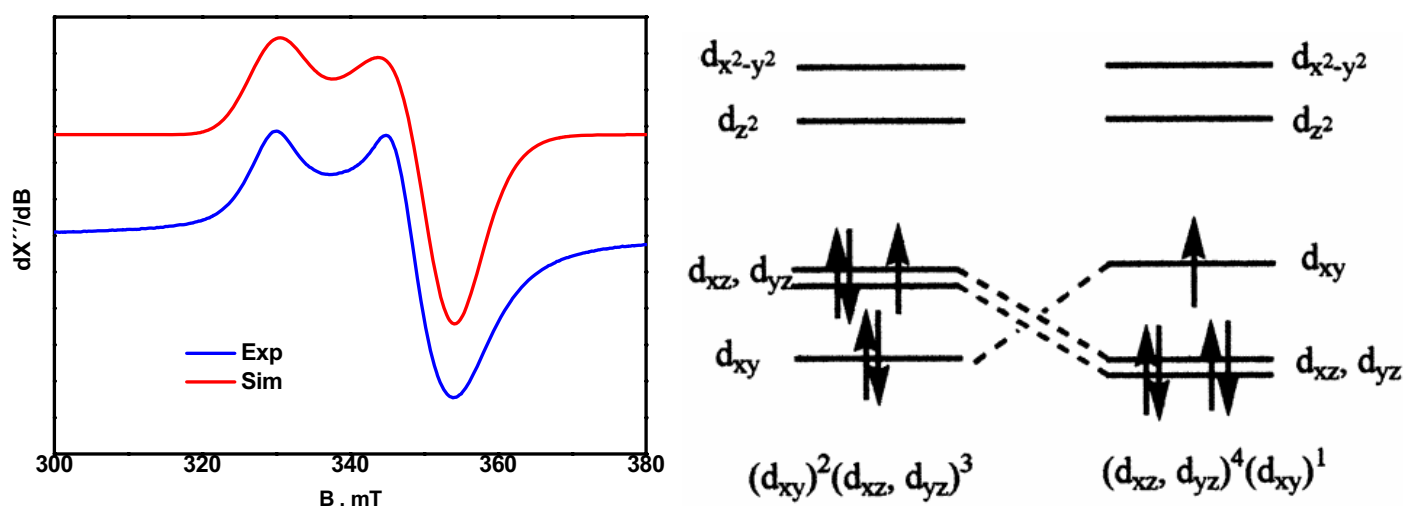


Figure 2.12. X-band EPR spectrum of one electron oxidized species of **2** in frozen CH_2Cl_2 10 K and electron configurations of low-Spin Iron(III) complexes.

From the above experimental result it is clear that the first reduction is ligand centered and therefore, the second reduction has to be metal centered as the center is the only one which can accept electron. In the case of oxidation process, three options are valid. First, oxidation of the aminophenolate part of the ligand to iminosemiquinone form, second, oxidation of iminosemiquinone form of the ligand to iminoquinone form, third, oxidation of Fe(III) to Fe(IV). Among these options the first option is presumably valid. The electrochemical transformation can be resumed as follows in Figure 2.13.

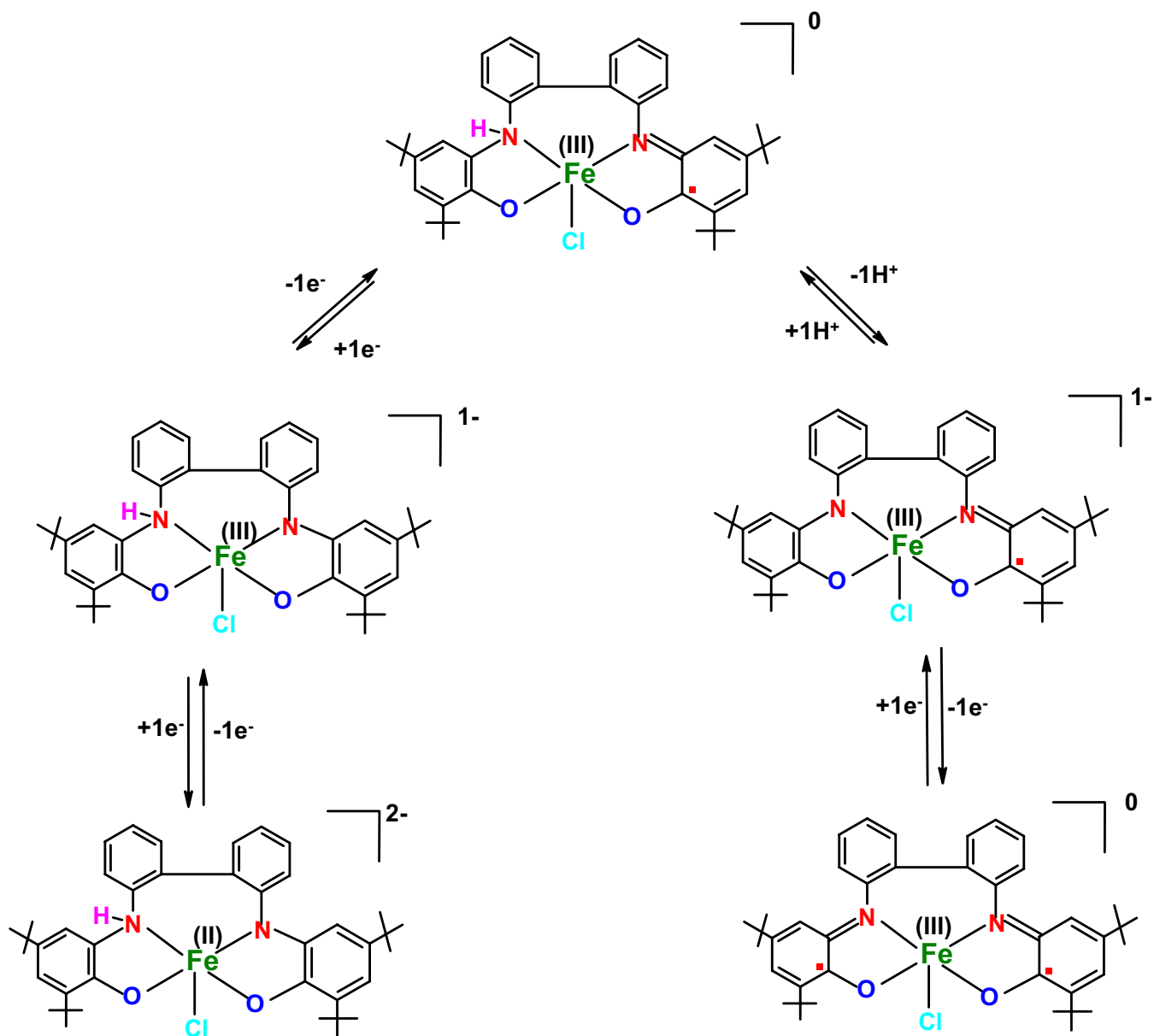


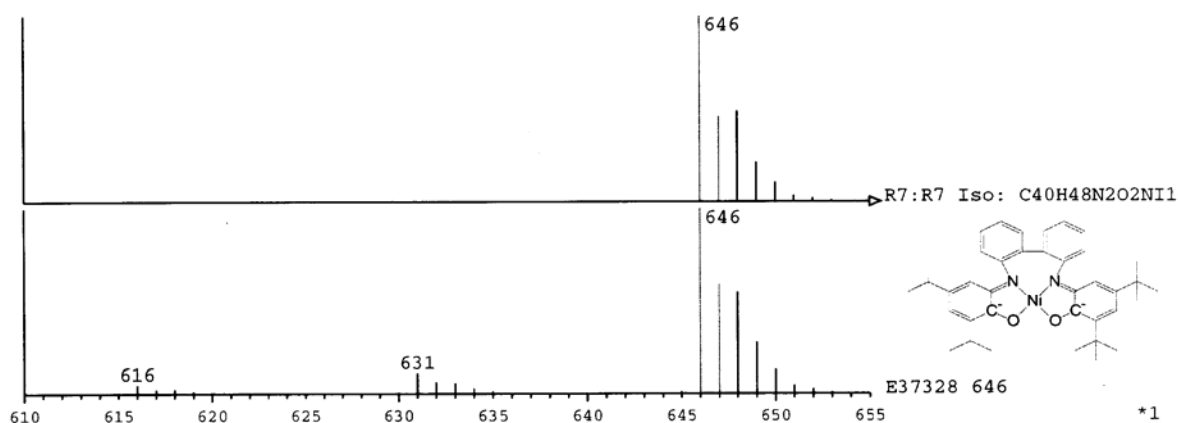
Figure 2.13. Different possible redox states of complex 2.

2.4 Distorted square planar Ni(II) and Pd(II) complexes

It is well known that Ni(II), Pd(II) and Pt(II) ions (d^8) form square planar complexes with ligands having O,O, N,N, N,O, N,S, and S,S donor sets. The square planar complexes of the above stated bidentate ligands with Ni(II), Pd(II) and Pt(II) have been studied exclusively.^{47, 51-62} Instead of the above bidentate ligands chemists have also employed tetradentate ligands⁵³ and have examined the properties of the square planar complexes. To understand the electro and spectroelectrochemical behaviour of the distorted square planar complexes of Ni(II) and Pd(II) the ligand H_4L have been introduced. In this section the two distorted square planar complexes, $[Ni^{II}(L^{••})]$ (**3**) and $[Pd^{II}(L^{••})]$ (**4**) will be discussed.

Complex **3** and **4** were synthesized in the following way; In 30 ml CH_3CN , H_4L (2 mmol), $NiCl_2 \cdot 6H_2O$ (2 mmol) or $PdCl_2$ (2 mmol) and 0.2 ml triethylamine were added and the solution was stirred under air for two hours. Microcrystalline solid of **3** or **4** was precipitated, was filtered and washed with CH_3CN . Yield ~75%.

The IR spectra of these complexes do not provide conclusive information about the oxidation state of the ligand except the coordination of the ligand. The absence of the sharp peaks in the 3434 cm^{-1} to 3320 cm^{-1} indicates the deprotonated form of the phenolic and amino groups and bands in the $2952\text{-}2866\text{ cm}^{-1}$ region are strong evidence for the coordination of the ligand to the metal ions. The complexes were examined by mass spectrometry in ESI (pos) mode in CH_2Cl_2 , and in EI-mode. The peaks obtained for the complexes in the mass spectrum have been calculated theoretically and shown in Figure 2.14.



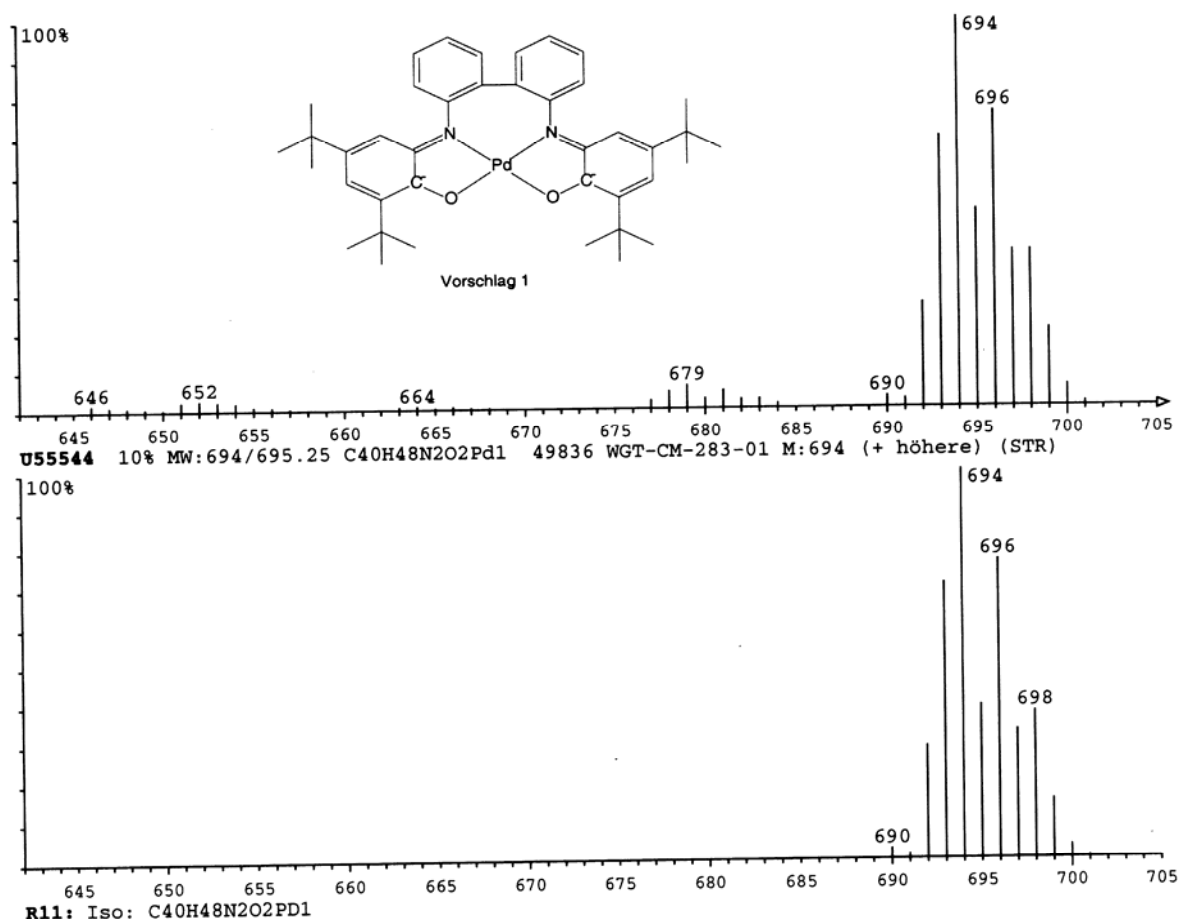


Figure 2.14. Experimental and theoretical mass spectra for complex **3** and **4**.

The mass spectra for both complexes (**3** and **4**) confirm that the composition of the complexes is same, $C_{40}H_{48}N_2O_2M_1$ ($M = Ni, Pd$). The elemental analysis for both complexes has been performed and the results support the composition obtained from the mass spectra.

The neutral complex $[Ni^{II}(L^{**})]$ (**3**) was crystallized from 1:1 dichloromethane/ acetonitrile solution as a deep brown crystal. The structure consists of one nickel atoms in a distorted square planar geometry with the dihedral angle between the C(7)-C(2)-O(1)-Ni(1)-N(8) and C(22)-C(27)-O(28)-Ni(1)-N(21) planes at 30.8° . ORTEP diagram with the labeling scheme and selected bond distances and angles are shown in Figure **2.15** and in Table **2.3**.

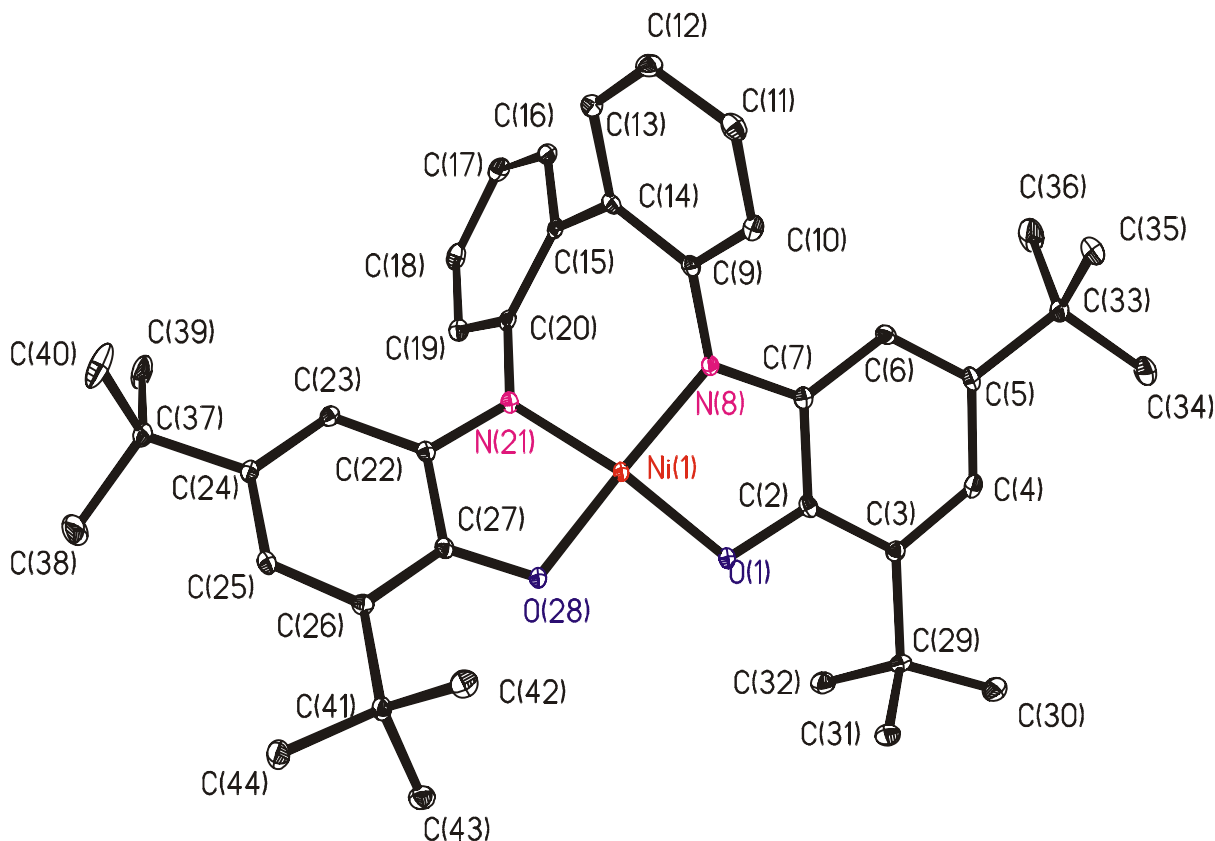


Figure 2.15. ORTEP diagram of **3**.

The ligand coordinates to the nickel centre through two deprotonated oxygen atoms and two deprotonated nitrogen atoms. The Ni(1)-O(1), Ni(1)-O(28), Ni(1)-N(8), Ni(1)-N(21) distances are 1.8435 (15), 1.8516(15), 1.8247(17) and 1.8276 (18) Å respectively. The radical nature of the ligand is supported by the average C=N imine bond lengths 1.360(2), and by the average angle of 121.33(17)° at C(7)-N(8)-C(9), indicative of a sp^2 hybridisation for the N atom. The shortening of the C(3)-C(4), C(5)-C(6), C(23)-C(24) and C(25)-C(26) bonds in contrast to the average C-C bond distances of the N-phenyl rings (1.39 ± 0.01 Å) clearly implies the collapse of the aromaticity of *tert*-butyl containing phenyl rings in the complex. Moreover, the shortening of the C(2)-O(1) and C(27)-O(28) bond lengths from the normal C-O single bond length is another indication of the radical nature of the ligand. Hence, the oxidation state for the nickel centre in the neutral complex is +II.

Table 2.3. Selected bond distances (Å) and angles (degree) for **3**

Ni(1)-N(8)	1.8276 (18)	C(4)-C(5)	1.416 (3)
Ni(1)-N(21)	1.8247 (17)	C(5)-C(6)	1.376 (3)
Ni(1)-O(1)	1.8435 (15)	C(6)-C(7)	1.407 (3)
Ni(1)-O(28)	1.8516 (15)	C(22)-N(21)	1.360 (3)
C(2)-O(1)	1.318 (2)	C(22)-C(23)	1.410 (3)
C(7)-N(8)	1.369 (3)	C(23)-C(24)	1.376 (3)
C(2)-C(7)	1.418 (3)	C(24)-C(25)	1.417 (3)
C(2)-C(3)	1.421 (3)	C(25)-C(26)	1.376 (3)
C(3)-C(4)	1.388 (3)	C(26)-C(27)	1.423 (3)
C(9)-N(8)	1.411 (3)	C(27)-O(28)	1.311 (2)
C(9)-C(10)	1.405 (3)	C(20)-C(15)	1.410 (3)
C(10)-C(11)	1.380 (3)	C(15)-C(16)	1.396 (3)
C(11)-C(12)	1.382 (3)	C(16)-C(17)	1.383 (3)
C(12)-C(13)	1.380 (3)	C(17)-C(18)	1.391 (3)
C(13)-C(14)	1.400 (3)	C(18)-C(19)	1.375 (3)
C(14)-C(9)	1.405 (3)	C(19)-C(20)	1.403 (3)
O(1)-Ni(1)-N(8)	85.95 (7)	O(1)-Ni(1)-O(28)	94.49 (7)
N(8)-Ni(1)-N(21)	101.54 (8)	O(1)-Ni(1)-N(21)	160.06 (7)
N(21)-Ni(1)-O(28)	85.52 (7)	O(28)-Ni(1)-N(8)	157.70 (7)
C(27)-O(28)-Ni(1)	112.47 (13)	C(2)-O(1)-Ni(1)	112.65 (14)
C(22)-N(21)-C(20)	121.07 (17)	C(7)-N(8)-C(9)	121.33 (17)
Ni(1)-N(21)-C(20)	124.19 (14)	C(9)-N(8)-Ni(1)	122.34 (14)
C(22)-N(21)-Ni(1)	113.75 (14)	C(7)-N(8)-Ni(1)	113.2 (14)

X-ray crystal analysis reveals the complex, [Pd (L^{••})], a mononuclear Pd (II) complex with a tetracoordinate distorted square-planar geometry. The dihedral angle between the C(7)-C(2)-O(1)-Pd(1)-N(8) and C(22)-C(27)-O(28)-Pd(1)-N(21) planes is 22.2°. ORTEP diagram with the labeling scheme is shown in Figure 2.16 and Table 2.4 contains selected bond distances and bond angles. In the discrete molecule, the central Pd ion is coordinated by the N, O, O, N donor set of the ligand. The Ni(1)-O(1), Ni(1)-O(28), Ni(1)-N(8), Ni(1)-N(21) are 1.993(3), 2.001(3), 1.951(4), 1.956(4) Å respectively. The C(7)-N(8), C(22)-N(21) bond distances are shorter than that of C(9)-N(8), C(20)-N(21) bond distances. This indicates that the *tert*-butyl group containing phenyl rings are different than the N-phenyl rings. From the given bond distances and bond angles (Table 2.4) it is quite clear that the complex contains two iminosemiquinone radicals.

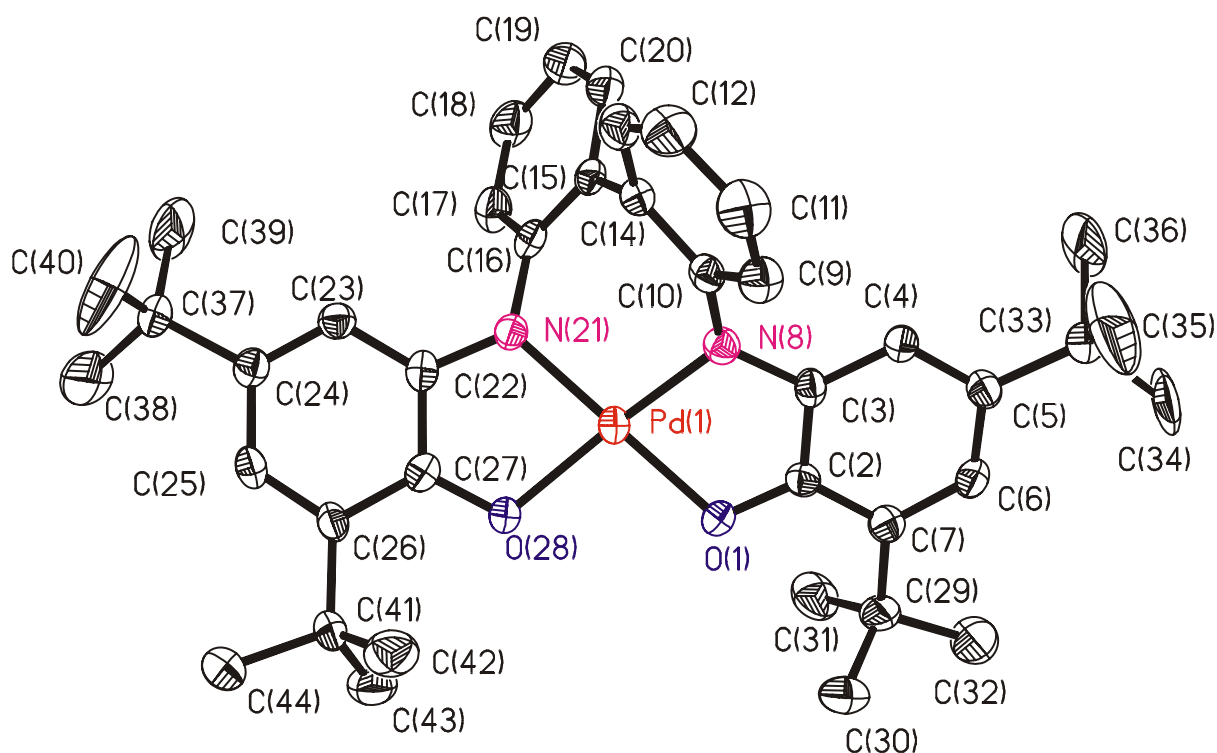


Figure 2.16. ORTEP diagram of 4.

Table 2.4. Selected bond distances (\AA) and angles (degree) for 4.

Pd(1)-N(8)	1.951 (4)	C(4)-C(5)	1.434 (5)
Pd(1)-N(21)	1.956 (4)	C(5)-C(6)	1.368 (5)
Pd(1)-O(1)	1.993 (3)	C(6)-C(7)	1.417 (5)
Cu(1)-O(28)	2.001 (3)	C(22)-N(21)	1.367 (6)
C(2)-O(1)	1.311 (5)	C(22)-C(23)	1.398 (6)
C(7)-N(8)	1.378 (6)	C(23)-C(24)	1.363 (6)
C(2)-C(7)	1.422 (6)	C(24)-C(25)	1.420 (5)
C(2)-C(3)	1.431 (6)	C(25)-C(26)	1.369 (6)
C(3)-C(4)	1.382 (6)	C(26)-C(27)	1.432 (6)
C(9)-N(8)	1.409 (5)	C(27)-O(28)	1.306 (5)
C(9)-C(10)	1.401 (6)	C(20)-C(15)	1.402 (6)
C(10)-C(11)	1.373 (7)	C(15)-C(16)	1.397 (6)
C(11)-C(12)	1.379 (7)	C(16)-C(17)	1.366 (7)
C(12)-C(13)	1.361 (5)	C(17)-C(18)	1.371 (7)
C(13)-C(14)	1.407 (6)	C(18)-C(19)	1.381 (6)
C(14)-C(9)	1.408 (6)	C(19)-C(20)	1.399 (6)
O(1)-Pd(1)-N(8)	81.96 (14)	O(1)-Pd(1)-O(28)	97.66 (12)
N(8)-Pd(1)-N(21)	101.95 (15)	O(1)-Pd(1)-N(21)	167.68 (14)
N(21)-Pd(1)-O(28)	81.38 (13)	O(28)-Pd(1)-N(8)	165.95 (14)
C(27)-O(28)-Pd(1)	111.8 (3)	C(2)-O(1)-Pd(1)	112.0 (3)
C(22)-N(21)-C(20)	122.5 (4)	C(7)-N(8)-C(9)	122.5 (4)
Pd(1)-N(21)-C(20)	121.0 (3)	C(9)-N(8)-Pd(1)	119.1 (3)
C(22)-N(21)-Pd(1)	114.3 (3)	C(7)-N(8)-Pd(1)	113.3 (3)

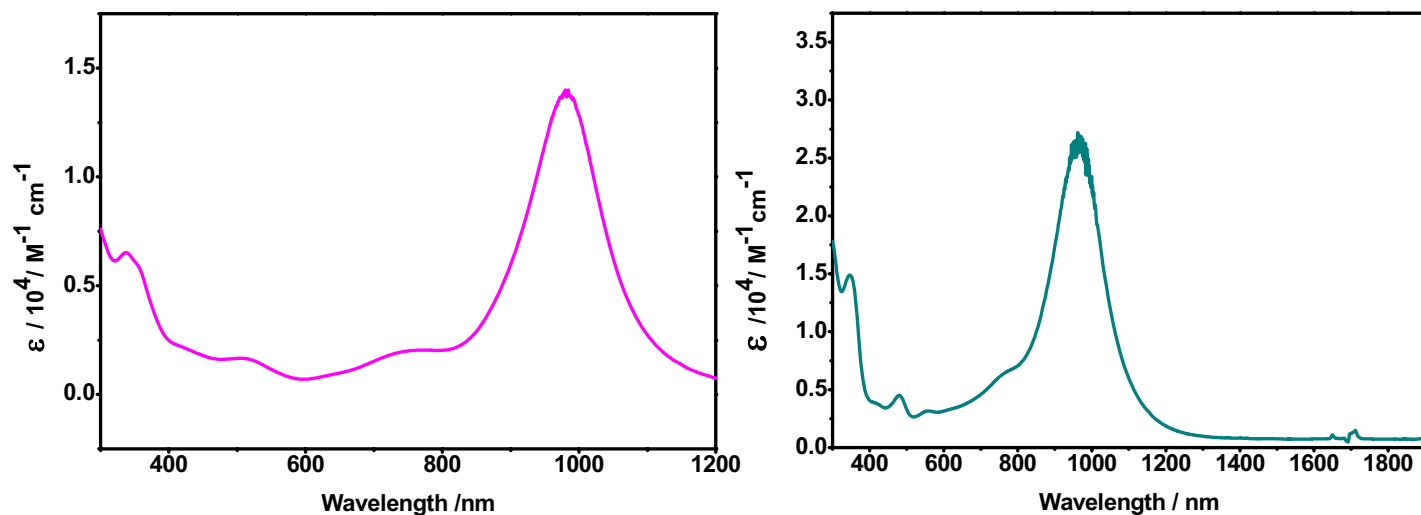


Figure 2.17. Electronic spectrum of complex **3** (left) and complex **4** (right) in CH_2Cl_2 at room temperature.

The most interesting feature in the UV–VIS/NIR spectrum for complex **3** and **4** (Figure 2.17) is the ligand-to-ligand charge transfer band that appears in the lower energy than that of the previously reported complexes.^{51–53} The Table 2.5 summarizes these results. This is presumably because of the highly distorted square planar geometry around the Ni(II) and Pd(II) ions relative to that of the previously reported complexes. The other bands appear due to the ligand-to-metal and ligand π - π^* transitions.^{51–53}

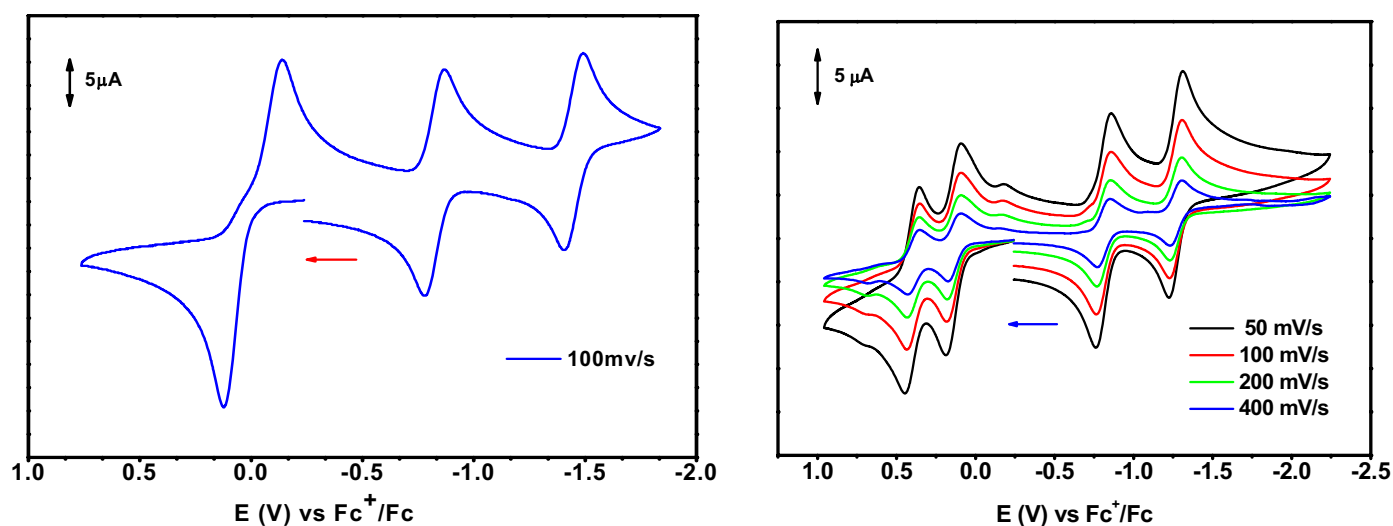


Figure 2.18. Cyclic voltammogram of complex **3** (left) and **4** (right) in CH_2Cl_2 at room temperature under an argon atmosphere.

Figure 2.18 displays the cyclic voltammograms (CVs) of **3** and **4** in CH₂Cl₂ solutions containing 0.1 M [N (*n*-Bu)₄] PF₆ as supporting electrolyte at a glassy carbon working electrode and a Ag/AgNO₃ reference electrode. Ferrocene was used as an internal standard, and potentials are referenced versus the ferrocenium/ ferrocene (Fc⁺/ Fc) couple. Table 2.6 summarizes these results. In the case of complex **3**, one reversible two-electron-transfer wave and two reversible one-electron-transfer waves are observed at E_{1/2} values 0.04, -0.82 and -1.45V vs (Fc⁺/ Fc). Controlled potential coulometric measurements established that E_{1/2}, 0.04V corresponds to one two-electron oxidation and the potentials at E_{1/2} -0.82 V and -1.45 V correspond to two successive one-electron reductions of complex **3**. It has been well established previously that the reduction processes are ligand centered.⁵¹⁻⁵³ In the case of the oxidation process, there are two options, first, direct oxidation of the ligand from iminosemiquinone to iminoquinone at the same potential, or; second, the Ni(II) ion oxidizes and becomes Ni(III) and then intramolecular electron transfer takes place between the Ni(III) center and iminosemiquinone part of the ligand (Figure 2.19). It is clear from the reduction potentials shown in Table 2.6 that the E_{1/2} values for the reduction processes are affected by the geometry around the Ni(II) center. As the oxidation potential does not change for all the biradical containing Ni(II) complexes (references in Table 2.6) the mechanism for the oxidation process of **3** should be similar as that suggested by Chaudhuri-Wieghardt *et. al.*⁵² Hence, the electrochemical behaviour of complex **3** can be summarized as shown in Figure 2.19.

Table 2.5. Spectroelectrochemical data of the complexes.

λ , nm (ϵ , M ⁻¹ cm ⁻¹) X 10 ⁴	Metal ion (II)	Ref.
860 (1.8), 450 (0.28), 300(1.35)	Ni	52
900 (1.6), 600 (0.2), 350 (0.3)	Ni	51
981 (1.4), 746 (0.2), 505 (0.17), 336 (0.64)	Ni	This work
854 (3.0), 581 (0.17), 416 (0.16), 293(1.4)	Ni	53
700 (2.5)	Pd	52
871 (2.7), 546(0.2), 403 (0.2)	Pd	51
961 (2.7), 756 (0.62), 554 (0.31), 475 (0.44), 345 (1.45)	Pd	This work
843 (3.1), 559 (0.29), 552 (0.24), 434 (3.1), 302 (1.9)	Pd	53

Table 2.6. Redox potentials of the complexes vs Fc^+/Fc .

$E^2_{Ox}(V)$	$E^1_{Ox}(V)$	$E^1_{Red}(V)$	$E^2_{Red}(V)$	Dihedral angle ($^\circ$)	$K_d (10^3)$	Metal ion	Ref.
0.040*		-1.1	-1.64	0		Ni(II)	52
0.040*		-1.0	-1.74	0		Ni(II)	51
0.040*		-0.82	-1.45	30.2		Ni(II)	This work
0.042*		-1.07	-1.67	-		Ni(II)	53
0.47	0.08	-1.0	-1.45	0	0.74	Pd(II)	52
0.65	0.17	-1.0	-1.54	0	3.4	Pd(II)	51
0.39	0.13	-0.8	-1.27	22.2	0.08	Pd(II)	This work
0.40	-0.03	-1.13	-1.68	-	1.4	Pd(II)	53

* For 2e process

Complex **4** shows four reversible one-electron-transfer waves which are observed at $E_{1/2}$ value of 0.39, 0.13, -0.80 and -1.27 V vs. (Fc^+/Fc). Clearly, two reversible one-electron oxidations and two reversible one-electron reductions are observed, as established by coulometry at fixed potential. The electrochemical transformations of complex **4** can be summarized as shown in Figure **2.20**. The difference in $E_{1/2}$ values of complex **4** with the previously reported $E_{1/2}$ values (Table **2.6**) may be assigned by considering the geometry around the Pd(II) center.

The disproportionation constant (corresponding to a conproportionation constant $K_c = K_d^{-1}$) for the equilibrium between monocationic forms of complexes **3**, **4** and those in ref.51-53 and their neutral and dicationic forms. These values can be calculated by use of the following equation,

$$K_d = \exp(nF(E^2_{Ox} - E^1_{Ox}))/RT = \exp((E^2_{Ox} - E^1_{Ox}))/0.059$$

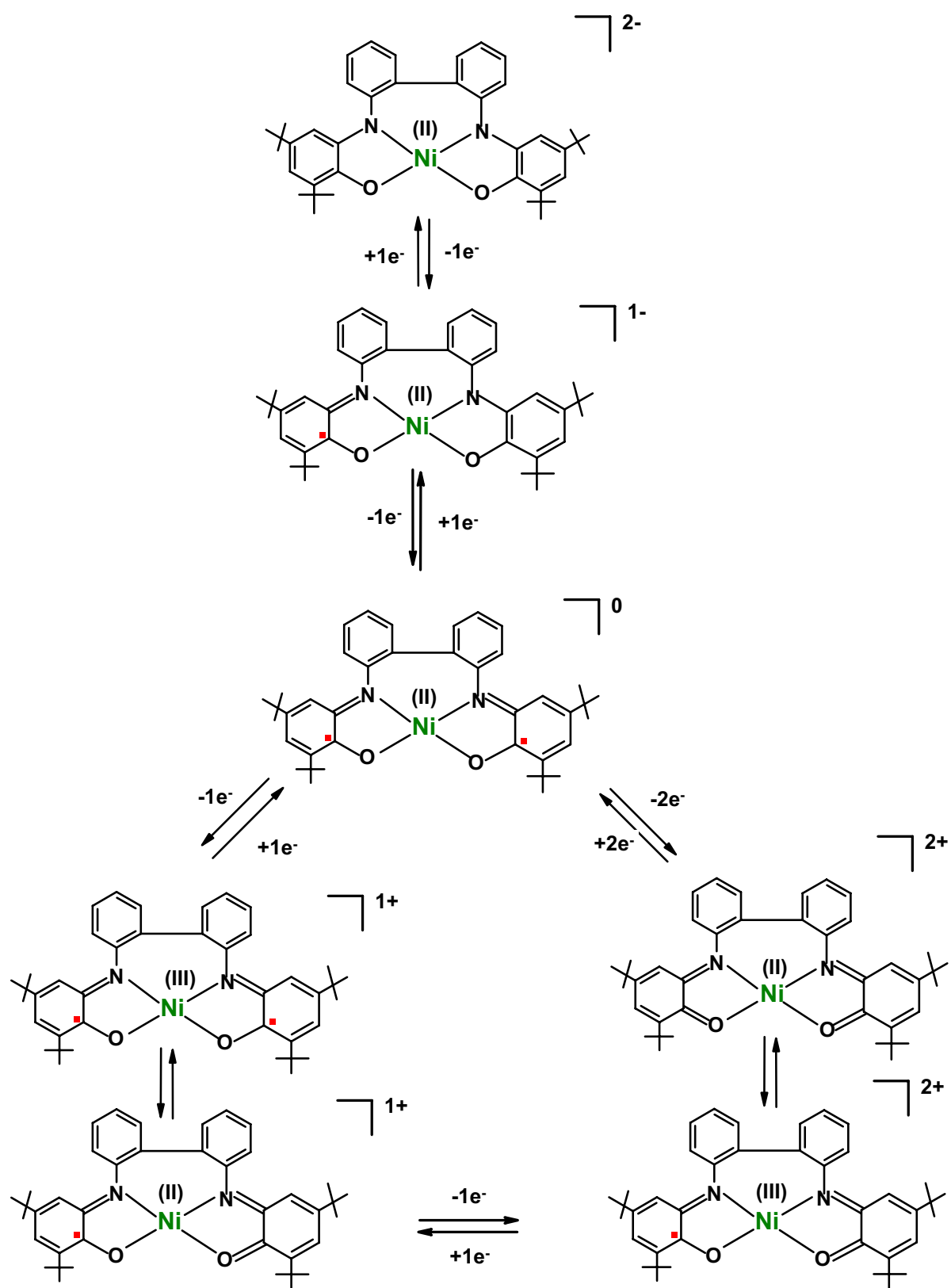


Figure 2.19. Different redox states of complex 3.

The results are summarized in Table 2.6. From these results it is clear that there is a correlation between the K_d values and dihedral angles. The K_d value for the complex (ref 51) differs a little bit from complexes (ref 52, 53) presumably due to electron-withdrawing $-CF_3$ substituent attached to the ligands. The appreciable difference in K_d values of complex **4** than the complexes in references (ref 51-53) emphasize the fact that due to the distortion from square planar geometry the electronic stabilization from delocalization of the π radical throughout the whole molecule is low.

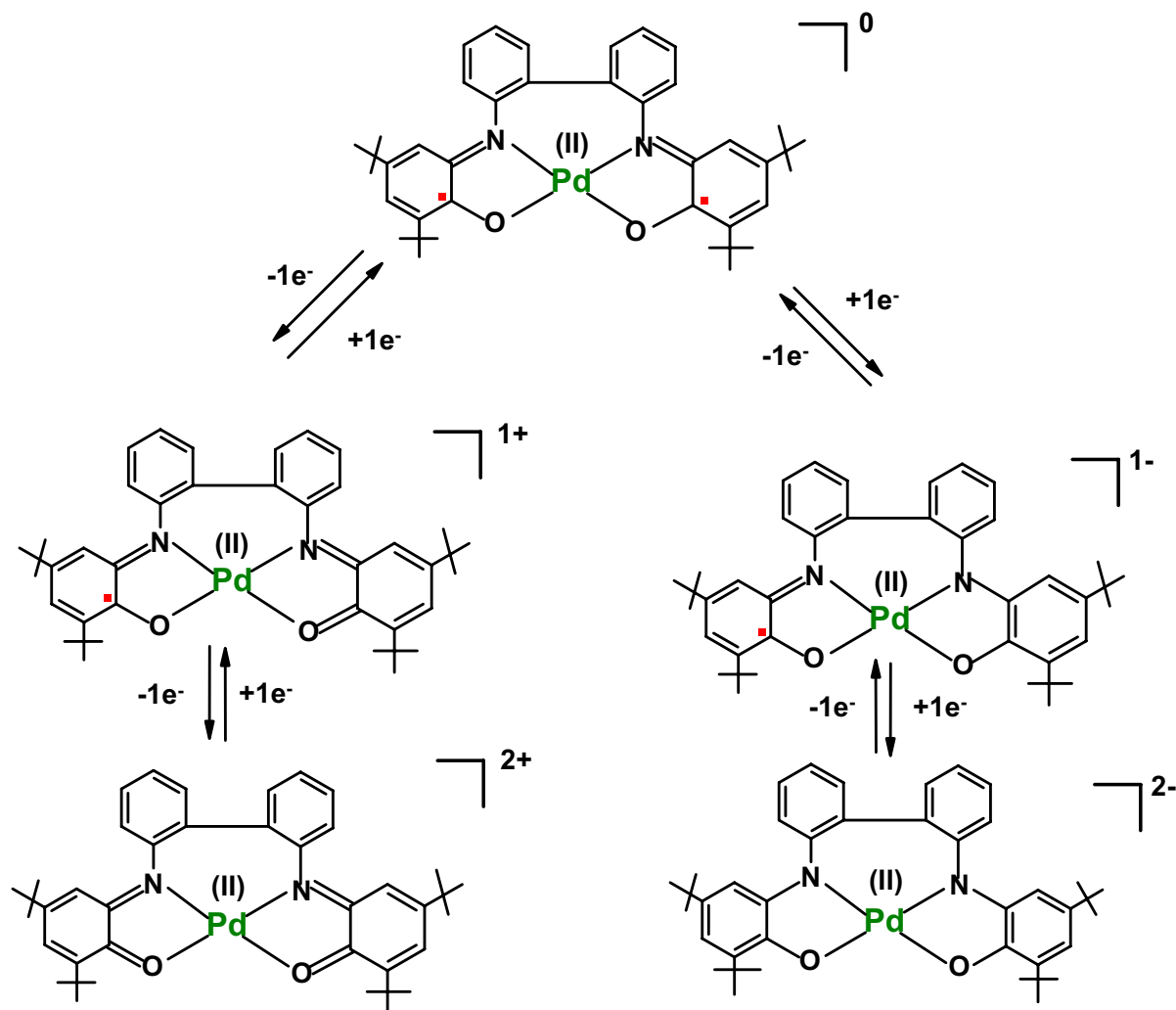


Figure 2.20. Different redox states of complex **4**.

Variable temperature (2 K-298 K) magnetic susceptibility measurement using SQUID magnetometer at 1T indicates that complexes **3** and **4** are diamagnetic. The ^1H NMR for both complexes **3** and **4** were measured in CH_2Cl_2 at RT and shown in the experimental section. The $^1\text{HNMR}$ spectra are quite similar with the ligands. No broadening of the lines is observed. Hence, the diamagnetic character of **3** and **4** was further proved from the NMR spectroscopy.

2.5 *Distorted square planar Cu (II) complex (5) and its catalytic reactivity*

To mimic the distorted square-planar coordination geometry and the catalytic activity of the copper-containing fungal enzyme Galactose Oxidase⁶³⁻⁷³ (GO_{ase}) a tetradentate ligand, N, N' (2-hydroxy-3, 5-di-*tert*-butyl-phenyl) 2,2' diaminobiphenyl (H₄L) (Figure 2.1), has been synthesized and used to form a complex with a copper(II) ion. The expectation is that the designed ligand with an N₂O₂ donor set will provide a distorted square planar copper(II) complex owing to its steric constraint. The ligand is non-innocent and will form mononuclear copper (II) complex, [Cu^{II}(L^{••})], with two iminosemiquinone radical centres. *Hence, the radical containing-copper(II) complex can be used as a true functional and structural model for Galactose Oxidase (GO_{ase}).*

2.5.1 *Synthesis and characterization of the complex (5)*

Complex **5**, [Cu^{II} (L^{••})] was synthesized in CH₃CN by 1:1 reaction of the ligand, H₄L and [Cu^I (CH₃CN)₄] ClO₄ salt in presence of triethylamine as a base under air or under argon atmosphere and followed by air exposure. X-ray quality single crystals were obtained by recrystallization of microcrystalline **5** from a 1:1 CH₂Cl₂ and CH₃CN solvent mixture. The elemental analysis data indicate a composition of C₄₀H₄₈N₂O₂Cu₁ for **5**. The ESI (m⁺/z, in CH₂Cl₂) shows a signal at 651.5(100%) and also supports a composition of C₄₀H₄₈N₂O₂Cu₁.

The structure of complex [Cu^{II} (L^{••})] (**5**) was determined by X-ray crystallography. The analysis confirms the formation of a copper complex with M : L ratio of 1:1. Complex **5** consists of a discrete neutral unit in which the copper ion adopts quite distorted square planar geometry with the dihedral angle between the C(7)-C(2)-O(1)-Cu(1)-N(8) and C(22)-C(27)-O(28)-Cu(1)-N(21) planes is 35.5°. ORTEP diagram with the atom labeling scheme is shown in Figure 2.21 and selected bond distances and angles are listed in Table 2.7. The tetradentate ligand coordinates through two oxygen and two nitrogen atoms, which are fully deprotonated. From the C-C bond distances of the *tert*-butyl containing phenyl rings, it is evident that the *tert*-butyl containing phenyl rings have lost their aromaticity after formation of the complex. The average C-O and the average C-N (N, O attached to the *tert*-butyl containing phenyl rings) bond distances are 1.295(3) and 1.356(4) Å, respectively.

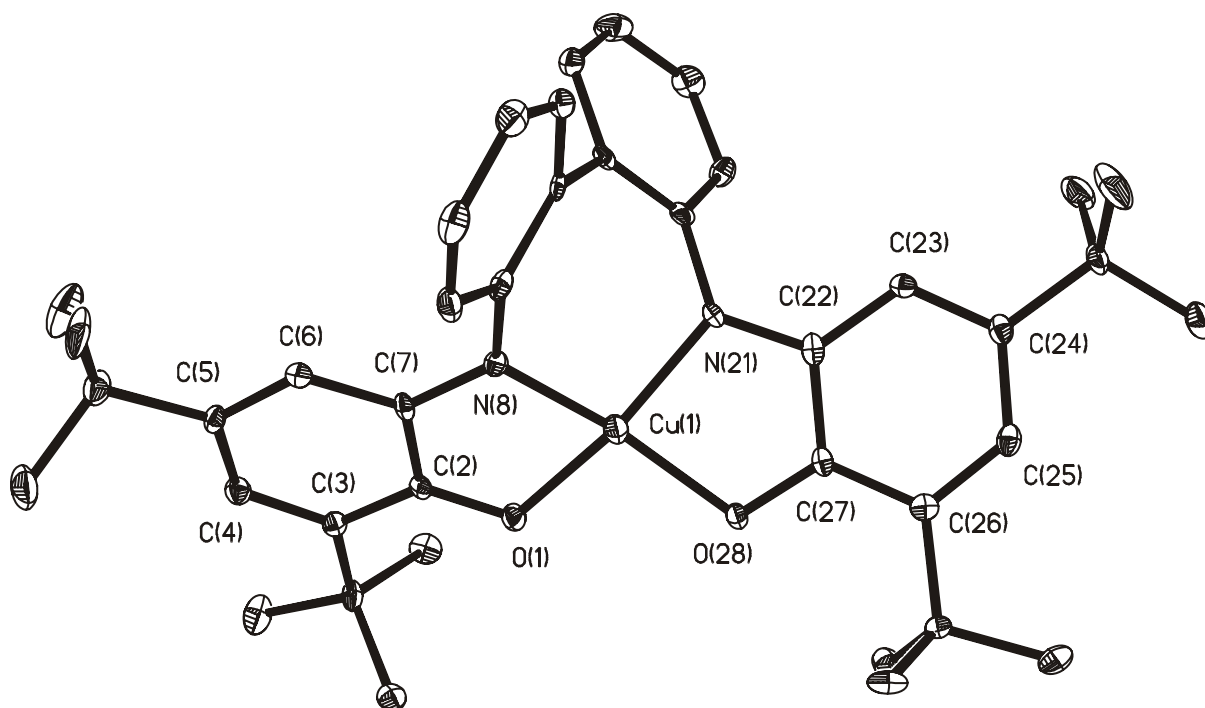


Figure 2.21. ORTEP diagram of **5**.

These clearly show that the *tert*-butyl substituted phenyl rings are in iminosemiquinone form. It is also quite clear from the structure that the ligand is non-innocent. The complex is neutral therefore the copper centre is in a +II oxidation state. The Cu(1)-O(1), Cu(1)-O(28), Cu(1)-N(8) and Cu(1)-N(21) distances are 1.925 (2), 1.925(2), 1.925(3) and 1.919 (3) Å respectively.

Table 2. 7. Selected bond distances (Å) and angles (degree) for **5**.

Cu(1)-N(8)	1.925 (3)	C(4)-C(5)	1.434 (5)
Cu(1)-N(21)	1.919 (3)	C(5)-C(6)	1.368 (5)
Cu(1)-O(1)	1.925 (2)	C(6)-C(7)	1.417 (5)
Cu(1)-O(28)	1.925 (2)	C(22)-N(21)	1.356 (5)
C(2)-O(1)	1.295 (4)	C(22)-C(23)	1.418 (5)
C(7)-N(8)	1.342 (4)	C(23)-C(24)	1.373 (5)
C(2)-C(7)	1.452 (5)	C(24)-C(25)	1.420 (5)
C(2)-C(3)	1.436 (5)	C(25)-C(26)	1.386 (5)
C(3)-C(4)	1.377 (5)	C(26)-C(27)	1.429 (5)
C(9)-N(8)	1.405 (5)	C(27)-O(28)	1.304 (5)
C(9)-C(10)	1.403 (5)	C(20)-C(15)	1.410 (5)
C(10)-C(11)	1.413 (5)	C(15)-C(16)	1.406 (5)
C(11)-C(12)	1.392 (5)	C(16)-C(17)	1.380 (5)
C(12)-C(13)	1.376 (5)	C(17)-C(18)	1.382 (5)
C(13)-C(14)	1.403 (5)	C(18)-C(19)	1.392 (5)
C(14)-C(9)	1.413 (5)	C(19)-C(20)	1.406 (5)
O(1)-Cu(1)-N(8)	84.49 (11)	O(1)-Cu(1)-O(28)	99.72 (10)
N(8)-Cu(1)-N(21)	100.23 (12)	O(1)-Cu(1)-N(21)	155.12 (10)
N(21)-Cu(1)-O(28)	85.3 (11)	O(28)-Cu(1)-N(8)	157.41 (11)
C(27)-O(28)-Cu(1)	111.2 (2)	C(2)-O(1)-Cu(1)	111.5 (2)
C(22)-N(21)-C(20)	123.2 (3)	C(7)-N(8)-C(9)	122.8 (3)
Cu(1)-N(21)-C(20)	121.8 (3)	C(9)-N(8)-Cu(1)	124.5 (3)
C(22)-N(21)-Cu(1)	111.6 (3)	C(7)-N(8)-Cu(1)	112.3 (2)

The cyclic voltammogram (CV) of complex **(5)** has been recorded in CH_2Cl_2 solutions containing 0.1 M $[\text{N}(n\text{-Bu})_4]\text{PF}_6$ as supporting electrolyte at a glassy carbon working electrode and a Ag/AgNO_3 reference electrode. Ferrocene was used as an internal standard, and potentials are referenced versus the ferrocenium/ferrocene (Fc^+/Fc) couple. Table 2.8 summarizes these results. Figure 2.22 shows the CV of **5** recorded in the potential range +1.5 V to -1.5 V. Four reversible one-electron-transfer waves are observed. Two reversible one-electron oxidations and two reversible one-electron reductions are observed, as established by coulometry at fixed potential. The oxidation and reduction processes are ligand centered in nature.^{1, 52} The electrochemical transformations of complex **(5)** can be summarized as follow (Figure 2.23).

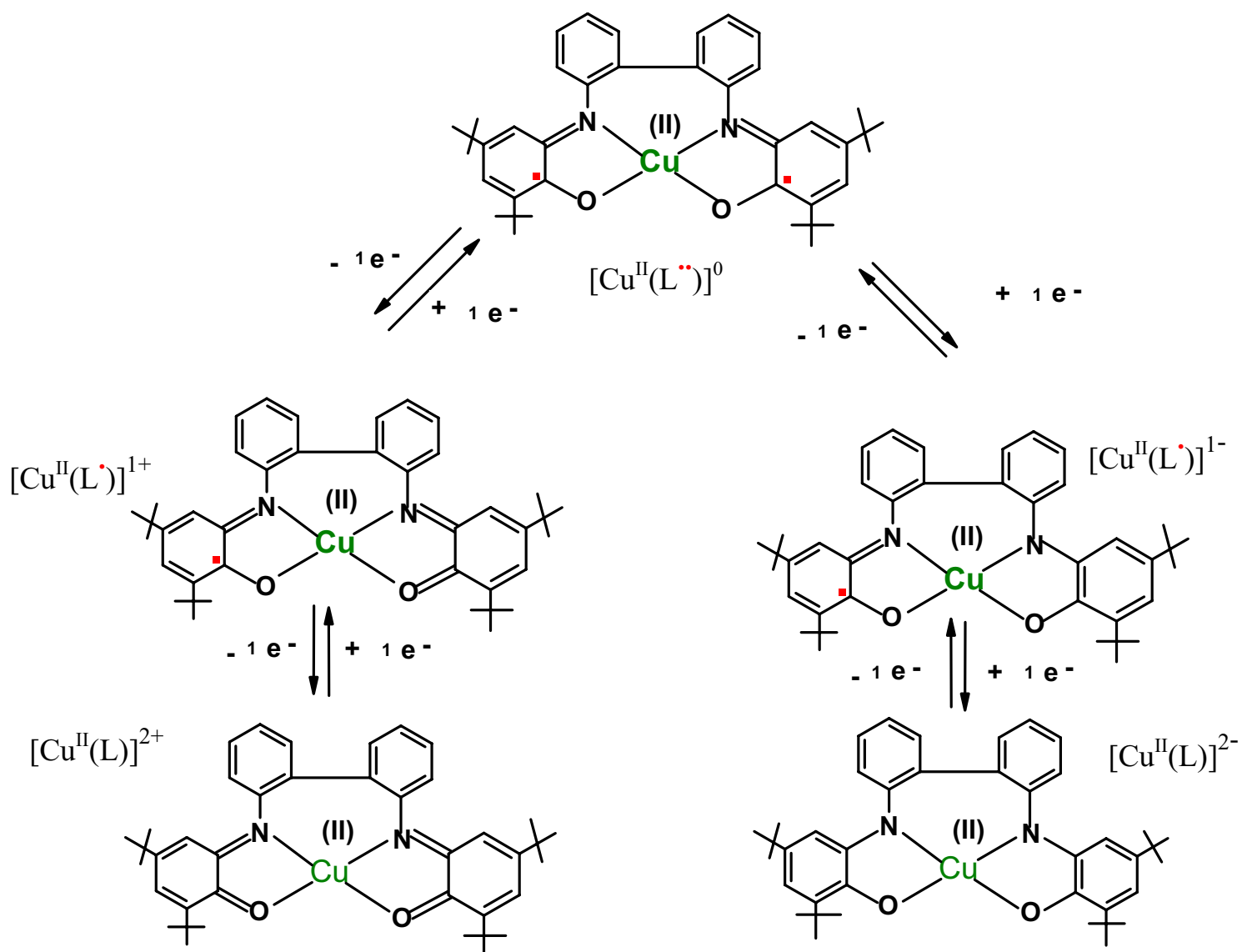


Figure 2.23. Different redox states of $[\text{Cu}^{\text{II}}(\text{L}^{\bullet\bullet})]$, **5**.

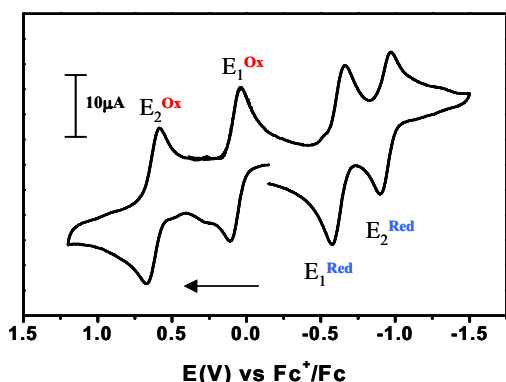


Table 2.8.

$$E_2^{\text{Ox}} = +0.347\text{V vs Fc}^+/\text{Fc}$$

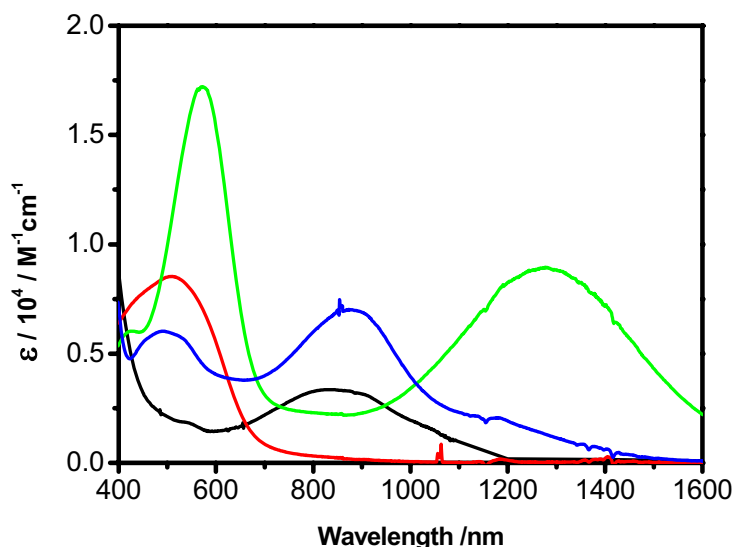
$$E_1^{\text{Ox}} = -0.16\text{V vs Fc}^+/\text{Fc}$$

$$E_1^{\text{Red}} = -0.614\text{V vs Fc}^+/\text{Fc}$$

$$E_2^{\text{Red}} = -0.984\text{V vs Fc}^+/\text{Fc}$$

Figure 2.22. Cyclic Voltammogram of the complex $[\text{Cu}(\text{L}^{\bullet\bullet})]$ in CH_2Cl_2 at 298K under an argon atmosphere.

The results of spectroelectrochemistry investigations in the UV-VIS/NIR regions are summarized in Figure 2.24. Upon reduction of $[\text{Cu}^{\text{II}}(\text{L}^{\bullet\bullet})]$ or more clearly 5^0 to 5^- the long-wavelength band attributed to intraligand (IL) and ligand-to-metal charge transfer (LMCT) are diminished with shifting of maxima from 882 nm to 825 nm and from 592 nm to 542 nm respectively. Spectroelectrochemically, one electron oxidation gives rise to a strong, broad,



$$[\text{CuL}^{\bullet\bullet}]^0 \quad 882 \text{ nm } (7000 \text{ M}^{-1}\text{cm}^{-1}), 492 \text{ nm } (5970 \text{ M}^{-1}\text{cm}^{-1})$$

$$[\text{CuL}^{\bullet}]^- \quad 825 \text{ nm } (3520 \text{ M}^{-1}\text{cm}^{-1}), 542 \text{ nm } (1800 \text{ M}^{-1}\text{cm}^{-1})$$

$$[\text{CuL}^{\bullet}]^+ \quad 1279 \text{ nm } (8900 \text{ M}^{-1}\text{cm}^{-1}), 571 \text{ nm } (17200 \text{ M}^{-1}\text{cm}^{-1})$$

$$[\text{CuL}]^{2+} \quad 507 \text{ nm } (8465 \text{ M}^{-1}\text{cm}^{-1})$$

Figure 2.24. Spectroelectrochemistry studies of complex **5** in $\text{CH}_2\text{Cl}_2/0.1 \text{ M } [\text{N}(\text{t-Bu})_4]\text{PF}_6$.

intervalence charge transfer band at around 1280 nm in addition to a strong, sharp absorption at 570 nm, possibly associated with the formation of a quinone ligand. Upon the second oxidation to $[\text{Cu}^{\text{II}}(\text{L})]^{2+}$ only the band, at 507 nm, arising from quinone π - π^* transition, is observed.

The electronic ground state of complex, $[\text{Cu}(\text{L}^{\bullet\bullet})]$ (**5**), has been established from variable-temperature (2-290 K) magnetic susceptibility measurements by using a SQUID magnetometer. The distorted square-planar complex (**5**) displays a temperature dependence of

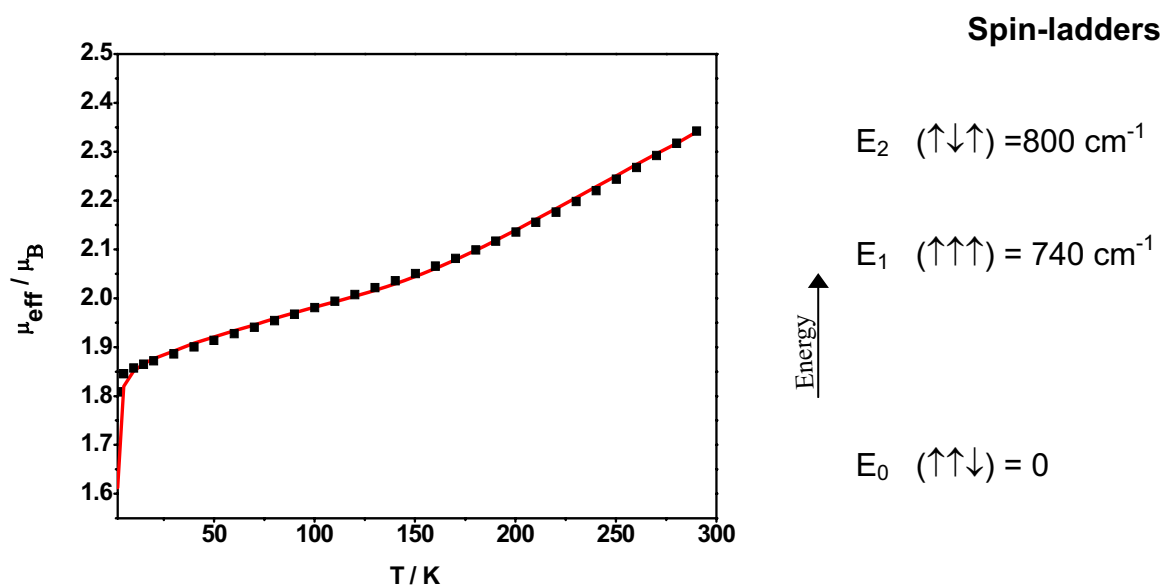


Figure 2.25. Temperature dependence of the magnetic moment of solid $[Cu^{II}(L^{\bullet\bullet})]$.

the effective magnetic moment as shown in Figure 2.25. At temperature $< 50K$, a nearly constant value of $1.83 \mu_B$ ($g_{Cu(II)} = 2.13$) is indicating of an $S_t = 1/2$ ground state. With increasing temperature ($> 50K$) μ_{eff} increases. This is an indication of thermal population of excited states with higher spin multiplicity than 2. This behaviour indicates the presence of more than one paramagnetic centre in complex **5**. Obviously, the complex (**5**) is a “multispin” system which has been proved previously from the high quality X-ray crystal structure. Indeed, it is a three spin molecule with $S_t = 1/2$ ground state. Such a system possesses three coupled states provided that exchange is the dominating spin interaction. The states are labelled by their total spin $S_t = S_{Cu} + S_{rad1} + S_{rad2}$ and a pair subspin $S^* = S_{rad1} + S_{rad2}$, $(S_t, S^*) = (3/2, 1), (1/2, 1), (1/2, 0)$, or, in a more symbolic fashion, by $(\uparrow\uparrow\uparrow), (\uparrow\downarrow\uparrow)$ and $(\uparrow\uparrow\downarrow)$ respectively. Considering symmetric coupling scheme for **5** with two coupling constants the energy of the coupled states are given by $E(3/2, 1) = -J-2J'$, $E(1/2, 1) = 2(J-J')$, and $E(1/2, 0) = 0$. J describes the coupling between a radical and an adjacent copper (II) ion whereas J' describes that between two remote radical anions. Hence, the relative order of these states depends critically on the values of J and J' . To determine the ground state electronic configuration, EPR spectroscopy is a useful tool. The nature of the spin ground state of the complex (**5**) can be sensitively probed by X-band EPR spectroscopy. This is possible because Cu (II) (d^9) ions exhibit significant g anisotropy and large hyperfine splitting contrasting in this respect to the coordinated organic radical anions. The EPR spectrum of **5** in a 1:1 CH_2Cl_2 and toluene solution mixture at 10 K (Figure 2.26) exhibits g values with rhombic distortions ($g_x = 2.064$, $g_y = 2.048$, $g_z = 2.195$). Interestingly, the spectrum shows a distinct ligand

hyperfine splitting which is barely resolved for the g_{\parallel} lines but clearly so at g_x and g_y . A satisfactory simulation was obtained with two equivalent ^{14}N nuclei ($I=1$) with $A_N = (45, 40, 20 \times 10^4 \text{ cm}^{-1})$ for complex (5). Still one question remains unclear. What is the nature of coupling between Cu(II) ion and radical anion? To get the answer the complex was oxidised by one electron using ferrocenium hexafluorophosphate (See experimental section).

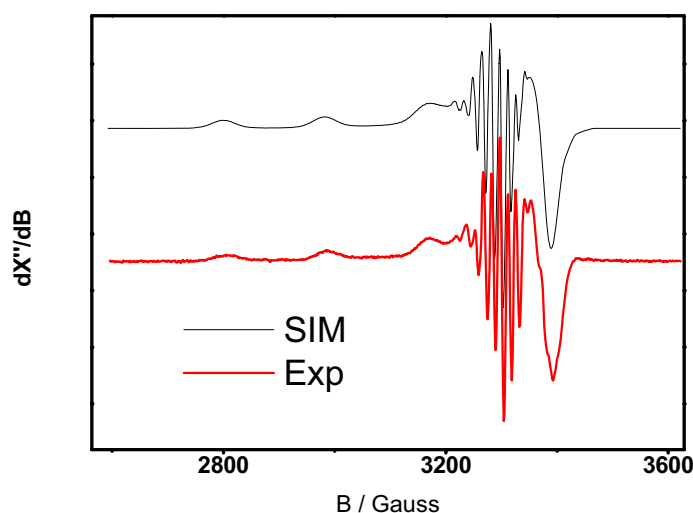
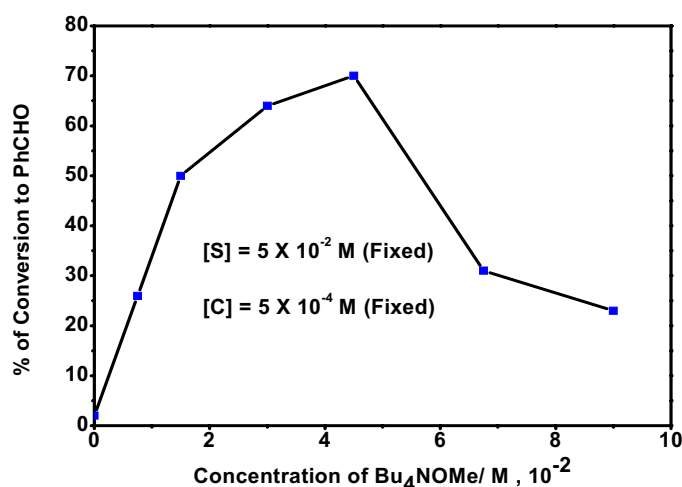


Figure 2.26. X-band EPR Spectrum of the $[\text{Cu}^{\text{II}}\text{L}^{\bullet\bullet}]$ in frozen CH_2Cl_2 at 10 K.

The one electron oxidized species could have $S_t = 1$ or 0 ground state depending on the nature of coupling between two $S = 1/2$ spins [Cu(II) ion and radical anion]. The magnetic susceptibility measurement shows diamagnetic character of the one electron oxidized species. Moreover, the one electron oxidized species is EPR silent. These two experimental evidences help to conclude the antiferromagnetic coupling between Cu (II) ion and radical anion. This is presumably due to the distortion from square planar geometry. The X-band EPR result indicates that the lowest spin state has predominantly copper character, from which it can be concluded that the ground state electronic configuration of the complex is $(\uparrow\uparrow\downarrow)$. Thus the antiferromagnetic radical anion-radical anion interaction (J') must be higher than that of the copper (II) and adjacent radical anion. A satisfactory simulation of the magnetic susceptibility was obtained with $g_{\text{Cu}} = 2.13$, $g_{\text{rad}} = 2.0$, $J' = -327 \text{ cm}^{-1}$ (or -273 cm^{-1}), $J = -62 \text{ cm}^{-1}$ (or -123 cm^{-1}), $\text{TIP} = 6.5 \times 10^{-4} \text{ cm}^3 \text{ mole}^{-1}$. It is noteworthy that a variety of J' and J values can be employed to simulate the experimental results. But from the metal centered X-band EPR result it can be argued that $J' > J$.

2.5.2 Catalytic reactivity, Aerial oxidation of benzyl alcohol; mimicking the function of Galactose Oxidase(GO_{ase})

When complex **5** was used as a catalyst for the aerial oxidation of the primary alcohol, benzyl alcohol ($PhCH_2OH$), it has been found that the complex is capable of oxidising benzyl alcohol in the presence of air at room temperature ($22 \pm 1^\circ C$) to benzaldehyde ($PhCHO$) with an yield % 65. So, it is clear that complex **5** can act as a good functional model of Galactose Oxidase (GO_{ase}), which, a fungal copper containing mononuclear metalloenzyme, catalyses the two electron oxidation of primary alcohols to their corresponding aldehydes in the presence of air (eq 1). The active site of the GO_{ase} contains one copper (II) ion and one Tyr 272 radical and here the copper complex is a copper (II)-biradical complex.



[S] = Concentration of $PhCH_2OH$

[C] = Concentration of $[Cu^{II}(L^{\bullet})]$

Concentration of product was measured by LC using Column, Nucl.-5-C18 Sel-214, UV = 250 nm, gas = MeOH / H_2O 1/1 (V/V).

Figure 2.27. Effect of concentration of base on the % of conversion to $PhCHO$.

This catalytic process is base-dependant. Using a weak base like triethylamine (Et_3N) only 7 TON (Turnover Number, ratio between the total concentration of product and catalyst) has been obtained. Alternatively, using a strong base like tetrabutylammonium methoxide (nBu_4NOMe) or tetrabutylammonium hydroxide (nBu_4NOH) a good TON can be achieved. The concentration of $PhCHO$ was measured by LC. By varying the concentration of base the percentage of yield can be improved and a maximum yield is obtained when the concentration of base (nBu_4NOMe) is 90% of the total concentration of substrate ($PhCH_2OH$). Further

increase in the concentration of base inhibits the catalytic process (Figure 2.27). The most probable reason is the coordination of excess base (MeO⁻) to the copper (II) centre, which protects deprotonated benzyl alcohol to coordinate to the copper (II) centre and hence, the percent yield decreases. It is noteworthy that **5** is incapable of oxidising methoxide to formaldehyde.

Using initial rate method at constant concentration of substrate (PhCH₂OH), the kinetic of the catalytic oxidation of benzyl alcohol has been measured by varying the concentration of [Cu^{II} (L^{••})] under air at room temperature (22 ± 1 ° C) in dichloromethane (Figure 2.28) or vice versa. The product concentration was monitored by UV-VIS spectroscopy at 290 nm ($\epsilon = 1220 \text{ M}^{-1}\text{cm}^{-1}$) taking same concentration of catalyst ([Cu^{II} (L^{••})] that has been used for the reaction as a blank. During kinetic measurements the concentration of base has been kept as a 90% of the total concentration of substrate. From these data the following rate law was deduced,

$$\text{Rate} = k [\text{Cu}^{\text{II}} (\text{L}^{\bullet\bullet})] [\text{PhCH}_2\text{OH}]$$

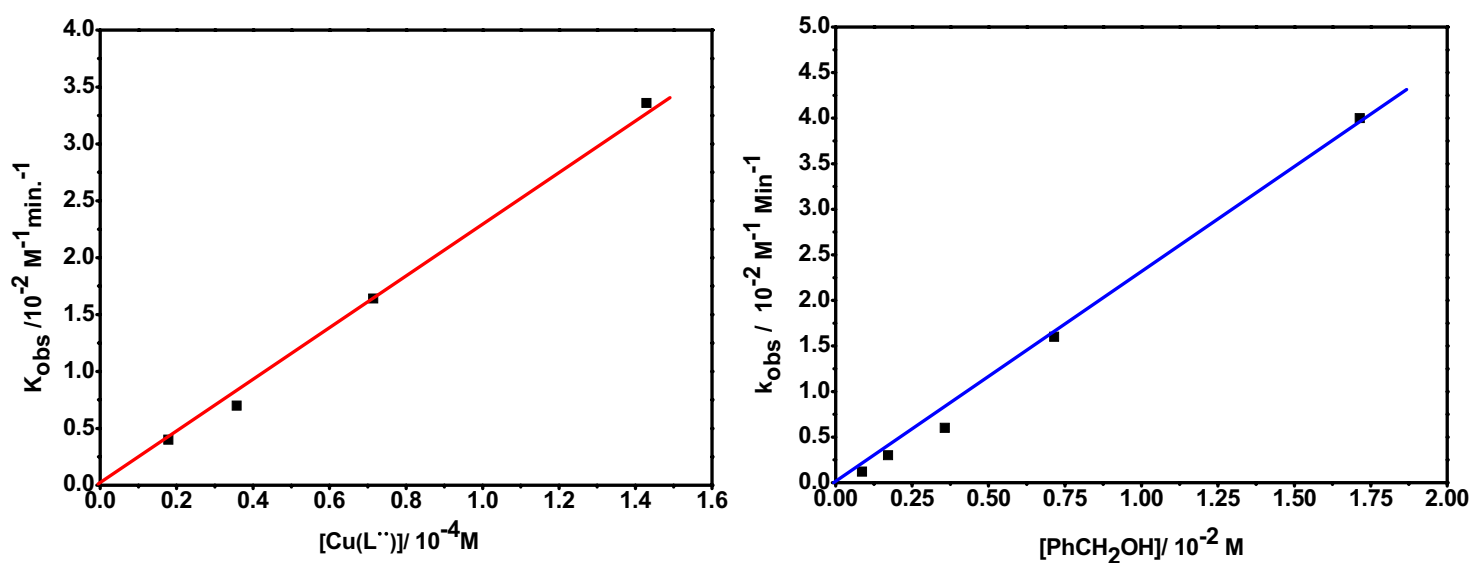


Figure 2.28. Kinetic data.

The TON (Turnover Number, Figure 2.29) of this catalytic process has been measured by varying the total concentration of substrate at constant concentration base 90 % of the total concentration of substrate. The catalyst concentration was kept constant.

With the selectively deuterated substrate PhCD₂OH kinetic isotope effect ($\text{KIE} = k_{\text{H}}/k_{\text{D}}$) of about 14 was evaluated (Figure 2.29). This indicates that the H-atom abstraction from the

α -C atom of the coordinatively bound alcoholate is the rate-determining step for this catalytic oxidation process. When the reaction was done under an anaerobic condition by allowing excess substrate to react with copper (II)-biradical complex, it has been found that the copper (II)-biradical complex has been converted to copper (II)-monoradical mono anionic species (Figure 2.30).

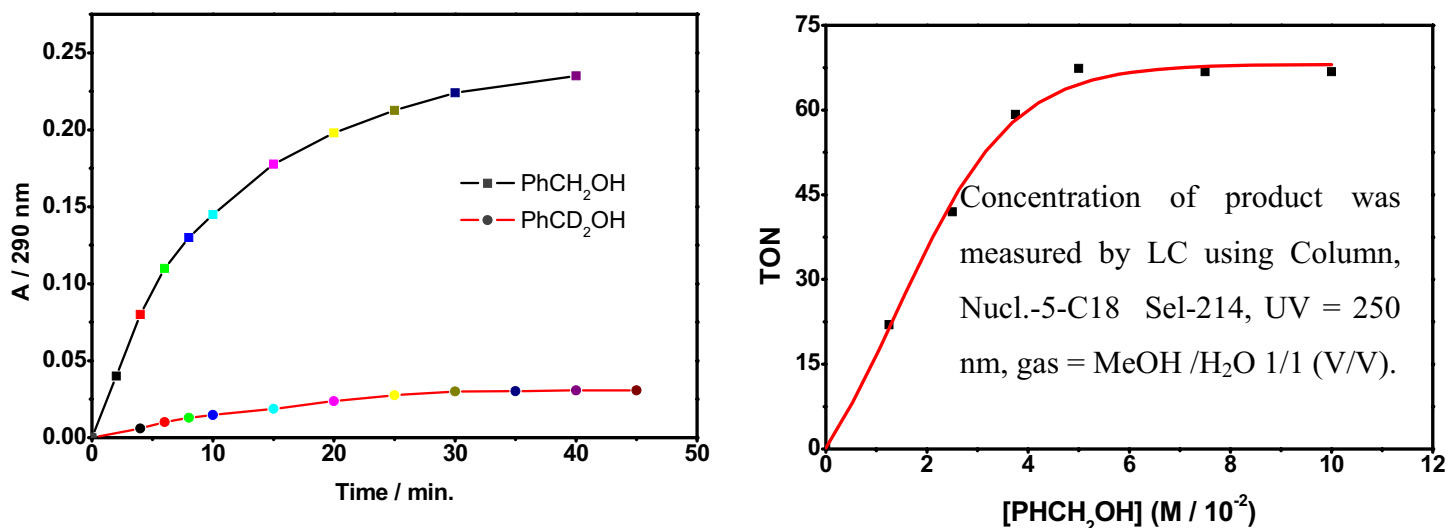


Figure 2.29. KIE plot and TON vs concentration plot for aerial oxidation of benzyl alcohol.

Interestingly, in the above reaction condition the yield of product (PhCHO) is just half of the total concentration of copper (II)-biradical complex. When that solution was kept under air, the copper (II)-monoradical mono anionic species goes back to copper (II)-biradical neutral complex. Here, air acts as an oxidant by reducing itself to hydrogen peroxide.

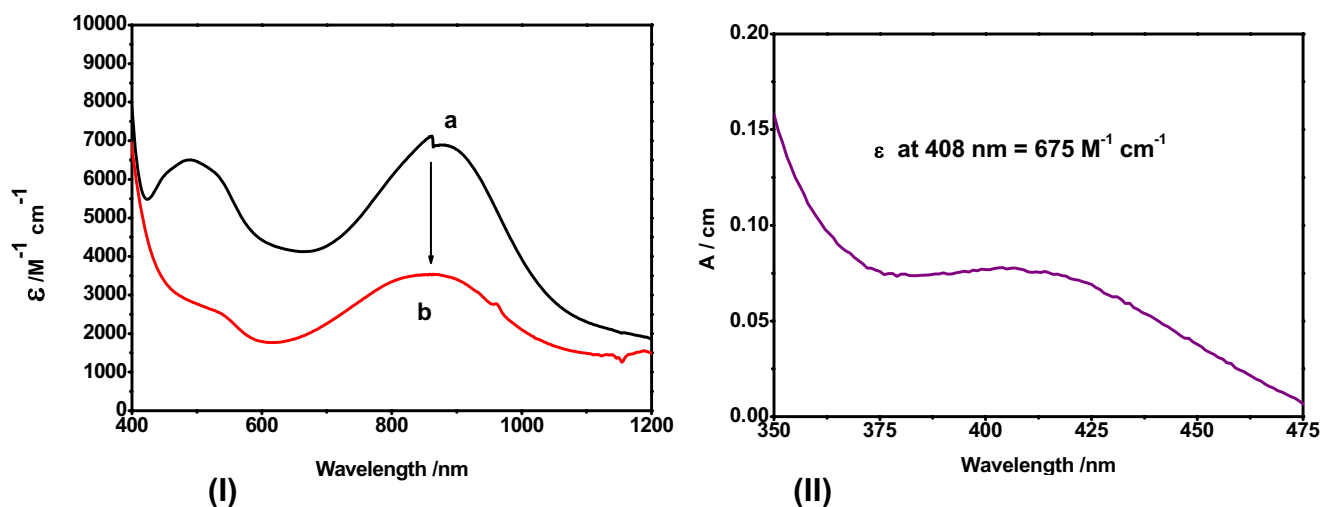


Figure 2.30. (I) Change in UV-VIS spectrum of the complex, $[Cu^{II}(L^{\bullet\bullet})]$, during stoichiometric type reaction with excess benzyl alcohol under an argon atmosphere. (a) Before addition of substrate (b) after addition of substrate (II) H_2O_2 obtained with the reaction of the air and reduced catalyst.

Extracting in water and using titanium sulphate in 9 M sulphuric acid medium the concentration of hydrogen peroxide was then determined by colorimetric method (Figure 2.30). The glove-box reaction *i.e.* the reaction under an anaerobic condition is an indication that the mechanism of this catalytic reaction is not similar to GO_{ase} .^{72, 74-75} The UV-VIS/NIR spectral measurements during the reaction show that in the reaction time the complex exists as copper (II)-monoradical mono anionic species and after the reaction time, 16h, the species goes back to copper (II)-biradical neutral complex (Figure 2.31). No further conversion is observed; even if the catalytic solution is kept for more than 48 hours under air. *This leads to the fact that the copper (II)-biradical neutral complex is not the active species but some other species is catalytically active.*

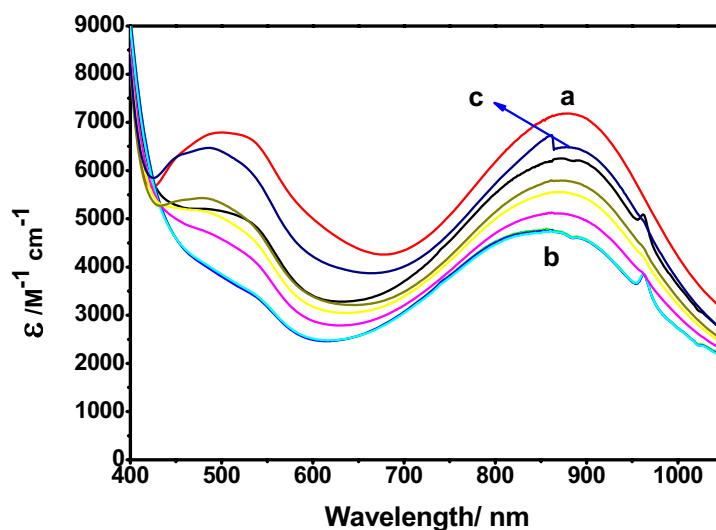


Figure 2.31. Change in UV-VIS spectrum of $[\text{Cu}^{\text{II}}(\text{L}^{\bullet\bullet})]$ during the catalysis. (a) Before addition of substrate, PHCH_2OH , and base, ${}^n\text{Bu}_4\text{NOMe}$. (b) During the catalysis under an aerial condition. (c) After 16h of the catalysis.

If additional base (${}^n\text{Bu}_4\text{NOMe}$) is added to the solution after 16h of the reaction time, the percent of yield increases from 65 to 98 within 48 hours. No change has been observed when the same reaction was repeated with triethylamine.

Effect of base

It has been stated earlier that the catalytic process is base-dependant, an attempt has been made to investigate the effect of the base. The effect of the base was observed when Et₃N and ⁿBu₄NOMe were added to the two different solutions containing the same concentration of **5** under an argon atmosphere and exposing those solutions to air. There is no change in the UV-VIS/NIR spectrum of the copper (II)-biradical complex in the presence of Et₃N but changes were observed in case of ⁿBu₄NOMe (Figure 2.32). To determine the effect of the base, three solutions with different concentration of [Cu^{II} (L^{••})] were made. To each solution different concentration of base (ⁿBu₄NOMe) was added under an argon atmosphere keeping the ⁿBu₄NOMe: [Cu^{II} (L^{••})] concentration ratio (6:1) fixed. The change in UV-VIS/NIR spectrum is given in Figure 2.32. If [Cu^{II} (L^{••})] disproportionates to [Cu^{II} (L[•])⁻] and [Cu^{II} (L[•])⁺] in presence of base (ⁿBu₄NOMe) then the absorption value observed at 880 nm would be equal to the sum of the absorption for 50% of [Cu^{II} (L[•])⁻] and 50% of [Cu^{II} (L[•])⁺] species relative to the total concentration of [Cu^{II}(L^{••})]⁰. Though the mechanism of this disproportionation reaction is not known, the results shown below support the assignment of a disproportionation reaction.

Effect of base and an indication of disproportionation reaction

Concentration of base (Bu ₄ NOMe, M)	Concentration of 5 (M, C ₀)	Base: 5 ratio	Initial absorption of 5 at 880 nm	Final absorption of 5 at 880 nm	Difference in absorption (ΔA) at 880 nm	Concentration of monopositive species.(M, X ₂)	Concentration of mononegative species(M, X ₃)
7.5 X 10 ⁻³	1.267 X 10 ⁻³	5.92 : 1	0.8873 [l = 0.1cm]	0.413 [l = 0.1cm]	0.474	5.6 X 10 ⁻⁴ 6.33 X 10⁻⁴	5.6 X 10 ⁻⁴ 6.33 X 10⁻⁴
4.2 X 10 ⁻³	0.694 X 10 ⁻³	6.04 : 1	0.486 [l = 0.1cm]	0.189 [l = 0.1cm]	0.3	3.49 X 10 ⁻⁴ 3.47 X 10⁻⁴	3.49 X 10 ⁻⁴ 3.47 X 10⁻⁴
2.86 X 10 ⁻³	0.475 X 10 ⁻³	6.02 : 1	0.333 [l = 0.1cm]	0.13 [l = 0.1cm]	0.2	2.35 X 10 ⁻⁴ 2.35 X 10⁻⁴	2.35 X 10 ⁻⁴ 2.35 X 10⁻⁴

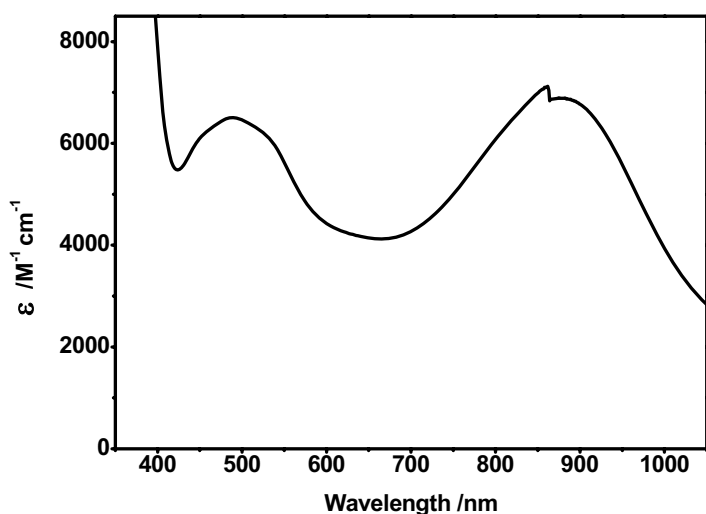
• Bold and italic are the calculated values.

$$\Delta A = [7000 C_0 - \{7000 (C_0 - X) + 3300 X_2 + 2200 X_3\}]$$

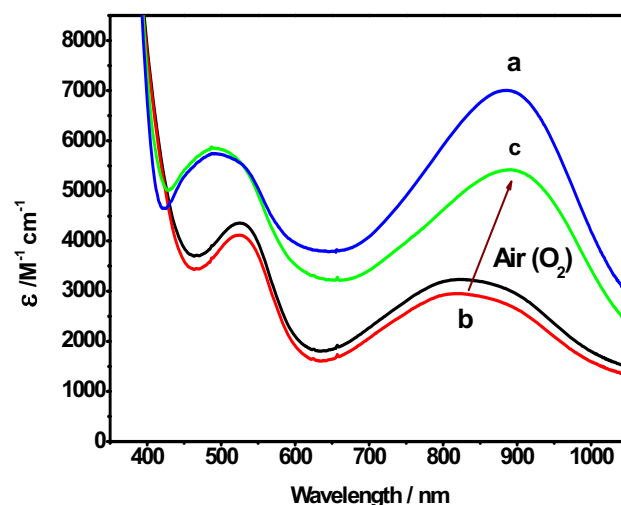
$$\Rightarrow \Delta A = \{7000 (X_2 + X_3) - (3300 X_2 + 2200 X_3)\}$$

$$\Rightarrow \Delta A = 3700 X_2 + 4800 X_3 \quad [\text{When, } X = X_2 + X_3]$$

$$\Rightarrow \Delta A = 8500 X_2 = 8500 X_3 \quad [\text{When, } X_2 = X_3]$$



(I)



(II)

Figure 2.32. (I) Change in UV-VIS/NIR spectrum of complex, $[Cu^{II}(L^{\bullet\bullet})]$, on addition of Et_3N under an argon atmosphere and then allow the solution to be in the air. (II) Change in UV-VIS/NIR spectrum of complex, $[Cu^{II}(L^{\bullet\bullet})]$, on addition of nBu_4NOMe under an argon atmosphere (a to b) and then exposure of the solution to air (b to c).

This above result helps to support a proposal that in the presence of strong base the copper (II)-biradical complex is converted to some other form that is catalytically active. The most probable species that can be catalytically active is the copper (II)-monoradical mono positive species as only copper (II)-monoradical mono negative species was obtained after reaction under anaerobic condition and that goes back to copper (II)-biradical complex in presence of air. From all these results a mechanism can be proposed as given below (Figure 2.33).

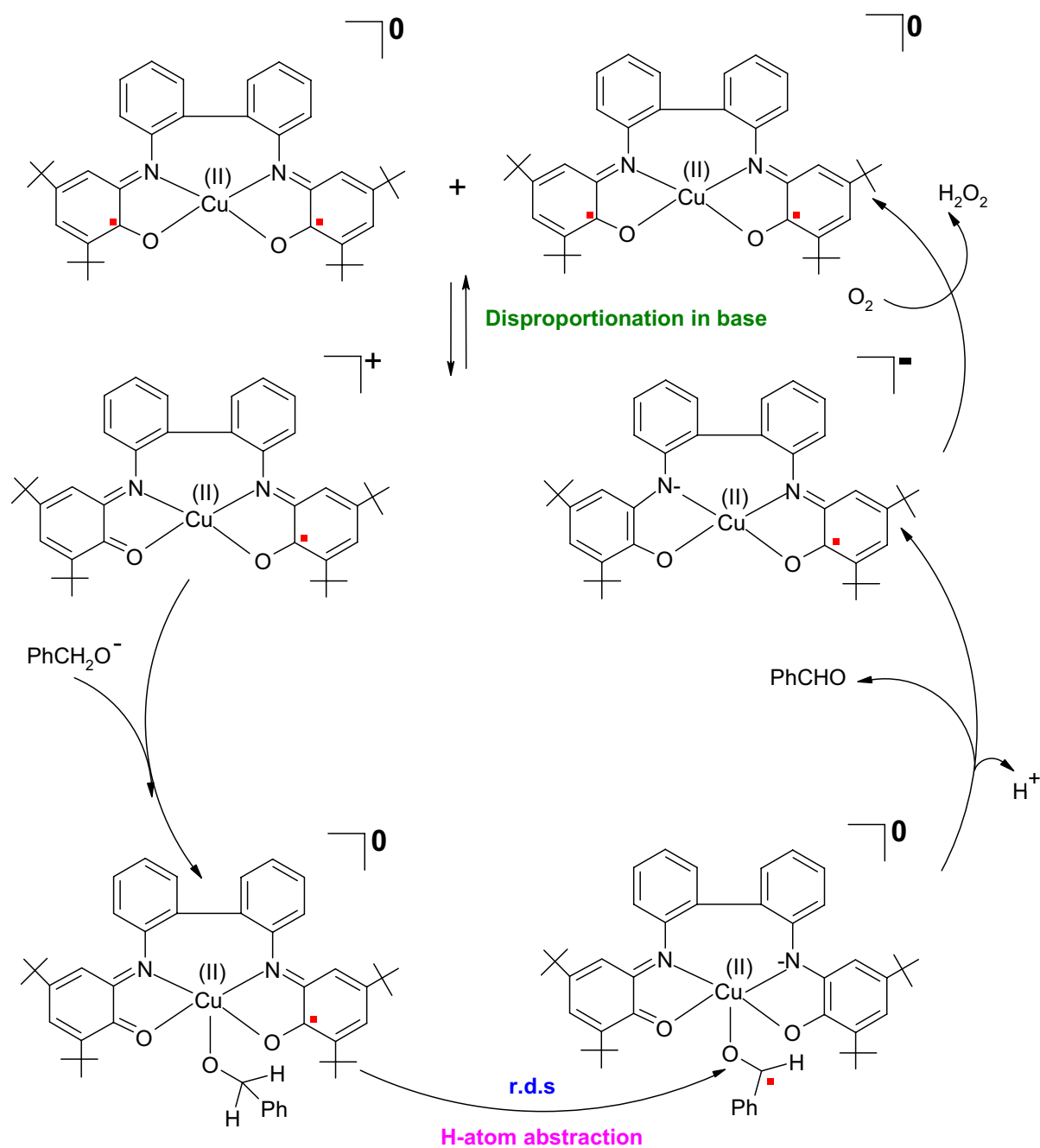


Figure 2.33. The Proposed mechanism for the aerial oxidation of benzyl alcohol.

2.6 References.

1. Chaudhuri, P.; Hess, M.; Müller, J.; Hildenbrandt, K.; Bill, E.; Weyhermüller, T.; Wieghardt, K. *J. Am. Chem. Soc.* **1999**, *121*, 9599.
2. Chaudhuri, P.; Wieghardt, K. *Prog. Inorg. Chem.* **2001**, *50*, 151.
3. Vilter, H. *Phytochemistry*, **1984**, *23*, 1387.
4. Plat, H.; Krenn, B. E.; Wever, R. *Biochem. J.*, **1987**, *248*, 277.
5. de Boer, E.; Boon, K.; Wever, R. *Biochemistry*, **1988**, *27*, 1629.
6. Arber, J. M.; de Boer, E.; Garner, C. D.; Hasnain, S. S.; Wever, R. *Biochemistry*, **1989**, *28*, 7968.
7. De Boer, E.; Kooyk, Y. van.; Tromp, M. G. M.; Plat, H.; Wever, R. *Biochim. Biophys. Acta*, **1986**, *48*, 869.
8. Robson, R. L.; Eady, R. R.; Richardson, T. H.; Miller, R. W.; Hawkins, M.; Postgate, J. R. *Nature*, **1986**, *322*, 388.
9. Hales, B. J.; Case, E. E.; Morningstar, J. E.; Dzeda, M. F.; Mauterrerr, L. A. *Biochemistry*, **1986**, *25*, 7251.
10. Harris, W. R.; Carrano, C. J. *J. Inorg. Biochem.*, **1984**, *22*, 201.
11. Bayer, E.; Koch, E.; Anderegg, G. *Angew. Chem.* **1987**, *99*, 570.
12. Bayer, E.; Koch, E.; Anderegg, G. *Angew. Chem., Int. Ed. Engl.*, **1987**, *26*, 545.
13. Carrondo, M. A. A. F. de C.; Duarte, T.M. T. L. S.; Pessoa, J. C.; Silva, J. A. L.; Silva, J. J. R. F. da.; Vaz, M. C. T. A.; Vilas-Boas, L. F. *J. Chem. Soc., Chem. Commun.*, **1988**, 1158.
14. Smith, M. J.; Kim, D.; Horenstein, B.; Nakanishi, K.; Kustin, K. *Acc. Chem. Res.*, **1991**, *24*, 117.
15. Bonadies, J. A.; Carrano, C. J. *J. Am. Chem. Soc.*, **1986**, *108*, 4088.
16. Bonadies, J. A.; Butler, W. M.; Pecoraro, V. L.; Carrano, C. J. *Inorg. Chem.*, **1987**, *26*, 1218.
17. Mazzanti, M.; Gambarotta, S.; Floriani, C.; Chiesi-Villa, A.; Guastini, C. *Inorg. Chem.*, **1986**, *25*, 2308.
18. Auerbach, U.; Della Vedova, B. S. P. C.; Wieghardt, K.; Nuber, B.; Weiss, J. *J. Chem. Soc., Chem. Commun.*, **1990**, 1004.
19. Cooper, Y. B.; Koh, ; Raymond, K. N. *J. Am. Chem. Soc.* **1982**, *104*, 5092.
20. Kabanias, T. A.; White, A. J. P.; Williams, D. J.; Woollins, J. D. *J. Chem. Soc., Chem. Commun.* **1992**, 17.

21. Neves, A.; Ceccato, A. S.; Vencato, I.; Mascarenhas, Y. P.; Erasmus-Buhr, C. *J. Chem. Soc., Chem. Commun.* **1992**, 652.
22. Kabanos, T. A.; Slawin, A. M. Z.; Williams, D. J.; Woollins, J. D. *J. Chem. Soc., Dalton Trans.* **1992**, 1423.
23. Bruni, S.; Caneschi, A.; Cariatia, F.; Delfs, C.; Dei, A.; Gatteschi, D. *J. Am. Chem. Soc.* **1994**, *116*, 1388.
24. Gergopoulos, V.; Jantzen, S.; Rodewald, D.; Rehder, D. *J. Chem. Soc., Chem. Commun.* **1995**, 377.
25. Klich, P. R.; Daniher, A. D.; Challen, P. R.; McConville, D. B.; Youngs, W. J. *Inorg. Chem.* **1996**, *35*, 347.
26. Farahbakhsh, V.; Schmidt, H.; Rehder, D. *J. Chem. Soc., Chem. Commun.* **1998**, 2009.
27. Kang, L.; Wenig, H.; Liu, D.; Wu, L.; Huang, C.; Lu, J.; Cai, X.; Chen, J.; Lu, J. *Inorg. Chem.* **1990**, *29*, 4873.
28. Ludwig, E.; Hefele, H.; Uhlemann, E.; Weller, F.; Kläui, W. *Z. Anorg. Allg. Chem.* **1995**, *23*, 621.
29. Hefele, H.; Ludwig, E.; Uhlemann, E.; Weller, F. *Z. Anorg. Allg. Chem.* **1995**, *23*, 1973.
30. Diamantis, A. A.; Snow, M. R.; Vanzo, J. A. *J. Chem. Soc., Chem. Commun.* **1976**, 264.
31. Comba, P.; Engelhardt, L. M.; Harrowfield, J. M.; Lawrence, G. A.; Martin, L. L.; Sargeson, A. M. White, A. H. *J. Chem. Soc., Chem. Commun.* **1985**, 174.
32. Diamantis, A. A.; Manikas, M.; Salam, M. A.; Snow, M. R.; Tiekink, E. R. T. *Aust. J. Chem.* **1988**, *41*, 453.
33. Woodlin, J. D. *J. Chem. Soc., Chem. Commun.* **1992**, 17.
34. Chun, H.; Chaudhuri, P.; Weyhermüller, T.; Wieghardt, K. *Inorg. Chem.* **2002**, *41*, 790.
35. Neves, A.; Ceccato, A. S.; Vencato, I.; Mascarenhas, Y. P.; Erasmus-Buhr, C. *J. Chem. Soc., Chem. Commun.*, **1992**, 652.
36. Paine, T. K.; Weyhermüller, T.; Wieghardt, K.; Chaudhuri, P. *Inorg. Chem.* **2004**, *43*, 7324.
37. Larsen, S. K.; Pierpont, C. G.; DeMunno, G.; Dolcetti, G. *Inorg. Chem.* **1986**, *25*, 4828.

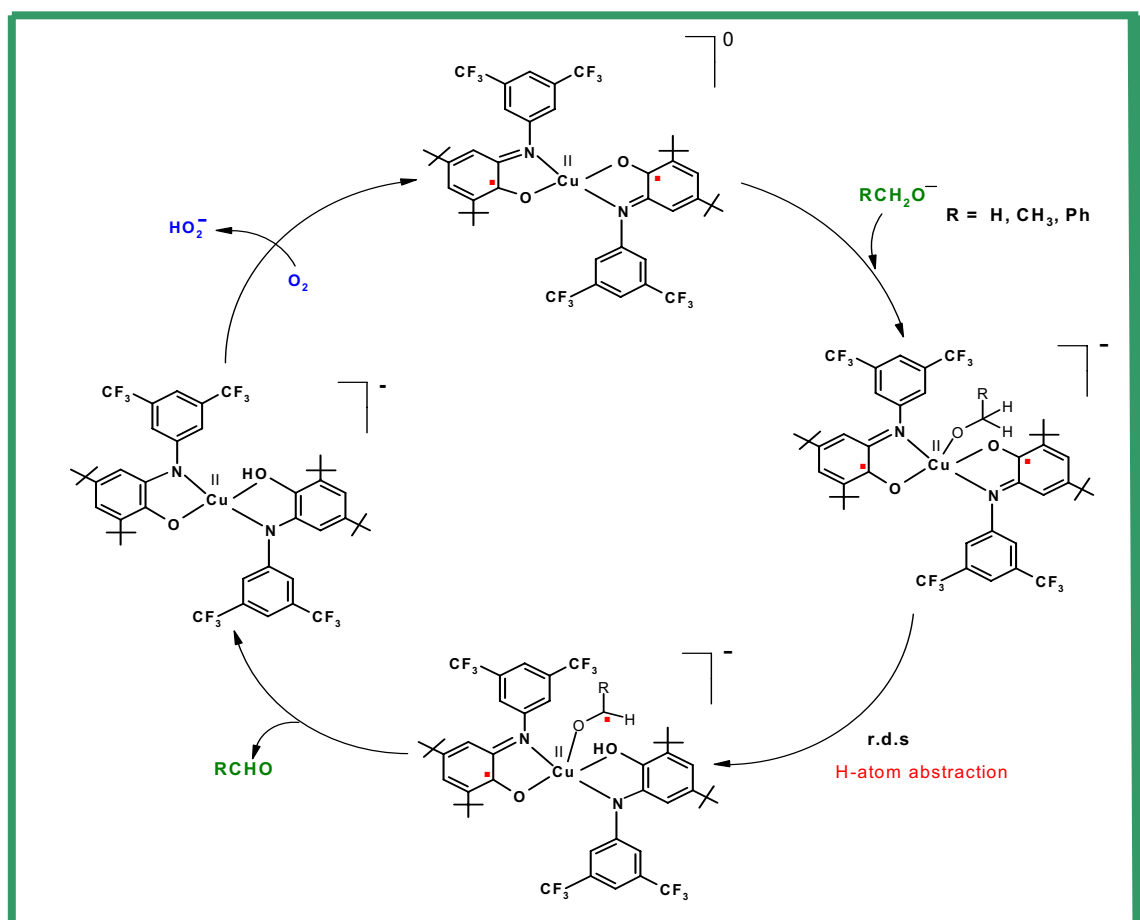
38. Lynch, M. W.; Valentine, M.; Hendrickson, D. N. *J. Am. Chem. Soc.* **1982**, *102*, 6982.
39. Chang, H.-C.; Ishii, T.; Kondo, M.; Kitagawa, S. *J. Chem. Soc., Dalton Trans.* **1999**, 2467.
40. Chang, H.-C.; Kitagawa, S. *Angew. Chem., Int. Ed.* **2002**, *41*, 130.
41. Chang, H.-C.; Kitagawa, S. *Angew. Chem., Int. Ed.* **2002**, *41*, 4444.
42. Cador, O.; Chabre, F.; Dei, A.; Sangregorio, C.; Van Slageren, J.; Vaz, M. G. F. *Inorg. Chem.* **2003**, *42*, 6432.
43. Lynch, M. W.; Hendrickson, D. N.; Fitzgerald, B. J.; Pierpont, C. G. *J. Am. Chem. Soc.* **1984**, *106*, 2041.
44. Larsen, S. K.; Pierpont, C. G. *J. Am. Chem. Soc.* **1988**, *110*, 1827.
45. Lynch, M. W.; Valentine, M.; Hendrickson, D. N. *J. Am. Chem. Soc.* **1982**, *104*, 6982.
46. Chun, H.; Weyhermüller, T.; Bill, E.; Wieghardt, K. *Angew. Chem., Int. Ed.* **2001**, *40*, 2489.
47. Chun, H.; Bill, E.; Bothe, E.; Weyhermüller, T.; Wieghardt, K. *Inorg. Chem.* **2002**, *41*, 5091.
48. Snodin, M.D.; Ould-Moussa, L.; Wallmann, U.; Lecomte, S.; Bachler V, Bill, E.; Hummel, H.; Weyhermüller, T.; Hildebrandt, P.; Wieghardt K, *Chem.Eur.J.* **1999**, *5*, No. 9, 2553.
49. "Do S, S'-Coordinated o-Dithiobenzosemiquinonate(1-) Radicals Exist in Coordination Compounds? A Combined Experimental and Computational Study", Thesis, Kallol Ray, Universität Bochum. **2005**.
50. Inness, D.; Soltis, S. M.; Strouse, C. E. *J. Am. Chem. Soc.* **1988**, *110*, 5644.
51. Kokatam, S.; Weyhermüller, T.; Bothe, E.; Chaudhuri, P. Wieghardt, K. *Inorg. Chem.*, **2005**, *44*, 3709.
52. Chaudhuri, P.; Verani, C. N.; Bill, E.; Bothe, E.; Weyhermüller, T.; Wieghardt, K. *J. Am. Chem. Soc.* **2001**, *123*, 2213.
53. Min, K. S.; Weyhermüller, T.; Bothe, E.; Wieghardt, K. *Inorg. Chem.*, **2004**, *43*, 2922.
54. Verani, C. N.; Gallert, S.; Bill, E.; Weyhermüller, T.; Wieghardt, K.; Chaudhuri, P. *J. Chem. Soc., Chem. Commun.* **1999**, 1747.
55. Chun, H.; Verani, C. N.; Chaudhuri, P.; Bothe, E.; Bill, E.; Weyhermüller, T.; Wieghardt, K. *Inorg. Chem.* **2001**, *40*, 4157.

56. Herebian, D.; Ghosh, P.; Chun, H.; Bothe, E.; Weyhermüller, T.; Wieghardt, K. *Eur. J. Inorg. Chem.* **2002**, 1957.
57. Chun, H.; Chaudhuri, P.; Weyhermüller, T.; Wieghardt, K. *Inorg. Chem.* **2002**, *41*, 790.
58. Min, K. S.; Weyhermüller, T.; Wieghardt, K. *J. Chem. Soc., Dalton Trans.* **2003**, 1126.
59. Balch, A. L.; Holm, R. H. *J. Am. Chem. Soc.* **1966**, *88*, 5201.
60. Holm, R. H.; Balch, A. L.; Davison, A.; Maki, A.; Berry, T. *J. Am. Chem. Soc.* **1967**, *89*, 2866.
61. Forbes, C. E.; Gold, A.; Holm, R. H. *Inorg. Chem.* **1971**, *10*, 2479.
62. Stiefel, E. I.; Waters, J. H.; Billig, E.; Gray, H. B. *J. Am. Chem. Soc.* **1965**, *87*, 3016.
63. Whittaker, J. W. In *Metal Ions in Biological Systems*; Sigel, H., Sigel, A., Eds.; Marcel Dekker: New York, **1994**; Vol. 30, pp 315.
64. Knowles, P. F.; Ito, N. In *Perspectives in Bio-inorganic Chemistry*; Jai Press Ltd.: London, **1994**; Vol. 2, pp 207-244.
65. Ito, N.; Phillips, S. E. V.; Stevens, C.; Ogel, Z. B.; McPherson, M. J.; Keen, J. N.; Yadav, K. D. S.; Knowles, P. F. *Nature*, **1991**, 350.
66. Ito, N.; Phillips, S. E. V.; Stevens, C.; Ogel, Z. B.; McPherson, M. J.; Keen, J. N.; Yadav, K. D. S.; Knowles, P. F. *Faraday Discuss.* **1992**, *93*, 75.
67. Ito, N.; Phillips, S. E. V.; Yadav, K. D. S.; Knowles, P. F. *J. Mol. Biol.* **1994**, 238, 794.
68. Wachter, R. M.; Montagne-Smith, M. P.; Branchaud, B. P. *J. Am. Chem. Soc.* **1997**, *119*, 7743.
69. Branchaud, B. P.; Montagne-Smith, M. P.; Kosman, D. J.; McLaren, F. R. *J. Am. Chem. Soc.* **1993**, *115*, 798.
70. Whittaker, M. M.; Whittaker, J. M. *Biophys. J.* **1993**, *64*, 762.
71. Wachter, R. M.; Branchaud, B. P. *J. Am. Chem. Soc.* **1996**, *118*, 2782.
72. Whittaker, M. M.; Whittaker, J. M. *Biophys. J.* **1993**, *64*, 762.
73. Whittaker, J. W.; Whittaker, M. M. *Pure Appl. Chem.* **1998**, *70*, 903.
74. Halfen, J. A.; Jazdzewski, B. A.; Mahapatra, S.; Berreau, L. M.; Wilkinson, E. C.; Que, L., Jr.; Tolman, W. B. *J. Am. Chem. Soc.* **1997**, *119*, 8217.
75. Halfen, J. A.; Young, V. G., Jr.; Tolman, W. B. *Angew. Chem., Int. Ed. Engl.* **1996**, *35*, 1687.

Chapter 3

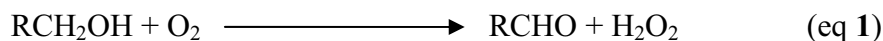
Synthesis, Characterization and Catalytic Reactivities of the Tetracoordinate Cu (II)-Complexes formed with the Ligands, $N(2\text{-hydroxy-3,5-di-tert-butylphenyl})\text{-3,5-di-substituted-aniline, } H_2L^X$ ($X = -CF_3, -F, -Cl, -OMe, -^tBu$)

Is there any effect of substituents at the 3,5 positions of the N-phenyl ring to the physical and chemical properties of the complexes?



3.1 Introduction

Radical containing Cu(II) complexes of the type shown in Figure 3.3 are known to catalyze ⁶ oxidation of primary alcohols to the corresponding aldehydes (eq 1)



A natural question to ask in the optimization of this catalytic process is how the steric and/or electronic effect of the ligand influences the geometries of the catalysts and also the catalytic activity.

To show these effects a few ligands (**1-5**) have been synthesized by varying the nature of the substituents at 3,5- positions of the N-phenyl group. Figure 3.1 shows the schematic diagram of the ligands (**1-5**).

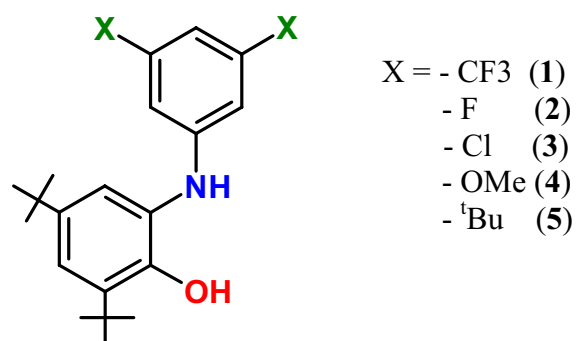


Figure 3.1. Schematic diagram of the ligands (**1- 5**).

To understand the nature of the effects, i.e. inductive effect or mesomeric effect, isomeric ligands (**6,7**) have been synthesized by changing the position of the substituent from the 3,5 positions to the 2, and the 4 positions. Figure 3.2 shows the schematic diagram of the ligands (**6, 7**).

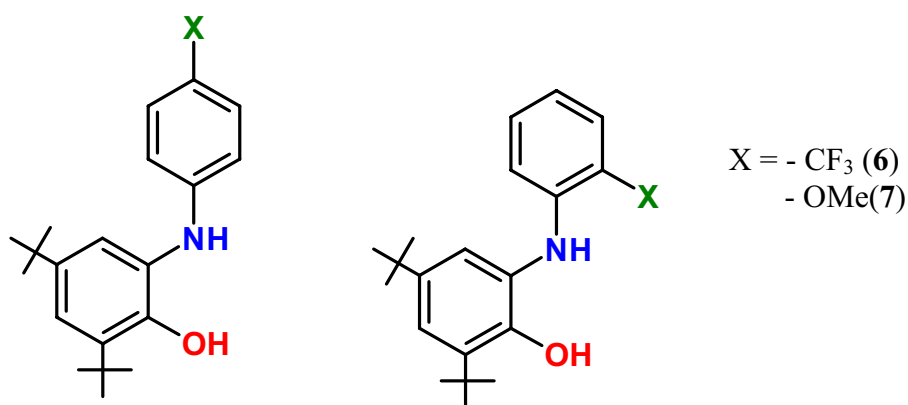


Figure 3.2. Schematic diagram of the ligands (6-7).

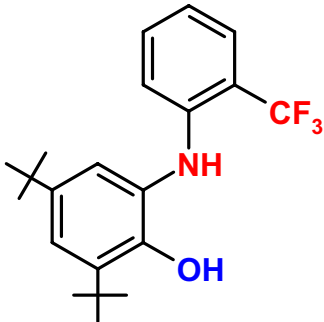
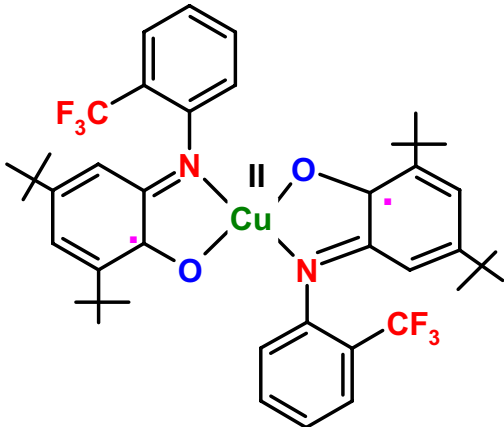
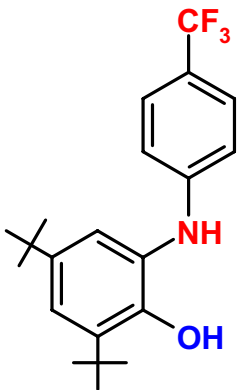
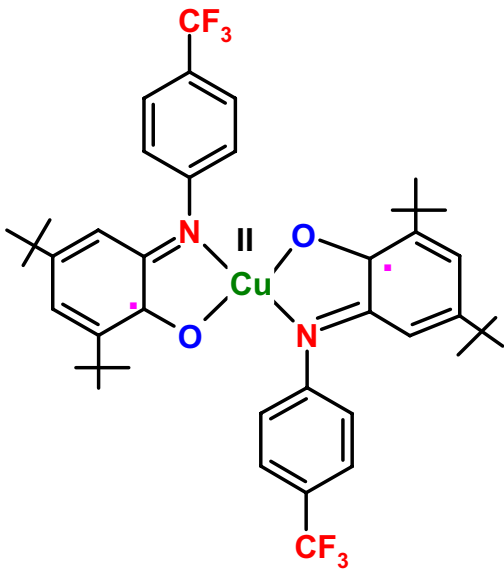
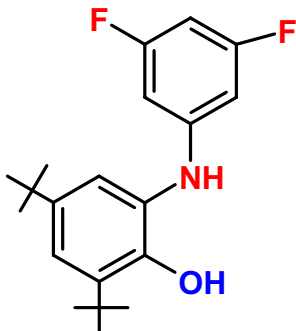
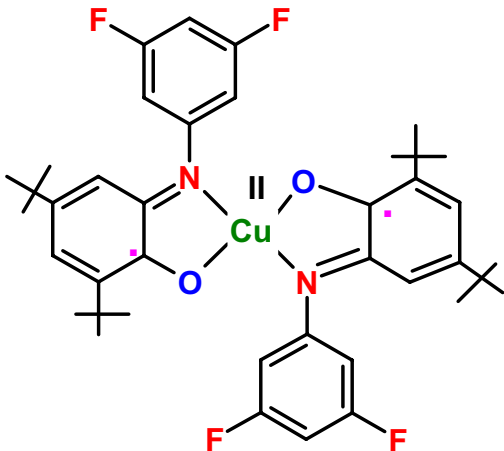
3.2 Synthesis and characterization

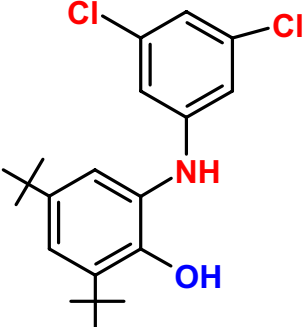
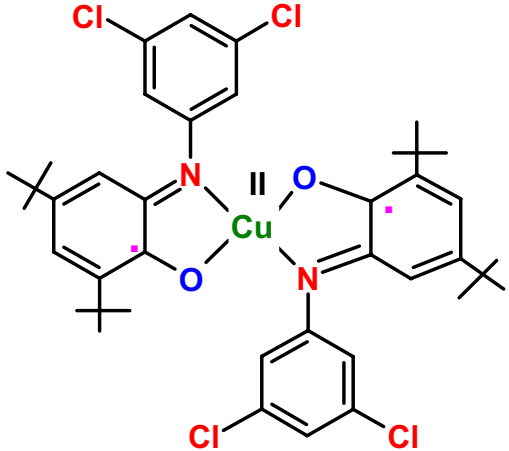
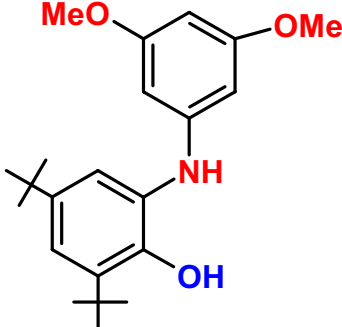
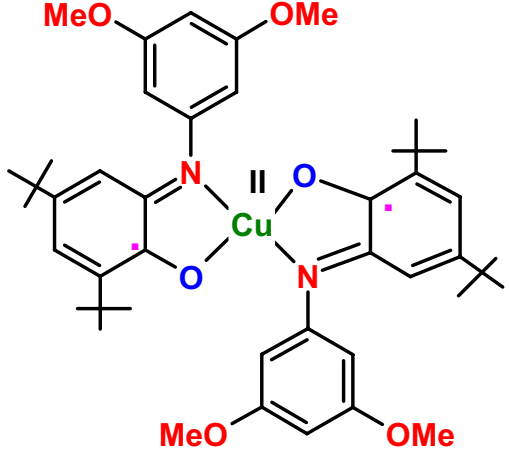
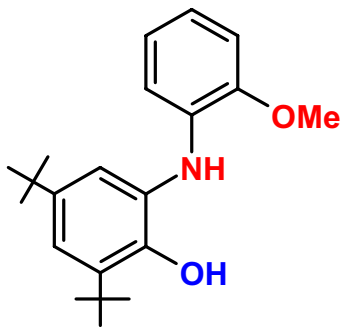
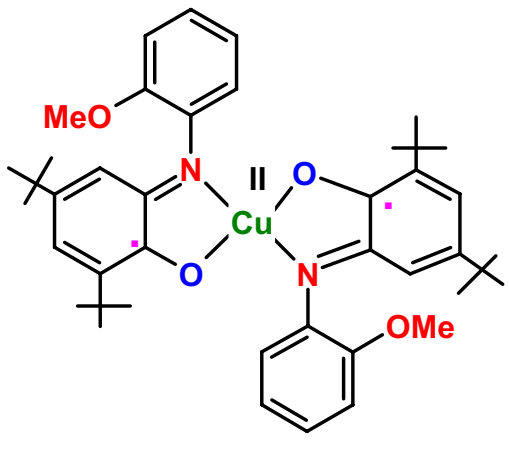
All the ligands were synthesized and characterized previously.¹⁻²

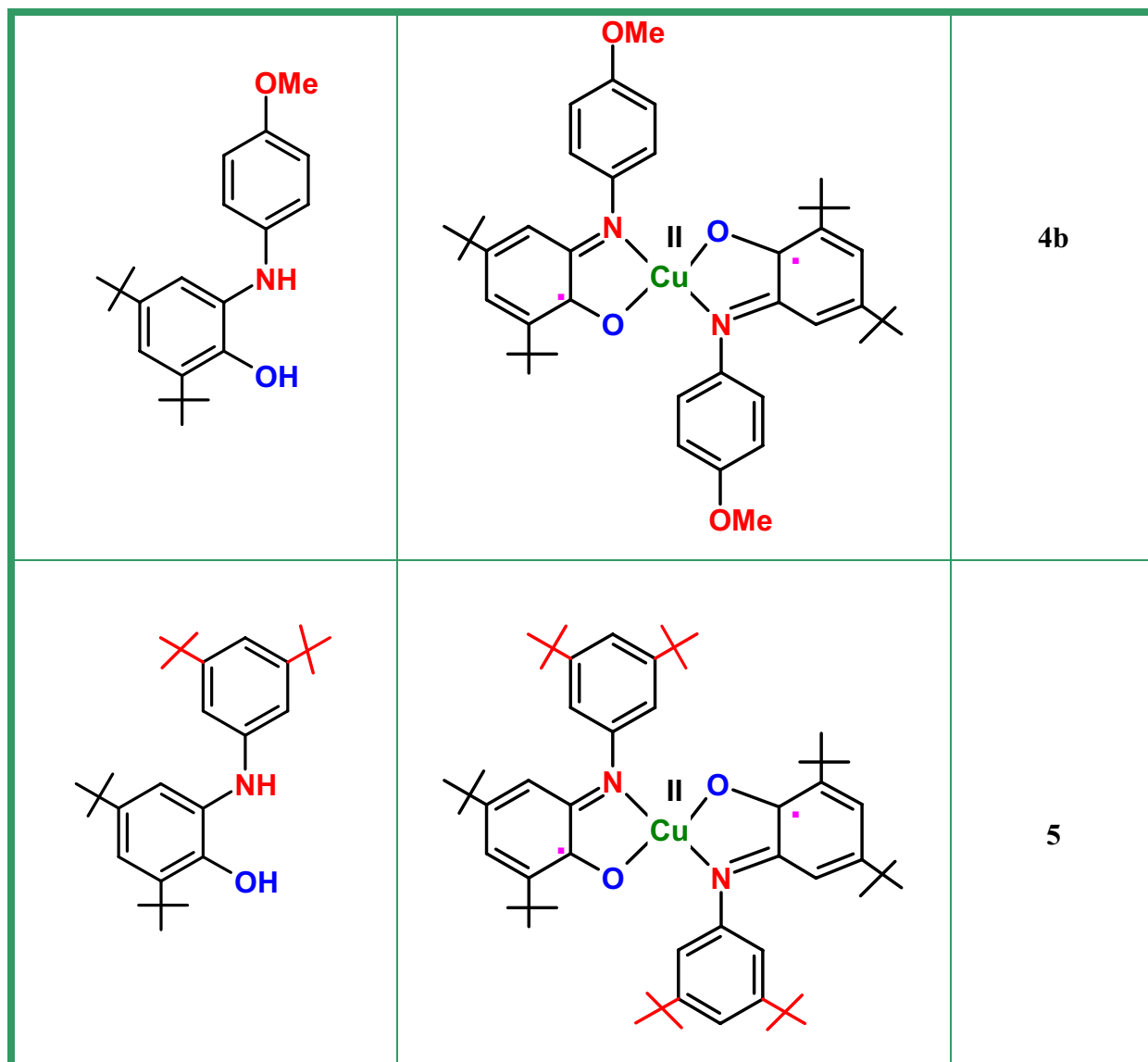
The reaction of [Cu^I(CH₃CN)₄]ClO₄ with N(2-hydroxy-3,5-di-*tert*-butylphenyl)-3,5-di-substituted-aniline and triethylamine in dry CH₃CN under argon produces a yellow solution that becomes deep green/blue-green upon exposure to air. From these solutions crystalline complexes listed in Table 3.1 precipitated out.

Table 3.1. The complexes.

Ligand	Complex	Complex No.
		1

		1a
		1b
		2

		3
		4
		4a



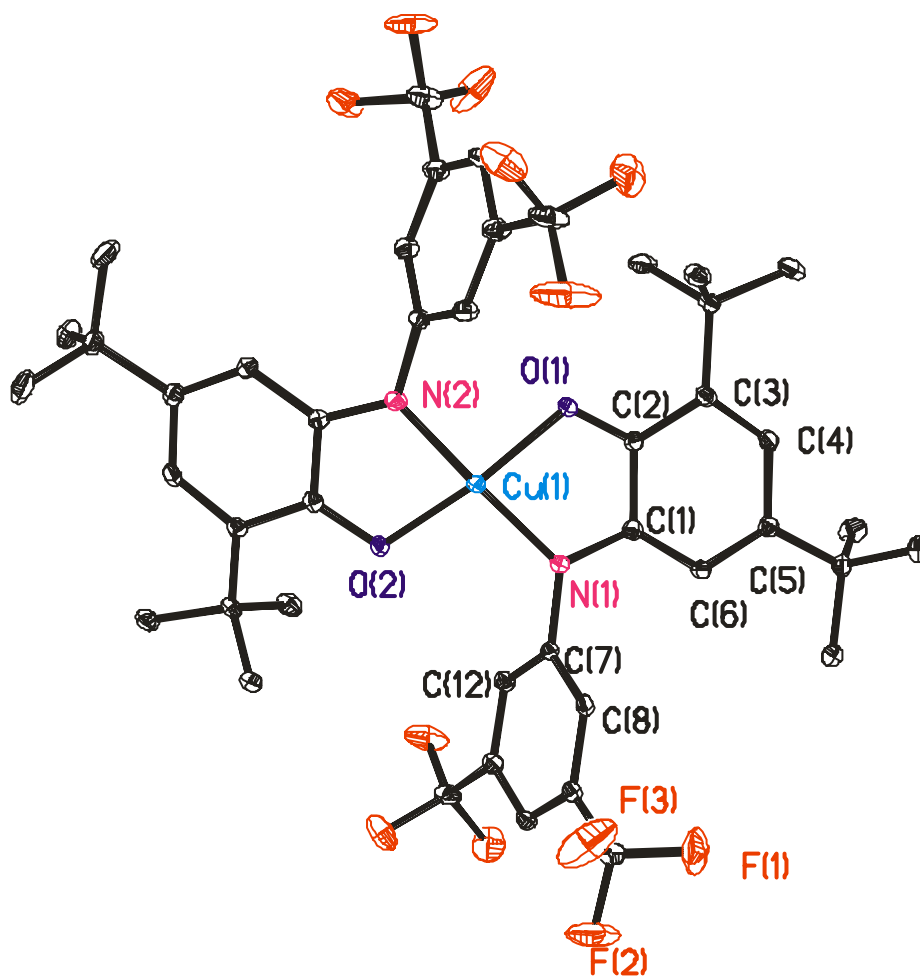


Figure 3.3. ORTEP diagram of **1**.

All complexes **1-5** have very similar structures with square-planar or distorted square planar geometry around the copper ion. Here, X-ray crystal structure of complex **1** is described.

X-ray quality single crystals were grown from a 1:1 dichloromethane, acetonitrile mixture. Figure 3.3 displays ORTEP diagram of the mononuclear neutral complex **1** and Table 3.2 contains selected bond lengths and bond angles. The X-ray structure of **1** shows that the copper ion is in a slightly distorted square-planar N_2O_2 environment. The dihedral angle between $Cu_1-O_1-C_2-C_1-N_1$ and $Cu_1-O_2-C_{24}-C_{23}-N_2$ planes is 24.2° . The $C(4)-C(5)$, $C(1)-C(6)$, $C(2)-C(3)$, $C(5)-C(6)$, $C(7)-C(8)$, $C(8)-C(9)$, $C(9)-C(10)$, $C(10)-C(11)$ and $C(11)-C(12)$ bond lengths are 1.434 (4), 1.414 (4), 1.432 (4), 1.364(4), 1.390 (4), 1.385 (4), 1.388 (4), 1.383 (4) and 1.391 (4) Å respectively. From the above C-C bond lengths it is quite clear that the aromaticity of the *tert*-butyl group containing phenyl ring has been destroyed in the

complex. From the bond angles around the N(1) and N(2) (shown in Table 3.2) it is clear that the hybridization of the both N atoms are sp^2 and they are deprotonated. The respective C(1)-N(1) and C(2)-O(1) bond lengths are 1.342(3) and 1.300(3) Å. These bond lengths indicate that C(1)-N(1) bond has double bond character and the C(2)-O(1) bond length is in between C-O and C=O, and hence suggests radical nature of the ligands. The Cu(1)-O(1), Cu(1)-O(2), Cu(1)-N(1) and Cu(1)-N(2) bond lengths are 1.932(2), 1.932(2), 1.925(2) and 1.929(2) Å respectively. From the Cu-O and Cu-N bond lengths it is clear that the oxidation state of the copper ion in neutral complex **1** is +II.

Table 3.2. Selected bond distances (Å) and angles (degree) for **1**.

Cu(1)-N(1)	1.925 (2)	C(4)-C(5)	1.434 (4)
Cu(1)-N(2)	1.929 (2)	C(5)-C(6)	1.364 (4)
Cu(1)-O(1)	1.932 (2)	C(6)-C(1)	1.414 (4)
Cu(1)-O(2)	1.932 (2)	C(23)-N(2)	1.345 (3)
C(2)-O(1)	1.300 (3)	C(26)-C(27)	1.443 (4)
C(1)-N(1)	1.342 (3)	C(23)-C(24)	1.456 (4)
C(2)-C(1)	1.457 (4)	C(24)-C(25)	1.434 (4)
C(1)-C(6)	1.414 (4)	C(25)-C(26)	1.368 (4)
C(3)-C(4)	1.369 (4)	C(28)-C(27)	1.368 (4)
C(7)-N(1)	1.415 (4)	C(24)-O(2)	1.297 (4)
C(8)-C(9)	1.385 (4)	C(29)-C(30)	1.390 (4)
C(10)-C(9)	1.388 (4)	C(30)-C(31)	1.387 (4)
C(11)-C(10)	1.383 (4)	C(31)-C(32)	1.394 (4)
C(12)-C(11)	1.391 (4)	C(32)-C(33)	1.382 (4)
C(7)-C(12)	1.388 (4)	C(33)-C(34)	1.402 (4)
C(7)-C(8)	1.390 (4)	C(29)-C(34)	1.381 (5)
O(1)-Cu(1)-N(1)	83.84 (8)	O(1)-Cu(1)-O(2)	162.27 (10)
N(1)-Cu(1)-N(2)	174.98 (10)	O(2)-Cu(1)-N(2)	83.62 (9)
N(2)-Cu(1)-O(1)	99.62 (11)	O(2)-Cu(1)-N(1)	94.19 (9)
C(24)-O(2)-Cu(1)	111.2 (2)	C(2)-O(1)-Cu(1)	111.8 (2)
C(23)-N(2)-C(29)	119.9 (2)	C(1)-N(1)-C(7)	123.0 (2)
Cu(1)-N(2)-C(23)	112.9 (2)	C(7)-N(1)-Cu(1)	122.5 (2)
C(29)-N(2)-Cu(1)	127.1 (2)	C(1)-N(1)-Cu(1)	113.0 (2)

The dihedral angle between the two coordinating planes of the Cu(II) ion differs according to the substituent attached at the 3 and 5 or 2 or 4 positions of the N-phenyl ring. Table 3.3 summarizes the dihedral angles for different complexes.

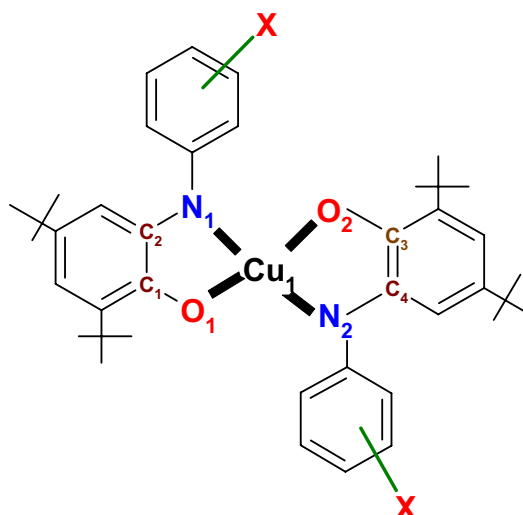


Table 3.3. Dihedral angles between $Cu_1-O_1-C_1-C_2-N_1$ and $Cu_1-O_2-C_3-C_4-N_2$ planes.

Complex	The dihedral angle between $Cu_1-O_1-C_1-C_2-N_1$ and $Cu_1-O_2-C_3-C_4-N_2$ planes
1(3,5-CF₃)	24.2 °
1a(2- CF₃)	25.4 °
2(3,5-F)	0 °
3(3,5-Cl)	0 °
4(3,5-OMe)	8.4 °
5(3,5-^tBu)	1.1 °

From Table 3.3 it is clear that steric effects do not play any role in the distortion around the Cu(II) center as described in the literature³ but electronic effects are responsible for the distortion.

X-band EPR spectra were measured for complexes **1**, **2**, **3**, **4** and **5**. The nature of entire spectrum is the same in the sense that all the signals are anisotropic with ^{14}N ($I = 1$) and ^1H ($I=1/2$) hyperfine coupling observed. As it has been shown by X-ray crystallography, all the complexes are neutral with a Cu(II) ion and two coordinated radical anions, hence, the system is in spin frustrating condition with three $S = 1/2$ spins. X-band EPR spectra provide information that the residual unpaired electron which is responsible for the paramagnetic nature of complexes, **1**, **2**, **3**, **4** and **5** is on the Cu(II) center. Moreover, from the spectrum it is clear that antiferromagnetic interactions between the Cu(II) center and the radical anions are weaker than that of the antiferromagnetic interactions between the two radical anions and the ground state electronic configuration for all the complexes is ($\uparrow\downarrow\downarrow$). The interaction between two radical anions in this type of systems must be antiferromagnetic while the interaction

between the Cu(II) and radical anion(s) may be ferromagnetic obeying the Goodenough-Kanamori rule or antiferromagnetic as shown in various cases⁴⁻⁶.

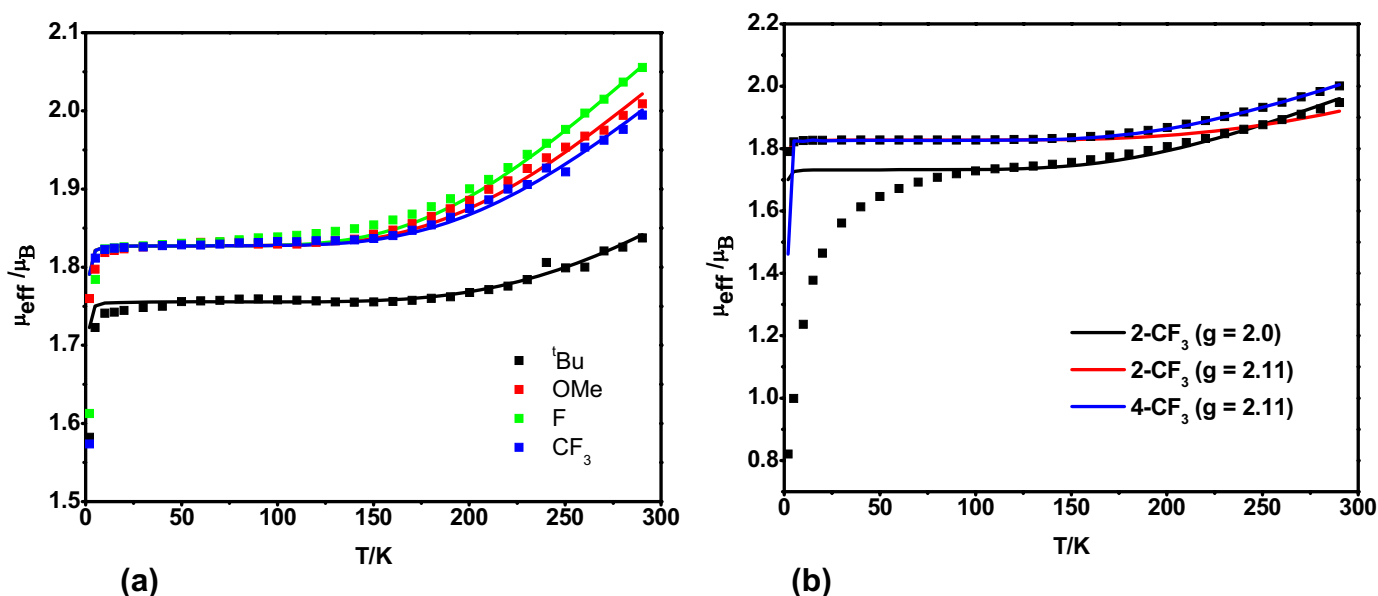


Figure 3.4. A μ_{eff} vs T plot for complex 1-5.

From Table 3.3 it is clear that there are distortions between the coordinating planes which depend on the nature of the substituent at the 3,5-positions of N-phenyl group. Hence, ferromagnetic interactions between the Cu(II) and radical anion(s) can not be accepted for all cases. Though ferromagnetic or antiferromagnetic coupling constants between Cu(II) and radical anion can be introduced to simulate the experimental magnetic behaviour of the complexes, an assumption was taken that there is neither ferromagnetic nor antiferromagnetic interaction between Cu(II) and radical anion(s), i.e., $J_{\text{Cu-R}}$ is zero, to investigate if the antiferromagnetic interaction constant between two radical anions depends on the nature of the substituent. Considering the above assumption the experimental magnetic susceptibility behaviour that has been measured at 1 T in the temperature range 2-290 K for complexes 1- 5 has been simulated. Figure 3.4 shows the plots and Table 3.4 summarizes the fitting parameters. From these parameters it is clear that the $J_{\text{R-R}}$ exchange coupling constant is antiferromagnetic and the value is similar for all the complexes except complexes 5 and 4a which have that coupling constants -435 and -440 cm^{-1} respectively. It is also noticeable that for complex 5 the $g_{\text{Cu(II)}}$ value is 2.03 and smaller than that of others. Hence, from the $J_{\text{R-R}}$ and $g_{\text{Cu(II)}}$ values it is quite clear that the magnetic behaviour is not affected appreciably by the nature of the substituent at the 3,5 positions.

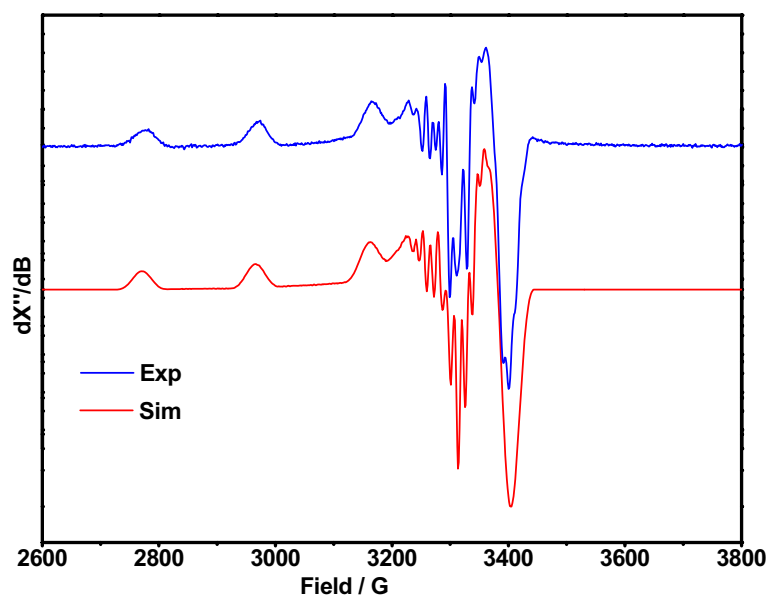


Figure 3.5. X-band EPR spectrum of complex **1** in frozen CH_2Cl_2 solution at 10 K.

Figure 3. **4b** shows the magnetic behaviour of the complexes **1a** and **1b**. The nature of magnetic behaviour for **1b** is similar to **1** with $S_t = 1/2$ ground state but that for **1a** is totally different. In the case of complex **1** and **1b** the μ_{eff} value, $1.83 \mu_{\text{B}}$, remains constant in the temperature range 2-150 K and then increases to $2.1 \mu_{\text{B}}$ at 290 K. But for **1a** the μ_{eff} value is $0.8 \mu_{\text{B}}$ at 2 K and increases to $1.71 \mu_{\text{B}}$ at 87 K. After that, the μ_{eff} value increases gradually with increase of temperature and reaches to $1.94 \mu_{\text{B}}$ at 290 K. The magnetic behaviour in the temperature range 2-90 K for **1b** may be due to intermolecular interactions. The X-band EPR spectrum together with the simulation appears in Figure 3.5 for complex **1**. The Fitting parameters are, $g_x = 2.058$, $g_y = 2.043$, $g_z = 2.197$, $W_x = 12.5 \text{ G}$, $W_y = 4.5 \text{ G}$, $W_z = 18.5 \text{ G}$, $A_x = 21 \times 10^{-4} \text{ cm}^{-1}$, $A_y = 21 \times 10^{-4} \text{ cm}^{-1}$, $A_z = 165 \times 10^{-4} \text{ cm}^{-1}$, $A_N(13, 10, 3 \times 10^{-4} \text{ cm}^{-1})$.

The dihedral angle between the $\text{Cu}_1\text{-O}_1\text{-C}_1\text{-C}_2\text{-N}_1$ and $\text{Cu}_1\text{-O}_2\text{-C}_3\text{-C}_4\text{-N}_2$ planes for complex **1** is 24.2° and that is 35.5° for the similar type of complex described in the Chapter 1. Both show a Cu(II) centered X-band EPR spectra. It has been shown in the literature that a biradical-containing Cu(II) complex with dihedral angle 32.8° exhibits ligand (radical) centered X-band EPR spectrum and the most probable reason behind of having that spectrum is the distortion around the Cu(II) center.³ It is clear from the Cu(II) centered X-band EPR

spectra of the described complexes that the dihedral angle is not solely responsible for the ligand centered EPR spectrum.

Table 3.4. Fitting parameters for the experimental temperature-dependent magnetic behaviours of the complexes.

Complex No.	$J_{\text{Cu-R}} (\text{cm}^{-1})$	$J_{\text{R-R}} (\text{cm}^{-1})$	$g_{\text{Cu(II)}}$	g_{R}
1(3,5-CF₃)	0 (Fixed)	-353	2.11	2.00
1a(2-CF₃)	0 (Fixed)	-422(-326)	2.11(2.00)	2.00
1b(4-CF₃)	0 (Fixed)	-352	2.11	2.00
2(3,5-F)	0 (Fixed)	-320	2.11	2.00
3(3,5-Cl)	0 (Fixed)	-323	2.08	2.00
4(3,5-OMe)	0 (Fixed)	-340	2.11	2.00
4a(2-OMe)	0 (Fixed)	-342	2.1	2.00
4b(4-OMe)	0 (Fixed)	-440	2.09	2.00
5(3,5-^tBu)	0 (Fixed)	-435	2.03	2.00

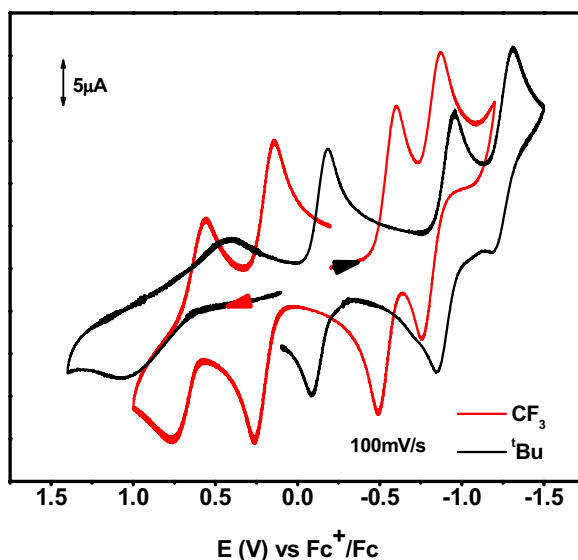
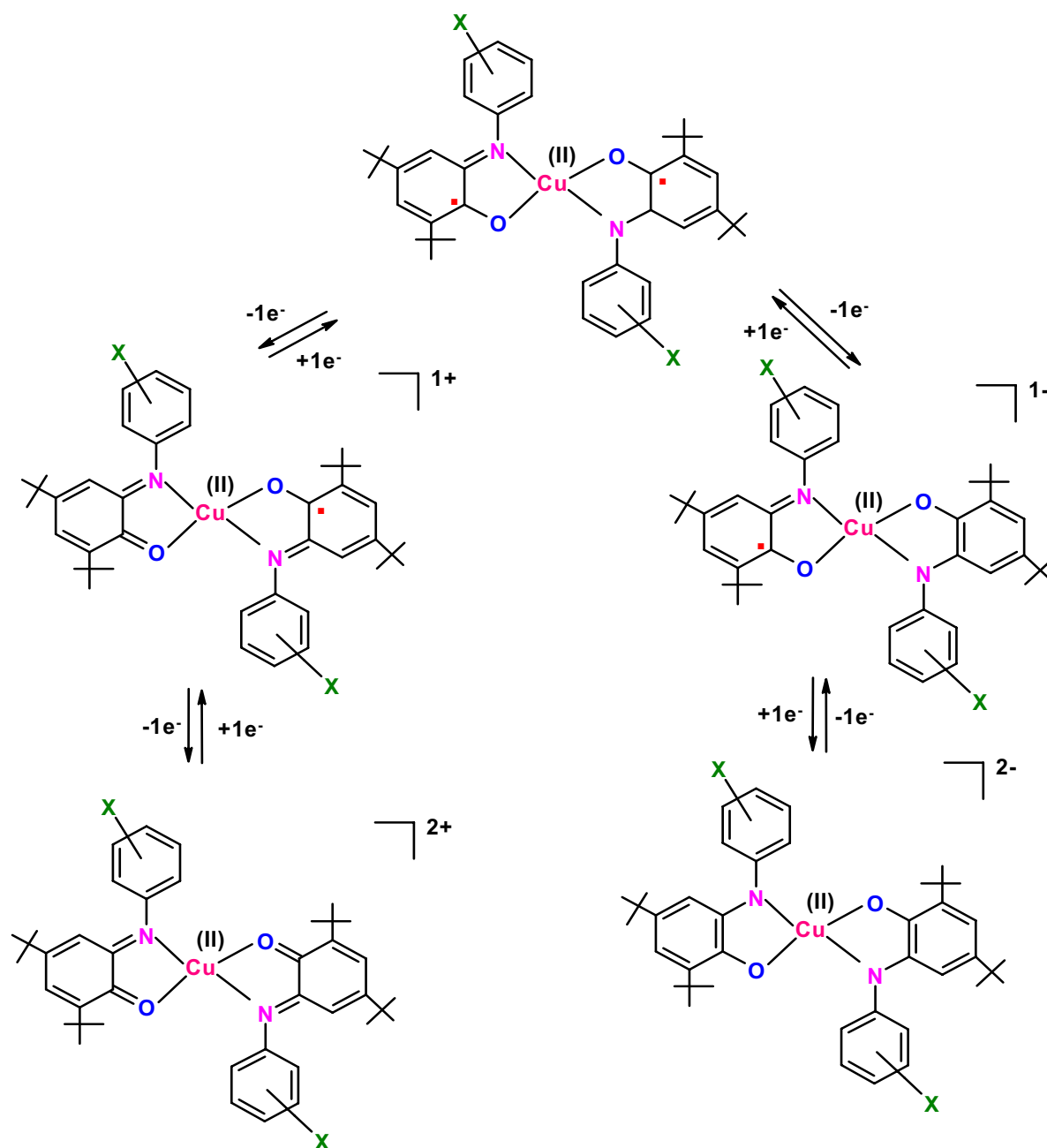


Figure 3.6. Cyclic voltammograms of complex **1** and **5** in CH_2Cl_2 under argon atmosphere.

Cyclic voltammograms (CVs) of complexes (**1-5**) have been recorded in CH_2Cl_2 solutions containing 0.1 M $[\text{N}(n\text{-Bu})_4] \text{PF}_6$ as supporting electrolyte at a glassy carbon working electrode and a Ag/AgNO_3 reference electrode. Ferrocene was used as an internal

standard, and potentials are referenced versus the ferrocenium/ ferrocene (Fc^+/Fc) couple. Figure 3.6 shows the CVs of **1** and **5** recorded in the potential range +1.75 V to -1.75 V. Four reversible one-electron-transfer waves are found. Two reversible one-electron oxidations and two reversible one-electron reductions are observed, as established by coulometry at fixed potential. Table 3.5 summarizes the results where Ox_1 and Ox_2 correspond to first and second oxidation potentials respectively and successive reduction potentials are represented by Red_1 and Red_2 . The oxidation and reduction processes are ligand centered and the redox behaviours of the complexes can be given as shown in Scheme 1.



Scheme 1. Different redox states for the complexes.

To explain the cyclic voltammogram results for complexes **1-5**, electrochemical behaviour of complex **1** and complex **5** will be discussed. It is well known that any electron donating or withdrawing group attached to the 3,5-or 3-or 5- positions of a phenyl ring system exhibits an inductive effect (σ -effect). *Tert*-butyl group shows +I effect (donation of electron) whereas, trifluoromethyl group exhibits -I effect (withdrawing of electron.). From Table 3.5 it is clear that the reduction potentials of complex **5** are higher than those of complex **1**. On the other hand, opposite is true for oxidation processes. The presence of *tert*-butyl group at the 3,5-positions of the N-phenyl rings increases the electron density of the N-phenyl rings. The opposite situation is valid for N-phenyl rings when 3, 5-positions of the rings are occupied by -CF₃ group. Hence, the Lewis acidity of complex **5** is lower than that of complex **1**. It is known⁷ that stronger Lewis acidity favours the acceptance capacity of electron and disfavour removal capacity of electron by the complex. Therefore, complex **5** should have higher reduction potentials and lower oxidation potentials than those in complex **1**.

Table 3.5. Redox potentials of the complexes vs Fc^+/Fc .

Complex	Ox ₁ (V)	Ox ₂ (V)	Red ₁ (V)	Red ₂ (V)
1(3,5-CF₃)	-0.06	0.41	-0.804	-1.07
1a(2-CF₃)	-0.13	0.54	-0.965	-1.14
1b(4-CF₃)	-0.12	0.36	-0.84	-1.05
2(3,5-F)	-0.12	0.365	-0.99	-1.445
3(3,5-Cl)	-0.11	0.36	-0.87	-1.1
4(3,5-OMe)	-0.30	0.318	-1.043	-1.289
4a(2-OMe)	-0.327	0.360	-1.035	-1.420
4b(4-OMe)	-0.116	0.57	-0.83	-1.18
5(3,5-^tBu)	-0.393	0.47	-1.16	-1.51

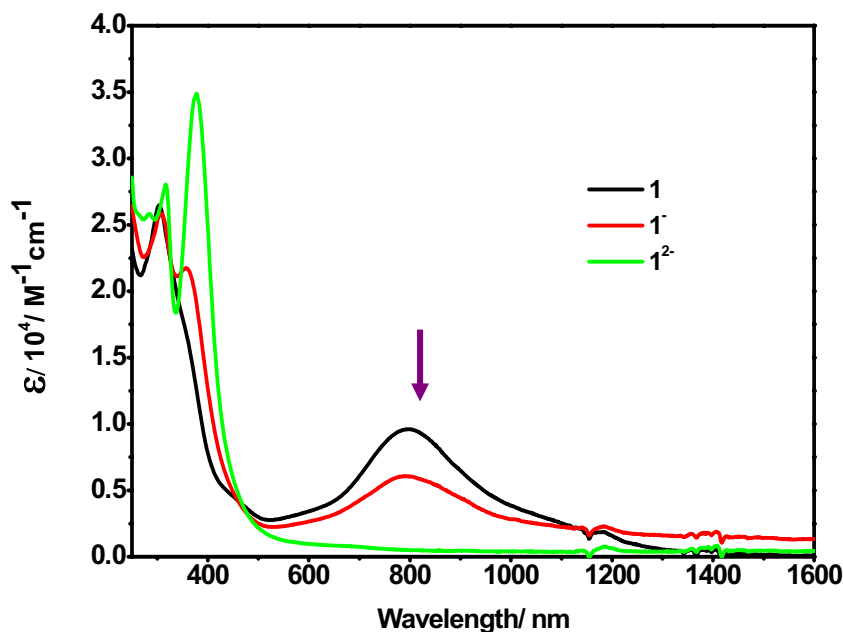


Figure 3.7. UV-VIS/NIR spectra of complex **1**, **1⁻** and **1²⁻**.

The UV-VIS/NIR spectra of all the complexes are quite similar. Figure 3.7 displays the spectra of complex $[\text{Cu}^{\text{II}}(\text{L}^{\text{CF}_3\bullet\bullet})]^0$, $[\text{Cu}^{\text{II}}(\text{L}^{\text{CF}_3\bullet})]^{1-}$, $[\text{Cu}^{\text{II}}(\text{L}^{\text{CF}_3})]^{2-}$ in CH_2Cl_2 solution and Table 3.6 contains the results for electronic spectra of all complexes. After Controlled potential one-electron reduction of complex **1**, the band assigned to ligand-to-ligand charge transfer band at around 800 nm diminishes. The ligand π - π^* charge transfer band at around 440 nm also diminishes and a new sharp band at 355 nm ($\epsilon = 23000 \text{ M}^{-1}\text{cm}^{-1}$) appears. Further reduction of complex **1** to **1²⁻** the band at 800 nm disappears and a sharp, strong band which can be assigned to ligand-to-metal charge transfer at 378 nm ($\epsilon = 37200 \text{ M}^{-1}\text{cm}^{-1}$) arises. The band at 656 nm ($\epsilon = 900 \text{ M}^{-1}\text{cm}^{-1}$) is probably due to the d-d transition of $\text{Cu}(\text{II})(\text{d}^9)$ ion.

Table 3.6. Spectroelectrochemical data of the complexes.

Complex	λ , nm (ϵ , $\text{M}^{-1}\text{cm}^{-1}$)
1 , $[\text{Cu}^{\text{II}}(\text{L}^{\text{CF}_3\bullet\bullet})]^0$	440 ^{sh} (5170), 800 (10200), 1040 ^{sh} (3300)
1⁻ , $[\text{Cu}^{\text{II}}(\text{L}^{\text{CF}_3\bullet})]^{1-}$	355 (23000), 790 (6500)
1²⁻ , $[\text{Cu}^{\text{II}}(\text{L}^{\text{CF}_3})]^{2-}$	378 (37200), 656 (900)
2 , $[\text{Cu}^{\text{II}}(\text{L}^{\text{F}\bullet\bullet})]^0$	435 (4720), 797 (7700), 1100 ^{sh} (2180)
4 , $[\text{Cu}^{\text{II}}(\text{L}^{\text{OMe}\bullet\bullet})]^0$	456 (5400), 791 (6650), 1085 ^{sh} (2570)
5 , $[\text{Cu}^{\text{II}}(\text{L}^{\text{tBu}\bullet\bullet})]^0$	350 (21500), 450 (10500), 780 (8200), 1050 (4000)

Solvent = Dichloromethane, Temperature = $22 \pm 1^\circ \text{C}$, Sh =shoulder

3.3 Catalytic reactivities,

Aerial oxidation of primary alcohols; mimicking the function of Galactose Oxidase(GO_{ase})

To get an idea if biradical-containing Cu(II) complexes with N₂O₂ environments and different substituents at the different positions of the N-phenyl ring can act as a catalyst complexes **1**, **1a**, **1b**, **2**, **3**, **4** and **5** were used for catalytic oxidation of primary as well as secondary alcohols to the corresponding two-electron oxidised products. The catalytic reaction was performed as describe below. In 20 ml CH₂Cl₂, 5.0 X10⁻⁴ M complex and 5.0 X10⁻² M substrate, benzyl alcohol, ethanol, methanol or isopropanol were added. After stirring the resulting solution under an aerial atmosphere for 16 hour and then passing an aliquot of the solution through a neutral Al₂O₃ column the concentration of aldehyde was analysed by LC or GC or by spectrophotometric methods.⁸⁻⁹ Table 3.7 summarizes the product yields for different substrates.

Table 3.7. Percent of Yields.

Complex	PhCHO(%yield)	HCHO(%yield)	MeCHO(%yield)	Me ₂ CO(%yield)
1(3,5-CF₃)	72	25	25	1
1a(2-CF₃)	-	15	20	-
1b(4-CF₃)	-	10	15	-
2(3,5-F)	63	16	<10	<1
-H(3,5positions)	70	10	-	-
4(3,5-OMe)	68	10	-	-
5(3,5-^tBu)	69	10	-	-

From Table 3.7, it is clear that for the oxidation of benzyl alcohol to benzaldehydes all the complexes are equally efficient by yielding 63-72% benzaldehyde. It is to be noted that during oxidation of benzyl alcohol to benzaldehyde tetrabutylammonium methoxide (4.50 X 10⁻⁴) was used as a base. That is why the formation of benzaldehyde with little amount of formaldehyde (3-16%) was found using the complexes. Though the concentration of methoxide was approximately same as the concentration of benzyl alcohol the yield of benzaldehyde is higher than that of formaldehyde. This fact can be explained easily from the C-H_α bond dissociation energy for benzyl alcohol and methanol/methoxide (105.5 and 124 kcal mole⁻¹ respectively).

In case of oxidation of methoxide to formaldehyde or ethoxide to acetaldehyde using tetrabutylammonium methoxide or tetrabutylammonium ethoxide as substrates maintaining above stated reaction conditions the maximum yield of 25 % was obtained for complex **1**. The yield can be improved further and 75-80% formaldehyde or acetaldehyde can be obtained using 1:25 complex: substrate ratio. The lesser yields for other complexes are due to the low stability of those complexes in the catalytic solution.

Very low yield, 1% or < 1%, for the oxidation of isopropanol to acetone of C-C coupled product, pinacol, (which is not formed at all after the catalysis) emphasized the fact that the complexes are not capable of oxidizing secondary alcohols to their corresponding aldehyde or C-C coupled product.⁴

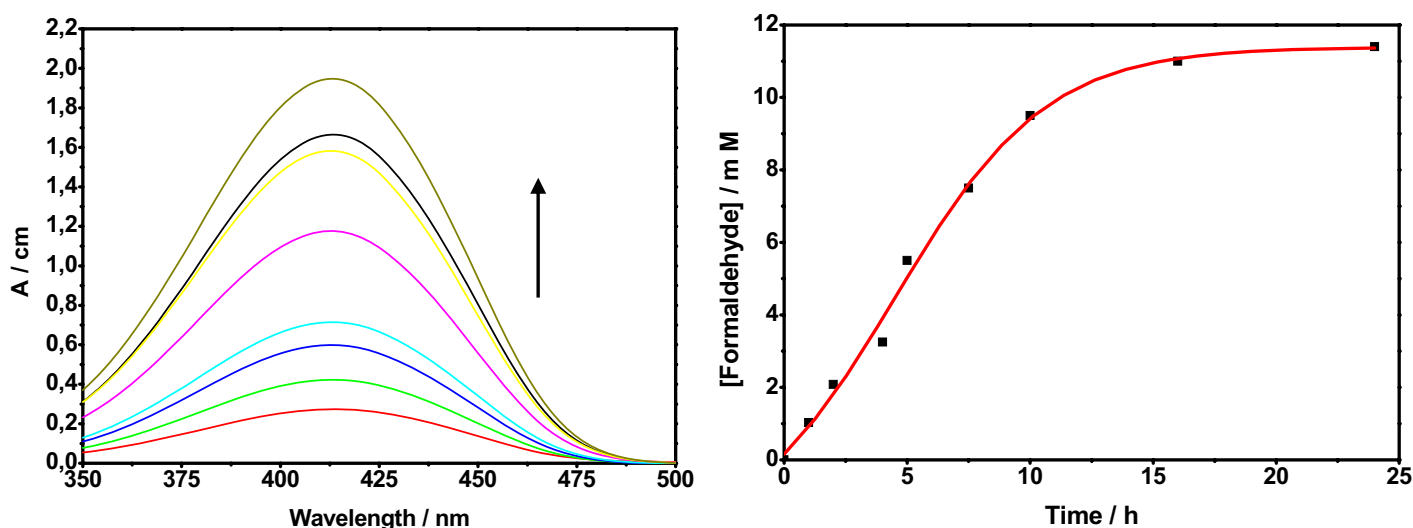


Figure 3.8. Kinetics measurement for the formation of formaldehyde at room temperature.

From Table 3.7, it is clear that complex **1** is the best catalyst. Hence complex **1** was used as a catalyst for oxidation of methoxide, ethoxide and benzyl alcohol. Kinetic studies were done using methoxide or ethoxide as a substrate. In both cases spectrophotometric methods were used to find out the concentration of formaldehyde or acetaldehyde with time. The formation of formaldehyde or acetaldehyde was verified by GC, GC-MS, Mass spectra (EI, ESI) using 2,4-dinitro-phenylhydrazine or 3-methyl-2-benzothiazolone hydrazine as reagent to form Schiff base products.

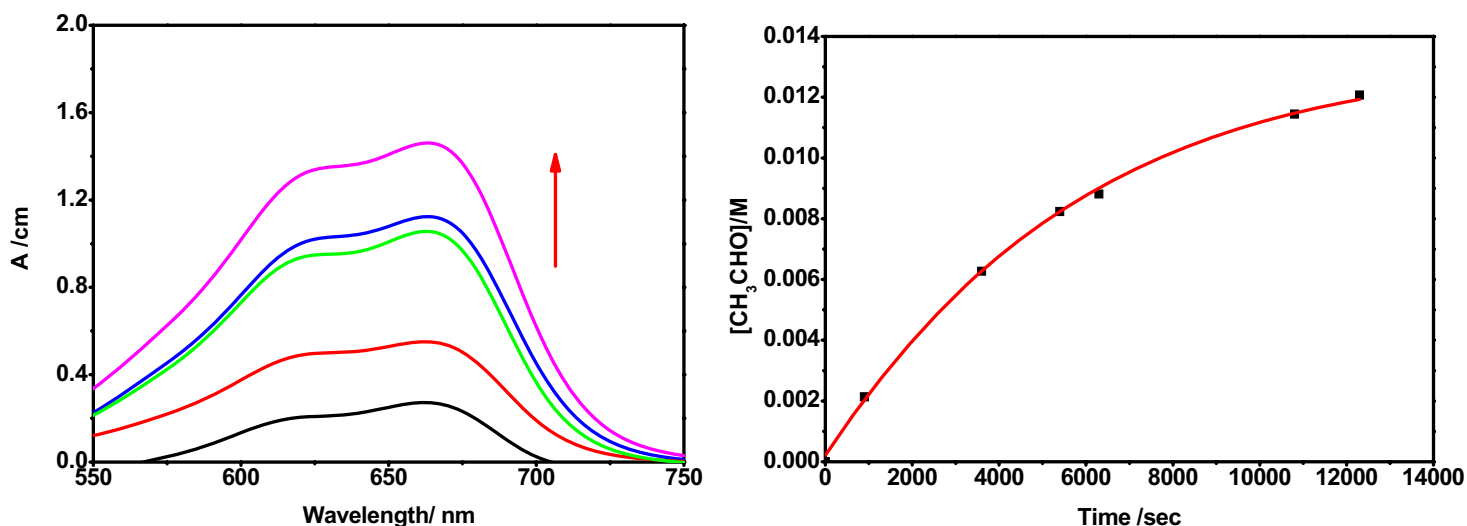


Figure 3.9. Kinetics measurement for the formation of acetaldehyde at room temperature.

Figures 3.8 and 3.9 show the changes in UV/VIS spectrum with time and increase of concentration of formaldehyde and acetaldehyde with time. The exact procedures for kinetics measurements using methoxide and ethoxide as substrates are written in the experimental section. From the experimental results at $22 \pm 1^\circ \text{C}$ in CH_2Cl_2 keeping the concentration of complex **1** ($5.0 \times 10^{-4} \text{ M}$) fixed and varying the concentration of substrate or vice versa, the rate law for the catalytic oxidation of methoxide or ethoxide was deduced as;

$$\text{Rate} = k [\text{Substrate}][\text{Complex}]$$

The kinetic of the oxidation of methoxide to formaldehyde using selectively deuterated substrate CD_3O^- has been measured under the same reaction condition.

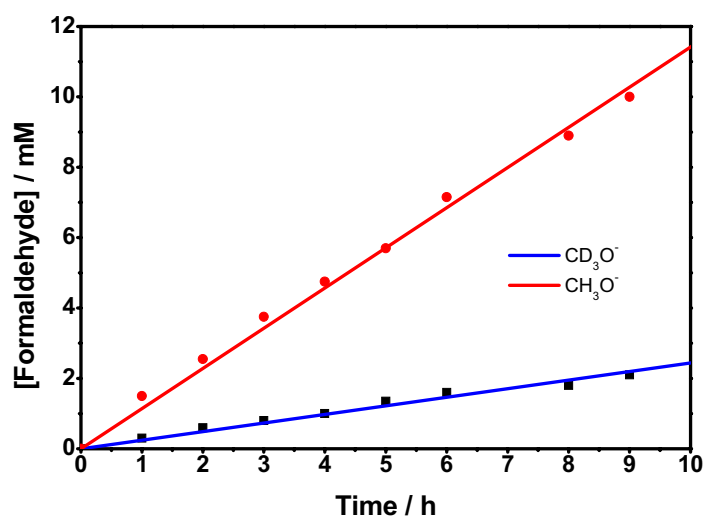


Figure 3.10. Plot of KIE (~ 5) at room temperature.

The k_H/k_D ratio of ~ 5 (Figure 3.10) indicates a small but significant kinetic isotope effect (KIE). This is a clear evidence that H-atom abstraction from the α -carbon atom of the coordinated alcoholate is the rate-determining step. The resulting ketyl radical anion is known to be a strong one-electron reductant ¹⁰⁻¹⁵ which is converted to aldehyde via an intramolecular electron-transfer step. In this case the intramolecular electron-transfer step could reduce the ligand or metal center. Here ligand center reduction takes place.

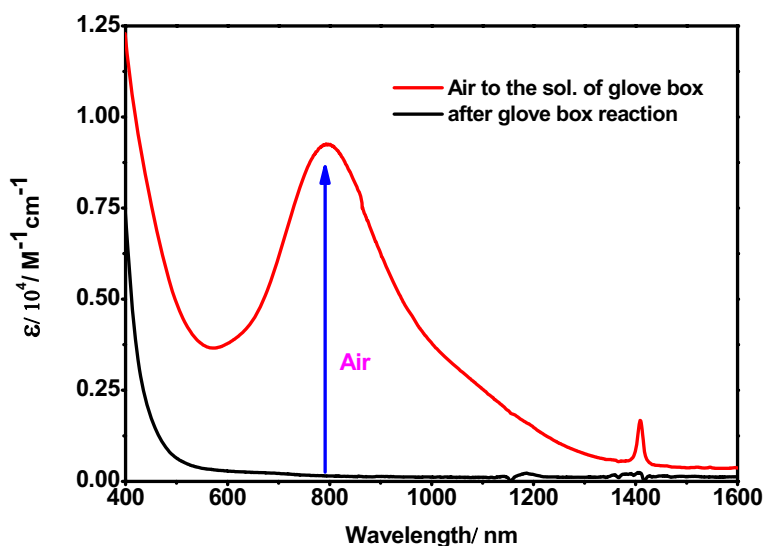
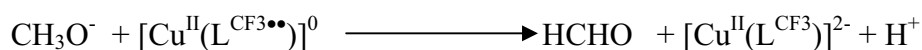


Figure 3.11. Change in UV–VIS/NIR spectrum after passing air through the solution obtained after glove-box reaction.

When a solution of complex **1** in dry CH_2Cl_2 was added to a 12.5 fold excess of methoxide under anaerobic conditions at $22 \pm 1^\circ$, the original blue-green color changed to yellow within a minute. The final UV/VIS spectrum of this solution corresponds to that of $[\text{Cu}^{\text{II}}(\text{L}^{\text{CF}_3})]^{2-}$ generated electrochemically. Figure 3.11, the UV/VIS spectrum of the solution obtained after the reaction under anaerobic condition. Subsequent exposure of the yellow solution to air, the band at 800 nm (ligand-to-ligand charge transfer band), which arises due to having radical in the complex, regenerated and thereby, proves the regeneration of radical in complex **1**. This fact also indicates that the radical takes part in the catalytic oxidation reaction. Using the spectrophotometric method ⁹ the concentration of formaldehyde of the resulting solution was measured and indicates the formation of about same concentration of formaldehyde as the concentration of complex **1**, $[\text{Cu}^{\text{II}}(\text{L}^{\text{CF}_3\bullet\bullet})]^0$ in the solution. The overall reaction can be summarized as shown in the following equation.



It is important to note that during aerial catalysis of the reaction stated above no H_2O_2 was detected. The catalytic reaction was also performed at $0\text{ }^\circ\text{C}$, $-10\text{ }^\circ\text{C}$ and $-25\text{ }^\circ\text{C}$, even in these conditions no H_2O_2 was detected. The complex does not show any catalase activity but due to use of strong base, CH_3O^- , as a substrate H_2O_2 was decomposed to H_2O and $1/2\text{O}_2$ as shown below,



Thus, complex **1** is capable of oxidizing primary alcohols to the corresponding aldehydes and forming the two electron reduced form $[\text{Cu}^{\text{II}}(\text{L}^{\text{CF}_3})]^{2-}$.

From the above results the mechanism for the catalytic oxidation of methoxide ethoxide and benzylalcoholate can be proposed as follows (Figure 3.12),

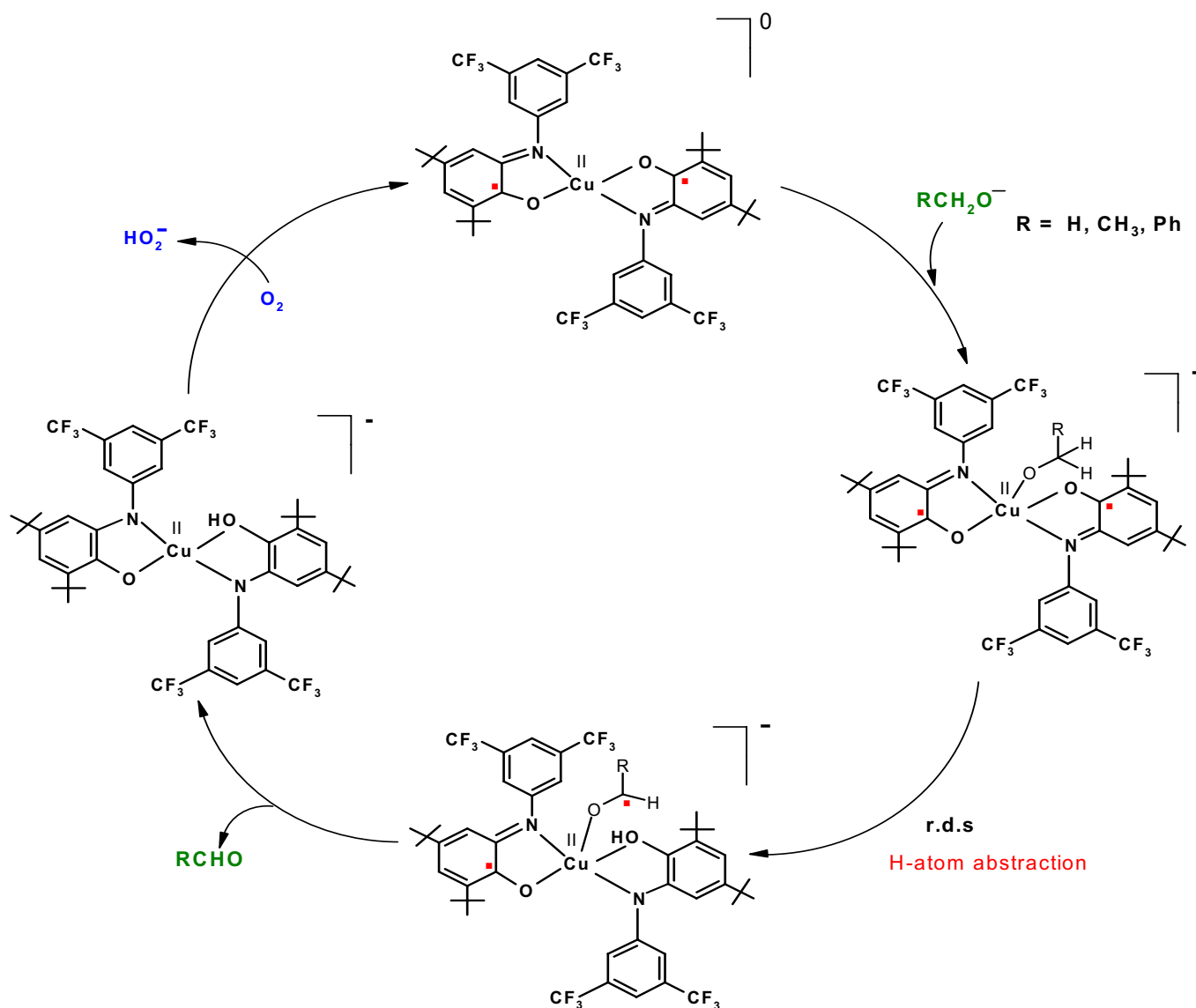


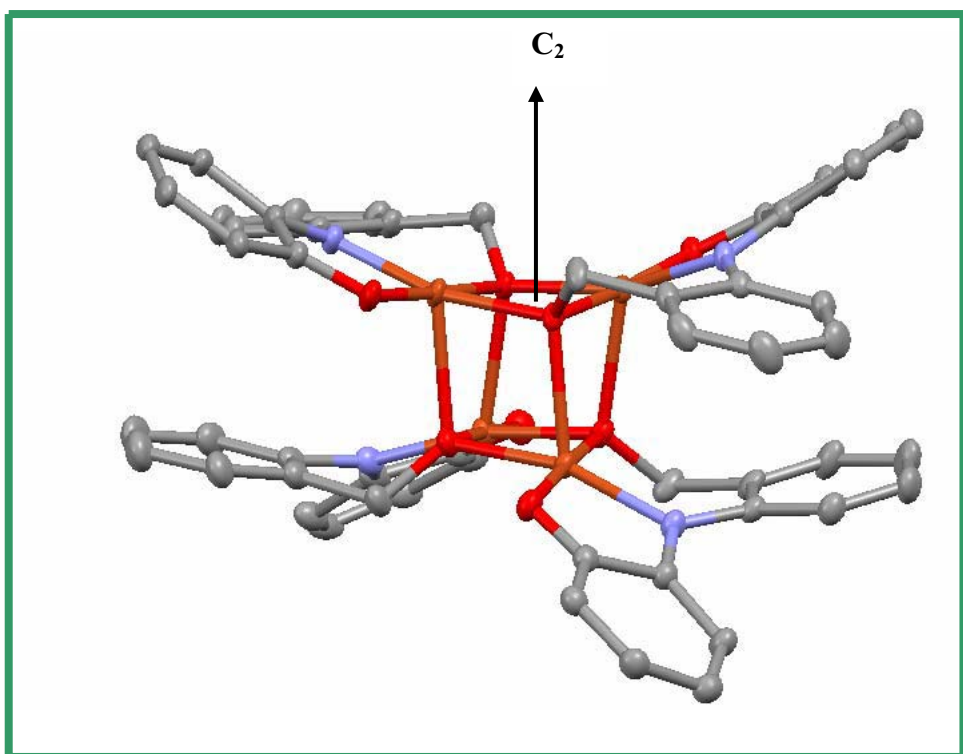
Figure 3.12. The proposed mechanism for the catalytic oxidation of benzyl alcohol, methanol and ethanol.

3.4 References

1. (a) *Transition Metal Complexes with Imino-Phenolate and Iminobenzosemiquinone Ligands; Synthesis, Characterization and Their Catalytic Reactivity*. Soumen Mukherjee; Thesis; **2003**, University of Paderborn.
(b) Pieper, U.; Chaudhuri, P; unpublished results.
2. Kokatam, S.; Weyhermüller, T.; Bothe, E.; Chaudhuri, P.; Wieghardt K. *Inorg. Chem.* **2005**, *44*, 3709.
3. Ye, S.; Sarkar, B.; Lissner, F.; Schleid, T.; Slageren, J. Van.; Fiedler, J. Kaim, W. *Angew. Chem. Int. Ed.* **2005**, *44*, 2103.
4. Chaudhuri, P.; Hess, M.; Flörke, U.; Wieghardt, K. *Angew. Chem. Int. Ed.* **1998**, *37*, No.16, 2217.
5. Chaudhuri, P.; Hess, M.; Weyhermüller, T.; Wieghardt, K. *Angew. Chem. Int. Ed.* **1999**, *38*, No. 8, 1095.
6. Chaudhuri, P.; Hess, M.; Müller, J.; Hildenbrand, K.; Bill, E.; Weyhermüller, T.; Wieghardt, K. *J. Am. Chem. Soc.* **1999**, *121*, 9599.
7. Itoh, S.; Kumei, H.; Nagatomo, S.; Kitagawa, T. Fukuzumi, S. *J. Am. Chem. Soc.* **2001**, *123*, 2165.
8. Sawicki, E.; Hauser, T. R.; Stanley, T. W.; Elbert, W. *Anal. Chem.* **1961**, *33*. No 1. 93.
9. Nash, T. *Biochem. J.* **1953**, *55*, 416.
12. Whittaker, J. W. In *Metal Ions in Biological Systems*; Sigel, H. and Sigel, A., Eds. Marcel Dekker: New York, **1994**, Vol. 30, pp 315.
13. Knowles, P. F.; Ito, N. In *Perspectives in Bio-inorganic Chemistry*, Jai Press Ltd. London, **1994**, Vol. 2, 207.
14. Sokolowski, A.; Leutbecher, H.; Weyhermüller, T.; Schnepf, R.; Bothe, E.; Bill, E.; Hildebrandt, P.; Wieghardt, K. *J. Biol. Inorg. Chem.* **1997**, *4*, 444.
15. Saint-Aman, E. *Biol. Inorg. Chem.* **1997**, *2*, 46.

Chapter 4

Synthesis, Characterization and Catalytic Reactivity of Polynuclear Transition Metal Complexes formed with N (2- hydroxy-3,5-di-tert-butylphenyl)-2-aminobenzylalcohol, $H_3L^{\underline{CH, OH}}_2$



4.1 Synthesis and characterization of the ligand, *N* (2-hydroxy-3,5-di-*tert*-butylphenyl)-2-aminobenzylalcohol, $H_3L^{CH_2OH}$

Condensation of 2-amino benzyl alcohol with 3,5-di-*tert*-butyl-catechol in the presence of triethylamine in air in *n*-hexane produces the tridentate ligand, $H_3L^{CH_2OH}$ (Figure 4.1). The IR spectrum of the ligand shows -O-H and -N-H stretching frequencies at 3514 and 3383 cm^{-1} respectively, strong bands for *tert*-butyl groups appear at 2962-2865 cm^{-1} , a sharp band at 1603 cm^{-1} which is the -C-N stretch and bands at 1504-1426 cm^{-1} of the skeletal vibration of the aromatic phenyl rings. The observed peak at 750 cm^{-1} is attributed to the tetrasubstituted phenyl rings. Mass spectroscopy in the EI-mode shows the molecular peak at m/z 327. GC and GC-MS analysis were performed to confirm purity and composition of the ligand. Elemental analysis shows the composition of the ligand as $C_{21}H_{29}NO_2$ and supports mass and GC-MS analysis.

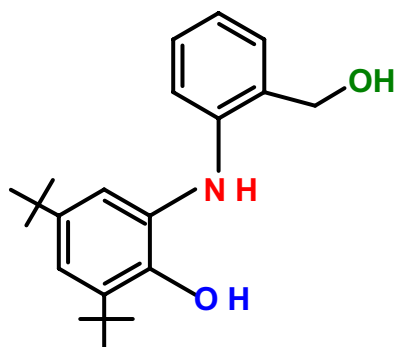
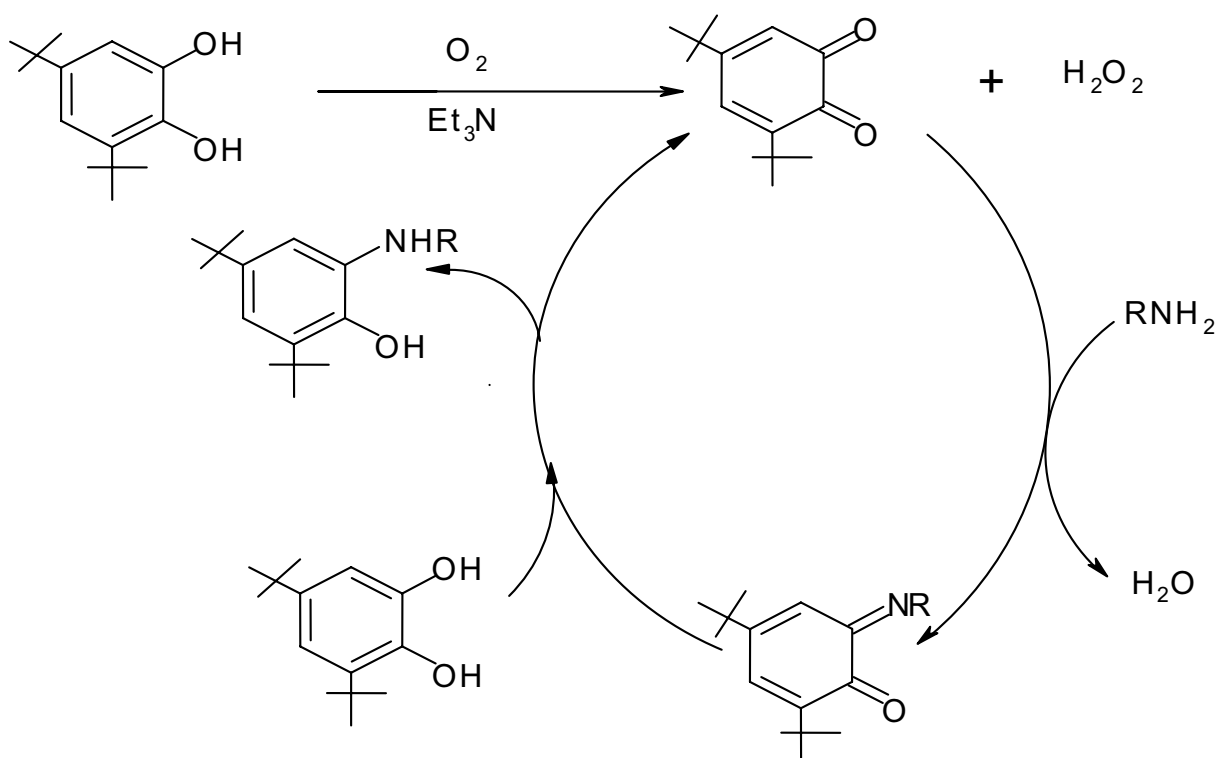


Figure 4.1. *N* (2-hydroxy-3,5-di-*tert*-butylphenyl)-2-aminobenzylalcohol.

The mechanism for the formation of this type of ligand is well established¹⁸ and is shown in scheme 1.



Scheme 1. The proposed mechanism for the formation of *N*-substituted aminophenol type ligands.

In the first step, 3,5-di-*tert*-butylcatechol is oxidized to the corresponding quinone in the presence of air (O₂) and base. Condensation of the amine with the less sterically hindered carbonyl moiety of 3,5-di-*tert*-butylquinone results in the 3,5-di-*tert*-butyl-iminoquinone product. This iminoquinone is reduced by two electrons by 3,5-di-*tert*-butylcatechol and N(2-hydroxy-3,5-di-*tert*-butylphenyl)amine is generated together with regeneration of 3,5-di-*tert*-butylquinone. According to the above mechanism, catalytic amounts of oxygen and base are necessary for the formation of the ligand, which can be considered as non-innocent because of its ability to change its redox state in the presence of metal ions and oxygen. Figure 4.2 shows the different redox states of the deprotonated ligand, $[(L^{CH_2OH})]^{3-}$.

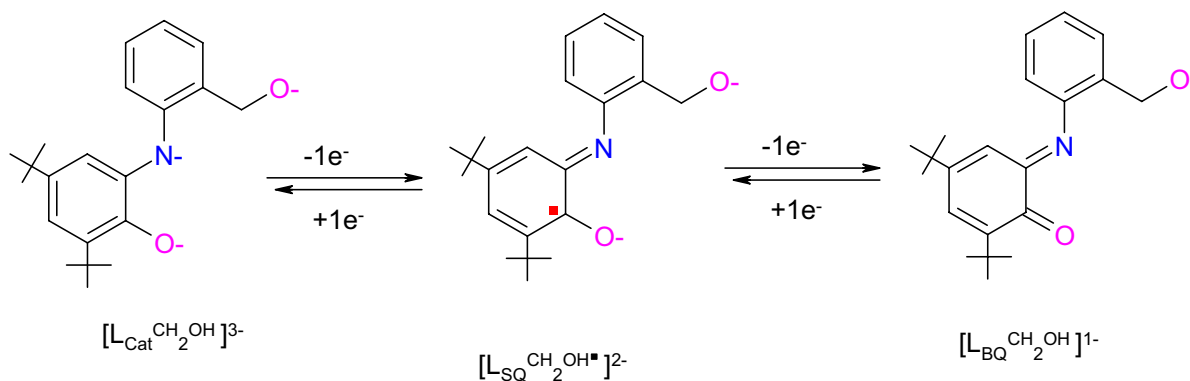


Figure 4.2. Different redox states of the fully deprotonated ligand $[L^{\text{CH}_2\text{OH}}]^{3-}$.

Polynuclear complexes are of interest in bioinorganic chemistry due to their structural and functional relevance to some metalloenzymes, e.g. Phenoxazinone Synthases (PHS), Photosystem II (PS II), Bromoperoxidase, etc.¹⁻¹⁶ and they are also important in understanding metal-metal and metal-ligand interactions.¹⁷ As the deprotonated ligand contains a strong π -donating alcoholate group, the ligand has very high tendency to form polynuclear metal complexes.

Using the above ligand a series of polynuclear complexes were synthesized. These complexes are, $[V^V_2O_2(\mu_2-O)_2(L_{\text{Cat}}^{\text{CH}_2\text{OH}})_2]$ (**1**), $[Mn^{II}Mn^{III}Mn^{IV}(L_{\text{SQ}}^{\text{CH}_2\text{OH}^\bullet})_2(L_{\text{BQ}}^{\text{CH}_2\text{OH}})(L_{\text{Cat}}^{\text{CH}_2\text{OH}})Cl]$ (**2**) and $[Cu^{II}_4(L_{\text{SQ}}^{\text{CH}_2\text{OH}^\bullet})_4]$ (**3**).

This chapter involves synthesis, characterization by X-ray crystallography, magnetic moments, spectro and spectroelectrochemical methods and catalytic reactivity of the above polynuclear complexes.

4.2 Alkoxide bridged dinuclear oxovanadium(V) complex (1)

Stirring a mixture of $\text{VO}(\text{SO}_4)_2 \cdot 5 \text{H}_2\text{O}$ (2 mmol), $\text{H}_3\text{L}^{\text{CH}_2\text{OH}}$ (2 mmol) and triethylamine (0.2 ml) in acetonitrile (30 ml), under aerobic conditions for two hours yields the deep blue complex **1**.

The sharp bands between 2961 cm^{-1} and 2869 cm^{-1} in the IR spectrum of complex **1** confirm coordination of the ligand to the metal. Complex **1** exhibits a sharp and strong band at 1001 cm^{-1} which is a clear indication of the $\text{V}=\text{O}$ unit in the complex. The absence of $-\text{O}-\text{H}$ and $-\text{N}-\text{H}$ stretching bands that are present in the ligand IR spectrum confirms deprotonated N and O atoms as chelating sites. The sharp, strong band at 1114 cm^{-1} can be assigned to C-O stretching of the alkoxide group attached to the metal ion. A sharp band observed at approximately 760 cm^{-1} is characteristic of $[\text{V}-(\mu\text{-O})-\text{V}]$ stretching. ESI-positive mass spectroscopy in dichloromethane yields a molecular ion peak at 782.3 (100%) and confirms $\text{C}_{42}\text{H}_{52}\text{N}_2\text{O}_6\text{V}_2$ composition for complex **1**.

Deep blue colored single crystals were obtained by recrystallization of the microcrystalline solid from a 1:1 CH_2Cl_2 and CH_3CN solvent mixture. X-ray analysis shows that complex **1** is a binuclear vanadyl complex. ORTEP diagram of the molecule with the atom labeling scheme is shown in Figure 4.3. Selected bond lengths and bond angles are listed in Table 4.1. In the discrete neutral binuclear complex **1**, two five coordinate vanadium atoms are each ligated to one $[\text{L}_{\text{Cat}}^{\text{CH}_2\text{OH}}]^{3-}$, one μ_2 alkoxide group and one oxo group. Both vanadium ions are linked through two bridging alkoxide groups to form a V_2O_2 ring, which is asymmetric in nature as the $\text{V}(1)-\text{O}(16)$ and $\text{V}(1)-\text{O}(16\text{A})$ bond distances are 1.994(3) and 1.958(3) Å respectively. The dihedral angle between the $\text{O}(1)-\text{N}(8)-\text{O}(16)-\text{O}(16\text{A})$ and $\text{O}(1\text{A})-\text{N}(8\text{A})-\text{O}(16)-\text{O}(16\text{A})$ planes is 0° and each vanadium ion is 0.636 Å away from the plane. Hence, each pentacoordinate vanadium center can be described as square-pyramidal one with oxygen atom at the apex. The $\text{V}\cdots\text{V}$ distance is 3.118(1) Å.

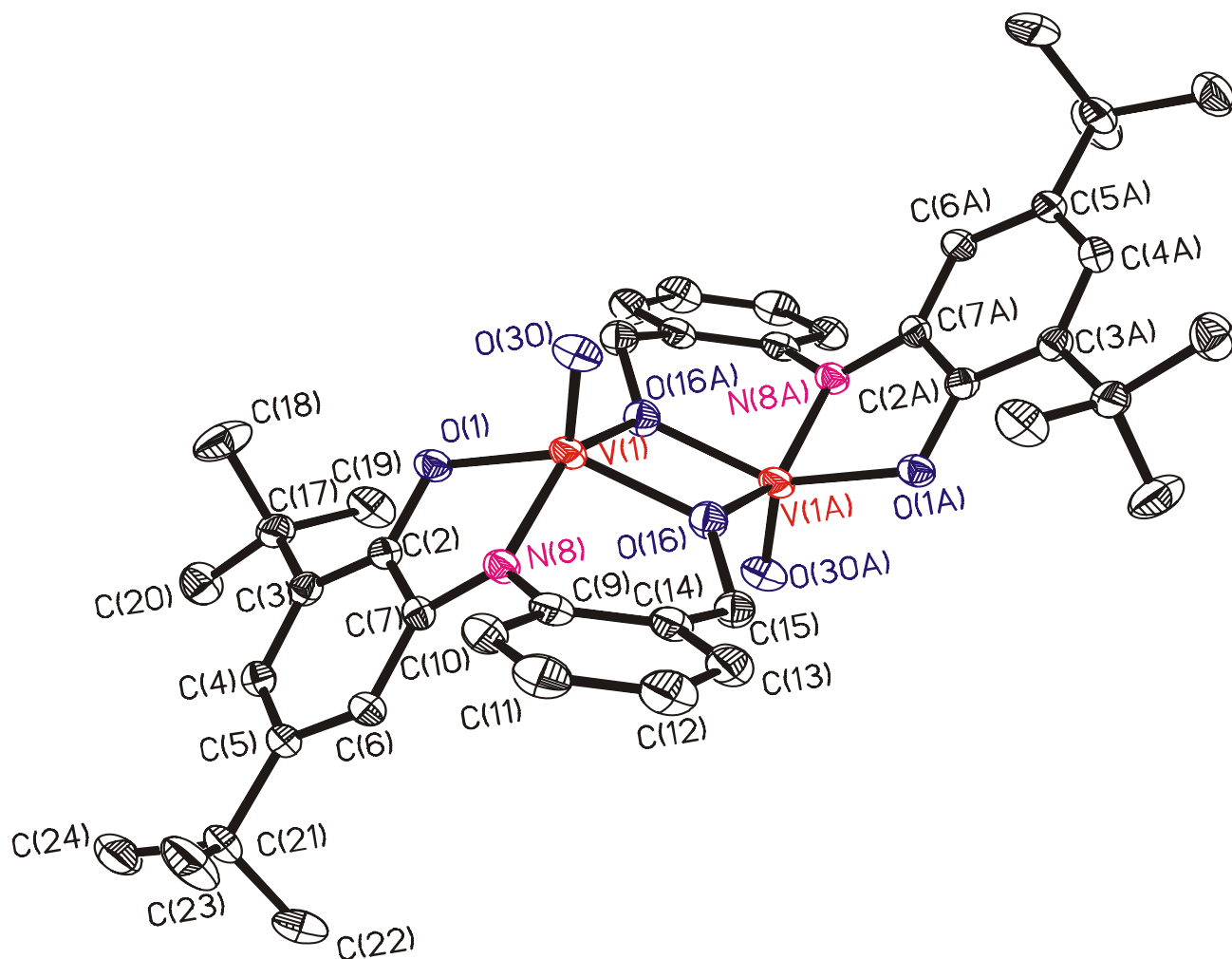


Figure 4.3. ORTEP diagram of complex **1**.

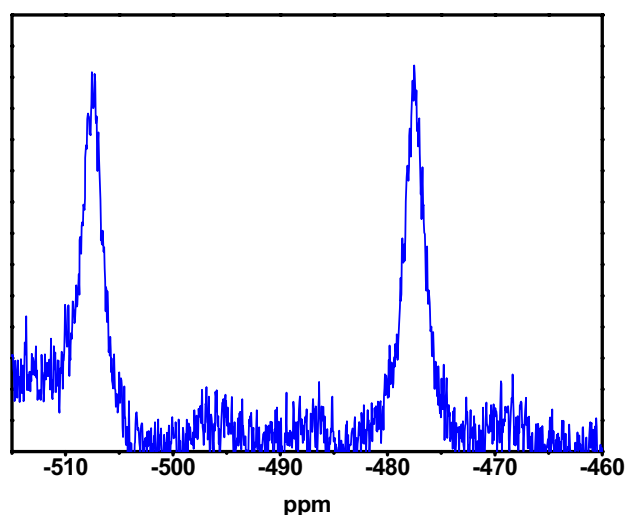
The vanadium ions in neutral complex **1** may have +IV or +V oxidation state with a one-electron oxidized form or a fully reduced amidophenolate form of the ligand respectively. The respective V(1)-O(1), V(1)-N(8), V(1)-O(16), V(1)-O(30) bond lengths are 1.9160(15), 1.9609(16), 1.9160(15) and 1.5886(15) Å. An amidophenolate form of the ligands is evidenced by C-C bond distances within the *tert*-butyl containing phenyl rings.¹⁹ The C(7)-N(8)-V(1), C(7)-N(8)-C(9) and C(9)-N(8)-V(1) bond angles are 112.57(13), 123.68(16), and 122.63(16)° respectively and support amidophenolate form of the N(8) atom. The O(1)-C(2), C(7)-N(8) and N(8)-C(9) bond lengths are 1.331(2), 1.362(3) and 1.419(3) Å respectively. The O(1)-C(2) and C(7)-N(8) bond distances do not correspond to either amidophenolate or iminosemiquinone form of the *tert*-butyl containing phenyl rings. From the crystal structure it is not possible to assign the oxidation states of the ligands and metal ions unambiguously but from the V-O, V-N and V=O²⁰⁻²¹ bond lengths it can be concluded that the neutral complex is composed of two vanadium (V) ions and two fully reduced ligands.

Table 4.1. Selected bond distances (Å) and angles (degree) for **1**.

C(2)-C(3)	1.414(3)	C(4)-C(5)	1.421(3)
C(2)-C(7)	1.436(3)	C(5)-C(6)	1.383(3)
C(3)-C(4)	1.386(3)	C(6)-C(7)	1.408(3)
O(30)-V(1)-O(1)	112.39(8)	O(30)-V(1)-O(16)	107.92(8)
O(1)-V(1)-O(16)	139.62(6)	O(30)-V(1)-N(8)	81.1(6)
O(16)-V(1)-N(8)	87.35(7)	O(30)-V(1)-O(16A)	104.75(7)
V(1)-O(16)-V(1A)	104.14(7)	V(1)-O(16A)-V(1A)	107.88(7)

Variable temperature (2-290 K) magnetic susceptibility measurement using a SQUID magnetometer at 1T indicates that complex **1** is diamagnetic. The diamagnetic nature was further confirmed by recording ^1H NMR spectrum in a CD_2Cl_2 solution at 300 K.

To further characterize the complex, a ^{51}V NMR spectrum in CD_2Cl_2 was recorded against VOCl_3 in C_6D_6 . Figure 4.4 shows the NMR spectrum. Owing to the quadrupole moment ($I = 7/2$) of the ^{51}V nucleus, the resonances are somewhat broadened. The oxovanadium complex **1** shows resonances at $\delta = -477.5$ ppm and $\delta = -507$ ppm. These two δ values are expected for a dioxovanadium(V) complex with O,N,O donor set.²²⁻²³

**Figure 4.4.** ^{51}V NMR spectrum of **1** in CD_2Cl_2 at room temperature.

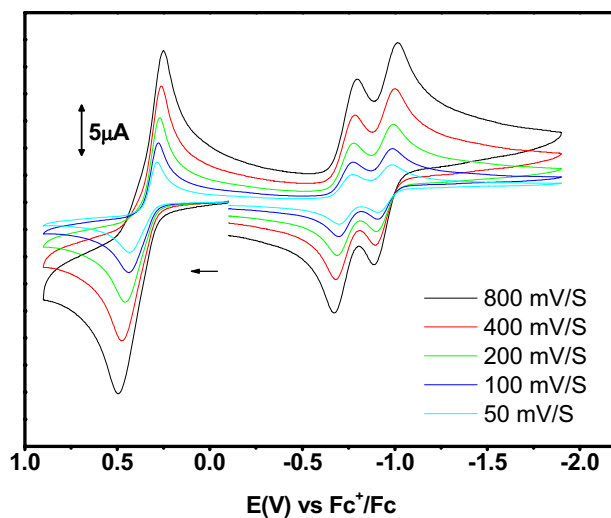


Figure 4.5. Cyclic voltammogram of complex **1** in CH_2Cl_2 at room temperature under an argon atmosphere.

The cyclic voltammogram (CV) of complex **1** has been recorded in CH_2Cl_2 solution containing 0.1 M $[\text{N}(\text{n-Bu})_4]\text{PF}_6$ as supporting electrolyte at a glassy carbon working electrode and a Ag/AgNO_3 reference electrode. Ferrocene was used as an internal standard, and potentials are referenced versus the ferrocenium/ferrocene (Fc^+/Fc) couple. Figure 4.5 shows the CV of **1** recorded in the potential range +1.75 V to -2.0 V. A reversible two-electron oxidation and two reversible one-electron reductions are observed, as established by coulometry at fixed potential. Hence, $E_{1/2}$ value at 0.423 V corresponding to one two-electron oxidation and $E_{1/2}$ values at -0.65 and -0.86 V are due to two successive one-electron reductions. As complex **1** contains two vanadium (V) ions with two fully reduced coordinating ligands ($[\text{L}_{\text{Cat}}^{\text{CH}_2\text{OH}}]^{3-}$) the oxidations should be ligand centered and reduction processes will be metal centered.

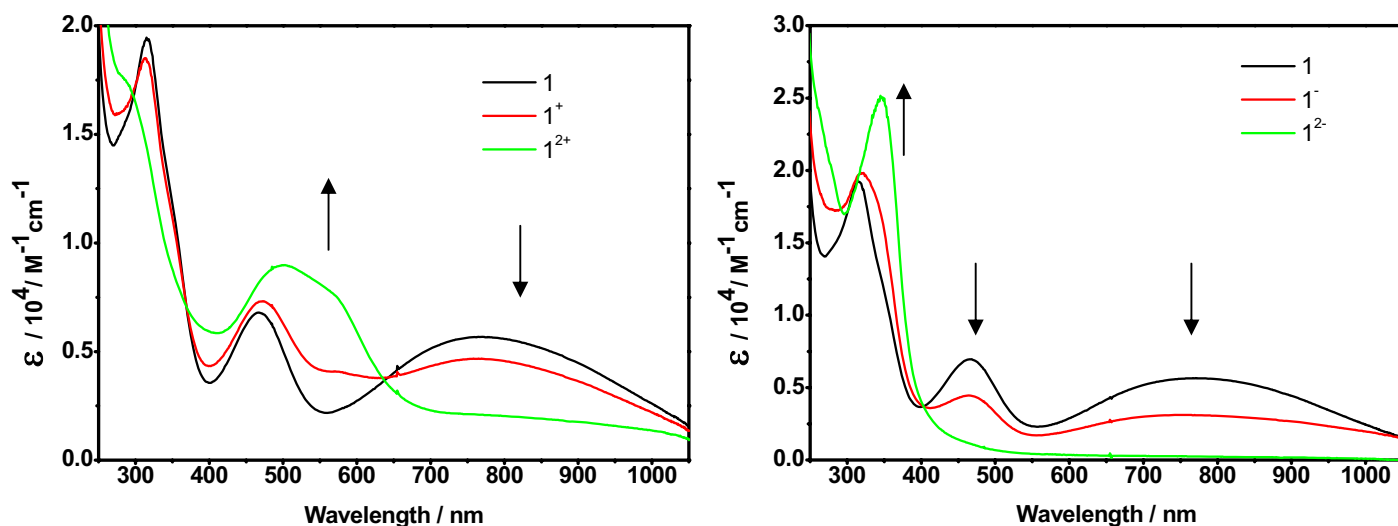


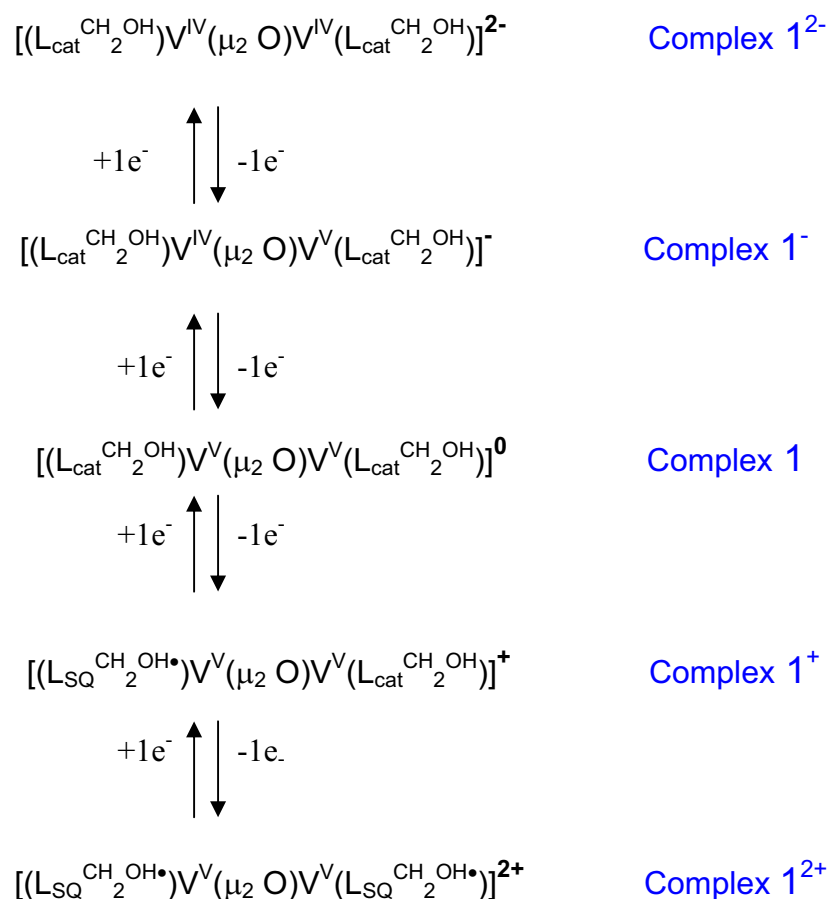
Figure 4.6. Electronic spectrum of complex **1**, 1^+ , 1^{2+} , 1^- and 1^{2-} in CH_2Cl_2 at -25°C .

The UV-VIS/NIR spectra of complex **1** together with its one (electron counted during coulometry) and two-electron oxidized as well as reduced species are depicted in Figure 4.6. Table 4.2 summarizes the spectroelectrochemical behaviours. Neutral complex **1** shows three absorption bands at 315, 467 and 760 nm. All the bands can be assigned to ligand-to-metal charge transfer bands or more clearly the bands at 467 and 760 nm are likely phenolate-to-vanadium (V) charge transfer bands²⁴ whereas the band at 315 nm is possibly an alkoxide to vanadium (V) charge transfer band.²⁵ Upon reduction by one electron the bands at 760 nm and 467 nm diminish while that at 315 nm increases slightly. The decrease in absorption on reduction could be due to reduction of vanadium (V) to vanadium (IV). Further reduction leads to a sharp and strong band at 345 nm and the assigned metal-to-phenolate charge transfer bands (760 and 476 nm) almost vanish indicating nonexistence of the vanadium (V) moiety after reduction in complex 1^{2-} . Upon oxidation by one electron the band at 760 nm diminishes slightly and the final absorption at that wavelength could be due to both ligand-to-metal and intervalence ligand-to-ligand (amidophenolate-to-iminosemiquinone) charge transfers. Similarly, ligand π - π^* and phenolate-to-vanadium (V) charge transfers explanation could be given for slight increase in absorption at 473 nm. After two electron oxidation of **1** the band at 760 nm becomes very broad and a new band at 495 nm with a shoulder at 563 nm appears. The band at 495 nm can be assigned to a ligand π - π^* transition, while, that at 563 nm is presumably due to ligand (iminosemiquinone)-to-vanadium (V) charge transfer.

Table 4. 2. Spectroelectrochemical data of the complexes.

Complex	λ , nm (ϵ , $M^{-1}cm^{-1}$, 10^4)
1	315 (1.95), 467(0.7), 760(0.56)
1⁻	314(2.0), 467(0.443), 760 (0.31)
1²⁻	345 (2.5)
1⁺	311(2.0), 473(0.73), 765(0.467)
1²⁺	495(0.9), 563(0.77)

From all these experimental results the electrochemical behaviour of complex **1** can be summarized as shown in Figure 4.7.

Figure 4.7. Different redox states of **1**.

4.3 A trinuclear Mn-cluster(2)

The reaction of anhydrous MnCl_2 (2 mmol) with the ligand (2 mmol), $\text{H}_3\text{L}^{\text{CH}_2\text{OH}}$, in methanol in the presence of triethylamine produces a brown colored solution. Addition of acetonitrile to this solution followed by slow evaporation gives deep brown colored solid.

The IR spectrum of **2** is complicated because both the quinone and iminosemiquinone forms of the ligand are attached to the metal. The bands at 1643 cm^{-1} and 1621 cm^{-1} are due to the C=O and C=N stretching vibrations respectively. The sharp peak at 1475 cm^{-1} is attributed to the presence of C-O• units. The moderate intensity peak at $1022\text{--}1074\text{ cm}^{-1}$ can be assigned to C-O stretching of the alkoxide group attached to the metal ions.

Complex **2**·2MeCN crystallizes in the triclinic spacegroup $P\bar{1}$. The neutral complex **2** (Figure 4.8) has nine anions (two monoradical dianions $[\text{L}_{\text{SQ}}^{\text{CH}_2\text{OH}}]^{2-}$, one trinegative ligand $[\text{L}_{\text{Cat}}^{\text{CH}_2\text{OH}}]^{3-}$, one mononegative ligand $[\text{L}_{\text{BQ}}^{\text{CH}_2\text{OH}}]^{1-}$ and one chloride) requiring that the sum of the charges on the three manganese ions to be +9 and resulting in the manganese oxidation state formulation of $[\text{Mn}^{\text{II}}\text{Mn}^{\text{III}}\text{Mn}^{\text{IV}}]^{9+}$. The alternative formulation of MnIII_3 can be unambiguously discarded from the different M–X bond lengths observed in the X-ray crystal structure.²⁶⁻²⁷ The structure contains a central six-coordinated Mn(II) ion, Mn(2), which is flanked by one six-coordinated Mn(IV), Mn(3), and one five-coordinated Mn(III), Mn(1) ions; manganese ions are linked to each other through two bridging μ_2 -alkoxo oxygens. The coordination sphere around Mn(3) is N₂O₄, in which the equatorial plane is comprised of O(61)O(91)O(76)O(106) and the nitrogen atoms N(68) and N(98) are disposed in *trans* positions with an angle N(68)–Mn(3)–N(98) of $168.2(2)^\circ$. The short Mn(3)–O and Mn(3)–N bond lengths (Table 4.3) and highly octahedral ligand arrangement are consistent with a Mn(IV)²⁶⁻²⁷ state for Mn(3) that shows no Jahn–Teller distortion, which would be a characteristic for a d^4 h.s. Mn(III) ion. The O(91)–C(92), C(97)–N(98), O(61)–C(62) and C(67)–N(68) bond lengths at 1.343(6), 1.393(7), 1.308(7) and 1.361(7) Å, respectively, indicate clearly that the two ligands attached to Mn(3) are in two different oxidation states, *i.e.* one in fully reduced amidophenolate form and the other in iminosemiquinone radical form. Thus, the coordination environment of Mn(3) is best described as $\text{Mn}(3)(\text{L}_{\text{Cat}}^{\text{CH}_2\text{OH}})(\text{L}_{\text{BQ}}^{\text{CH}_2\text{OH}\bullet})$. O(76) and O(106) make μ_2 -alkoxo bridges between the Mn(3) and Mn(2) centers. The Mn(2)–O and Mn(2)–N bond lengths lying between 2.103(4)–2.231(5) Å strongly indicate the high-spin Mn(II)-character for the Mn(2) center. The

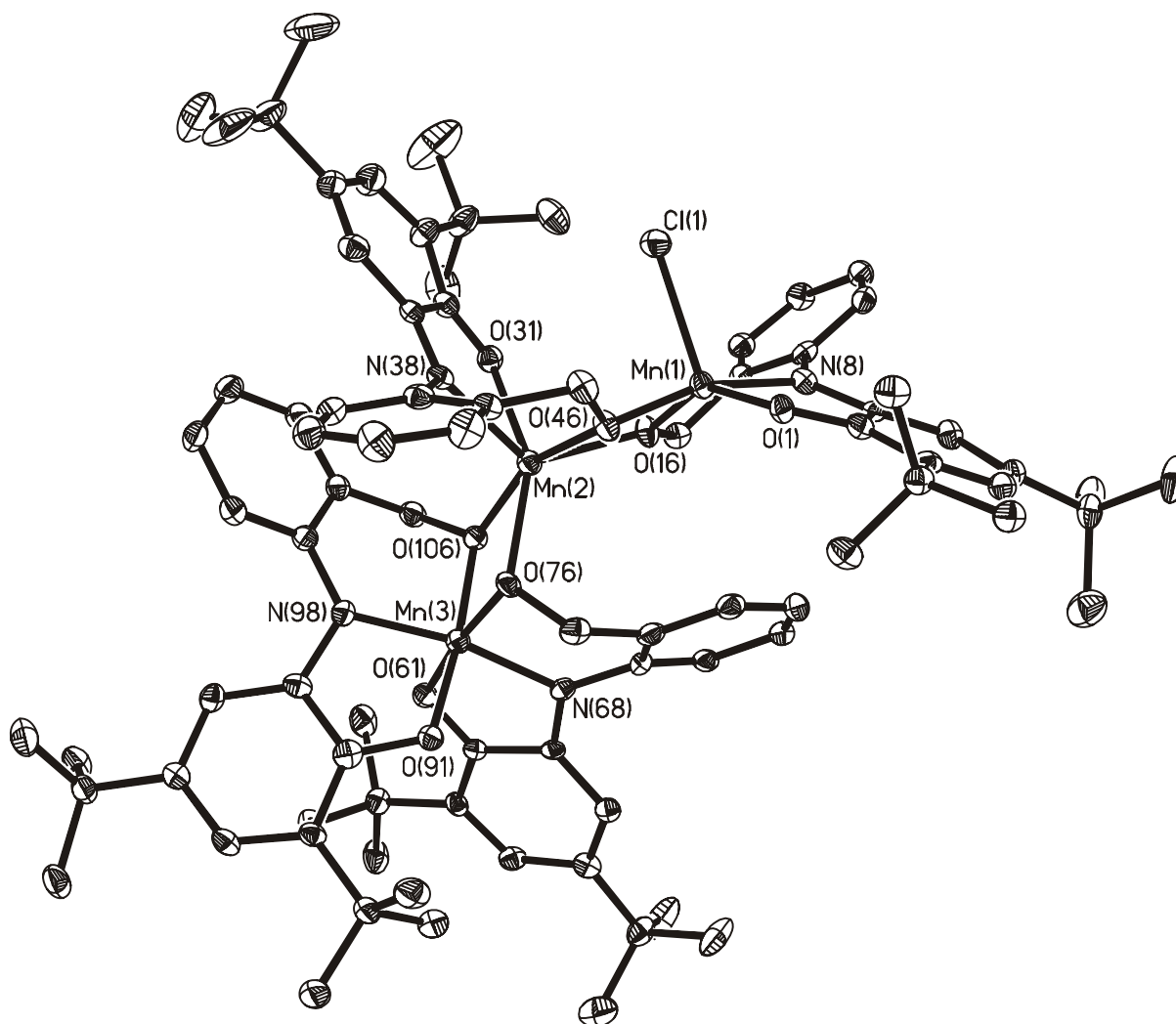
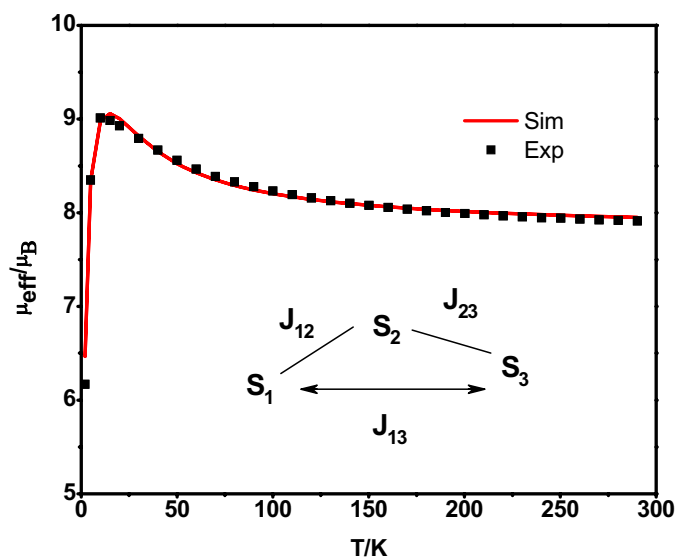


Figure 4.8. ORTEP diagram of complex **2**.

respective O(31)–C(32) and C(37)–N(38) bond lengths at 1.227(6) and 1.288(7) Å are in accord with the assignment that the ligand attached to the Mn(2) centre is in fully oxidized iminoquinone form ($L_{BQ}^{CH_2OH} \cdot$).²⁷ The Mn(1) centre is in a square-pyramidal geometry with an axial Cl^- ion, Cl(1). The Mn(1) atom is about 0.437 Å above the NO_3 equatorial plane. The Mn(1)–O and Mn(1)–N bond lengths are in full conformity with the reported parameters for h.s. d^4 Mn(III). O(1)–C(2) and N(8)–C(9) bond lengths at 1.310(6) and 1.376(7) Å give a clear indication that the ligand chelating with the Mn(1) centre is in the iminosemiquinone radical form, thus making Mn(1) a five-coordinated Mn(III) centre bound to a p-radical anion. Summarily, the neutral trinuclear complex **2** with the composition $[Mn_3L_4^{CH_2OH}Cl]$ consists of valence-trapped Mn(IV), Mn(II) and Mn(III) ions with two iminosemiquinone radical dianion, one iminoquinone monoanion and one amidophenolate trianion ligand system.

Table 4.3. Selected bond lengths (Å) and angles (degree) for **2**.

Mn(1)–O(46)	1.884(4)	Mn(3)–O(76)	1.917(3)
Mn(1)–O(16)	1.898(3)	Mn(3)–N(98)	1.928(4)
Mn(1)–N(8)	1.927(4)	Mn(3)–N(68)	1.950(4)
Mn(1)–O(1)	1.929(4)	Mn(1) ⋯ Mn(2)	3.121(1)
Mn(1)–C1(1)	2.366(2)	Mn(2) ⋯ Mn(3)	3.117(1)
Mn(2)–O(16)	2.103(4)	Mn(1) ⋯ Mn(3)	5.856(1)
Mn(2)–O(76)	2.136(4)	O(1)–C(2)	1.310(6)
Mn(2)–O(106)	2.139(3)	N(8)–C(7)	1.376(7)
Mn(2)–O(46)	2.190(4)	O(31)–C(32)	1.227(6)
Mn(2)–N(38)	2.231(5)	N(38)–C(37)	1.288(7)
Mn(2)–O(31)	2.293(4)	O(61)–C(62)	1.308(6)
Mn(3)–O(91)	1.883(4)	N(68)–C(67)	1.361(7)
Mn(3)–O(61)	1.905(3)	O(91)–C(92)	1.343(6)
Mn(3)–O(106)	1.915(4)	N(98)–C(97)	1.393(7)
Mn(1)–O(16)–Mn(2)	102.4(2)	Mn(2)–O(76)–Mn(3)	103.1(2)
Mn(1)–O(46)–Mn(2)	99.7(2)	Mn(2)–O(106)–Mn(3)	103.1(2)

**Figure 4.9.** A Plot of μ_{eff} vs. T for complex **2**.

Variable-temperature solid-state magnetic susceptibility was measured on a powdered sample of **2** in the temperature range 2–290 K in an applied magnetic field of 1 T, shown as Figure 4.10, to discern the type of exchange interactions for this valencetrapped trinuclear complex. The effective magnetic moment, μ_{eff} of **2** increases gradually from 7.6 μ_{B} at 290 K to 8.48 μ_{B} at 10 K, below which μ_{eff} decreases, reaching 5.8 μ_{B} at 2 K. To describe the magnetic properties of **2**, the Heisenberg spin exchange Hamiltonian in the form $\hat{H} = -2JS$

$\hat{S}_i \bullet S \hat{S}_j$ was used. It has been shown previously that the interactions, Mn(III)–radical (R) and Mn(IV)–radical (R) are very strongly antiferromagnetic in nature.²⁶⁻²⁷ Hence, the experimental magnetic moment curve was fitted using only three (instead of five) spin-carriers with $S_1 = 1.0$ [Mn(IV)–R], $S_2 = 2.5$ [Mn(II)] and $S_3 = 1.5$ [Mn(III)–R]. As the distances Mn(1)⋯Mn(2) of 3.121(1) and Mn(2)⋯Mn(3) 3.177(1) Å result in a too long distance 5.856 Å between Mn(1) and Mn(3) to be significant for the exchange interaction, we have considered a “2- J ” model for simulation: J_{12} represents the exchange interaction between the spin S_1 and S_2 , whereas J_{23} the exchange parameter between S_2 and S_3 . To avoid overparametrization and to include the single-ion zero-field splitting parameter D_1 of the manganese(III) centre, whose inclusion in simulation is evidenced by nesting of the variable-temperature variable field (1, 4 and 7 T) plots, we have used the constraint $g_1 = g_2 = g_3$ during simulation.

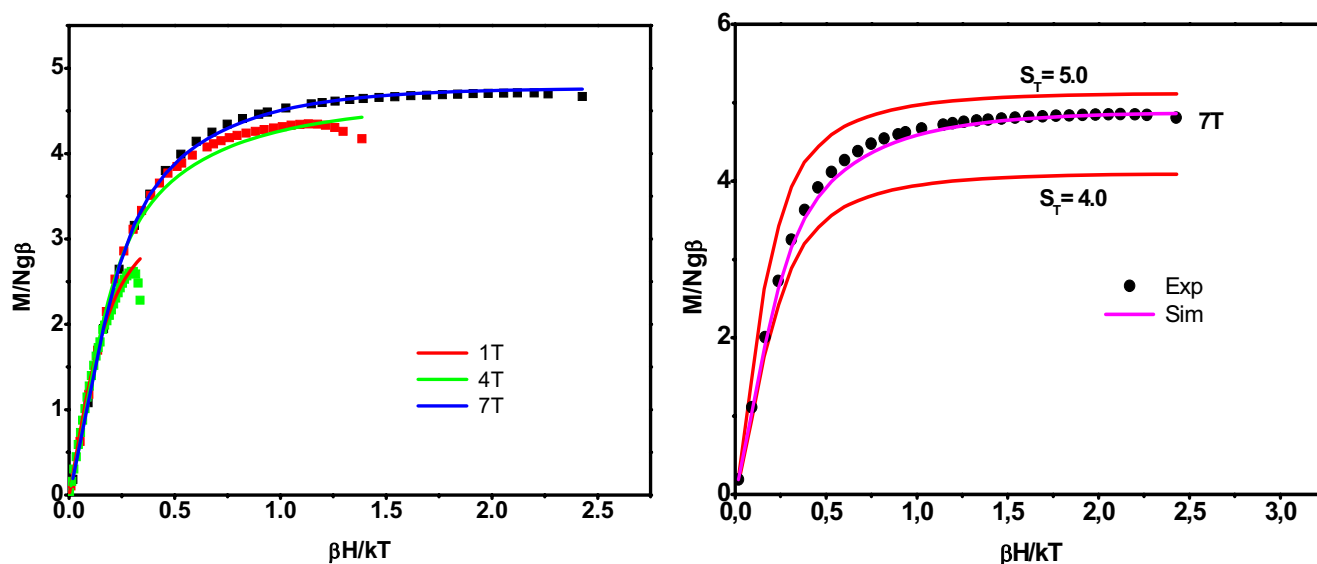


Figure 4.10. $M/Ng\beta$ vs $\beta H/kT$ plot for complex 2 (dotted lines are for experimental and solid lines are for simulation).

A satisfactory simulation, shown as the solid line in Figure 4.10, is obtained with the fitting parameters, $J_{12} = 2.7 \text{ cm}^{-1}$, $J_{23} = -0.30 \text{ cm}^{-1}$, $g_1 = g_2 = g_3 = 2.05$, $D_1 = 8.0 \text{ cm}^{-1}$. Thus, the magnetic measurements also corroborate the three different oxidation states of the manganese centers in **2**. Variable-temperature (2–290 K), variable-field (1, 4 and 7 T) magnetization measurements were also simulated with very similar parameters. Figure 4.10 shows the simulation of the experimental data at 7 T with the parameters, $J_{12} = +2.6 \text{ cm}^{-1}$, $J_{23} = -0.1 \text{ cm}^{-1}$, $g_1 = g_2 = g_3 = 2.05$, $D = 8.0 \text{ cm}^{-1}$, together with the theoretical Brillouin curves with $g = 2.05$. Figure 4.10 shows clearly that the ground state of the molecule is higher than S_T

= 4.0 and the low-lying states are very near to each other in energy. It has been noticed that keeping J_{23} fixed at zero, the quality of simulation reduces and becomes unacceptable. As J 's and D are of similar magnitude it is not possible to calculate the ground state in the form of an S_T value; S is not a good quantum number to describe the ground state, but rather M_S .

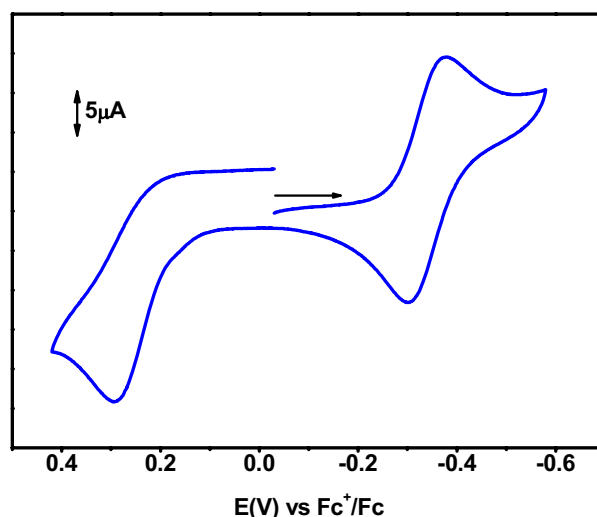


Figure 4.11. Cyclic voltammogram of complex **2** in CH_2Cl_2 at room temperature under an argon atmosphere.

The cyclic voltammogram (CV) of complex **2** was recorded at room temperature in CH_2Cl_2 solutions containing 0.1 M $[\text{N}(\text{n-Bu})_4] \text{PF}_6$ as supporting electrolyte at a glassy carbon working electrode and an Ag/AgNO_3 reference electrode. Ferrocene was used as an internal standard, and potentials are referenced versus the ferrocenium/ferrocene (Fc^+/Fc) couple. Figure 4.11 shows the CV of **2** recorded in the potential range +0.70 V to -0.5 V. In that potential range two one-electron-transfer waves were found. Controlled potential coulometric analysis at -25°C in CH_2Cl_2 indicates that the $E_{1/2}$ value at -0.335 V corresponds to reversible one-electron reduction of **2** whereas, the $E_{1/2}$ value at +0.263 V corresponds to a two-electron oxidation of complex **2**. It is interesting to note that the wave at +0.263 V becomes reversible and double in height with decreasing the temperature of the medium (CH_2Cl_2). This behaviour is generally associated with a metal centered redox process(es).²⁸

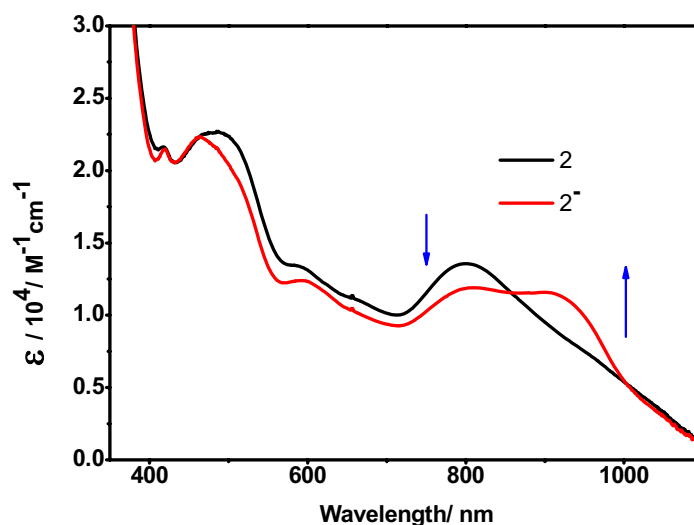
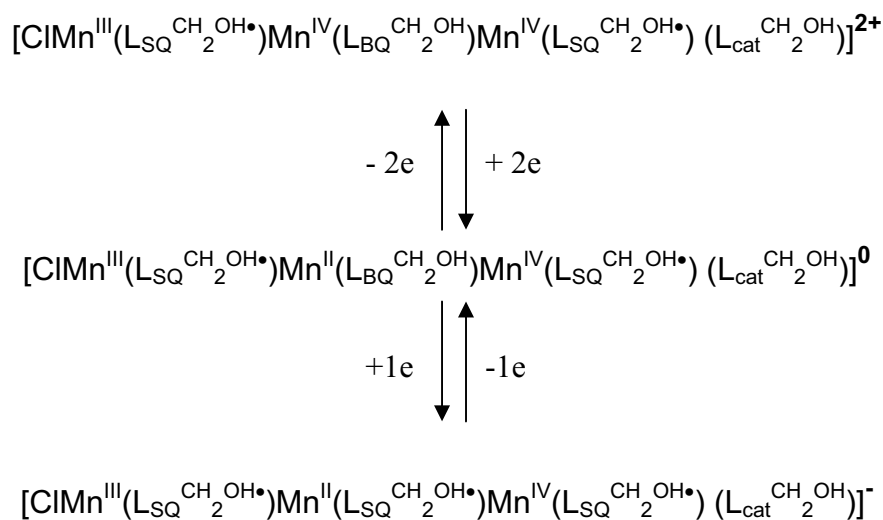


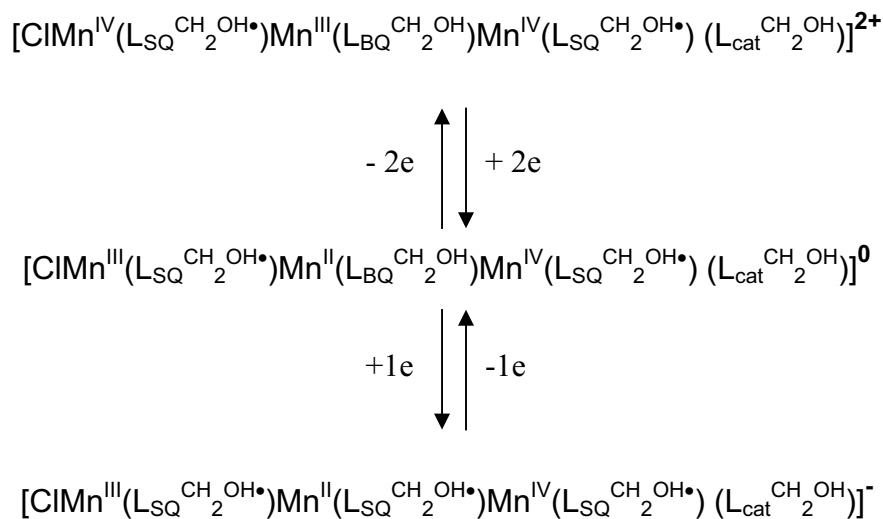
Figure 4.12. Electronic spectrum of complex **2** and **2^{•-}** in CH_2Cl_2 at -25°C .

Figure 4.12 shows the UV-VIS/NIR spectra of **2** and its electrochemically generated one-electron reduced species. In complex **2**, a broad band at 800 nm ($\epsilon = 13500 \text{ M}^{-1}\text{cm}^{-1}$) with a shoulder at around 940 nm ($\epsilon = 7700 \text{ M}^{-1}\text{cm}^{-1}$) and another broad band at 490 nm ($\epsilon = 22700 \text{ M}^{-1}\text{cm}^{-1}$) are observed. The first two bands may be assigned as intervalence ligand-to-ligand charge transfer bands while the latter is likely ligand-to-metal charge transfer. Upon reduction of complex **2** by one electron the band at 800 nm decreases slightly ($\epsilon = 11870 \text{ M}^{-1}\text{cm}^{-1}$) and a new broad band at around 910 nm ($\epsilon = 11500 \text{ M}^{-1}\text{cm}^{-1}$) appears. The appearance of the new, broad low energy band could be due to the reduction of the fully oxidized ligand, iminoquinone, to iminosemiquinone and hence provides intervalence ligand-to-ligand charge transfer. The band at 490 nm shifts to 466 nm ($\epsilon = 22300 \text{ M}^{-1}\text{cm}^{-1}$) after one-electron reduction of **2**. The exact assignment of the electrochemical behaviours of the complex is not possible because it is polynuclear with multiredox centers. But from the coulometric and spectroelectrochemical results (Figure 4.12) two proposals shown in Scheme 2 can be given.

(A)



(B)



Scheme 2. Different redox states of complex 2.

4.4 A Cu_4O_4 cubane complex (3)

4.4.1 Synthesis and characterization of the complex(3)

To synthesize complex **3**, $H_3L^{CH_2OH}$ (2 mmol) was added to a solution of Copper(II) acetate monohydrate (2 mmol) in acetonitrile (30 ml). The solution was stirred under air for 24 h; a dark red / pink color powder was filtered and recrystallized from a 1:1 methanol, dichloromethane solution mixture.

In the IR spectrum of complex **3**, the bands at 1025 cm^{-1} arises due to the Cu-OR stretching vibration.³ The sharp bands at $2961\text{--}2868\text{ cm}^{-1}$ are due to the $-C-H$ stretching of the *tert*-butyl group and the band at 1627 cm^{-1} is an indicative of the presence of $-C=N$ unit in complex **3**.

X-ray quality single crystals were obtained after recrystallization of the microcrystalline solid from a 1:1 MeOH / CH_2Cl_2 solution mixture. ORTEP diagram of the tetrameric copper complex is shown in Figure 4.13. Selected bond lengths as well as bond angles are listed in Table 4.4. The diagram shows cubane geometry of the complex with a Cu_4O_4 core. The complex contains C_2 axes that pass vertically through the planes of the cubane (Figure 4.14). Complex **3** contains copper ions in the alternating corners of the cube and each copper ion is linked with each other through μ_3 oxygen atoms of the alcoholate group of the ligands. The respective $C_{phenyl-O}$ and $C_{phenyl-N}$ bond lengths are 1.305(3), 1.367(3) Å. The six C-C distances in the *tert*-butyl groups containing phenyl rings are not equidistant, whereas those distances in the N-phenyl part are same within experimental error (1.390(3) Å). The C(1)-C(2), C(2)-C(3), C(3)-C(4), C(4)-C(5), C(5)-C(6) and C(6)-C(2) bond lengths are 1.434(3), 1.379(3), 1.434(3), 1.368(3), 1.423(3) and 1.452(3) Å respectively. As similar kind of bond lengths are observed for all the *tert*-butyl containing phenyl rings, hence, it can be concluded that all the *tert*-butyl containing phenyl rings are in the iminosemiquinone form with quinoid type distortion, i.e. alternative long and short C-C bonds. Each copper ion is pentacoordinate with one imine N atom, one phenoxy atom and three μ_3 alkoxo O atoms from the three ligands. The geometry around each copper ion is distorted square pyramidal [$\tau = \alpha - \beta / 60$, α and β are two largest angles around the central atom, $\tau = 0$ and 1 for perfect square pyramidal and trigonal bipyramidal geometries, respectively. $\tau = 0.2$ (Cu1), $\tau = 0.23$ (Cu2), $\tau = 0.18$ (Cu3), $\tau = 0.26$ (Cu4)]. The molecule is a neutral one and so, the oxidation state of all copper ions, which have more or less same Cu-O and Cu-N bond lengths, should

be +II and all the ligands are in iminosemiquinone form.²⁹ The Cu-O_{al} bond lengths and Cu-O_{al}-Cu (O_{al} stands for alkoxo oxygen atom) bond angles are shown in Figure 4.15.

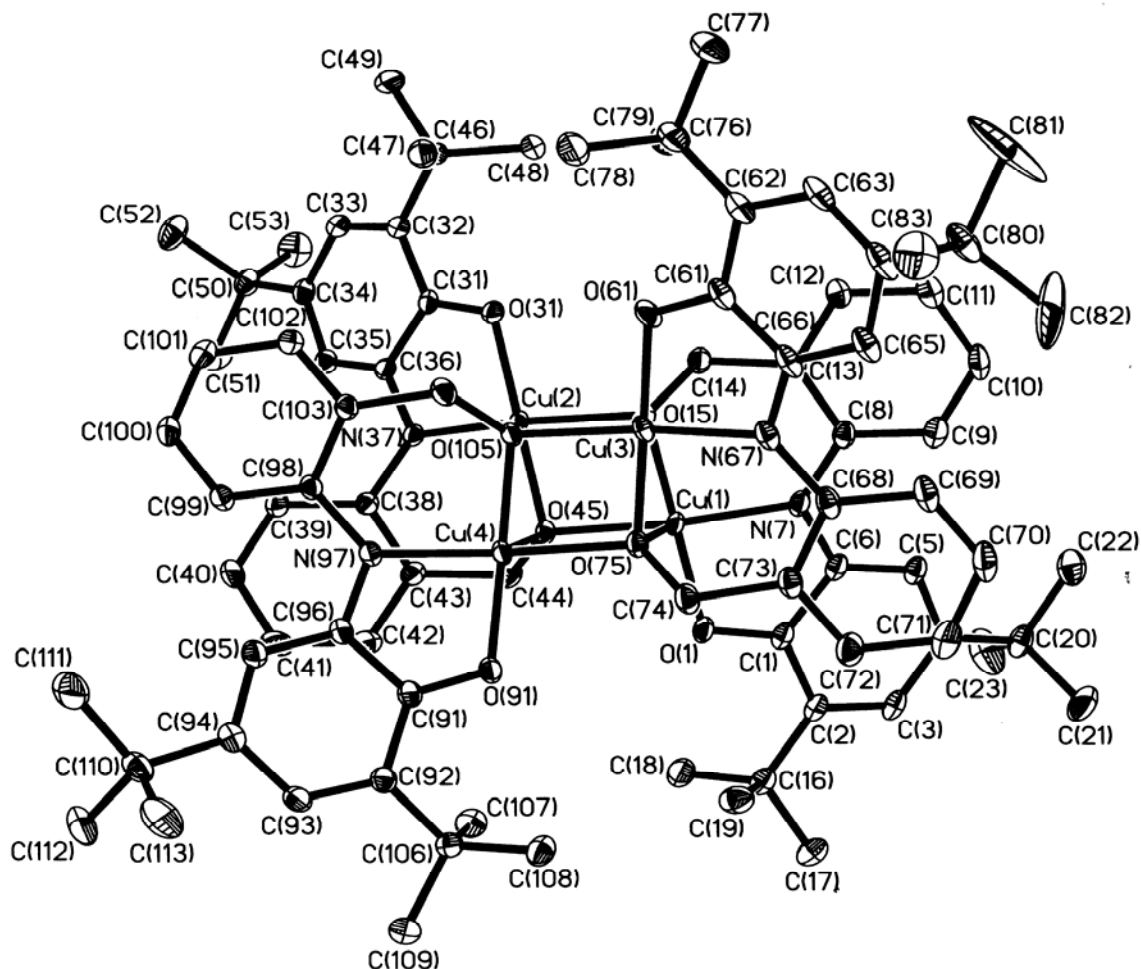


Figure 4.13. ORTEP diagram of 3.

Table 4.4. Selected bond lengths (Å) and angles (degree) for 3.

Cu(1)-O(1)	1.9076(15)	Cu(4)-N(97)	1.9448(18)
Cu(1)-N(7)	1.9579(14)	Cu(1)...Cu(2)	2.956(3)
Cu(2)-O(31)	1.9295(14)	Cu(1)...Cu(3)	3.089(3)
Cu(2)-N(37)	1.9441(17)	Cu(1)...Cu(4)	3.332(3)
Cu(3)-O(61)	1.9137(15)	Cu(2)...Cu(3)	3.324(3)
Cu(3)-N(67)	1.9562(16)	Cu(2)...Cu(4)	3.119(3)
Cu(4)-O(91)	1.9211(15)	Cu(3)...Cu(4)	2.954(3)

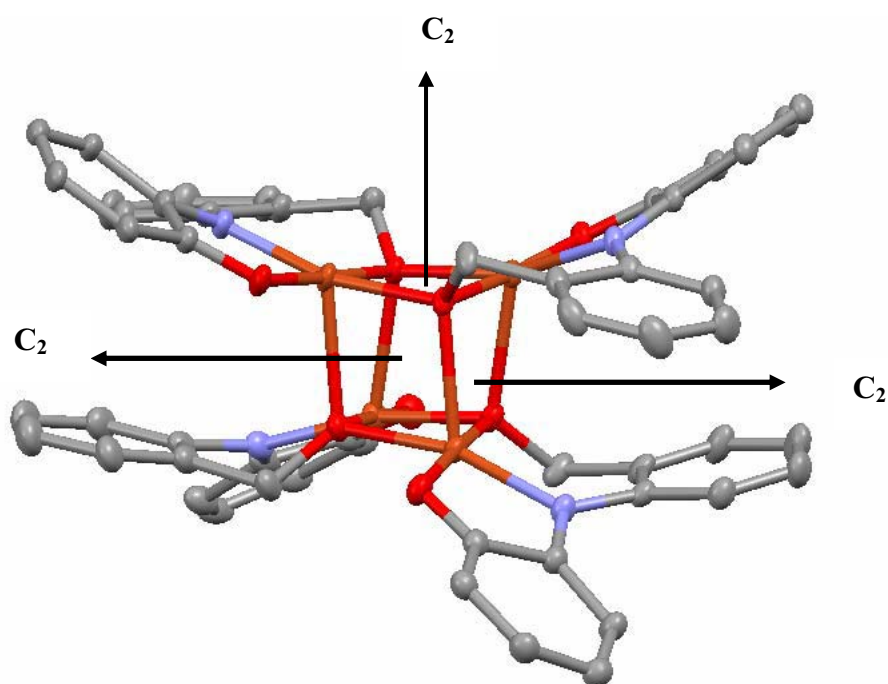


Figure 4.14. Symmetry diagram for complex 3.

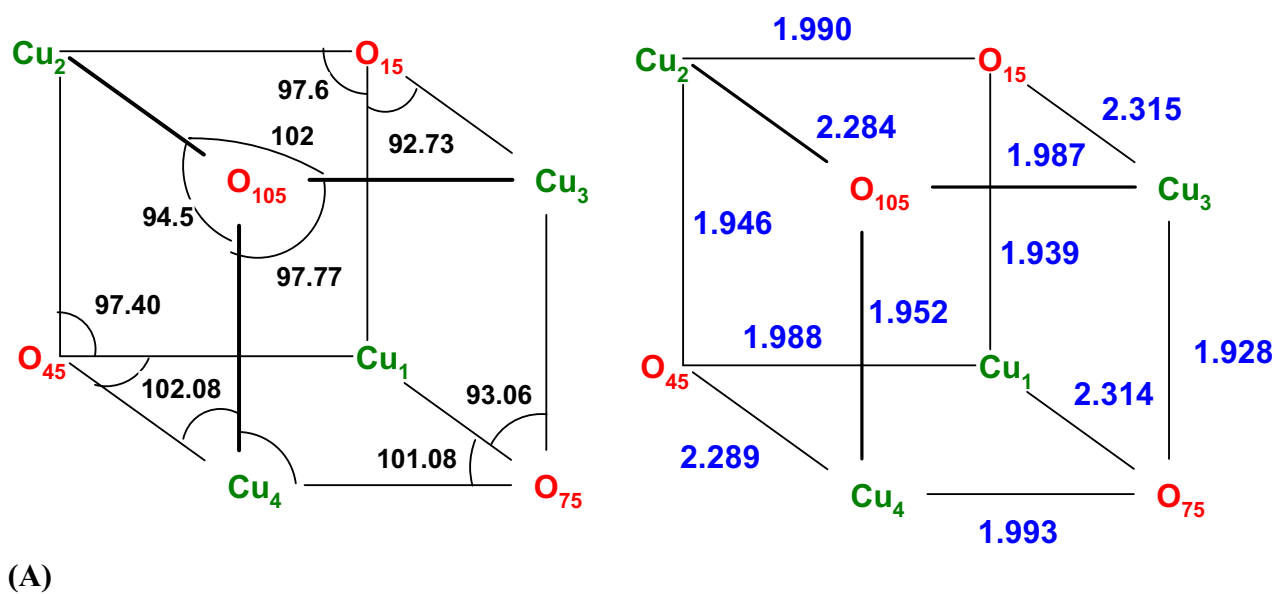


Figure 4.15. (A) The Cu-O_{at}-Cu bond angles and (B) Cu-O_{at} bond lengths.

Variable-temperature magnetic susceptibility measurements were carried out in the temperature range of 2-290 K at a magnetic field of 1 T on a solid sample of **3** with a SQUID magnetometer. Figure 4.16 illustrates the temperature dependence of the magnetic susceptibility of the tetradical-containing tetranuclear copper (II) distorted cubane cluster in the form of the $\chi_M T$ vs T . The curve for complex **3** shows antiferromagnetically coupled tetradical-containing tetranuclear copper(II) cluster with a decrease of $\chi_M T$ from a high temperature value of $3.13 \text{ cm}^3 \text{ K mol}^{-1}$ to a value close to 0 at low temperature indicating that all the eight paramagnetic centers are coupled together to form an $S_t = 0$ ground state.

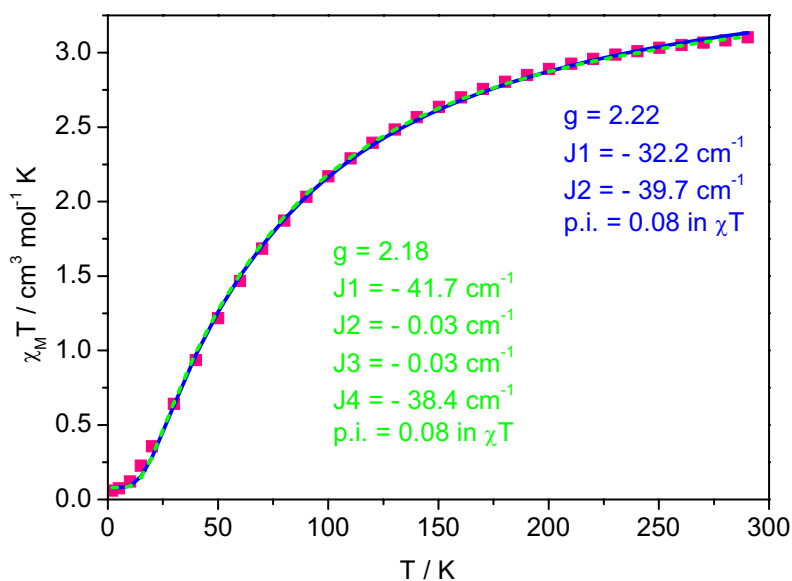
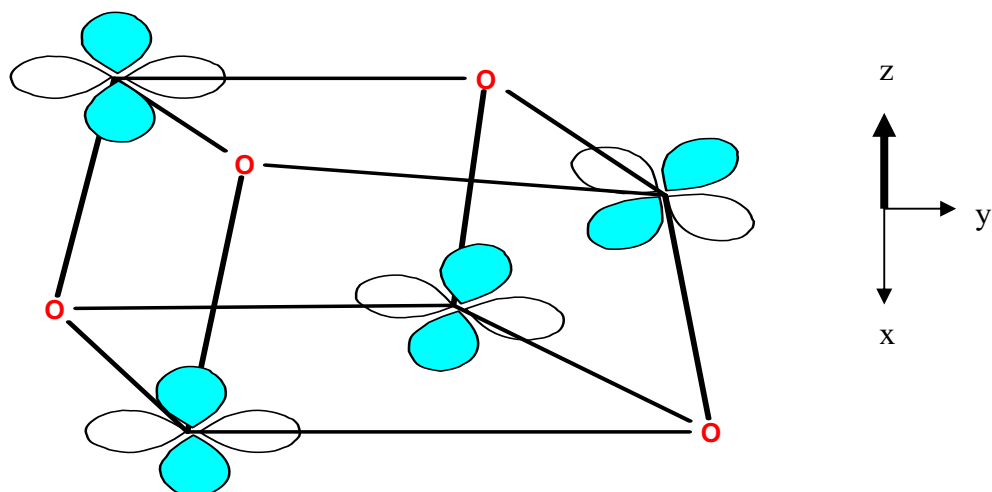


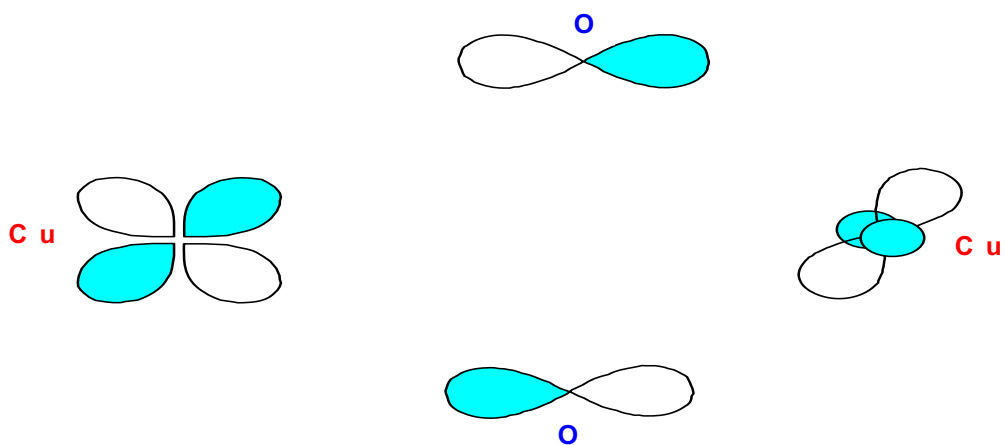
Figure 4.16. A plot of $\chi_M T$ vs T for complex **3**.

This result can be rationalized by considering (Figure 4.17) the orientation of the $d_{x^2-y^2}$ orbital of the Cu(II) ions deduced from the structural analysis and presented in Figure 4.17(A). It appears that both of the oxygen bridges of coppers of the same pairs (1, 4 and 2, 3) are axial to one metal atom and equatorial to the other; this gives rise to the overall situation shown in Figure 4.17(C). It is clear that this arrangement does not lead to a strong overlap between the $d_{x^2-y^2}$ orbitals on any bridging atom, and, therefore, the interaction cannot be important. The interpair interaction, on the other hand, implies two different types of bridges: one of the axial-equatorial type as above, but also, one of the equatorial-equatorial type. As illustrated in Figure 4.17(B), the latter combination produces a significant overlap on one bridging oxygen, thus providing a pathway to the magnetic interaction.

(A)



(B)



(C)

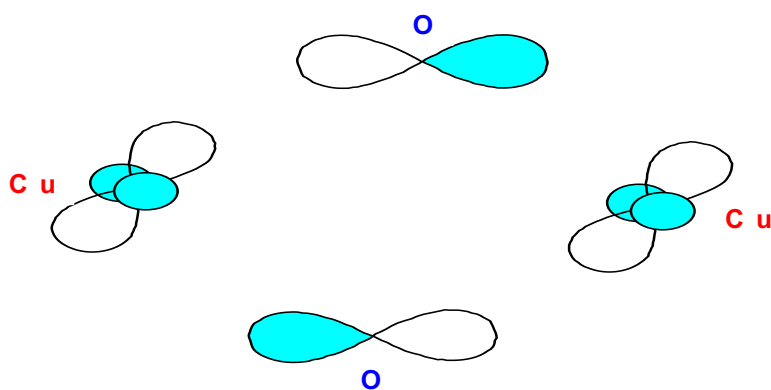


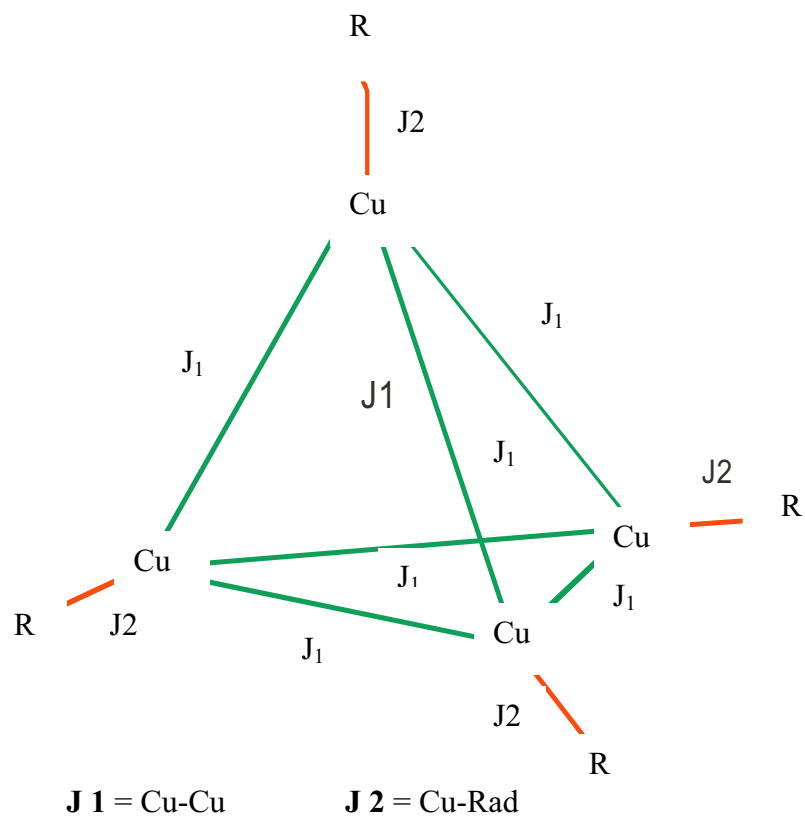
Figure 4.17. A. Orientation of the $d_{x^2-y^2}$ orbitals of Cu(II) ions within the tetranuclear cluster.

B. Equatorial- equatorial and axial- equatorial interpair interactions.

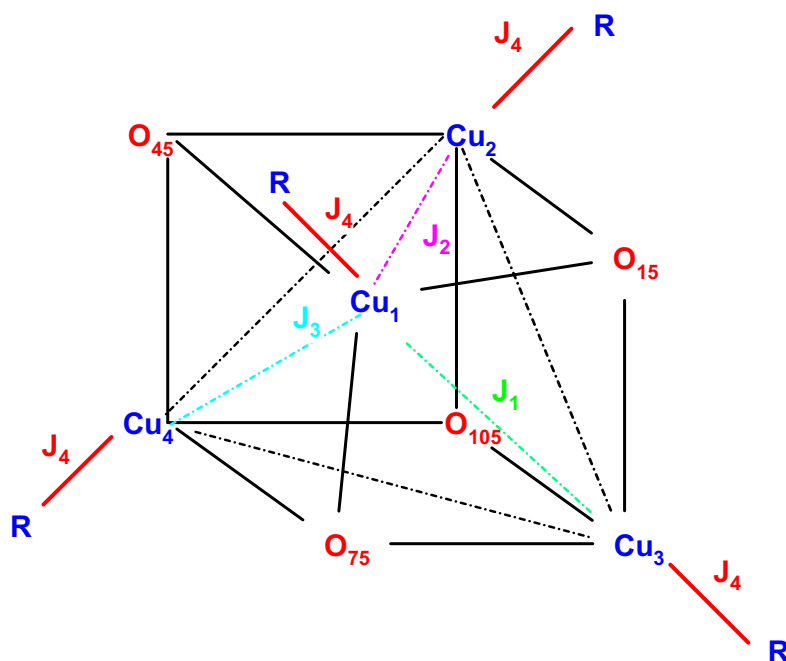
C. Axial- equatorial intrapair interactions.

Coupling schemes (3):

Scheme A



Scheme B



Cu(1)-O(15)-Cu(2)	= 97.60	J3	Cu(1)-O(15)-Cu(3)	= 92.73	J2
Cu(1)-O(45)-Cu(4)	= 102.08	J1	Cu(1)-O(45)-Cu(2)	= 97.40	J3
Cu(1)-O(75)-Cu(4)	= 101.08	J1	Cu(1)-O(75)-Cu(3)	= 93.06	J2
Cu(2)-O(15)-Cu(3)	= 100.82	J1	Cu(2)-O(45)-Cu(4)	= 94.05	J2
Cu(2)-O(105)-Cu(3)	= 102.00	J1	Cu(2)-O(105)-Cu(4)	= 94.50	J2
Cu(3)-O(75)-Cu(4)	= 97.77	J3	Cu(3)-O(105)-Cu(4)	= 97.18	J3
Cu(1)-Rad	J4	Cu(2)-Rad	J4	Cu(3)-Rad	J4
		Cu(4)-Rad	J4		

To simulate the experimental magnetic properties of complex **3**, the Heisenberg spin-exchange Hamiltonian $\hat{H} = -2\sum_{i<j} J_{ij} \hat{S}_i \bullet \hat{S}_j$ was used, in which J_{ij} represents the exchange constants and the subscripts i and j number the pairwise interacting paramagnetic centers. Two different assumptions are taken into account. Firstly, it has been assumed that the interactions between the Cu-Cu centers are the identical and the Cu-radical interaction for the individual Cu-radical unit is same to the other Cu-radical units (Scheme **3A**). The following parameters are obtained from the best fit to the experimental result taking above assumption into account. $g = 2.22$, $J1 = -32.2 \text{ cm}^{-1}$, $J2 = -39.7 \text{ cm}^{-1}$, $p.i. = 0.08$. Considering all the Cu-O bond lengths and Cu-O_{al}-Cu bond angles (Scheme **3B**) three different types of exchange-interaction have been taken for the interactions among the copper ions. As the Cu-radical bond lengths and the bond angle Cu-O-C_R (R= radical containing-carbon center) are same, radical-copper interaction is taken as same for all the four copper-radical units. Hence, four different interactions were the second assumption (Scheme **3B**). According to this assumption the best fit result is, $g = 2.18$, $J1 = -41.7 \text{ cm}^{-1}$, $J2 = -0.03 \text{ cm}^{-1}$, $J3 = -0.03 \text{ cm}^{-1}$, $J4 = -38.4 \text{ cm}^{-1}$, $p.i. = 0.08$. Both simulations provide a good fit to the experimental results.

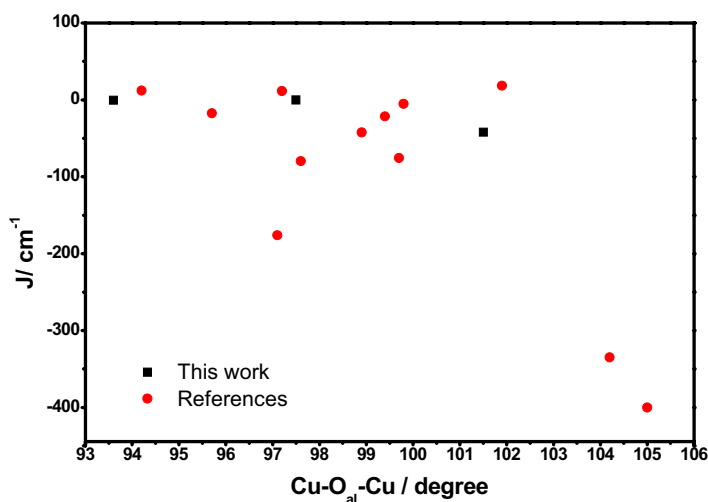


Figure 4.18. A plot of J vs Cu-O_{al}-Cu bond angles.

Hence, it is conclusive that the exchange interaction constant between two copper(II) ions, which are linked through μ_3 -alkoxo bridges, remains approximately zero in the range of Cu-O_{al}-Cu bond angle 92.73 to 97.77°. These results fairly close to the previously reported results.³⁰⁻³⁴ No correlation between the exchange coupling constant (J) and Cu-O_{al}-Cu angle is possible as shown in Figure 4.18. Table 4.5 summarizes the exchange coupling results.

Table 5. Cu-O_{al}-Cu bond angle and J data.

Cu-O-Cu , °	J, cm⁻¹	Reference
99.4	-21.4	33
104	12.3	33
94.2	12.3	33
97.1	-176	34
99.8	-5	34
104.2	-335	30
105	-400	30
99.1	-122.5	30
95.7	-17.4	30
97.6	-79.6	30
99.7	-75.5	31
98.9	-42.35	31
101.9	18.5	31
97.2	11.7	31
101.5	-41.7	This work
97.5	0	This work
93.6	0	This work

Cyclic voltammogram (CV) and square wave voltammogram (SQW) of complex **3** have been measured in CH_2Cl_2 solution containing 0.1 M $[\text{N}(\text{n-Bu})_4]\text{PF}_6$ as supporting electrolyte at a glassy carbon working electrode and an Ag/AgNO_3 reference electrode. Ferrocene was used as an internal standard, and potentials are referenced versus the ferrocenium/ferrocene (Fc^+/Fc) couple. Figure 4.19 shows the SQWs of complex **3** recorded in the potential range +0.70 V to -0.4 V and -0.6 V to -1.4 V.

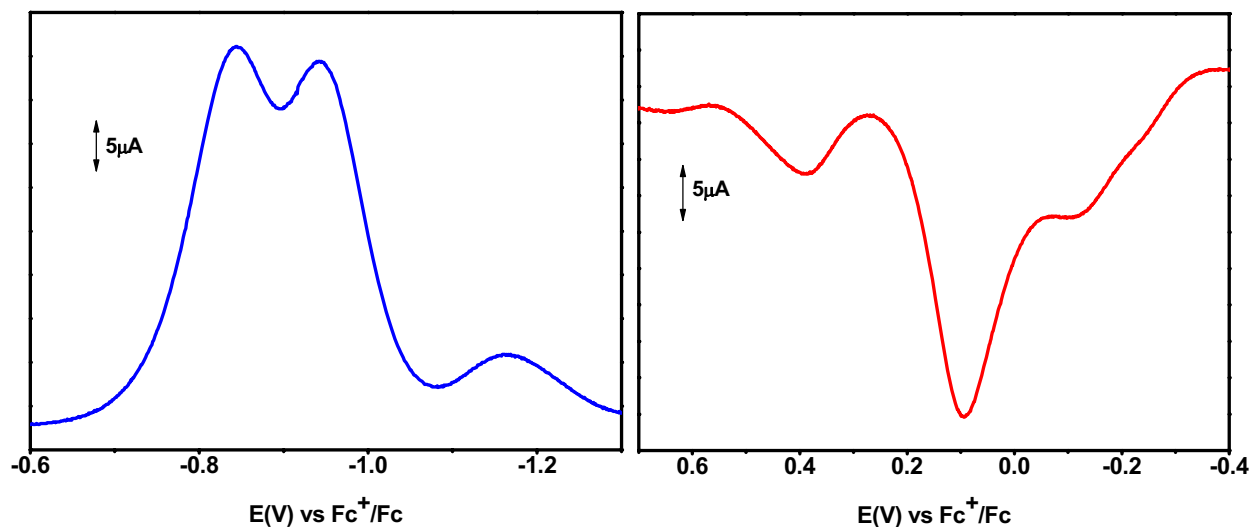


Figure 4.19. Square wave voltammograms of complex **3** in CH_2Cl_2 at room temperature under an argon atmosphere.

Coulometric experiments at fixed potential show that the waves at $E_{1/2}$, 0.34, 0.094 and -0.110 V are corresponding to oxidations while that at -1.166, -0.94 and -0.84 V are corresponding to reductions of complex **3**. $E_{1/2}$, -0.94, -0.84 and 0.094 V are two-electron oxidation processes and others are one electron processes. All the oxidations and reductions processes are reversible.

Figure 4.20 shows UV-VIS/NIR spectral changes during stepwise four-electron coulometric reduction of complex **3** and Table 4.6 summarizes the results.

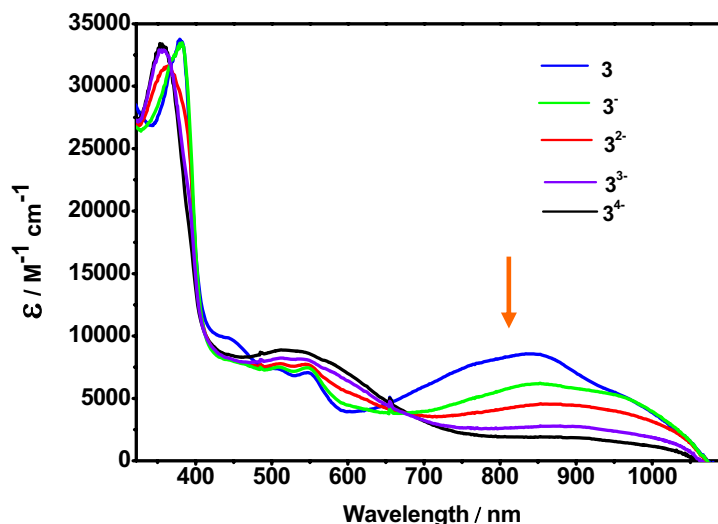


Figure 4.20. Electronic spectrum of complex **3**, **3^{•-}**, **3²⁻**, **3³⁻** and **3⁴⁻** in CH_2Cl_2 at $-25\text{ }^\circ\text{C}$.

The UV-VIS/NIR spectrum of complex **3** shows strong and sharp absorption bands at 380, 550 and 507 nm with absorption coefficient (ϵ , $\text{M}^{-1}\text{cm}^{-1}$) 33600, 7065, and 7500 respectively. All the bands may be assigned to ligand-to-metal charge transfer band. The broad band centered at around 840 nm is probably arising due to ligand-to-ligand charge transfer. During four stepwise one-electron reductions the broad band at around 840 nm shifts to longer wavelength and decreases in intensity. The final absorption coefficient after four-electron reductions is $1950\text{ M}^{-1}\text{cm}^{-1}$ and most probably arising due to the d-d transition of the four copper(II) ions. Hence, ligand centered reduction is the speculation.

Table 4.6. Spectroelectrochemical data of the complexes.

Complex	λ , nm (ϵ , $\text{M}^{-1}\text{cm}^{-1}$)
3	845(8600), 550(7065), 507(7500), 447(9830), 380(33600)
3^{•-}	952(5430), 840(6140), 546(7475), 507(7600), 380(33300)
3²⁻	860(4500), 544(7800), 507(7800), 362(31600)
3³⁻	875(2764), 541(8190), 511(8294), 355(33000)
3⁴⁻	875(1950), 523(8900), 355(33000)

The X-band EPR spectra, recorded in frozen solution of CH_2Cl_2 , of one-electron and three-electron reduced species of complex **3**, symbolically **3^{•-}** and **3³⁻** are depicted in Figure 4.21.

It is noteworthy that complex **3** contains little bit impurity of mononuclear Cu(II) species which is EPR active. Hence, the X-band EPR spectrum of the starting material (**3**) contains a weak Cu(II)-centered signal.

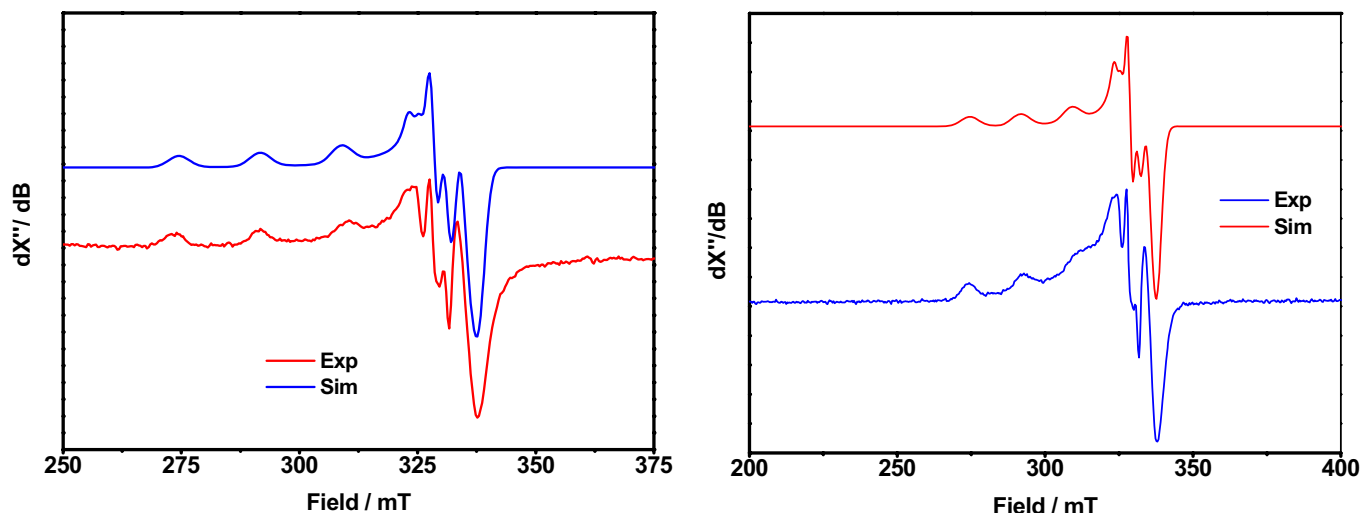


Figure 4.21. X-Band EPR spectra of 3^{3-} (left) and 3^{-} (right), measured at 30 K.

Indeed, the intensity of the X-band EPR spectra obtained for 3^{-} and 3^{3-} species are much stronger than that of the starting material (**3**). The simulations of the experimental results for complexes 3^{-} and 3^{3-} provide the following parameters;

Parameters	Complex 3^{-}	Complex 3^{3-}
g_x	2.06	2.0275
g_y	2.033	2.0575
g_z	2.245	2.245
W_x (G)	25	30
W_y (G)	30	25
W_z (G)	60	80
A_x (10^{-4} cm^{-1})	20	10
A_y (10^{-4} cm^{-1})	0	20
A_z (10^{-4} cm^{-1})	180	180

Hence, from the X-band EPR spectra it is clear that the first four reduction processes are ligand centered in nature and the spectroelectrochemical behaviors of complex **3** can be summarized as shown in Figure 4.22.

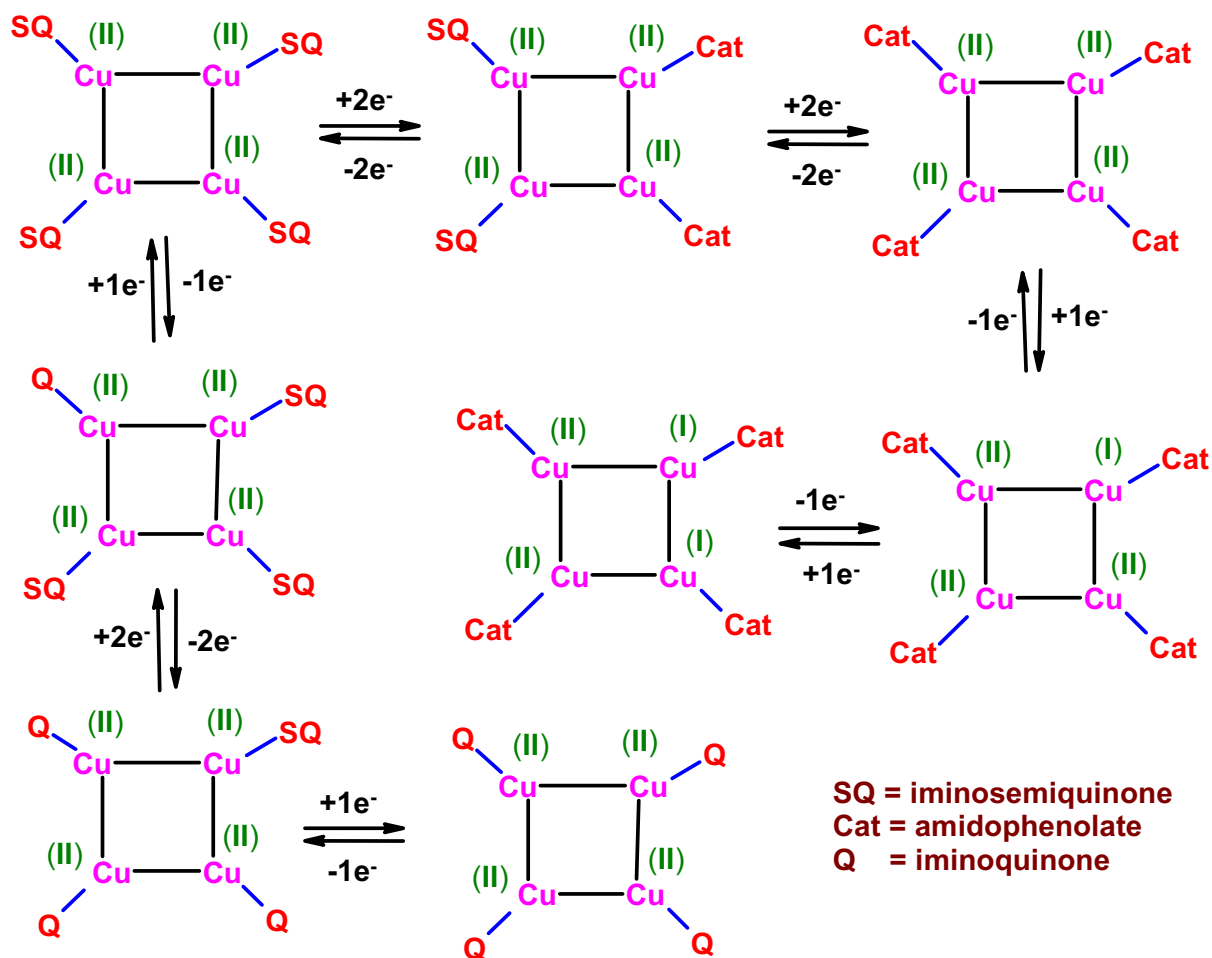
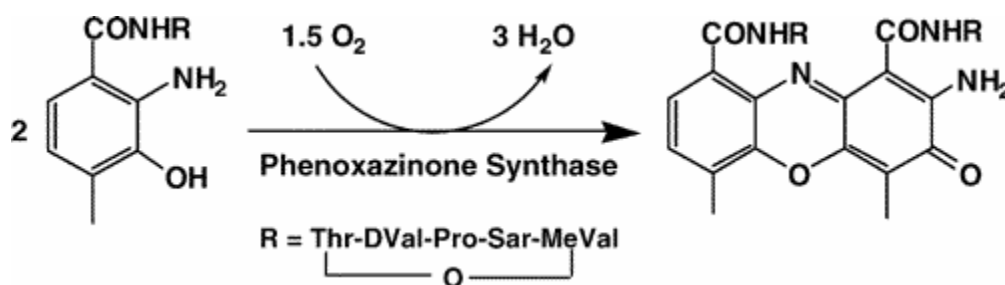


Figure 4.22. Different redox states of complex **3**.

4.4.2 Catalytic reactivity,

Aerial oxidation of 2-aminophenol; Mimicking the function of Phenoxazinone Synthase(PHS)

Actinomycin D, one of the most potent antineoplastic agents known, is synthesized by the actinomycete *Streptomyces antibioticus*. This compound inhibits DNA-dependent RNA synthesis by intercalation of the phenoxazinone chromophore to DNA. The last step in the biosynthesis of actinomycin D, namely, the oxidative condensation of two molecules of 3-hydroxy-4-methylantranilic acid pentapeptide lactone to form actinocin (Scheme 4), is catalyzed by the enzyme Phenoxazinone Synthase (PHS). PHS is a multicopper oxidase produced in two distinct oligomeric forms: low activity dimers and high activity hexamers. The relative amount of the two forms is regulated; young cultures that do not produce actinomycin predominantly contain the dimeric form, whereas older actinomycin-producing cultures mostly contain the hexameric form.³⁵ The dimers and hexamers are distinct stable molecular forms and are not related by a simple equilibrium-aggregation phenomenon.³⁵ The regulation and structural differences between these two oligomeric forms is currently unknown.



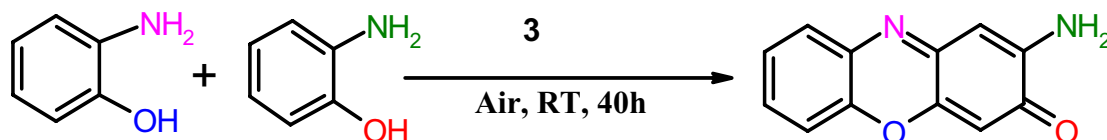
Scheme 4. Reaction catalyzed by PHS.

When Begley et.al.³⁶ have proposed the mechanism of the six-electron oxidative coupling as radical-base process, Simóndi and co-workers³⁷ have proposed similar type of mechanism using Co(II), Fe(II)-salen or oximate complexes as functional models. Using various Cu(II) and Cu(I)-salts and molecular oxygen at 60 °C, phenoxazinone chromophore can be synthesized catalytically using 2-aminophenol as substrate.³⁸ Indeed, PHS is a multinuclear copper containing metalloenzyme. The crystal structure of PHS has been described in Chapter 1. It is noteworthy that still to date there is not a single structural as well

as functional model complex in literature that can oxidise 2-aminophenol to phenoxazinone chromophore catalytically in the presence of air.

Considering active site structural feature and proposed mechanism for the catalytic processes, complex **3** has been employed as a catalyst for the aerial oxidation of 2-aminophenol.

When 2-aminophenol (2.35×10^{-2} M) was added to complex **3** (2.38×10^{-4} M) in methanol (20 ml), the color of the solution slowly turns to deep yellow-red color. After 40 h, it was found that $\sim 100\%$ of the 2-aminophenol has been converted to 2-amino-phenoxazine-3-one.



Using initial rate method the rate equation of the above catalytic reaction has been determined by varying the concentration of substrate (2-aminophenol) keeping the concentration of catalyst (complex **3**) as constant and vice versa. From the experimental results shown in Figure 4.23 the rate equation was deduced as,

$$\text{Rate} = k [\text{2-aminophenol}]^2 [\text{Complex 3}]$$

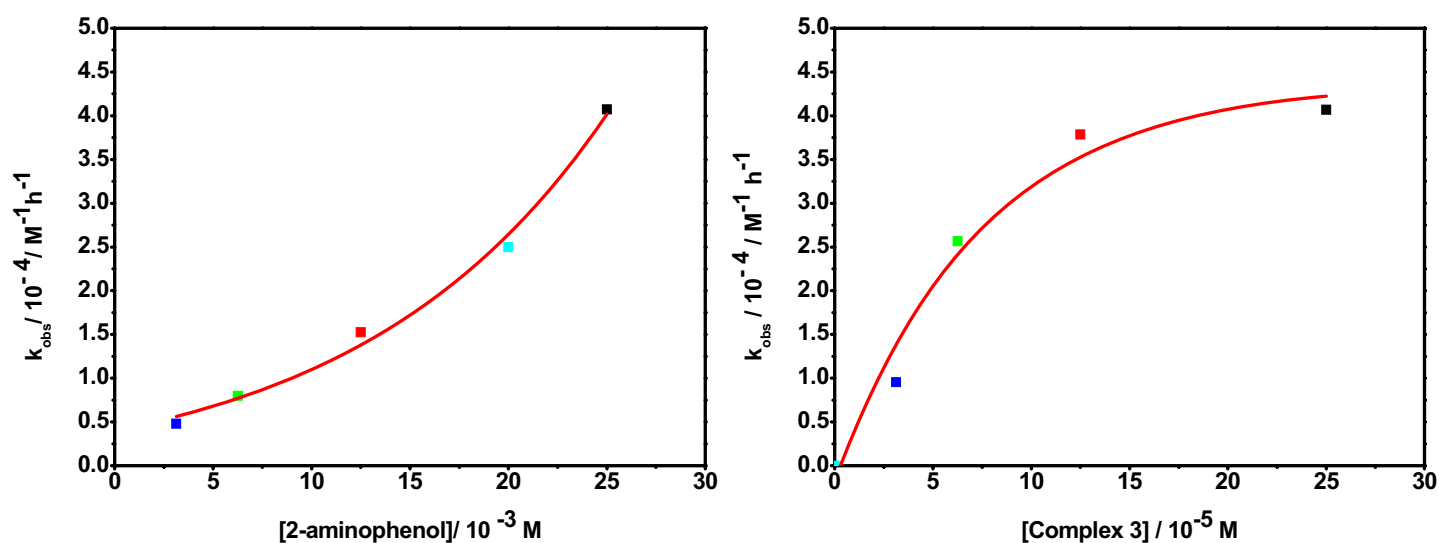


Figure 4.23. Kinetic data.

When 1 equivalent of complex **3** was allowed to react with approximately 10 equivalent of 2-aminophenol under an argon atmosphere (Glove Box) for 40 h, one equivalent of product to the concentration of complex **3** has been found to form by spectrophotometric method at 435 nm and depicted in Figure 4.24. The above experiment implies that two molecules of 2-aminophenol reacts with one molecule of complex **3** to form one molecule of phenoxazinone chromophore. Exposure of the solution to air increase the concentration of the phenoxazinone chromophore, thus the oxidation process is an aerial oxidation process. This is the first example of aerial oxidation of 2-aminophenol to phenoxazinone chromophore takes place. No hydrogen peroxide was detected. This could be due to the catalase activity of the complex **3**. Moreover due to sluggish nature of the reaction determination of H_2O_2 at lower temperature than that of room temperature was not possible.

It has been discussed earlier that the first four oxidation processes are ligand centered, hence, reduction of four radical centers together with reduction of two Cu(II) centers should happen as product : complex **3** concentration ratio obtained after Glove Box reaction is approximately 1. Moreover, the participation of Cu(II) centers during the oxidative reaction can be speculated by comparing the UV-VIS/NIR spectrum (Figure 4.24) of the solution obtained after Glove Box reaction with the UV-VIS/NIR spectrum obtained after four-electron reductions of complex **3**. The band at around 775 nm with an absorption coefficient, $3400 \text{ M}^{-1}\text{cm}^{-1}$ can be taken as an intervalence metal-to-metal charge transfer band as shown by Thomson and co-workers.³⁹

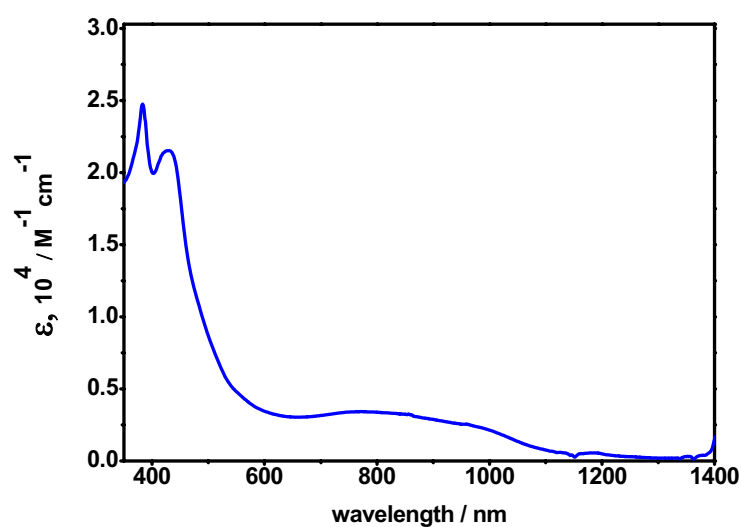


Figure 4.24. UV-VIS/NIR spectrum obtained after Glove-Box reaction.

Hence, from the above experimental results the mechanism for the oxidative coupling of two molecules of 2-aminophenol by catalytic activity of complex **3** in the presence of air can be proposed as shown in Figure 4.25.

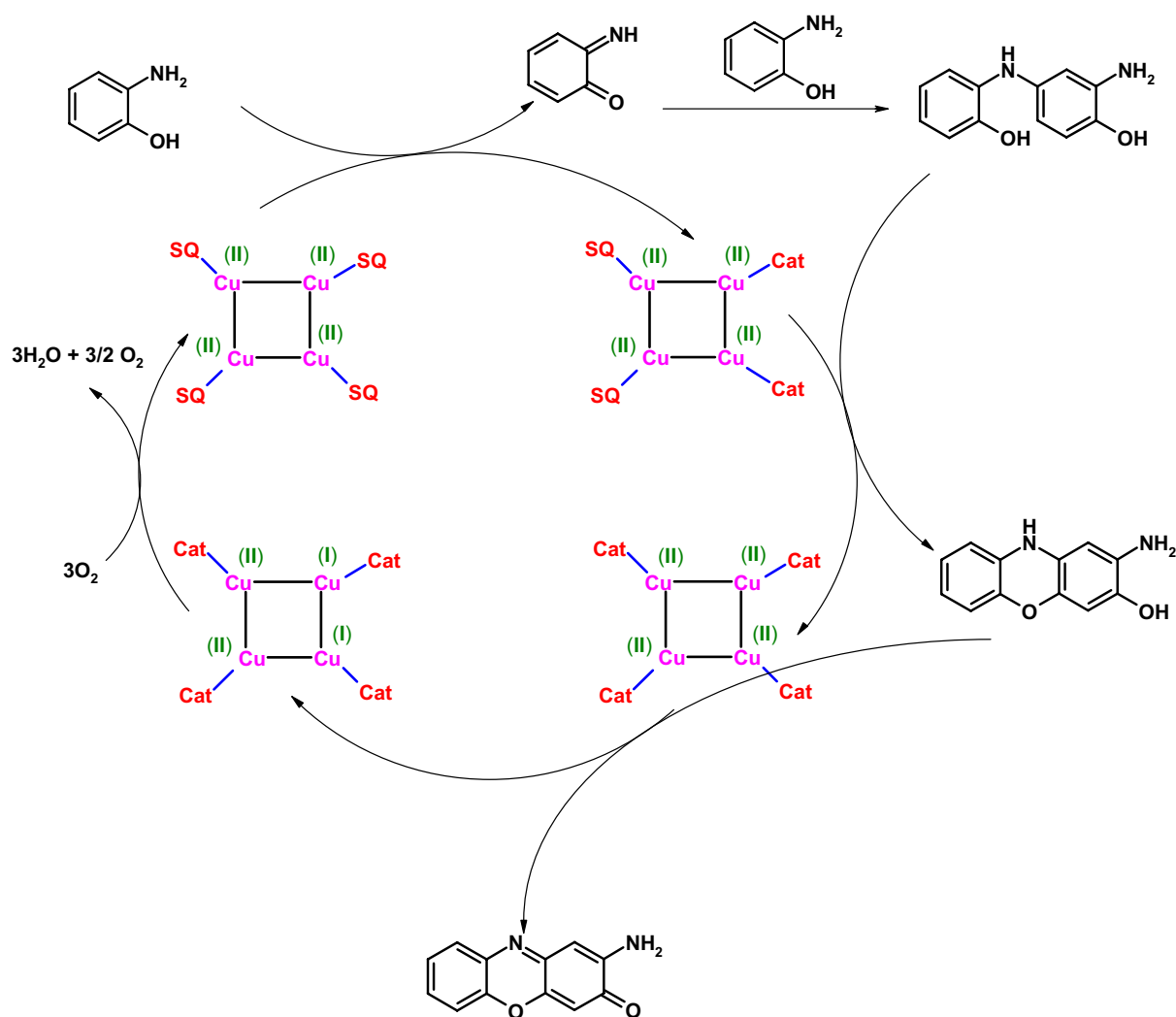


Figure 4.25. The proposed mechanism for the formation of phenoxazinone chromophore.

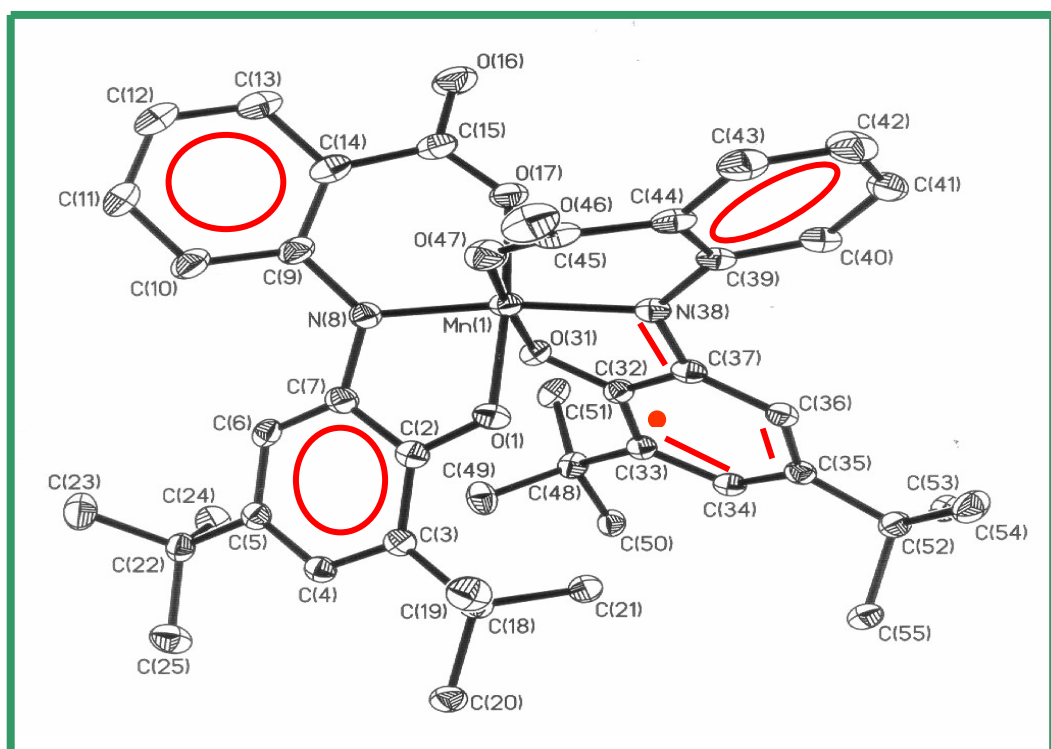
4.5 References

1. Holm, R.H.; Solomon, E.I. *Chem. Rev.* **2004**, *104*, 347.
2. *Vanadium Compounds, Chemistry, Biochemistry and Therapeutic Applications* (Eds.: A. S. Tracey, D. C. Crans), ACS Symp. Ser. **1998**, 711.
3. *J. Inorg. Biochem.* **2000**, *80* (Special Issue on Biological Aspects of Vanadium; Guest Eds.: D. Rehder, V. Conte).
4. *Vanadium and Its Role in Life* (vol. 31 of *Metal Ions in Biological Systems*; Eds.: H. Sigel, A. Sigel), Marcel Dekker, New York, **1995**.
5. Rehder, D. *Coord. Chem. Rev.* **1999**, *182*, 297.
6. *Vanadium in the Environment* (Ed.: J. O. Nriagu), Wiley, New York, **1998**.
7. Hirao, T. *Chem. Rev.* **1997**, *97*, 2707.
8. Arends, J. W. C. E.; Pellizon, M.; Sheldon, R. A. *Stud. Surf. Sci. Catal.* **1997**, *110*, 1031.
9. Thompson, K. H.; McNeill, J. H.; Orvig, C. *Chem. Rev.* **1999**, *99*, 2561.
10. Shechter, Y.; Li, J.; Meyerovitch, J.; Gefel, D.; Bruck, R.; Elberg, G.; Miller, D. S.; Shisheva, A. *Mol. Cell Biochem.* **1995**, *153*, 39.
11. Brink, H. B. ten; Tuynman, A.; Dekker, H. L.; Hemrika, W.; Izumi, Y.; Oshiro, T.; Shoemaker, H. E.; Wever, R. *Inorg. Chem.* **1998**, *37*, 6780.
12. Andersson, M. A.; Allenmark, S. G. *Tetrahedron.* **1998**, *54*, 15293.
13. Schmidt, H.; Bashirpoor, M.; Rehder, D. *J. Chem. Soc., Dalton Trans.* **1996**, 3865.
14. Bolm, V.; Bienewald, V. *Angew. Chem. Int. Ed. Engl.* **1995**, *34*, 2883.
15. Nakajima, K.; Kojima, K.; Fujita, V. *Bull. Chem. Soc. Jpn.* **1990**, *63*, 2620.
16. Xie, Y.; Jiang, H.; Chan, A. S.-C.; Liu, Q.; Xu, X.; Du, C.; Zhu, Y. *Inorg. Chim. Acta* **2002**, *333*, 138.
17. Fallon, G.D.; Moubaroki, B.; Murra, K.S.; Van Den Bergen, A. M.; West, B. O. *Polyhedron.* **1993**, *12*, 1989.
18. (a) Corei, E.J.; Achiva, K. *J. Am. Chem. Soc.* **1969**, *91*, 1429. (b) Girgis, A.Y.; Balch, A.L. *Inorg. Chem.* **1975**, *14*, 2724.
19. Chun, H.; Verani, C. N.; Chaudhuri, P.; Bothe, E.; Bill, E.; Weyhermüller, T.; Wieghardt, K. *Inorg. Chem.* **2001**, *40*, 4157.
20. Asgedom, G.; Sreedhara, A.; Kivikoski, J.; Valkonen, J.; Kolehmainen, E.; Rao, C.P. *Inorg. Chem.* **1996**, *35*, 5674.

21. Cornman, C. R.; Colpas, G.J.; Hoeschele, J. D.; Kampf, J.; Pecoraro, V.L. *J. Am. Chem. Soc.* **1992**, *114*, 9925.
22. Rehder, D.; Weidemann, C.; Duch, A.; Priebisch, W. *Inorg. Chem.* **1988**, *27*, 584.
23. Howarth, O. W. *Progr. Magn. Reson. Spectrosc.* **1990**, *22*, 453.
24. Asgedom, G.; Sreedhara, A.; Rao, C. P.; Kolehmainen, E. *Polyhedron.* **1996**, *15*, 3731.
25. Asgedom, G.; Sreedhara, A.; Kivikoski, J.; Valkonen, J.; Kolehmainen, E.; Rao, C. P. *Inorg. Chem.* **1996**, *35*, 5674.
26. Mukherjee, S.; Weyhermüller, T.; Bothe, E.; Wieghardt, K.; Chaudhuri, P. *J. Chem. Soc., Dalton Trans.* **2004**, 3842.
27. Chun, H.P.; Chaudhuri, P.; Weyhermüller, T.; Wieghardt, K. *Inorg. Chem.* **2002**, *140*, 790.
28. Slep, L.D.; Mijovilovich, A.; Meyer-Klaucke, W.; Weyhermüller, T.; Bill, E.; Bothe, E.; Neese, F.; Wieghardt, K. *J. Am. Chem. Soc.* **2003**, *125*, 15554.
29. Chaudhuri, P.; Verani, C. N.; Bill, E.; Bothe, E.; Weyhermüller, T.; Wieghardt, K. *J. Am. Chem. Soc.* **2001**, *123*, 2213.
30. Merz, L.; Haase, W. *J. Chem. Soc., Dalton Trans.*, **1980**, 875.
31. Schwabe, L.; Haase, W. *J. Chem. Soc., Dalton Trans.*, **1985**, 1909.
32. Wang, S.; Zheng, J.C.; Hall, J.R. *Polyhedron.* **1994**, *13*, 1039.
33. Merz, L.; Haase, W. *J. Chem. Soc., Dalton Trans.*, **1978**, 1594.
34. Trzebiatowska, B.J.; Olejnik, S.; Lis, T. *J. Chem. Soc., Dalton Trans.*, **1981**, 251.
35. Choy, H. A.; Jones, G. H. *Arch. Biochem. Biophys.* **1981**, *211*, 55.
36. Barry, C. E.; Nayar, P. G.; Begley, T. P. *Biochemistry*, **1989**, *28*, 6323.
37. Simóndi, T.M.; Simóndi, L.I.; Györ, M.; Rockenbauer, A.; Gomory, A. *J. Chem. Soc., Dalton Trans.*, **2004**, 1056 and there in.
38. Horváth, T.; Kaiser, J.; Speier, G. *Journal of molecular catalysis A: Chemical.* **2004**, *215*, 9.
39. Farrar, J.A.; Lappalainen, P.; Zumft, W.G.; Saraste, M.; Thomson, A.J. *Eur J Biochem.* **1995**, *232*, 294.

Chapter 5

Synthesis, Characterization and Catalytic Reactivities of a Monoradical-Containing Mononuclear Mn(IV) complex



5.1 Synthesis and characterization of the ligand, N (2-hydroxy-3,5-di-tert-butylphenyl) anthranilic acid, H_3L^{COOH}

Radical-containing metal complexes are of interest in understanding the metal-radical interactions of natural systems. These complexes can be useful as functional and/or structural models of metalloenzymes and can be studied not only to gain deeper insight into the electronic structure but also as catalysts for new oxidation reactions for synthetic and industrial purposes.

In this chapter synthesis, characterization and catalytic activities of a monoradical-containing Mn(IV) complex (**1**), having a new non-innocent ligand, N (2-hydroxy-3,5-di-tert-butylphenyl) anthranilic acid, H_3L^{COOH} (Figure 5.1), will be discussed.

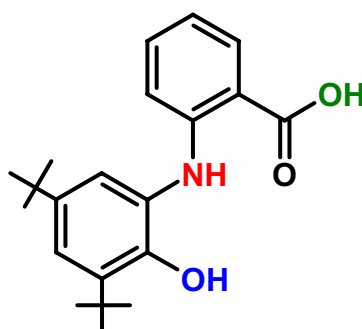


Figure 5.1. Schematic representation of the ligand N (2-hydroxy-3,5-di-tert-butylphenyl) anthranilic acid.

Condensation of 3,5-di-*tert*-butyl-catechol with anthranilic acid in the presence of triethylamine for 24 h under air in *n*-hexane produces the ligand, H_3L^{COOH} . It is important to note that an excess amount of triethylamine causes decomposition and polymerization of the ligand, therefore only two drops of triethylamine (0.01 ml) should be added for 10 mmol scale reaction (see experimental section). The ligand was characterized by IR, NMR, GC, GC-MS and mass spectroscopy. The ligand shows characteristic peaks in the IR spectrum due to $-O-H$ and $-N-H$ stretches at 3456 cm^{-1} and 3336 cm^{-1} respectively. The peaks in the range from 2959 to 2868 cm^{-1} are due to the $-C-H$ stretching of the *tert*-butyl group, the sharp bands at 1667 cm^{-1} and 1595 cm^{-1} are $C=O$ and $-C-C$ stretching bands of the carboxylic acid group of the aromatic rings, respectively. The bands in the range from 1500 to 1420 cm^{-1} appear from the skeletal vibrations of phenyl rings. The $-C-N$ stretch appears at 1577 cm^{-1} . The band at 1255 cm^{-1} is due to $C-O$ stretch. The sharp peak at 753 cm^{-1} is due to the $-C-H$ stretching of the tetrasubstituted aromatic rings. GC and GC-MS coupling measurements have been done to check the purity and composition of the ligand. EI mass-spectroscopy confirms the composition $C_{21}H_{27}NO_3$ (341 gm / mole) for H_3L^{COOH} . The tridentate ligand (H_3L^{COOH}) is able to lose its acidic proton, phenolic proton and the proton on the nitrogen atoms. The different oxidation states ranging from 1- to 3- exhibited by the ligand owing to its non-innocent character are illustrated in Figure 5.2.

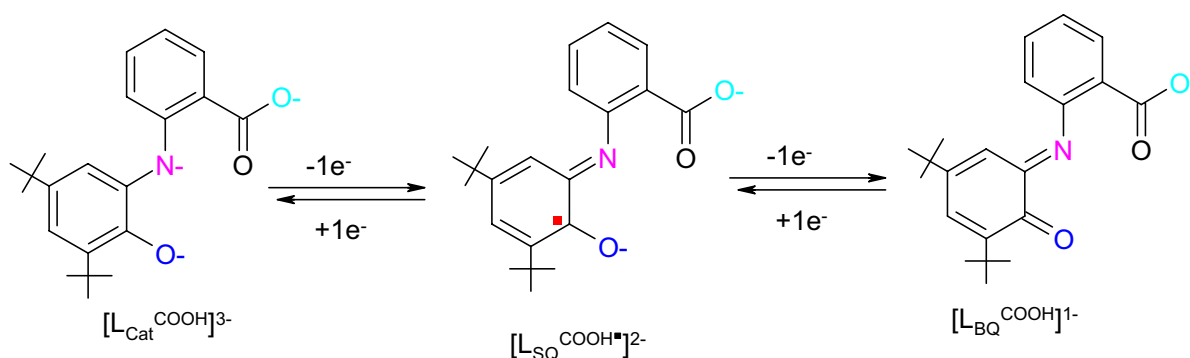


Figure 5.2. Different redox States of the fully deprotonated ligand, $[L^{COOH}]^{3-}$.

5.2 Synthesis and characterization of the complex (1)

2 mmol of $\text{Mn}^{\text{II}}(\text{acetate})_2 \cdot 4\text{H}_2\text{O}$ was dissolved in 30 ml of MeOH, and 2 mmol of $\text{H}_3\text{L}^{\text{COOH}}$ was added. To this solution 0.3 ml Et_3N was added and the mixture was stirred under air for 2 h. A Deep brown colored microcrystalline solid precipitated. Yield: 1.05 gm (63%).

The IR spectrum of complex **1** was taken as a KBr pellet. In the IR spectrum of **1** sharp and strong bands in 2950 to 2870 cm^{-1} region arise due to $-\text{C}-\text{H}$ stretches of the *tert*-butyl group. This could be taken as a preliminary indication for coordination of ligand(s) to metal. The sharp band at 1594 cm^{-1} arises due to the $-\text{C}=\text{N}$ group. The strong, sharp bands at 1574, 1255, and 1104 cm^{-1} show the existence of the ligands in the complex in both iminosemiquinone and amidophenolate forms.¹⁻⁹ ESI-positive and negative mode mass spectra in dichloromethane show molecular peaks at 102 (100%) and 735 (100%) respectively and confirm the composition $\text{C}_{42}\text{H}_{48}\text{N}_2\text{O}_6\text{Mn}$ as the negatively charged ion and $(\text{C}_2\text{H}_5)_3\text{NH}^+$ as the positively charged ion. C, H, N and Mn analysis show the composition of complex **1** is $\text{C}_{48}\text{H}_{64}\text{N}_3\text{O}_6\text{Mn}$.

Single crystals suitable for X-ray analysis were obtained from a 1:1 CH_2Cl_2 , CH_3CN solution mixture. The result of the crystallographic study shows that a manganese complex is formed in the M:L ratio 1:2. ORTEP drawing of the complex with the atom labeling scheme is shown in Figure 5.3. Selected bond lengths and bond angles are listed in Table 5.1. The geometry around the metal is six coordinate with an N_2O_4 . Each ligand acts as a meridional O,N,O donor. The MnN_2O_4 coordination sphere has a nearly perfect N_2O_2 equatorial with respect to which the two O atoms are located in trans positions. The equatorial plane is formed by O(1), N(8), O(17), N(38) all of which have bond lengths (Mn(1)-O(1), 1.881(3) Å, Mn(1)-N(8), 1.913(3) Å, Mn(1)-O(17), 1.925 Å, Mn(1)-N(38), 1.933 Å. In terms of angles with coordination sphere MnN_2O_4 is very close to an ideal octahedral geometry. The dihedral angle between the planes, N(8)-O(17)-N(38)-O(1) and O(47)-O(17)-O(31)-O(1), is 88.7°. The short metal-ligand bond lengths and highly octahedral ligand arrangement are consistent with a Mn (IV) centre with no evidence of an axial Jahn-Teller distortion, characteristic of Mn (III) ions. Thus, structurally this complex is best described as a Mn (IV) species.

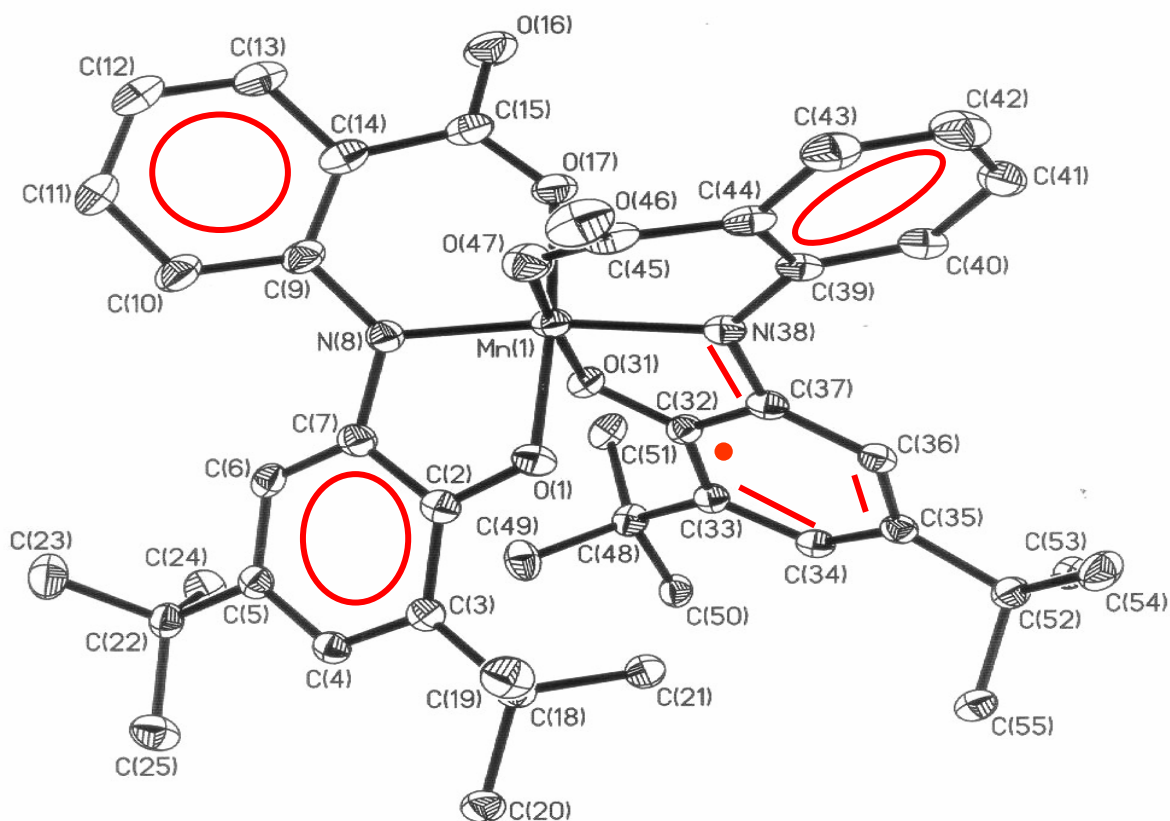


Figure 5.3. ORTEP diagram of complex 1.

Table 5.1. Selected bond lengths (Å) and angles (degree) for 1

Mn(1)-N(8)	1.913 (4)	C(4)-C(5)	1.401 (5)
Mn(1)-N(38)	1.933 (3)	C(5)-C(6)	1.381 (6)
Mn(1)-O(1)	1.881 (3)	C(6)-C(7)	1.396 (5)
Mn(1)-O(47)	1.911 (3)	C(37)-N(38)	1.378 (5)
Mn(1)-O(17)	1.925 (3)	C(39)-N(38)	1.398 (5)
C(2)-O(1)	1.336 (5)	C(32)-C(33)	1.418(5)
C(7)-N(8)	1.393 (5)	C(32)-C(37)	1.430 (6)
C(2)-C(7)	1.423 (6)	C(33)-C(34)	1.387 (5)
C(2)-C(3)	1.405 (5)	C(34)-C(35)	1.419 (6)
C(3)-C(4)	1.391 (6)	C(35)-O(36)	1.373 (5)
C(9)-N(8)	1.391 (5)	C(36)-C(37)	1.411 (6)
C(9)-C(10)	1.408 (6)	C(39)-C(40)	1.402 (6)
C(10)-C(11)	1.379 (5)	C(39)-C(44)	1.417 (6)
C(11)-C(12)	1.391 (8)	C(40)-C(41)	1.370 (6)
C(12)-C(13)	1.377 (8)	C(41)-C(42)	1.394 (7)
C(13)-C(14)	1.400 (6)	C(42)-C(43)	1.375 (7)
C(14)-C(9)	1.419 (6)	C(43)-C(44)	1.394 (6)
C(15)-O(16)	1.239 (5)	C(45)-O(46)	1.233 (5)
O(31)-C(32)	1.314 (5)		
O(1)-Mn(1)-N(17)	175.15 (13)	O(1)-Mn(1)-O(31)	87.95 (12)
O(31)-Mn(1)-O(47)	174.83 (13)	O(1)-Mn(1)-O(47)	89.99 (12)
N(8)-Mn(1)-N(38)	170.92 (14)	O(1)-Mn(1)-N(8)	83.96 (13)
N(8)-Mn(1)-O(17)	91.19 (14)	O(31)-Mn(1)-N(8)	89.90 (13)
O(1)-Mn(1)-N(38)	90.23 (13)	O(47)-Mn(1)-N(8)	94.60 (14)

The MnN_2O_4 unit is mono-negative. The cationic part is triethylammonium. There is H-bonding between the carbonyl oxygen atom of the ligand and the H-atom of the triethylammonium cation (not shown in the ORTEP diagram). The bond lengths, C(37)-N(38) (1.378(5) Å) and C(31)-C(32) (1.315(5) Å), are shorter than C(7)-N(8) (1.393(5) Å), O(1)-C(2) (1.336(5) Å). The C(37)-N(38) (1.378(5) Å) and O(31)-C(32) (1.314(5) Å) bond lengths are typical for an iminosemiquinone system. The alternating short and long C-C bond lengths (Table 1) also support the assignment of the iminosemiquinone form. On the other hand, C(7)-N(8) (1.393(5) Å) and O(1)-C(2) (1.336(5) Å) bond lengths support amidophenolate system. So, it is quite clear that among the two of the tridentate ligands (O,N,O) one is in iminosemiquinone form with 2- charge and the other is in amidophenolate form with 3- charge.

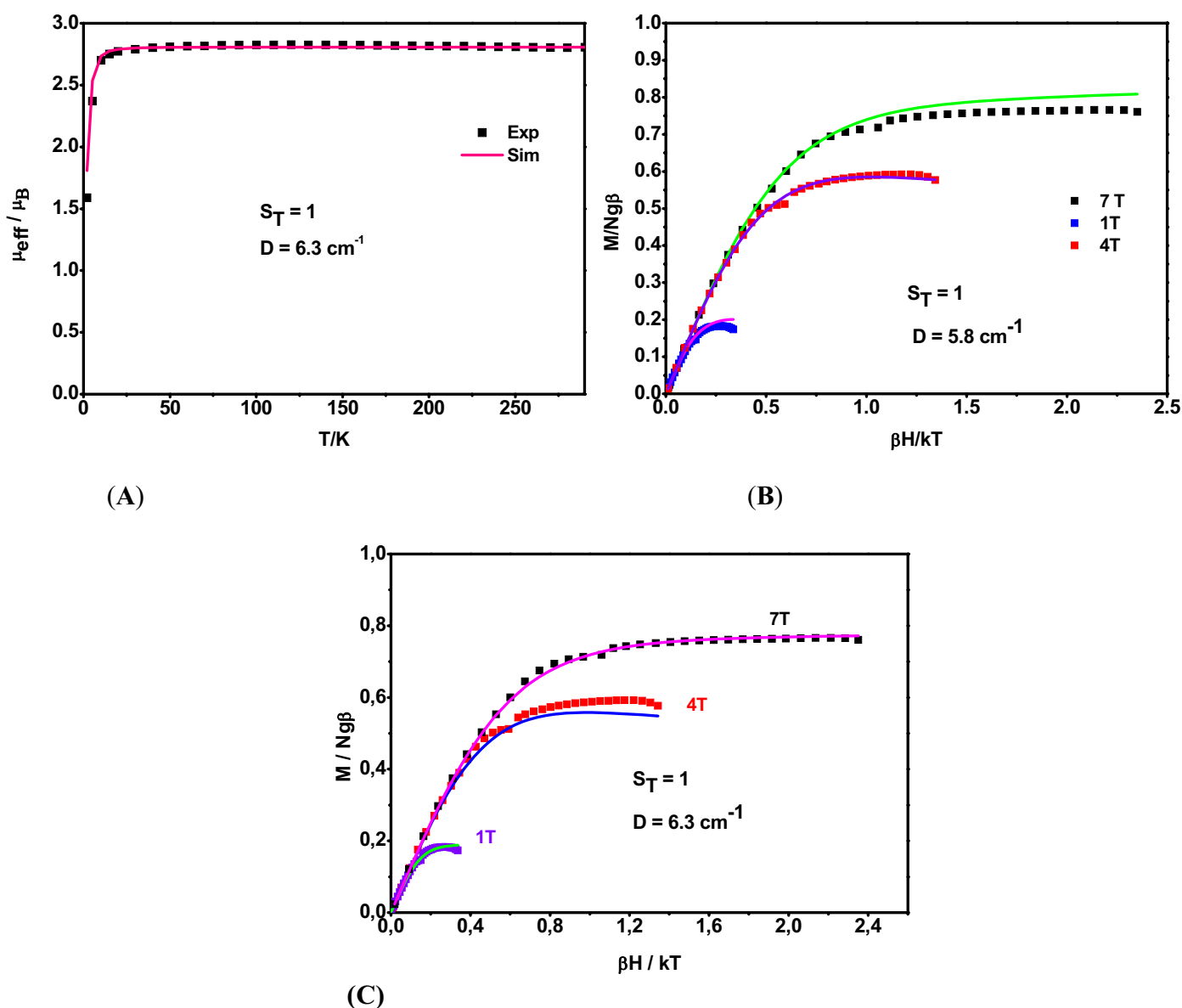


Figure 5.4. Plots of μ_{eff}/μ_B vs. T/K and magnetization measurements at 1T, 4T and 7T.

The temperature dependence of the magnetic susceptibility of **1** in the solid state was measured in the temperature range 2-290 K (Figure 5.4). The magnetic moment in temperature range 20-290 K is constant with a value of $2.82 \pm 0.03 \mu_B$. This value is indicative of an $S_t = 1$ ground state for complex **1**. As there is no change in the μ_{eff} value with increasing temperature, it can be concluded that there is no thermal population of the higher excited states within the temperature range. Complex **1** contains of two paramagnetic centres. One is Mn (IV), $S = 1.5$ and the other is a radical-anion, $S = 0.5$. The strong antiferromagnetic interaction between the two paramagnetic centres is the origin of $S_T = 1$ ground state.¹⁰⁻¹²

Temperature dependent magnetic susceptibility measured at 1 T external field as well as VTVH results were also simulated by taking $S_t = 1$ as there are no changes in μ_{eff} values in the temperature range. The parameters obtained for the simulation of the temperature dependent magnetic susceptibility measured at 1 T external field are; $g_{\text{Mn}} = 1.985$ and $D = |6.3| \text{ cm}^{-1}$. The parameters obtained for the best fit of the experimental results obtained at 7 T and 1T are; $g_{\text{Mn}} = 1.985$ and $D = |6.3| \text{ cm}^{-1}$ (Figure 5.4). It is noteworthy, that using $g_{\text{Mn}} = 1.987$, and $D = |5.8| \text{ cm}^{-1}$ the experimental result obtained at 4 T can be simulated. Hence, from the fitting parameters it can be said that the zero field splitting, D , for the system is $|6.05 \pm 0.25| \text{ cm}^{-1}$.

At room temperature the electronic spectrum of **1** in CH_2Cl_2 and $\text{ClCH}_2\text{CH}_2\text{Cl}$ solution exhibits a distinct band in the NIR range with a maximum at 945 nm. The intensity of this band depends on the concentration of **1**, being higher at higher concentrations (Figure 5.5 A) where the molar absorption coefficients $\epsilon(945)$ are plotted vs. the concentration (c) of **1**. Apparently complex **1** can form dimers in solution. It is seen, that the limiting $\epsilon(945)$ value for infinite dilution is zero and the value at high concentrations approaches a value of $\epsilon(945)_{\text{lim}} = 4.8 \times 10^3 \text{ M}^{-1} \text{ cm}^{-1}$. The fraction $\epsilon(945)/\epsilon(945)_{\text{lim}}$ should then correspond to dimeric fraction of **1** and $(1 - \epsilon(945)/\epsilon(945)_{\text{lim}})$ to the degree of dissociation, α . If the α values thus obtained are plotted vs. the concentration of **1** according to Ostwald's law of dilution, the same association constant $K_a = 4 \times 10^4 \text{ M}^{-1}$ is obtained for all concentrations and degrees of dissociations ($0.12 < \alpha < 0.85$), within the experimental error. This clearly shows that dimerisation occurs indeed.

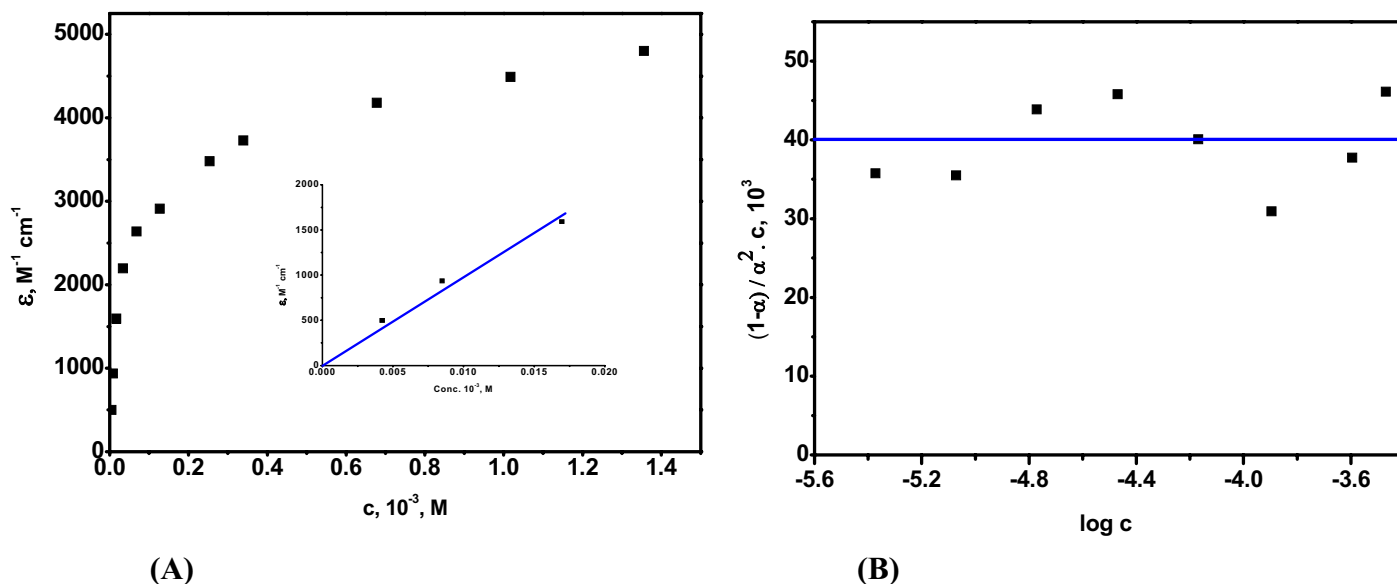


Figure 5.5. A plot of ϵ vs. concentration (left) and $(1-\alpha)/\alpha^2 C$ vs. $\log c$ (right).

The height of the band at 945 nm can also be influenced by the temperature: when the temperature is decreased, the intensity of the band increases, i.e. low temperatures favour dimerisation. The spectral changes were found to be reversible and isosbestic behaviour at 415 nm and 475 nm showed that only two species are present in the solution, which are reversibly interconverted by varying the temperature. At a concentration of **1** of 1.8×10^{-4} M the OD (945) values as a function of temperature are shown in Figure 5.6.

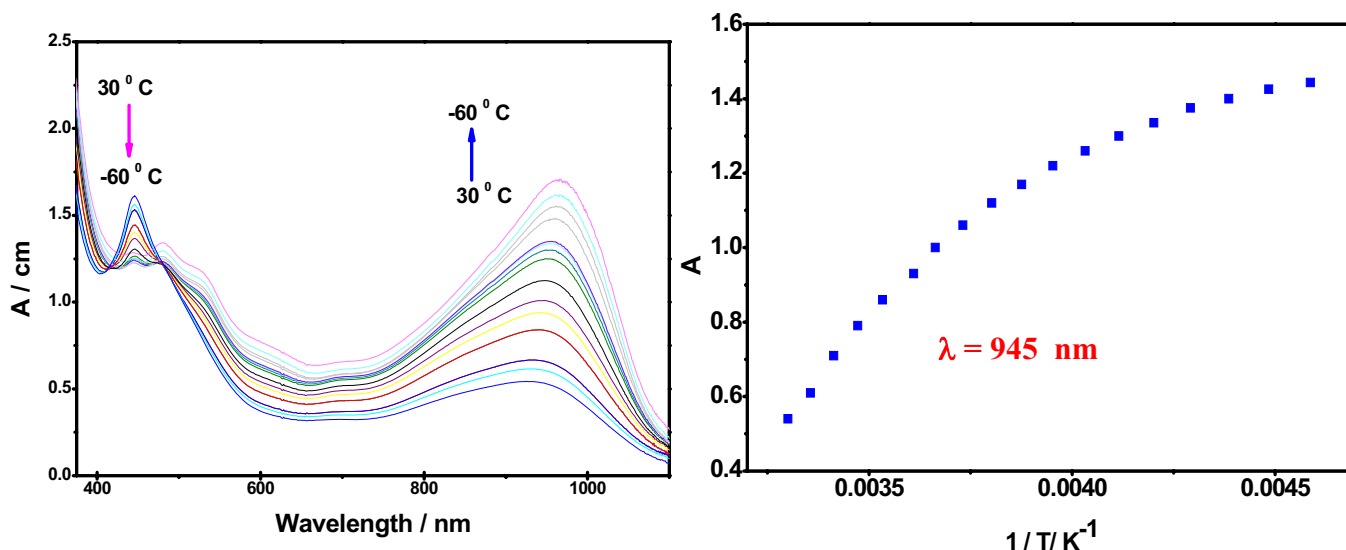


Figure 5.6. Temperature dependence of the electronic absorption spectrum of a dichloromethane solution of complex **1** (left) and absorption versus $1/T$ plot at 945 nm (right).

It is seen that in the accessible temperature range (+30 °C to -60 °C) the limiting values of the high and low temperature forms are not reached. However, the diagram suggests that the limiting OD values of the pure forms are close to zero at high temperatures and around 1.6 for low temperatures. Using these values, equilibrium constants K for the different temperatures could be calculated. If they are plotted in the form $\ln K$ vs. T^{-1} according to van't Hoff's law ($d \ln K/d T^{-1} = \Delta H/R$), a reasonable straight line is indeed obtained (Figure 5.7). The ΔH value obtained from the plot amounts to -22 kJ mol^{-1} . Using the equilibrium constant at 300 K, it is calculated that $\Delta G_{300} = +1.2 \text{ kJ mol}^{-1}$ and $\Delta S_{300} = -77 \text{ J mol}^{-1} \text{ K}^{-1}$ (from the relationships $\Delta G_{300} = RT \ln K_{300}$ and $\Delta G_{300} = \Delta H - T\Delta S_{300}$). The signs of the thermodynamic data were taken for the direction of cooling i.e. for *formation* of $([\text{Mn}^{\text{IV}}(\text{L}_{\text{cat}}^{\text{COOH}})(\text{L}_{\text{SQ}}^{\text{COOH}\bullet})])_2$.

Scheme 1

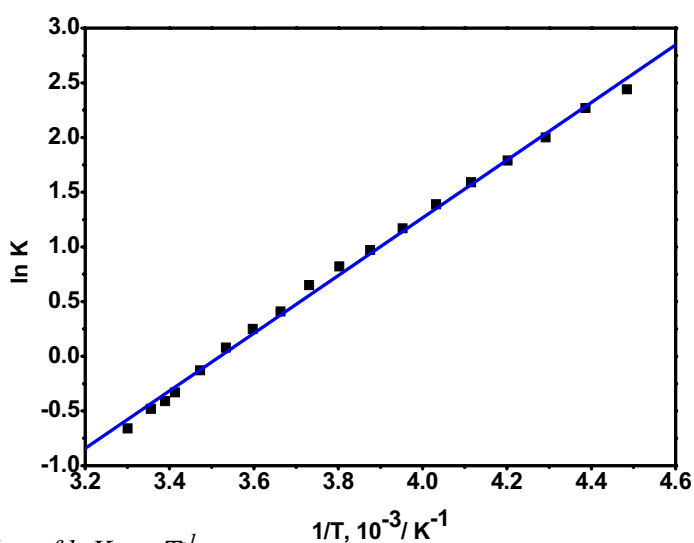
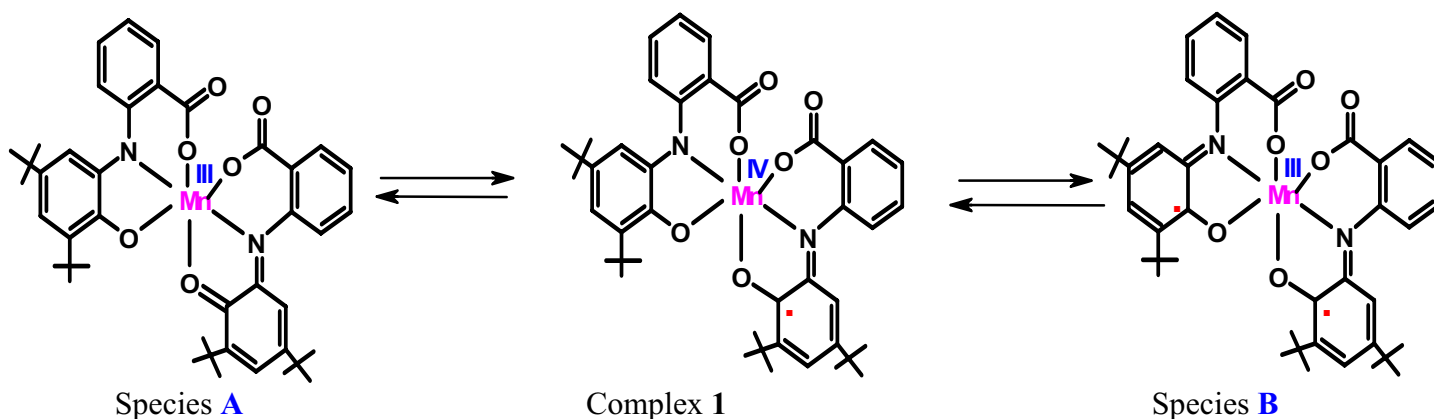


Figure 5.7. A plot of $\ln K$ vs. T^{-1} .

If the process was a valence tautomerism then the complex 1 would be in equilibrium with species A or species B as shown in Scheme 1. The stabilization of species A is quite

unlikely as it contains ligands in the strong oxidizing iminoquinone form and the strong reducing amidophenolate form. Hence, disproportionation will be the result. Moreover, entropy of the system decreases on cooling. On the other hand, if complex **1** shifts to species **A** or species **B** then entropy should increase as oxidation state of the metal decreases from +IV to either +III or +II (for 2e transfer process). Therefore, the thermodynamic data support again dimerization not valence tautomerism.¹³⁻²⁸

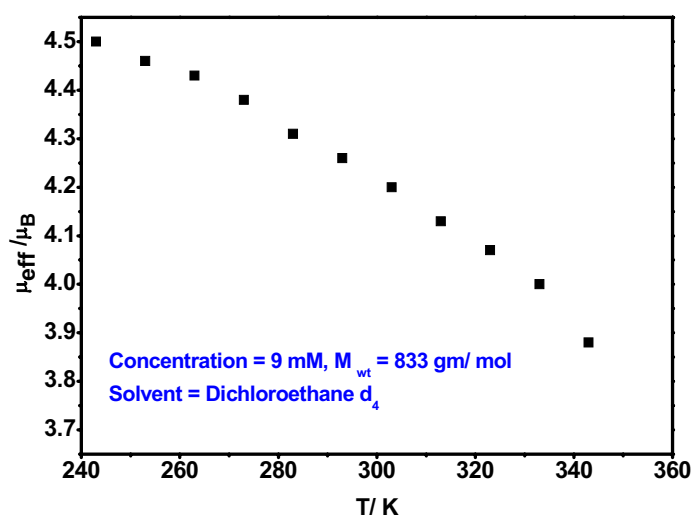
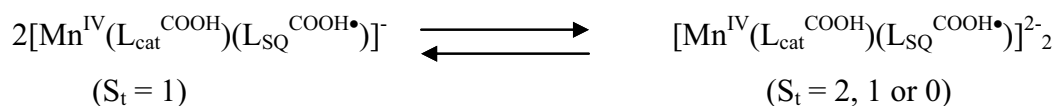


Figure 5.8. Change in μ_{eff} with temperature.

Further support for the formation of dimer on cooling the solution was obtained by ^1H NMR ($\text{ClCD}_2\text{CD}_2\text{Cl}$) spectra measured in the temperature range $+70\text{ }^\circ\text{C}$ to $-40\text{ }^\circ\text{C}$. The monomeric form has an $S_t = 1$ ground state whereas the dimeric form could have $S_t = 2$, 0 or two degenerate $S_t = 1$ ground states. Figure 5.8 shows μ_{eff} vs. T plot. The μ_{eff} values were calculated using Evan's method.²⁹ At $-40\text{ }^\circ\text{C}$ μ_{eff} of the 9 mM $\text{ClCD}_2\text{CD}_2\text{Cl}$ solution of **1** is $4.5\ \mu_{\text{B}}$. On increasing the temperature of the solution μ_{eff} value decreases gradually and reaches to $3.82\ \mu_{\text{B}}$ at $+70\text{ }^\circ\text{C}$. The decrease in μ_{eff} value with increase in temperature of the solution indicates dissociation of the dimeric species to monomeric species and at $+70\text{ }^\circ\text{C}$ both dimeric and monomeric species exist in the solution. Measurements of ^1H NMR spectra above $+70\text{ }^\circ\text{C}$ were not possible as the complex decomposed above the temperature.

5.3 Catalytic reactivities,

5.3.1 Aerial oxidation of primary amines; mimicking the function of Amine Oxidases (AO_s)

Copper-containing amine oxidases (AO_s) play a crucial role in metabolic oxidative deamination of primary amines to the corresponding aldehydes, with the concomitant production of hydrogen peroxide and ammonia (eq 1).³⁰



The reaction mechanism for the oxidative deamination reaction is not yet understood. It is evident that the reaction proceeds through a transamination mechanism mediated by the active site, 2,4,5-trihydroxy-phenylalanine quinone (TPQ), a organic cofactor.

To mimic the function of amine oxidases complex **1** has been used. Employment of primary amines with two α -H atoms, like benzyl amine, ethylenediamine, 2-aminoethanol, etc, provides the corresponding Schiff base or aldehyde product. No oxidation of secondary amines or amines with one α -H atom was found. Three primary amines, ethylenediamine, 2-aminoethanol, benzyl amine were introduced as substrates for the catalytic oxidative deamination reaction. Employment of ethylenediamine provides glyoxal as product, which was identified by GC, GC-MS after formation of the corresponding Schiff base products with 2,4-dinitrophenylhydrazine (DNPH) and 3-methyl-2-benzothiazolene hydrazine hydrochloride. The percent of yield 35 was determined by spectrophotometric methods using the standard reagent, 3-methyl-2-benzothiazolene hydrazine hydrochloride.³¹ Glyoxal and 2-hydroxy-acetaldehyde in a 2:1 ratio were identified by GC, GC-MS as Schiff base products with DNPH and 3-methyl-2-benzothiazolene hydrazine hydrochloride, when 2-aminoethanol was used as a substrate. After 15 hours there was no more conversion and the final percent of yields, 54 and 27 for glyoxal and 2-hydroxy-acetaldehyde were determined by spectrophotometric methods taking the total absorption as the sum of absorptions of the species ($A_t = A_{\text{glyoxal}} + A_{\text{2-hydroxy-acetaldehyde}}$, $\epsilon_{\text{glyoxal}} = 28000 \text{ M}^{-1}\text{cm}^{-1}$ and $\epsilon_{\text{2-hydroxy-acetaldehyde}} = 51000 \text{ M}^{-1}\text{cm}^{-1}$). When catalytic amount of complex **1** (10^{-5} mole) was introduced for the aerial oxidation of a large excess of benzyl amine (10^{-3} mole), 20 % of benzyldinebenzylamine was detected by GC using ⁿhexadecane as an internal standard in 6 hours. No more conversion was noted after 6 hours. This is because of the decomposition of

complex **1** after that period. Though decomposition of hydrogen peroxide occurred due to the catalyse activity of the manganese complex at room temperature, hydrogen peroxide is detected at $-25\text{ }^{\circ}\text{C}$. Ammonia was detected qualitatively. The kinetics for this catalytic reaction were studied by varying the total concentration of benzyl amine (10^{-2} to 2.5×10^{-6} mole) keeping the concentration of complex **1** as constant and vice versa. The rate law as deduced from the experimental data is,

$$\text{Rate} = k [\text{Amine}][\text{Complex}]$$

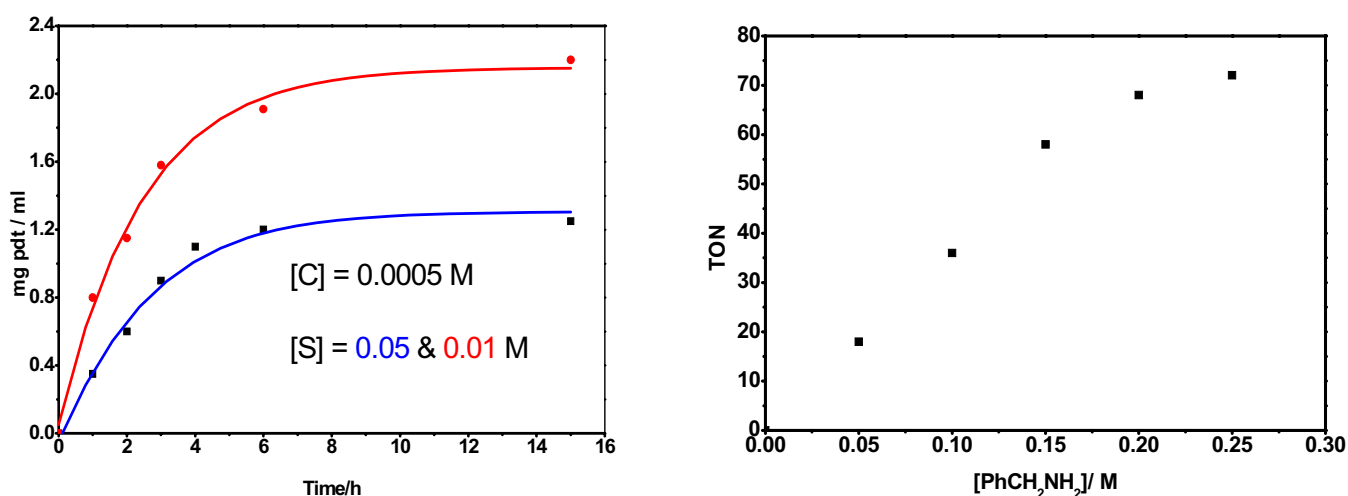
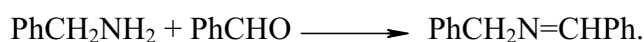


Figure 5.10. Kinetic data for the aerial oxidation of benzyl amine.

The maximum TON (the ratio between the concentration of product and catalyst) that has been achieved for the above catalytic process is 72 and shown in Figure 5.10. With the selected deuterated substrate at the α -C atom, PhCD_2NH_2 ,³² a kinetic isotope effect ($\text{KIE} = k_{\text{H}}/k_{\text{D}}$) of about 1 was evaluated and depicted in Figure 5.11. This indicates clearly that the H-atom abstraction from the α -C atom of the substrate is not the rate-determining step for the catalysis. The rate determining step could be;

- (i) One of the two steps for the formation of Schiff base, benzyldinebenzylamine,



or

- (ii) The formation of H-bond between the substrate and catalyst.

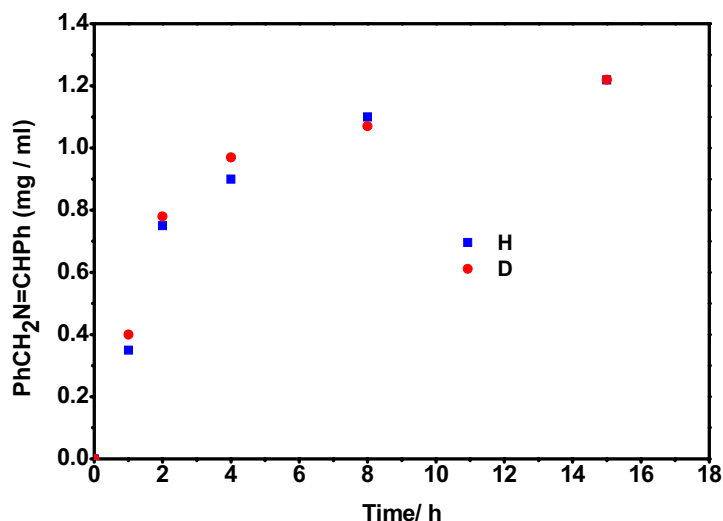


Figure 5.11. Kinetic isotope effect for the aerial oxidation of benzyl amine.

When 12.5 equivalent of benzyl amine was allowed to react with 1 equivalent of complex 1 under anaerobic condition, about 1.5 equivalent benzylidenebenzylamine was found to form by GC analysis. The X-band EPR spectrum at 10 K and UV-VIS/NIR spectrum at RT of the solution were measured and depicted in Figure 5.12. The X-band EPR spectrum shows a signal indicative of a Mn(II) species with six major hyperfine lines centered around $g = 2$ which originate from the hyperfine splitting of the central transition $M_s = 1/2$ to $M_s = -1/2$ of $S = 5/2$ paramagnet with $I = 5/2$ of the ^{55}Mn nucleus. From the simulation of the EPR spectrum the following parameters are obtained; $g_x = g_y = g_z = 2.0$, $A_x = A_z = 95 \times 10^{-4} \text{ cm}^{-1}$, $A_y = 85 \times 10^{-4} \text{ cm}^{-1}$, $|D| = 200 \times 10^{-4} \text{ cm}^{-1}$ and $E/D = 0.06$.

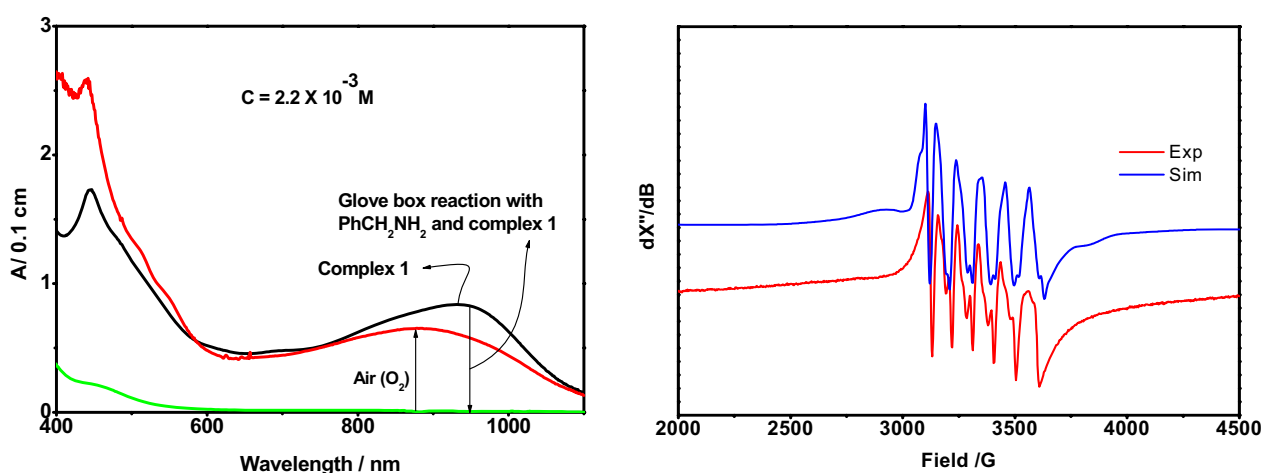


Figure 5.12. Change in UV-VIS/NIR spectrum during stoichiometric-type reaction under Ar-atmosphere (left) and X-band EPR spectrum at 10K of the solution obtained after Glove-box reaction (right).

Hence, from the X-band EPR spectrum it is quite clear that the Mn(IV) center has been converted to Mn(II) in presence of benzyl amine under anaerobic condition. The UV-VIS/NIR spectrum shows clearly that there is no absorption band at around 930 nm that was present in complex **1**. This band may be assigned to the intervalence ligand-to-ligand charge transfer band (between iminosemiquinone and amidophenolate forms of the ligand).¹² The absence of that charge transfer band in the presence of substrate under anaerobic conditions is an indication that the radical involved in the catalysis and iminosemiquinone form of the ligand has been reduced to its amidophenolate form. When the solution was exposed to air the absorption spectrum feature changes and shows the regeneration of radical containing species by reproducing the band at around 930 nm.

From the above experiments a mechanism for the formation of benzilidenebenzylamine can be proposed as shown in Figure 5.13.

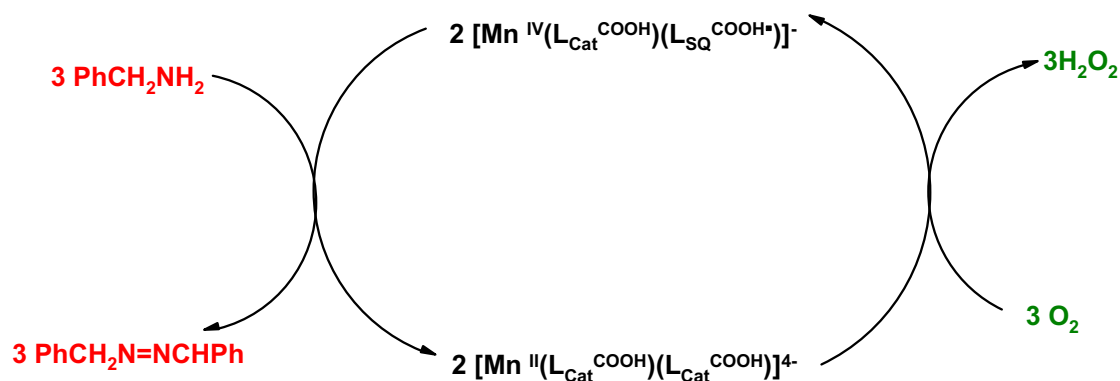
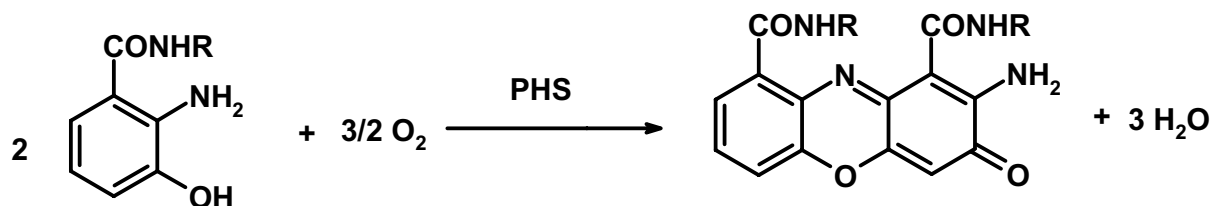


Figure 5.13. The proposed mechanism for the catalytic oxidation of benzyl amine.

5.3.2 Aerial oxidation of 2-aminophenol; mimicking the function of Phenoxazinone Synthase (PHS)

Actinomycin D is a member of an interesting class of natural products in which the yellow-red 2-aminophenoxazinone chromophore is linked to two cyclic pentapeptides.³³ These compounds are among the most potent antineoplastic agents known.³³

The biosynthesis of actinomycin D involves the conversion of tryptophane to 3-hydroxy-anthanic acid in a multistep sequence.³³ The pentapeptide lactone is then attached and resulting 2-aminophenol undergoes a 6-electron oxidative coupling to form actinomycin D. The latter reaction is catalyzed by Phenoxazinone Synthase (PHS), a multicopper containing metalloenzyme.



This enzyme has been isolated from *Streptomyces antibioticus*. It has a subunit molecular weight of 88 Kda and in its native form is a mixture of oligomers, with the dimer and the hexamer predominating.³⁵⁻³⁶ The crystal structure of the enzyme has been described in Chapter 1.

When complex **1** was used as a catalyst for the oxidation of 2-aminophenol to 2-aminophenoxazine-3-one by aerial oxygen at room temperature (RT) in methanol or a 1:1 dichloromethane, methanol solvent mixture 84% conversion of 2-aminophenol to 2-aminophenoxazine-3-one was found within 2 hours. The reaction was monitored by spectrophotometric methods ($\epsilon = 24000 \text{ M}^{-1} \text{ cm}^{-1}$ at 435 nm) at 435 nm (Figure 5.14).

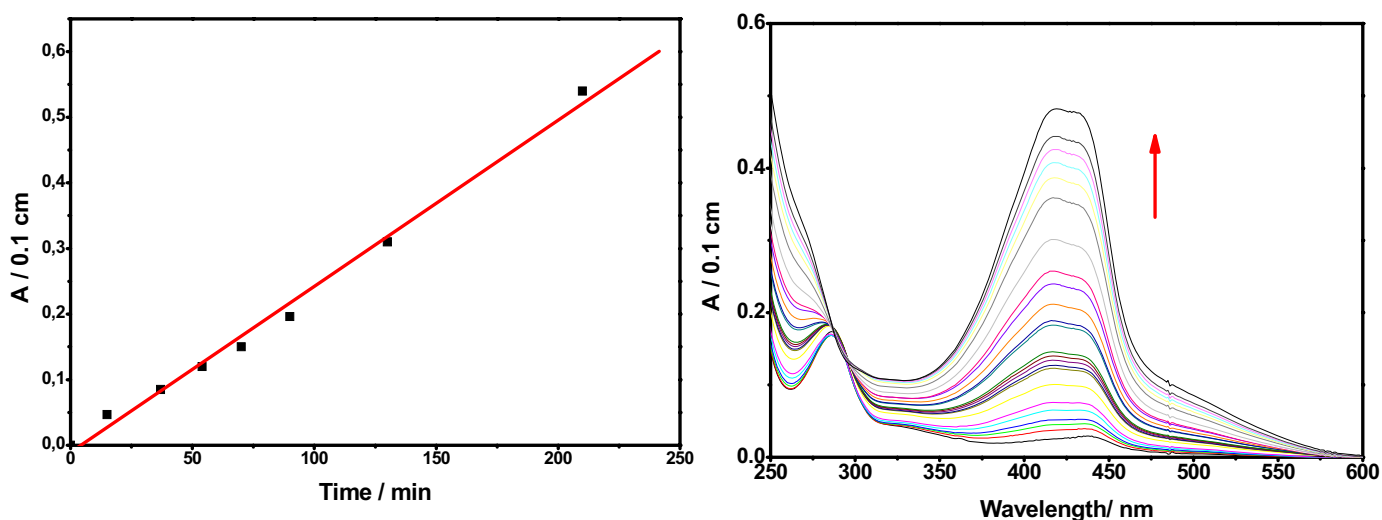


Figure 5.14. Formation of phenoxazinone chromophore with time.

Moreover, after 2 hours of the catalytic reaction, the solvent was removed and the solid was examined by mass spectrometry. The mass spectrum shows a peak that has a composition similar to the 2-aminophenoxazine-3-one compound.³⁵⁻³⁶ GC and GC-MS analysis was performed after passing the solution through a neutral Al_2O_3 column (0.5 gm neutral Al_2O_3 was taken) in order to find out the number of products, percent of yield and the composition. GC and GC-MS results showed the formation of 2-aminophenoxazine-3-one by aerial oxidation of 2-aminophenol as a sole product with a composition of $\text{C}_{12}\text{H}_8\text{N}_2\text{O}_2$.

To find out the rate equation of the above stated catalytic reaction the concentration of the substrate, i.e. 2-aminophenol, was varied keeping the concentration of complex 1 constant and vice versa. The rate law that has been deduced from the experimental results (Figure 5.15) is shown below;

$$\text{Rate} = k [\text{2-Aminophenol}][\text{Complex 1}]$$

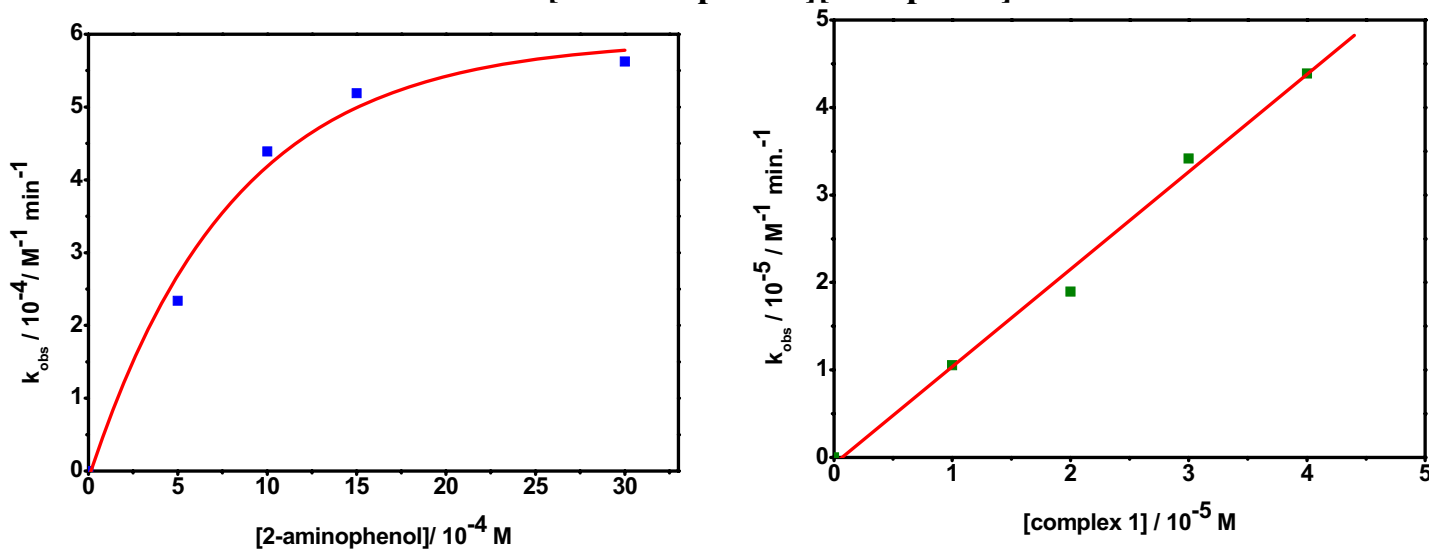
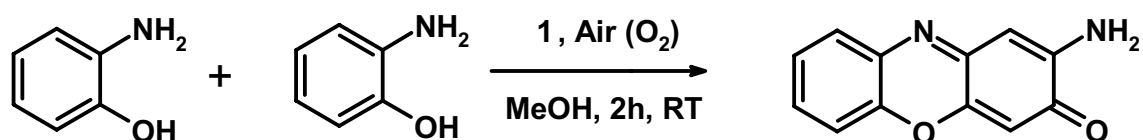


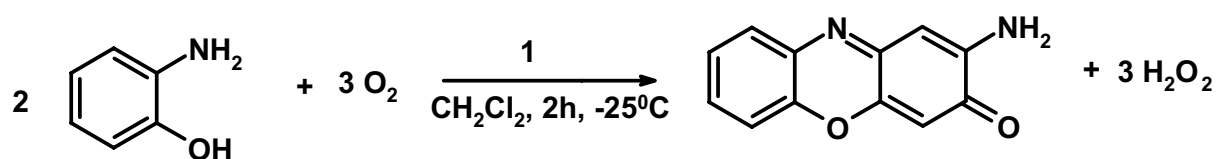
Figure 5.15. Kinetic data for aerial oxidation of 2-aminophenol.

Catalase activity by manganese complexes is quite common. Complex **1** is not exceptional as confirmed by allowing methanolic solution of the complex to react with 30% H_2O_2 . Moreover, in the aerial oxidation of 2-aminophenol by catalytic activity of the complex **1** no H_2O_2 was detected using TiO^{2+} in 9 M H_2SO_4 .

Oxygen uptake measurements using complex **1** as catalyst at 25°C and -25°C were carried out using a gas-burette method until saturation of O_2 uptake occurred. At 25°C , there is very small amount of oxygen up taken by the system. This is probably due to the decomposition of hydrogen peroxide due to the catalase activity of complex **1**. Moreover, no hydrogen peroxide is detected using TiO^{2+} . Hence, from the above experiments, it can be proposed that the oxidation process at room temperature follows the following equation;



When the reaction was monitored at -25°C in a 39:1 dichloromethane, methanol solvent mixture the volume of oxygen up taken by the system increased with time linearly and then saturation appeared. The volume of O_2 is up taken by the system at -25°C vs. time plot is illustrated in Figure 5.14. Extraction of the solution into water and addition of TiO^{2+} in 9 M H_2SO_4 produced yellow color and the UV-VIS spectrum (Figure 5.16) confirmed the formation of H_2O_2 during the catalysis. The concentration of hydrogen peroxide as determined by spectrophotometric method ($\lambda = 415 \text{ nm}$ $\epsilon = 675 \text{ M}^{-1} \text{ cm}^{-1}$) is approximately 3/2 times to concentration of the substrate and is same to the amount of oxygen up taken by the system. Hence, the stoichiometry at -25°C was found to follow the equation;



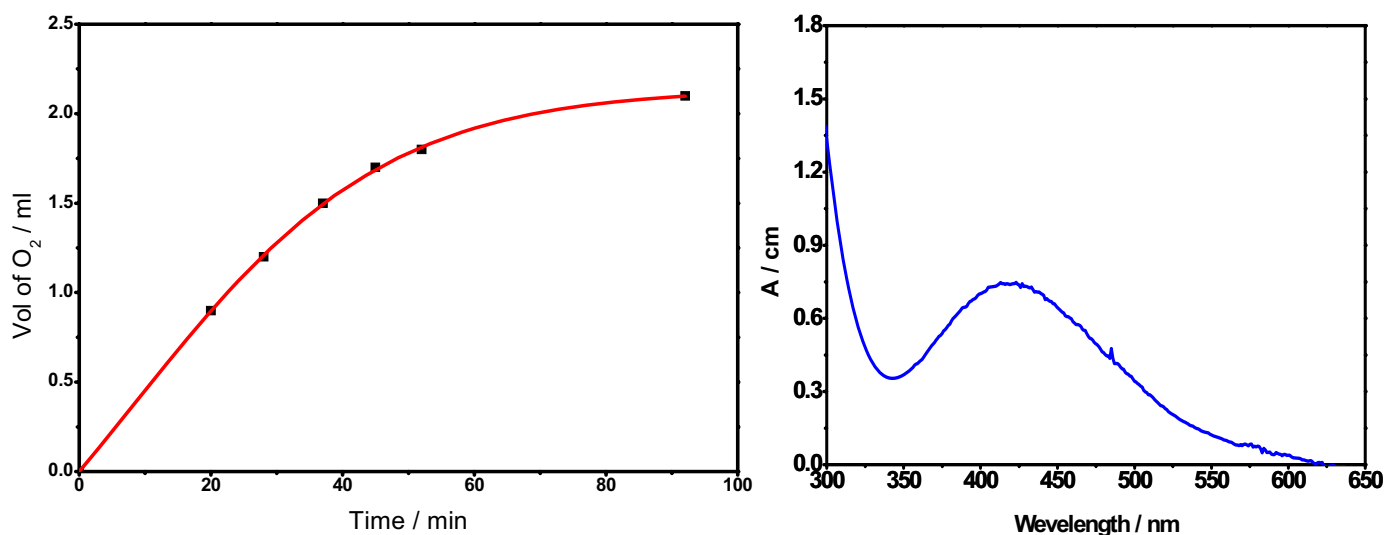


Figure 5.16. Vol of O_2 /ml vs time plot (left) and measurement of conc. of H_2O_2 using TiO^{2+} in $9M H_2SO_4$.

When 1 equivalent of **1** was allowed to react with approximately 10 equivalent of 2-aminophenol under an argon atmosphere at room temperature in MeOH for 2 h, 0.5 equivalent of phenoxazinone chromophore to the concentration of complex **1** was found to form spectrophotometrically at 435 nm. The X-band EPR spectrum feature of the solution at 10 K is same as shown in Figure 5.12, *i.e.* the formation of Mn(II) species. Exposure of the solution to air increases the concentration of phenoxazinone chromophore. Hence, the process is an aerial oxidation process. A few functional model complexes are known to catalyze the oxidation reaction in the literature.³⁷⁻³⁸ This is the first example where aerial oxidation of 2-aminophenol to phenoxazinone chromophore takes place catalytically by complex **1**. A mechanism can be proposed from the above experimental results as shown in Figure 5.17.

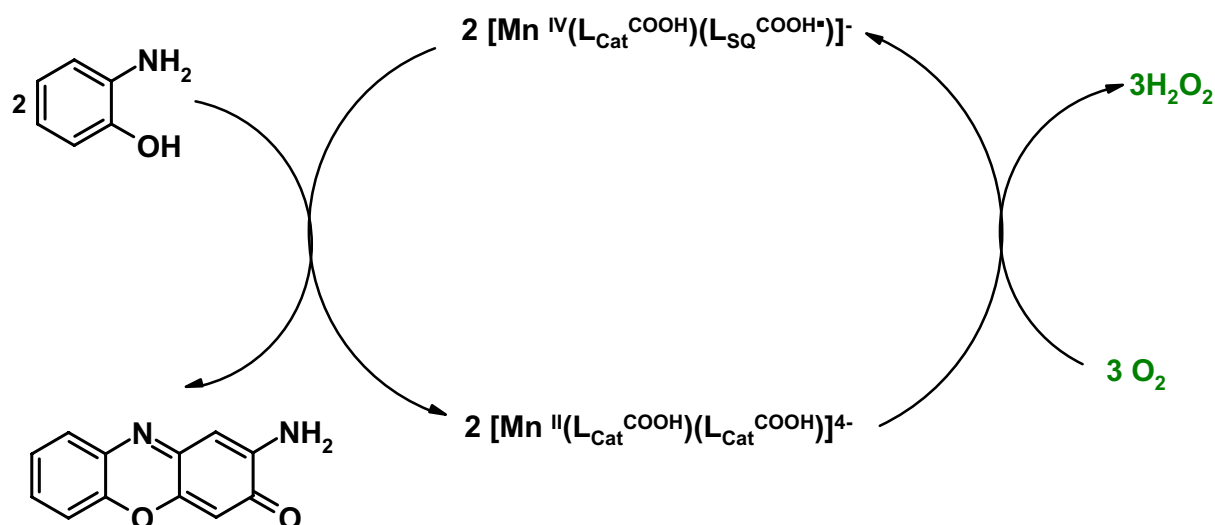


Figure 5.17. The proposed mechanism for the formation of phenoxazinone chromophore.

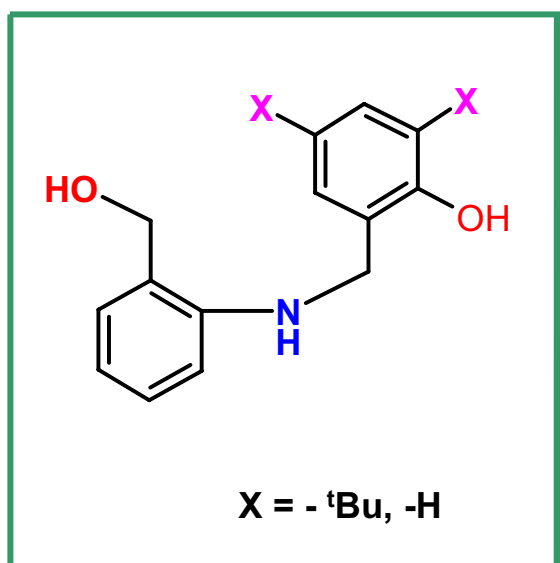
5.4 References

1. Larsen, S. K.; Pierpont, C. G.; DeMunno, G.; Dolcetti, G. *Inorg. Chem.* **1986**, *25*, 4828.
2. Lynch, M. W.; Valentine, M.; Hendrickson, D. N. *J. Am. Chem. Soc.* **1982**, *102*, 6982.
3. Chang, H.-C.; Ishii, T.; Kondo, M.; Kitagawa, S. *J. Chem. Soc., Dalton Trans.* **1999**, 2467.
4. Chang, H.-C.; Kitagawa, S. *Angew. Chem., Int. Ed.* **2002**, *41*, 130.
5. Chang, H.-C.; Kitagawa, S. *Angew. Chem., Int. Ed.* **2002**, *41*, 4444.
6. Cadore, O.; Chabre, F.; Dei, A.; Sangregorio, C.; Van Slageren, J.; Vaz, M. G. F. *Inorg. Chem.* **2003**, *42*, 6432.
7. Lynch, M. W.; Hendrickson, D. N.; Fitzgerald, B. J.; Pierpont, C. G. *J. Am. Chem. Soc.* **1984**, *106*, 2041.
8. Larsen, S. K.; Pierpont, C. G. *J. Am. Chem. Soc.* **1988**, *110*, 1827.
9. Lynch, M. W.; Valentine, M.; Hendrickson, D. N. *J. Am. Chem. Soc.* **1982**, *104*, 6982.
10. Chun, H.; Verani, C. N.; Chaudhuri, P.; Bothe, E.; Bill, E.; Weyhermüller, T.; Wieghardt, K. *Inorg. Chem.* **2001**, *40*, 4157.
11. Mukherjee, S.; Weyhermüller, T.; Bothe, E.; Wieghardt, K.; Chaudhuri, P.; *J. Chem. Soc., Dalton Trans.* **2004**, 3842.
12. Chun, P.; Chaudhuri, P.; Weyhermüller, T.; Wieghardt, K. *Inorg. Chem.* **2002**, *41*, 790.
13. Kahn, O.; Launay, J. P. *Chemtronics*, **1988**, *3*, 140.
14. Day, P. *Int. Rev. Phys. Chem.* **1981**, *1*, 149.
15. Creutz, C. *Prog. Inorg. Chem.* **1983**, *30*, 1.
16. Richardson, D. E.; Taube, H. *Coord. Chem. Rev.* **1984**, *60*, 107.
17. Prassidis, K. (Ed.) *Mixed Valency Systems: Applications in Chemistry, Physics, and Biology*; NATO ASI Series C343; Kluwer Academic Publishers: Dordrecht, The Netherlands, **1991**.
18. Gütlich, P. *Struct. Bonding*, **1981**, *44*, 83.
19. König, E. *Progr. Inorg. Chem.* **1987**, *35*, 527.
20. Beattie, J. K. *Adv. Inorg. Chem.* **1988**, *32*, 1.
21. Toftlund, H. *Coord. Chem.* **1989**, *94*, 67.
22. Gütlich, P.; Hauser, A.; Spiering, H. *Angew. Chem., Int. Ed. Engl.* **1994**, *33*, 2024.
23. Kahn, O.; Martinez, C. J. *Science*, **1998**, *279*, 44.
24. Pierpont, C. G.; Lange, C. W. *Prog. Coord. Chem.* **1993**, *41*, 381.

25. Adams, D. M.; Dei, A.; Rheingold, A. L.; Hendrickson, D. N. *J. Am. Chem. Soc.* **1993**, *115*, 8221.
26. Gütllich, P.; Dei, A. *Angew. Chem., Int. Ed. Engl.* **1997**, *36*, 2734.
27. Hendrickson, D. N.; Adams, D. M.; Wu, C.-C.; Aubin, S. M. J. *A Supramolecular Function*; Kahn, O., Ed.; NATO ASI Series C484; Kluwer Academic Publishers: Dordrecht, The Netherlands, **1996**, p 357.
28. Dei, A.; Gatteschi, D.; Sangregorio, C.; Sorace, L. *Acc. Chem. Res.*, *37* (11), **2004**, 827.
29. Evans, D. F. *J. Chem. Soc.* **1959**, 2003.
30. Janes, S. M.; Mu, D.; Wemmer, D.; Smith, A. J.; Kaur, S.; Maltby, D.; Burlingame, A. L.; Klinman, J. P. *Science*, **1990**, *248*, 981.
31. E. Sawicki, T. R.; Hauser, T.; Stanley, W.; Elbert, W. *Anal. Chem.* *33*. No 1. 1961, 93.
32. Edward, A.; Wintner, A.; Belinda, T.; Rebek, J. Jr. *J. Org. Chem.* **1995**, *60*, 7997.
33. Hollstein. U. *Chem. Rev.* **1974**, *74*, 625.
34. Barry, C.E., Nayar, P.G., and Begley, T.P. *Biochemistry*, **1989**, *28*, 6323.
35. Smith, A.W., Camara-Artigas, A., Olea, C. Jr., Francisco, W.A., and Allen, J.P. *Acta Cryst.* **2004**. D *60*, 1453.
36. Barry, C.E., Nayar, P.G., and Begley, T.P. *J. Am. Chem. Soc.* **1988**. *110*, 3333.
37. Simandi, T.M.; Simandi, L.I.; Gyor, M.; Rockenbauer, A.; Gomory, A. *J. Chem. Soc., Dalton Trans.*, **2004**, 1056 and there in.
38. Horváth, T.; Kaiser, J.; Speier, G. *Journal of molecular catalysis A: Chemical.* **2004**, *215*, 9.

Chapter 6

Conclusions and Perspectives



6.1 Conclusions

The main aim of this work was to synthesize of radical-containing transition metal complexes which are relevant as functional and structural model of some metalloenzymes. Use of these structural and functional model complexes can bring new information regarding the active site(s) of the metalloenzymes. Moreover, radical-containing transition metal complexes can be used as catalysts for aerial oxidation of some small organic molecules, hence, invention of new systems as oxidants and utilization of bioinspired catalytic processes.

A few non-innocent ligands symbolically, H_4L , H_2L^x , $H_3L^{CH_2OH}$, and, H_3L^{COOH} , were synthesized and used to prepare radical-containing transition metal complexes. The conclusions that have been drawn from the structural, spectroscopic studies and catalytic reactivities of the complexes are summarized below.

Chapter 1.

1. A monoradical-containing pentacoordinate high-spin Fe(III) complex has been synthesized and characterized by X-ray crystallography, magnetic, spectro and spectroelectrochemical methods. The complex has $S_T = 2$ ground state with $\mu_{\text{eff}} = 4.92 \mu_B$, that remains constant in 4-290 K temperature range. This feature leads to the conclusion that there is strong antiferromagnetic coupling between the Fe(III) center and radical anion.
2. Oxovanadium complexes are common and well studied but non-oxovanadium or “bare” vanadium complexes are very rare. Due to biological relevance, non-oxovanadium vanadium complexes are important. A dinuclear methoxide bridged non-oxovanadium(V) complex has been synthesized and characterized. VO^{2+} and VO_2^+ ions do not have intense metal-to-ligand charge transfer bands. Moreover, vanadium-containing metalloenzymes, Bromoperoxidases, and tyrosinate proteins Transferrin do not show any strong absorption band in 600 nm region, whereas the complex shows an intense metal-to-ligand charge transfer band in the UV-VIS region. This information can be used to determine that vanadium(IV) and vanadium(V) must both be bound to the tyrosinate proteins Transferrin and Bromoperoxidases, as the VO^{2+} and VO_2^+ forms and tyrosine may not be a ligand to the vanadium in the Bromoperoxidases, or the active site vanadium may be in the form of the pervanadyl moiety rather

than bare vanadium(V) or VO^{3+} . Hence, complex **1** can be used as marker to assign the active site of tyrosinate proteins Transferrin and bromoperoxidases.

3. Two distorted square planar complexes, Ni(II) and Pd(II), have been synthesized and characterized via. IR, mass, X-ray crystallography, magnetism, NMR, spectro and spectroelectrochemically. It shown that the lower energy ligand-to-ligand charge transfer band around 970 nm for both complex **3** and **4** has similar absorption coefficient to the reported complexes but appear at lower energy compared to that complexes (Table 2.5). This feature leads to the fact that the symmetry of the orbitals involved for the charge transfer is same as previously reported (ref 51-53) but the energy difference between two orbitals are presumably lower in energy in this case. It is also shown that the geometry around the metal ion affects the delocalization of the π radical through the whole molecule and therefore, shows more destabilized monoanionic or monocationic species than that of the reported square planar complexes.⁵⁰⁻⁵²
4. A distorted square planar copper (II) complex having N2O2 environment has been synthesized. A high quality X-ray crystal structure, measured at 100(2) K and various spectroscopic methods have proved unambiguously that complex **5** contains two π radicals coordinated to the central copper (II) ion. When complex **5** was used as a functional model for Galactose Oxidase, to oxidize primary alcohol, benzyl alcohol, it has been found that **5** can oxidize benzyl alcohol to a two electron oxidised product, benzaldehyde, with a good TON (65). Hence, biradical-containing copper (II) complex with N2O2 not only behaves as structural model but also as functional model for Galactose Oxidase.

Chapter 2.

1. Biradical-containing Cu(II) complexes with N2O2 coordination sites and different substituents at the different positions of the N-phenyl ring have been synthesized and characterized viz. X-ray crystallography and various spectroscopic methods. Distortion from the square planar geometry has been found for $-\text{CF}_3$ substituted complexes. Zero degree dihedral angle between two coordination

planes to Cu(II) ion for complex with ^tBu substituent at 3,5 positions of the N-phenyl ring emphasizes that the distortion around the Cu(II) ion is an electronic effect instead of steric effect. Primary alcohols like benzyl alcohol, ethanol, and, methanol, can be oxidized to their corresponding aldehydes using the biradical-containing Cu(II) complexes. All the complexes are equally efficient for oxidising benzyl alcohol to benzaldehyde but for ethanol and methanol respective 75% and 78% yield have been achieved using complex **1** in 25:1 substrate: complex ratio. Kinetics and methanistic studies shows that the complexes can be considered as functional as well as structural models for Galactose Oxidase.

Chapter 3.

1. A valence-trapped trinuclear manganese complex has been synthesized and characterized. Complex **2** is the first example of discrete trinuclear manganese ions in three different oxidation states Mn^{III}, Mn^{II}, Mn^{IV} and iminosemiquinone, iminoquinone, amidophenolate and chloride ligands. Moreover, it has been shown from the magnetic susceptibility and magnetization measurements that the exchange coupling between the Mn^{III} and Mn^{II} is ferromagnetic whereas that for Mn^{II} and Mn^{IV} is antiferromagnetic.
2. A tetradical-containing Cu₄O₄ cubane core crystal structure of a new tridented non-innocent ligand containing amino, alkoxo and phenoxo functionalities has been shown. This is the first example of a tetradical-containing Cu₄O₄ cubane core. The unique magnetic properties have been discussed. These results give further investigation of metal-metal and metal-radical (ligand) interactions and insights into the design and synthesis of polynuclear complex with new structure and magnetic properties. Moreover, this cubane core can be used as a functional model for Phenoxazinone synthase.

Chapter 4.

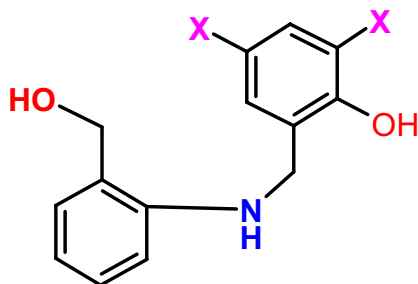
1. Monoradical-containing Mn(IV) complex can be used as a functional model for Amine Oxidases and Phenoxazinone Synthase. Variable temperature UV-VIS/NIR spectra in CH₂Cl₂ solution of **1** show that the complex can exhibit valence tautomerism in solution.

6.2 Perspectives

1. Addition of H₄L ligand to VOSO₄·5H₂O in methanol produces “non-oxo” dinuclearvanadium(V) complex. This above reaction can be carried out in the presence of PPh₃ to find out if during reaction the complex acts as an oxo-transferring agent or not.
2. Titanium and Chromium complexes with the H₄L ligand can be synthesized and their coordination chemistry can be studied.
3. Pentacoordinated square pyramidal iron, cobalt and manganese complexes can be utilized as starting materials to synthesize similar types of complexes by varying the nature of the ligand situated at the axial position. These complexes can be useful to synthesize high-spin, intermediate-spin or low spin complexes. Iron and manganese complexes can be used as catalysts for the catalytic epoxide formation from the corresponding ene compounds.
4. Theoretical calculation can be performed to find out the molecular energy levels in the distorted square planar Cu(II), Ni(II) and Pd(II) complexes formed with the H₄L ligand and the bands appeared in the UV-VIS/NIR spectrum of those complexes can be assigned unambiguously.
5. Theoretical calculations can be performed to find out the effect of substituents to the 3, 5-positions of the N-phenyl group to the geometry of the Cu(II) complexes formed with the H₂L^X ligand.
6. Having strong π-donation capability of the ligand, H₃L^{CH₂OH}, forms polynuclear complexes. Cobalt, chromium, titanium and other transition metals can be used to synthesize polynuclear complexes and their coordination chemistry can be studied as polynuclear complexes are useful in the study of metal-ligand interactions and functional model for metalloenzymes.
7. [V₂O₂(L^{CH₂OH})₂]⁰ Complex can be oxidized and reduced chemically and all these species can be isolated and their coordination chemistry can be studied. Racal-containing vanadium complexes are rare hence, the radical containing vanadium complex is of significant interest. Moreover, the complex can be examined as a drug for antiameobic effect and its activity towards insulin can be examined.
8. ⁿBu₄N[MnO₄] compound can be prepared from KMnO₄ and can be used as an oxidant to oxidize [Mn₃(L_{IQ}^{CH₂OH}•)₂(L_{AP}^{CH₂OH})(L_{BQ}^{CH₂OH})Cl]⁰ and forming a

tetranuclear Mn-complex. That complex can be examined as a functional model for PS II.

9. Without radical-containing star-shaped tetranuclear iron complex can be synthesized using the following ligand. That complex may have single molecule magnetic behavior.



10. Ligand $\text{H}_3\text{L}^{\text{COOH}}$ can be introduced to synthesize corresponding vanadium, iron, chromium, palladium, nickel and copper complexes and their coordination chemistry as well as catalytic activities can be studied.

Chapter 7

Equipment and Experimental work

7.1 *Methods and equipments*

All the analyses were performed at the Max-Planck-Institut für Bioanorganische Chemie, Mülheim an der Ruhr, unless otherwise mentioned. Commercial grade chemicals were used for the synthetic purposes and solvents were distilled and dried before use.

Infrared Spectroscopy

Infrared spectra were measured from 4000 to 400 cm⁻¹ as KBr pellets at room temperature on a 'Perkin-Elmer FT-IR-Spectrophotometer 2000'.

NMR Spectroscopy

¹H-, ¹³C- and ⁵¹V NMR spectra were measured using a 'Bruker ARX 250, DRX 400 or DRX 500'. The spectra were referenced to TMS, using the ¹³C or residual proton signals of the deuterated solvents as internal standards. VOCl₃ was used as reference in ⁵¹V NMR spectra.

Mass Spectroscopy

Mass spectra in the Electron Impact mode (EI; 70 eV) were recorded on a Finnigan MAT8200 mass spectrometer. Only characteristic fragments are given with intensities. The spectra were normalised against the most intense peak having intensity 100. Electron Spray Ionization (ESI) mass spectra were recorded either on a Finnigan Mat 95 instrument or a Hewlett-Packard HP 5989 mass spectrometer. ESI- and EI- spectra were measured by the group of Dr. W. Schrader at the Max-Planck-Institut für Kohlenforschung, Mülheim an der Ruhr.

Elemental Analysis

The determination of the C, H, N and metal content of the compounds was performed by the 'Mikroanalytischen Labor H. Kolbe', Mülheim an der Ruhr, Germany.

UV-VIS Spectroscopy

UV-Vis spectra were recorded on a 'Perkin-Elmer UV-vis Spectrophotometer Lambda 19' or on a Hewlett-Packard HP 8452A diode array spectrophotometer in the range 200-1200 nm. For UV-vis spectro-electrochemical investigations the HP 8452A diode array spectrophotometer was used, by employing a coulometry cuvette and Bu₄NPF₆ as supporting electrolyte.

Electrochemistry

Cyclic voltammetry, square wave voltammetry and linear sweep voltammetry experiments were performed using an 'EG&G Potentiostat / Galvanostat 273A'. A standard three-electrode-cell was employed with a glass-carbon working electrode, a platinum-wire auxiliary electrode and Ag/AgCl (saturated LiCl in EtOH) reference electrode. Measurements were made under an inert atmosphere at room temperature. The potential of the reference electrode was determined using Fc⁺/Fc as the internal standard.

Magnetic Susceptibility Measurements

The measurements of the temperature or field dependent magnetization of the sample were performed in the range 2 to 295 K at 1, 4 or 7 T on a '*Quantum Design SQUID-Magnetometer MPMS*'. The samples were encapsulated in gelatin capsules and the response functions were measured four times for each given temperature, yielding a total of 32 measured points. The resulting volume magnetization from the samples had its diamagnetic contribution compensated and was recalculated as volume susceptibility. Diamagnetic contributions were estimated for each compound by using Pascal's constants. The experimental results were fitted with the programme JULIUS calculating through full-matrix diagonalization of the Spin-Hamiltonian. The following Hamiltonian-operators were used:

$$H_{ZE} = \mu_B \sum g_i \hat{S}_i \cdot \mathbf{B}$$

$$H_{HDVV} = -2 \sum J_{ij} \hat{S}_i \cdot \hat{S}_j$$

$$H_{ZFS} = \sum D_i [\hat{S}_{iz}^2 - \{S_i(S_i+1)/3\}] + E_i/D_i (\hat{S}_{ix}^2 - \hat{S}_{iy}^2)$$

Indexes i,j indicate individual spins. For the magnetic measurement the calculated g values obtained during simulation is the isotropic.

EPR Spectroscopy

First derivative X-Band EPR spectra of powdered or frozen solution samples were measured with a '*Bruker ESP 300 Spectrometer*' coupled to an '*Oxford Instruments ESR 910-Cryostat*'. Spin-Hamiltonian simulations of the EPR spectra were performed with a program which was developed from the S = 5/2 routines of Gaffney and Silverstone and which specifically makes use of the resonance search procedure based on a Newton-Raphson algorithm as described therein.

⁵⁷Fe-Mössbauer Spectroscopy

⁵⁷Fe-Mössbauer spectra were measured with an *Oxford Instruments* Mössbauer spectrometer in the constant acceleration mode. ⁵⁷Co/Rh was used as the radiation source. The minimum experimental linewidths were 0.24 mm/s. The temperature of the sample was controlled by an '*Oxford Instruments* Variox Cryostat'. Isomer shifts were determined relative to α -iron at 300K. The measurements were carried out at 80K and 100K with solid samples containing the isotope ⁵⁷Fe.

Crystallography

X-ray diffraction data were collected on an '*Enraf-Nonius* CAD4 Diffractometer' or on a '*Siemens* Smart System'. Graphite-monochromatized Mo-K α with $\lambda = 0.71073 \text{ \AA}$ was employed. Data were collected by the 2θ - ω scan method ($3 \leq 2\theta \leq 50^\circ$). The data were corrected for absorption and Lorenz polarization effects. The structures were solved by direct methods and subsequent Fourier-difference techniques, and refined anisotropically by fullmatrix least-squares on F^2 with the program SHELXTL PLUS. Hydrogen atoms were included at calculated positions with $U < 0.08 \text{ \AA}^2$ in the last cycle of refinement.

GC / GC-MS Analysis

GC of the organic products were performed either on HP 6890 instruments using RTX-5 Amine 13.5 m S-63 columns respectively. GC-MS was performed using the above column coupled with a HP 5973 mass spectrometer with mass selective detector.

LC Analysis

LC of the complexes were performed on HPLC instrumentation using a Gilson M305 pump, and the Diode-Array-Detector (DAD) SPDM 10 AV (Shimadzu corporation). MeOH and water in the ratio 3:1 with flow velocity 0.8 ml/ min was used as eluent through a Luna-5 phenylhexyl column.

7.2 Experimental Work

7.2.1 Synthesis of Ligands

(i) Synthesis of *N, N'*-bis(2-hydroxy-3,5-di-*tert*-butylphenyl)-2,2'-diamino Biphenyl compound (H_4L)

Step 1: Synthesis of 2,2' dinitrobiphenyl compound

2-Iodonitrobenzene (35.5 gm, 0.14 mol) and pure dry copper powder (25.4 gm, 0.4 mol) were ground together and then transfer to a flask which was immersed in an oil-bath pre-heated to 150-160°C, when the internal temperature was raised during 15 minutes to 190-200°C and maintained there for 24 hours. The solid cake was obtained on cooling to room temperature dissolved in chloroform. The solution was passed through a alumina column (30 × 4 cm) and orange eluate was evaporated. Yield: 55 % (10.9 mg, 0.055 mol)

Step 2: Synthesis of 2,2' diamino biphenyl compound

A slurry of 1.8 gm of 10 % Pd-C catalyst was stirred in 250 ml of methanol while bubbling argon through the mixture. A solution of 3.6 gm (96 mmol) of sodium borohydride in 100 ml of water was added, and the purging continued. Over the next five minutes, 3.8 gm (16 mmol) of 2,2'-dinitrobiphenyl in 300 ml of methanol was added in three portions. The mixture was stirred at room temperature for one hour, filtered under suction through a pad of celite filter aid and taken to dryness by rotary evaporation at 80° C. The residue was extracted with dichloromethane (200 ml) and ether (200 ml). The combined extracts were taken to dryness by rotary evaporation yielding 2.7 gm (94 %) of 2,2'-diaminobiphenyl. Recrystallized from *n*-hexane. ^1H NMR (CD_2Cl_2): 7.31 (dd, 2h, $J= 2.3, 7.1$ Hz), 7.59 (m, 2H), 7.69 (m, 2H), 8.3 (dd, 2H, $J= 1.5, 8.5$). ^{13}C NMR (CD_2Cl_2): 143.2 (C-1), 147.2 (C-2), 124.8 (C-3), 129.2(C-4), 130.9(C-6), 133.4(C-5).

Step 3: Synthesis of H₄L

2,2'-Diaminobiphenyl (2 gm; 10 mmol), 3,5-di-*tert*-butylcatechol (4.5gm; 20 mmol) and 1 ml Et₃N were taken in 100 ml *n*-hexane. The solution was stirred under air for 15 hours. Filtered and washed with *n*-hexane to get white color solid, N, N' (2-hydroxy-3, 5-di-*tert*-butyl-phenyl)-2,2'-diaminobiphenyl.

Yield: 4.75 gm (80%)

Mass (EI) : 592 gm/mol

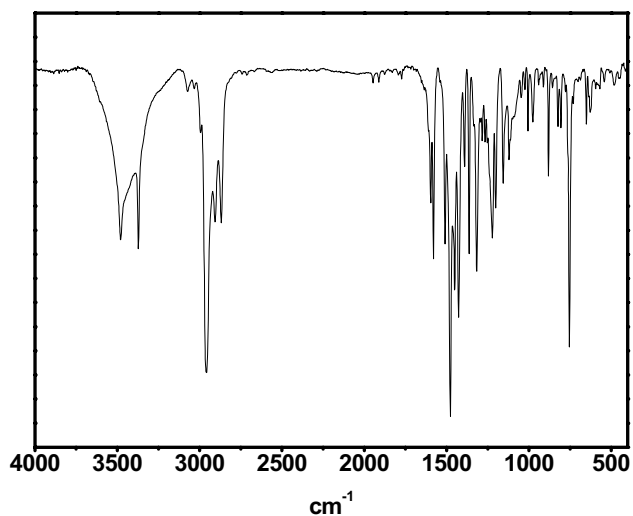
m.p: 196-198° C.

¹H NMR (CD₂Cl₂, ppm): 1.23 (s, 18 ^tBu H), 1.40 (s, 18 ^tBu H), 5.16 (s, 2H), 6.56-7.3 (12 H from aromatic ring).

Elemental analysis.



	%C	%H	%N
Calculated	81.08	8.78	4.73
Found	80.57	9.07	4.85



(ii) Synthesis of *N*(2-hydroxy-3,5-di-*tert*-butylphenyl)-2-aminobenzylalcohol compound ($H_3L^{CH_2OH}$)

2-Aminobenzylalcohol (1.25 gm; 10 mmol), 3, 5-di-*tert*-butyl-catechol (2.25gm; 10 mmol) and 0.2 ml Et₃N was taken in 50 ml *n*-hexane. The solution was stirred under air for 2 days. Filtered and washed with *n*-hexane to get white color solid, *N* (2-hydroxy-3, 5-di-*tert*-butylphenyl)-2aminobenzylalcohol.

Yield: 58% (1.9 gm).

m.p: 126-128°C.

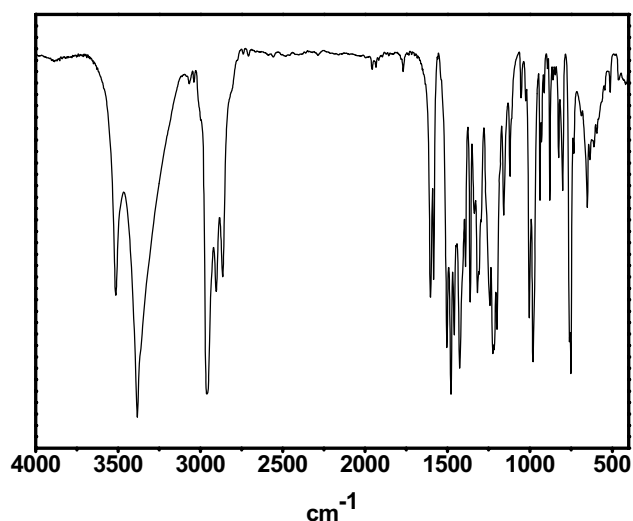
Mass (EI): 327.

¹H NMR (CD₂Cl₂, ppm): 1.29 (s, 9 ^tBu-H), 1.45 (s, 9 ^tBu-H), 4.81 (s, CH₂ -H).6.31-7.25(6-H from aromatic rings).

Elemental analysis.

C₂₁H₂₉NO₂

	%C	%H	%N
Calculated	77.00	8.85	4.30
Found	76.9	8.80	4.30



(iii) Synthesis of N(2-hydroxy-3,5-di-tert-butylphenyl)-anthranilic acid compound (H_3L^{COOH})

Anthranilic acid (1.45 gm; 10 mmol), 3,5-di-tert-butyl-catechol (2.25gm; 10 mmol) and 0.01 ml Et_3N was taken in 50 ml n-hexane. The solution was heated to reflux for 5 h and then stirred under air for 2 days. Filtered and washed with water and then n-hexane to get white color solid, N (2-hydroxy-3, 5-di-tert-butylphenyl) anthranilic acid.

Yield: 56% (1.9 gm),

m.p.: $>220^\circ C$.

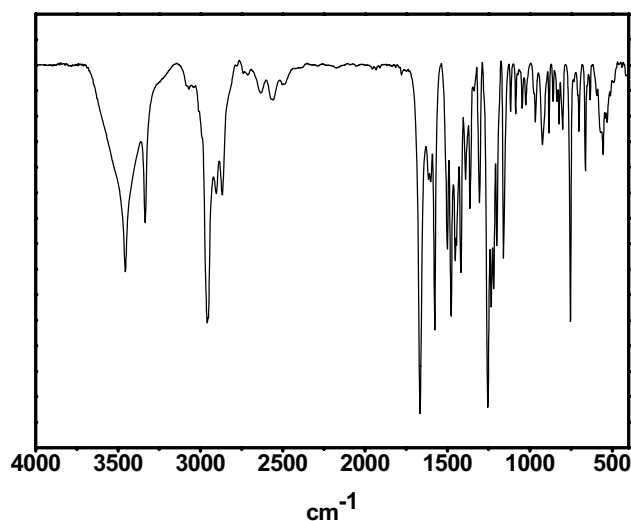
Mass (EI): 341.

1H NMR (CD_2Cl_2 , ppm): 1.27 (s, 9 tBu H), 1.44 (s, 9 tBu H), 6.12 (s, 1 NH H) 6.5-8.4 (6 H from aromatic ring), 8.75 (s, 1 COOH H).

Elemental analysis.

$C_{21}H_{27}NO_3$

	%C	%H	%N
Calculated	73.90	8.0	4.10
Found	74.5	7.67	3.93



7.2.2 Synthesis of complexes

(i) Synthesis of $[V(L)(\mu_2OMe)_2(L)V]^0$

To a solution of the ligand, H₄L (1.05 gm, 2 mmole) in MeOH (30 ml) under an argon atmosphere VO(SO₄).5H₂O (0.51gm, 2 mmole) was added. Upon addition of Et₃N the color of the solution changed to dark blue. After being stirred under argon atmosphere air for 1h and then under air for 2h, the dark blue solution was allowed to stand at room temperature. Microcrystalline complex was precipitated which was collected by filtration.

Yield: 0.47 g (35%).

Molecular Weight: 1340.0

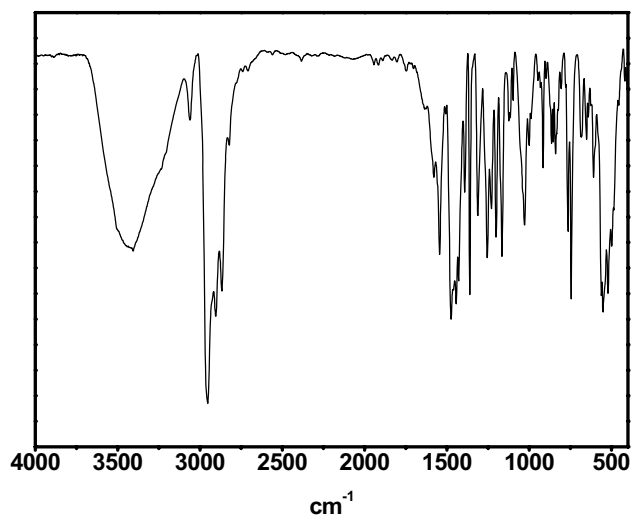
m/z : 1340.0 [M]⁺.

¹H NMR (CD₂Cl₂, ppm): 1.23 (s, 18 ^tBu H), 1.40 (s, 18 ^tBu H), 5.16 (s, 2H), 6.56-7.3 (12 H from aromatic ring).

Elemental analysis.



	%C	%H	%N	%V
Calculated	73.43	7.67	4.18	7.61
Found	73.1	7.54	4.25	7.82



(ii) Synthesis of $[Fe(HL)Cl]^0$

A CH_3CN solution (30 ml) of anhydrous $FeCl_3$ (0.33gm, 1 mmol), H_4L (0.592g, 1 mmol), and triethylamine (0.1 ml) was stirred under an aerial atmosphere at room temperature for 1h. A dark greenish-blue microcrystalline solid precipitated out. Filtered and washed with CH_3CN . Single crystals suitable for X-ray structure analysis were obtained by slow evaporation of a 1:1 CH_2Cl_2 , CH_3CN solution mixture.

Yield: 0.520 g (76%).

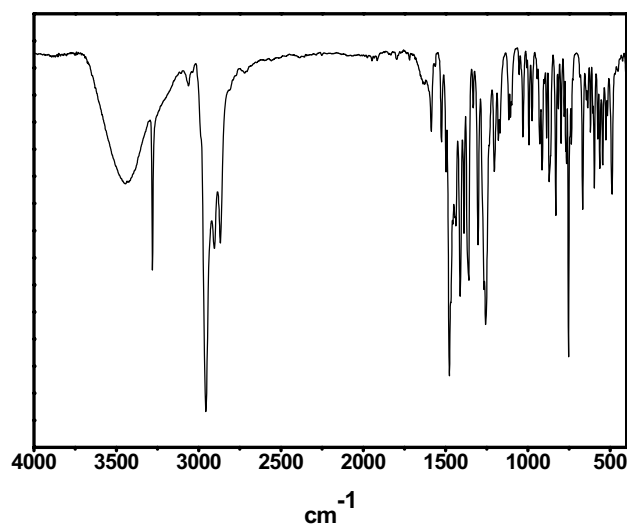
Molecular Weight: 680.5

m/z : 679.5 $\{M\}^+$.

Elemental analysis.



	%C	%H	%N	%Fe
Calculated	70.69	7.21	4.12	7.22
Found	70.81	7.22	4.45	7.24



(iii) Synthesis of $[Ni(L^{••})]^{0}$

To a solution of the ligand, H_4L (1.185 gm; 2 mmol) in CH_3CN (30 ml) was added $NiCl_2 \cdot 6H_2O$ (0.475 gm; 2 mmol) at room temperature in the presence of air and 0.2 ml triethylamine. From this solution, a microcrystalline brown precipitate formed within 1 h which was collected by filtration and washed with CH_3CN thoroughly. Dried under air. Single crystals suitable for X-ray crystallography were obtained by slow evaporation of 1:1 CH_3CN , CH_2Cl_2 solution.

Yield: 0.960 g (74%).

Molecular Weight: 646.0

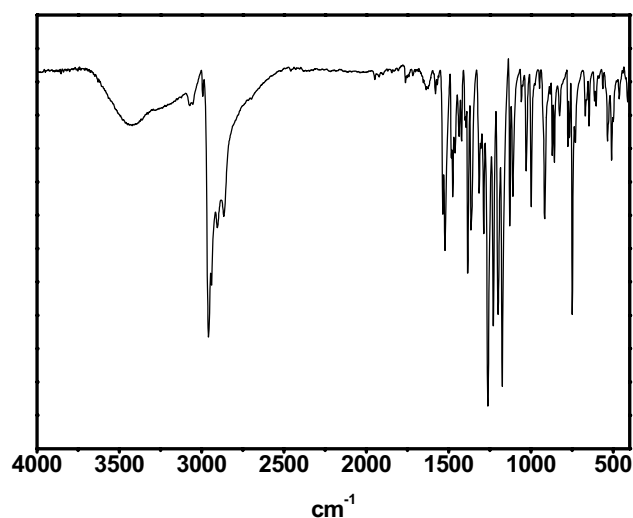
m/z : 646 $[M]^+$.

1H NMR (CD_2Cl_2 , ppm): 1.14 (s, 9 tBu H), 1.26 (s, 9 tBu H), 1.53 (s, 9 tBu H), 1.56 (s, 9 tBu H), 6.75-7.55 (12 H from aromatic ring).

Elemental analysis.

$C_{40}H_{48}N_2O_2Ni$

	%C	%H	%N	%Ni
Calculated	74.2	7.47	4.33	9.06
Found	73.9	7.54	4.25	9.00



(iv) Synthesis of $[Pd(L^{})]^0$**

To a solution of $PdCl_2$ (0.345 gm; 2 mmol) in CH_3CN (30 ml) was added with stirring solid H_4L (1.185 gm; 2 mmol) and triethylamine (0.2 ml) at room temperature in the presence of air. From this solution a microcrystalline dark brown precipitate formed within 1h which was collected by filtration, washed with CH_3CN , and air dried. Single crystals suitable for X-ray crystallography were obtained by slow evaporation of 1:1 CH_3CN , CH_2Cl_2 solution.

Yield: 1.05 g (75%).

Molecular Weight: 696.0

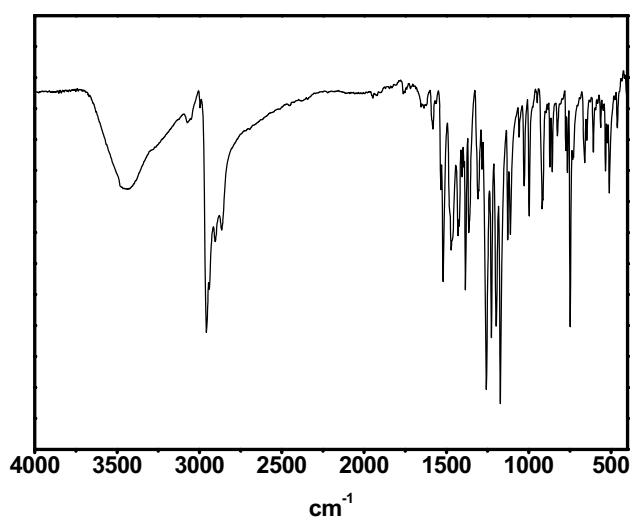
m/z : 696 $[M]^+$.

1H NMR (CD_2Cl_2 , ppm): 1.19 (s, 9 tBu H), 1.26 (s, 9 tBu H) 1.54 (s, 9 tBu H), 1.6 (s, 9 tBu H), 6.8-7.61 (12 H from aromatic ring).

Elemental analysis.

$C_{40}H_{48}N_2O_2Pd$

	%C	%H	%N	%Pd
Calculated	69.1	6.96	4.03	15.31
Found	68.75	7.00	4.15	15.45



(v) Synthesis of $[\text{Cu}(\text{L}^{\bullet\bullet})]^{0}$

The ligand, H_4L (1.185 gm; 2 mmol), $[\text{Cu}^{\text{I}}(\text{CH}_3\text{CN})_4] \text{ClO}_4$ (0.655 gm; 2 mmol) and 0.1 ml Et_3N were taken in 30 ml dry CH_3CN . The solution was stirred under argon atmosphere for 0.5 h and then under air for 1h. On slow evaporation of a 1:1 CH_3CN , CH_2Cl_2 solution mixture crystalline complex precipitated.

Yield: 0.975 g (75%).

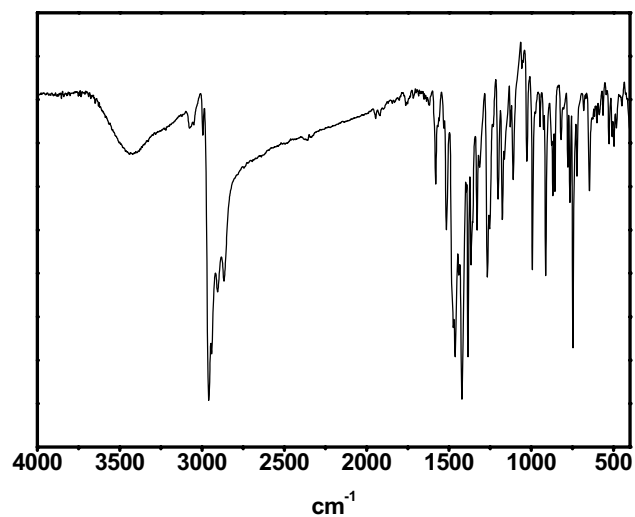
Molecular Weight: 651.5

m/z : 651.4 $\{\text{M}\}^+$.

Elemental analysis.



	%C	%H	%N	%Cu
Calculated	73.62	7.36	4.29	9.73
Found	73.09	7.54	4.25	9.82



(vi) Synthesis of $[\text{Cu}(\text{L}^{\bullet})][\text{PF}_6]$

To the stirring complex $[\text{Cu}^{\text{II}}(\text{L}^{\bullet})]^0$ (0.65 gm; 1mmol), ferrocenium hexafluorophosphate (0.33 gm; 1 mmol) was added under argon blanketing atmosphere in 20 ml degassed CH_2Cl_2 solution. The solution was stirred for 1h and then to that solution 10 ml degassed *n*-hexane was added. Slow evaporation of the solution provides microcrystalline solid.

Yield: 0.270 g (34%).

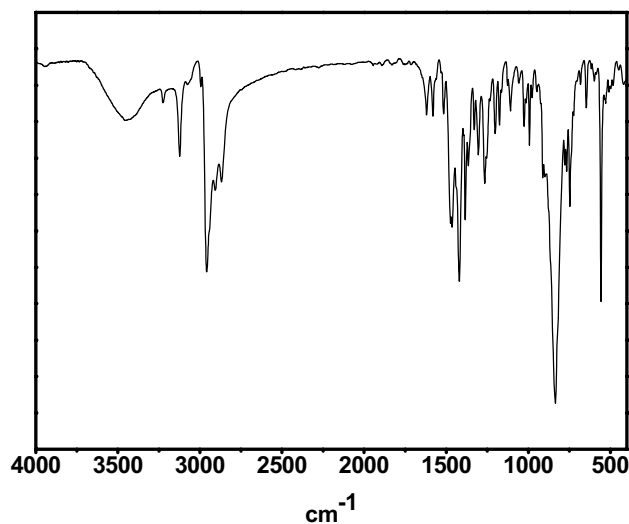
Molecular Weight: 796.5

m/z : 651.4 $[\text{M}]^+$, 145 $[\text{PF}_6]^-$

Elemental analysis.



	%C	%H	%N	%Cu	%P	%F
Calculated	60.26	6.02	3.51	7.97	3.89	14.31
Found	60.19	6.14	3.35	7.82	3.90	14.1



(vii) General method for the Synthesis of Cu(II) complexes with H_2L^X ligands, $[Cu(L^X)_2]^0$

To a solution of H_2L^X (2 mmol) in CH_3CN (30 ml) were added $[Cu^I(CH_3CN)_4]ClO_4$ (0.655 gm; 2 mmol) and 0.2 ml triethylamine. The solution was stirred for 2h in the presence of air. From the filtered solution a dark green, microcrystalline precipitate was formed. Single crystals suitable for X-ray crystallography were obtained by slow evaporation of 1:1 CH_3CN , CH_2Cl_2 solution.

Yields and elemental analysis (C, H, N, Cu, X) results are in Table below.

Complex	Composition	Mol. Wt	Yield %	C%	H%	N%	Cu%	X%
1	$C_{44}H_{46}F_{12}N_2O_2Cu$	925	45	57.05	5.01	3.02	6.86	24.61
1a	$C_{42}H_{48}F_6N_2O_2Cu$	789	65	63.82	6.12	3.54	8.04	14.42
1b	$C_{42}H_{48}F_6N_2O_2Cu$	789	70	63.82	6.12	3.54	8.04	14.42
2	$C_{40}H_{46}F_4N_2O_2Cu$	725	50	66.14	6.38	3.86	8.75	10.46
3	$C_{40}H_{46}Cl_4N_2O_2Cu$	791	73	60.65	5.85	3.54	8.02	17.9
4	$C_{44}H_{58}N_2O_6Cu$	773	77	68.23	7.55	3.62	8.2	-
4a	$C_{42}H_{54}N_2O_4Cu$	713	56	70.61	7.62	3.92	8.9	-
4b	$C_{42}H_{54}N_2O_4Cu$	713	65	70.61	7.62	3.92	8.9	-
5	$C_{50}H_{82}N_2O_2Cu$	879	67	76.54	9.4	3.2	7.3	-

Complex No. is same as used in Chapter 3

(viii) Synthesis of $[V_2O_2(L_{Cat}^{CH_2OH})_2]^0$

To a stirred solution of $H_3L^{CH_2OH}$ (0.655 gm; 2 mmol) in MeOH (30 ml) was treated with $VOSO_4 \cdot 5H_2O$ (0.51 gm; 2 mmol). The mixture was stirred under an aerial atmosphere for 2h in the presence of triethylamine. Deep blue solid was separated out and filtered off, washed with MeOH. X-ray quality deep blue colored single crystals were obtained by recrystallization of the microcrystalline solid from a 1:1 CH_2Cl_2 and CH_3CN solvent mixture.

Yield: 1.095 g (70%).

Molecular Weight: 783.0

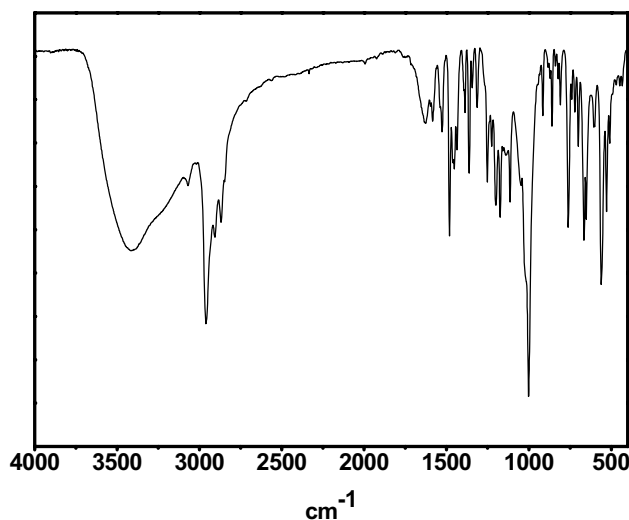
m/z : 782.7 $[M]^+$.

1H NMR (CD_2Cl_2 , ppm): 1.14 (s, 9 tBu H), 1.26 (s, 9 tBu H), 1.53 (s, 9 tBu H), 1.56 (s, 9 tBu H), 6.75-7.55 (12 H from aromatic ring).

Elemental analysis.



	%C	%H	%N	%V
Calculated	64.45	6.70	3.58	13.02
Found	64.1	6.54	3.5	13.10



(ix) Synthesis of $[Mn_3(L_{SQ}^{CH_2OH})_2(L_{Cat}^{CH_2OH})(L_{BQ}^{CH_2OH})Cl]^0$

The stirring ligand, $H_3L^{CH_2OH}$ (0.655 gm; 2 mmol), anhydrous $MnCl_2$ (0.25 gm; 2 mmol), and 0.2 ml triethylamine were added in MeOH (30 ml). The solution was stirred for 2h under air. Slow evaporation of the methanolic solution followed by addition of CH_3CN to the concentrated methanolic solution produces crystalline complex.

Yield: 0.48 gm (32%).

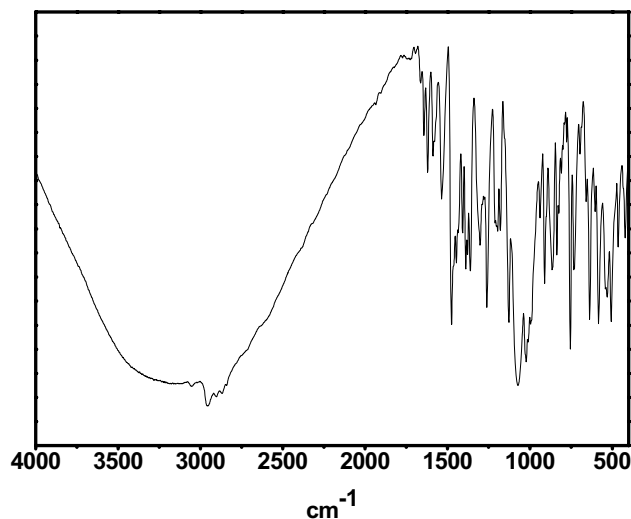
Molecular Weight: 1496.5

m/z : 1496.2 $[M]^+$, 1461 $[M-Cl]^+$.

Elemental analysis.



	%C	%H	%N	%Mn	Cl%
Calculated	67.35	7.00	3.74	11.00	2.37
Found	67.3	6.82	3.62	11.2	2.4



(x) Synthesis of $[Cu_4(LSQ^{\overset{CH}{2}OH})_4]^0$

To CH₃CN (30 ml) solution of H₃L^{CH₂OH} (0.655 gm; 2 mmol), Cu^{II}(OAc)₂.H₂O (0.4 gm; 2 mmol), and 0.2 ml triethylamine were added. After stirring for 24h the solution was filtered and residue was washed thoroughly with CH₃CN.

Yield: 0.55 gm (71%).

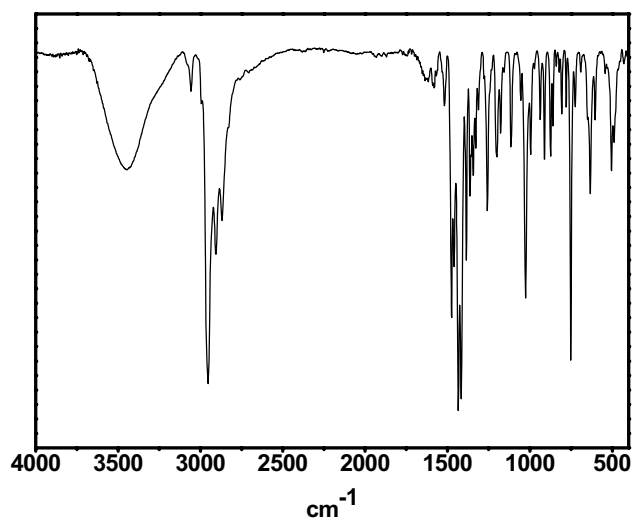
Molecular Weight: 1550.0

m/z : 1550.2 [M]⁺.

Elemental analysis.



	%C	%H	%N	%Cu
Calculated	65.00	6.75	3.61	16.38
Found	65.80	6.10	3.12	15.62



(xi) Synthesis of $[Mn(L_{SQ}^{COOH})(L_{Cat}^{COOH})][HNEt_3]$

$Mn^{II}(\text{acetate})_2 \cdot 4H_2O$ (0.49 gm; 2 mmol) was dissolved in 30 ml of MeOH, and H_3L^{COOH} (0.68 gm; 2 mmol) was added. To the solution 0.3 ml Et_3N was added and stirred under air for 2 h. Microcrystalline solid precipitated.

Yield: 1.05 gm (63%).

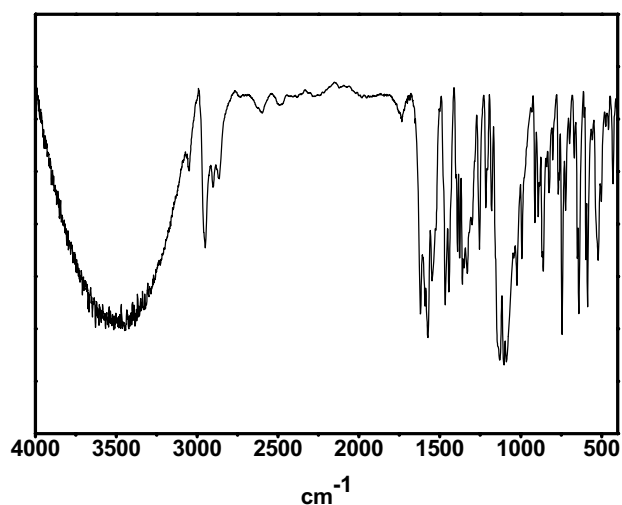
Molecular Weight: 833.0

m/z : 102 $[HNEt_3]^+$, 731 $[M]^-$.

Elemental analysis.

$C_{48}H_{64}N_3O_6Mn$

	%C	%H	%N	%Mn
Calculated	69.2	7.73	5.05	6.60
Found	69.00	7.75	4.97	6.56



7.2.3 Reactivity studies,

General procedure for the oxidation of benzyl alcohol and determination of the concentration of benzaldehyde

In 20 ml dichloromethane, 5×10^{-4} M catalyst, 5×10^{-2} M benzyl alcohol and 4.5×10^{-2} M tetrabutylammonium methoxide was added. The resulting solution was stirred under air for 15 h and then LC was measured. Concentration of product (benzaldehyde) was calculated against the area obtained for a standard benzaldehyde solution.

General procedure for the oxidation of ethanol (ethoxide) and determination of the concentration of acetaldehyde

In 20 ml dichloromethane, 5×10^{-4} M catalyst and 5×10^{-2} M tetrabutylammonium ethoxide was added. The resulting solution was stirred under air for 3 to 5 h and then 0.5 ml of the catalytic solution was extracted by 10 ml water. To the 0.5 ml water part, 0.5 ml 1 % aqueous 3-methyl-2-benzothiazolone hydrazine hydrochloride was added and the mixture was allowed to stand for 30 min. 2.5 ml 2 % freshly prepared aqueous FeCl_3 solution was added. Following a five minutes waiting period, the mixture is diluted to 10 ml with acetone. The absorbance is then determined at 635 nm and 670 nm against a blank.

General procedure for the oxidation of methanol (methoxide) and determination of the concentration of formaldehyde

(a) Preparation of Hentzsch solution: 25 gm (0.325 mol) ammonium acetate, 3 ml 100% acetic acid, 0.2 ml (19.4 mmol) acetyl acetone was taken in 100 ml volumetric flux. Volume was made up 100 ml by water.

(b) Determination of formaldehyde: In 20 ml dichloromethane, 5×10^{-4} M catalyst and 5×10^{-2} M tetrabutylammonium methoxide was added. The resulting solution was stirred under air for 15 h. To 0.5 ml reaction solution 10 ml water is added. Water part was separated out.

To the 5 ml water part 5 ml Hentzsch reagent was added. The mixture was heated at 60 °C for 5 min., cooled at room temperature and UV-VIS spectrum was measured ($\epsilon = 8000 \text{ M}^{-1} \text{ cm}^{-1}$ at $\lambda = 414 \text{ nm}$) against blank.

(c) Preparation of Bu₄NOCD₃: 1.07 gm (27.4 mmol) potassium was taken in 30 ml dry toluene. To that 4.5 ml (114 mmol) CD₃OD was added and stirred for 8h (until total potassium dissolved). 4 ml KOCD₃ / CD₃OD is separated out. To that solution 9.35 gm (27.4 mmol) tetrabutylammonium perchlorate is added. On addition of dry ether potassium perchlorate and excess tetrabutylammonium perchlorate were separated out as precipitate. Filtered under argon atmosphere and excess CD₃OD was evaporated.

General procedure for the oxidation of benzyl amine and determination of the concentration of benzilidinebenzylamine

In 20 ml methanol, $5 \times 10^{-4} \text{ M}$ catalyst and $5 \times 10^{-2} \text{ M}$ benzylamine was added. The resulting solution was stirred under air for 15 h and then 1 ml of the catalytic solution was passed through a neutral alumina (0.5 gm) and the column was washed with 9 ml methanol. To the resulting 10 ml solution 5 μl *n*-hexadecane was added as standard. GC and GC-MS was measured. Concentration of benzilidinebenzylamine was calculated against the standard.

General procedure for the oxidation of ethylenediamine and 2-aminoethanol and determination of the concentration of glyoxal and 2-hydroxy-acetaldehyde

In 20 ml methanol, $5 \times 10^{-4} \text{ M}$ catalyst and $5 \times 10^{-2} \text{ M}$ ethylenediamine or 2-aminoethanol was added. The resulting solution was stirred under air for 15 h and then 0.5 ml of the catalytic solution was extracted by 10 ml water. To the 0.5 ml water part, 0.5 ml 1 % aqueous 3-methyl-2-benzothiazolone hydrazine hydrochloride was added and the mixture was allowed to stand for 30 min. 2.5 ml 2 % freshly prepared aqueous FeCl₃ solution was added.

Following a five minutes waiting period, the mixture is diluted to 10 ml with acetone. The absorbance is then determined at 634 nm and 664 nm against a blank.

General procedure for the oxidation of 2-aminophenol and determination of the concentration of phenoxazinone chromophore

In 20 ml methanol or dichloromethane, 2.5×10^{-4} M catalyst and 2.5×10^{-2} M 2-aminophenol was added. The resulting solution was stirred under air for 2 h or 40 h. The solution was diluted as required and UV-VIS spectrum at 435 nm ($\epsilon = 24000 \text{ M}^{-1} \text{ cm}^{-1}$) was measured against blank.

Appendices

- (1) Crystallographic data*
- (2) Magnetochemical data*
- (3) Curriculum Vitae*

(I) Crystallographic data

	[Cu(L^{••})]⁰	[Pd(L^{••})]⁰
Identification code	4633	4850
Empirical formula	C ₄₀ H ₄₈ CuN ₂ O ₂	C ₄₀ H ₄₈ N ₂ O ₂ Pd
Formula weight	652.34	695.2
Temperature	100(2) K	100(2) K
Wavelength (MoK α)	0.71073 Å	0.71073 Å
Crystal system	Monoclinic	Monoclinic
Space group	P2 ₁ /n	P2 ₁ /n, No. 14
Unit cell dimensions	a = 9.4200(6) Å, b = 18.5916(14) Å, c = 19.784(2) Å, α = 90° β = 101.55(1)° γ = 90°	a = 9.5172(6) Å, b = 18.5949(12) Å, c = 20.29(2) Å, α = 90° β = 100.88(1)° γ = 90°
Volume (Å ³), Z	2394.7(5), 4	3526.2(5), 4
Density (calc.) Mg/m ³	1.276	1.310
Absorption coeff	0.68 mm ⁻¹	0.562 mm ⁻¹
F(000)	1388	1456
Crystal size (mm)	0.18 x 0.06 x 0.06	0.14 x 0.02 x 0.02
θ range for data collect.	3.42 to 26.00 deg	3.00 to 23.35
Index range	-10 \leq h \leq 11, -22 \leq k \leq 22, -24 \leq l \leq 24	-10 \leq h \leq 10, -20 \leq k \leq 20, -22 \leq l \leq 21
Reflections collected	45253	20043
Independent reflect.	6630 [R(int) = 0.1060]	5081 [R(int) = 0.0889]
Absorption correction	Not corrected	Gaussian, Face-indexed
Data/restraints/param.	6630 / 0 / 406	5081 / 31 / 419
Goodness-of-fit on F ²	1.039	1.018
Final R indices [I $>$ 2 σ (I)]	R1=0.0580, wR2=0.1244	R1=0.0461, wR2=0.0829
R indices (all data)	R1=0.0936, wR2=0.1409	R1=0.0813, wR2=0.0943

	$[\text{Ni}(\text{L}^{\bullet})]^{0}$	$[\text{Fe}(\text{HL}^{\bullet})\text{Cl}]^{0}$
Identification code	4682	5142
Empirical formula	$\text{C}_{40}\text{H}_{48}\text{N}_2\text{Ni O}_2$	$\text{C}_{40}\text{H}_{49}\text{Cl Fe N}_2\text{O}_2$
Formula weight	647.51	681.11
Temperature	100(2) K	100(2) K
Wavelength (MoK α)	0.71073 Å	0.71073 Å
Crystal system	Monoclinic	Triclinic
Space group	P2 ₁ /n	P-1, No. 2
Unit cell dimensions	a = 9.4934(6) Å, b = 18.4206(14) Å, c = 19.7027(2) Å, $\alpha = 90^\circ$ $\beta = 101.49(1)^\circ$ $\gamma = 90^\circ$	a = 9.1566(5) Å, b = 10.1701(12) Å, c = 19.7866(2) Å, $\alpha = 94.374(5)^\circ$ $\beta = 96.805(5)^\circ$ $\gamma = 91.558(5)^\circ$
Volume (Å ³), Z	2376.4(2), 4	1823.07(15), 2
Density (calc.) Mg/m ³	1.274	1.241
Absorption coeff	0.612 mm ⁻¹	0.523 mm ⁻¹
F(000)	1384	724
Crystal size (mm)	0.12x 0.06 x 0.06	0.14 x 0.06 x 0.03
θ range for data collect.	3.42 to 27.50 deg	2.96 to 27.50
Index range	-12 \leq h \leq 12, -23 \leq k \leq 23, -25 \leq l \leq 25	-11 \leq h \leq 11, -13 \leq k \leq 13, -25 \leq l \leq 25
Reflections collected	53654	29940
Independent reflect.	7708 [R(int) = 0.1047]	8345 [R(int) = 0.0786]
Absorption correction	Not corrected	None
Data/restraints/param.	7708 / 0 / 406	8345 / 0 / 430
Goodness-of-fit on F ²	1.029	1.070
Final R indices [I $>$ 2 σ (I)]	R1=0.0462, wR2=0.0910	R1=0.0617, wR2=0.1196
R indices (all data)	R1=0.0659, wR2=0.0986	R1=0.0930, wR2=0.1324

	$[\text{V}(\text{L})(\mu_2\text{OMe})_2(\text{L})\text{V}]^0$	$[\text{Cu}(\text{L}^{3,5\text{-CF}_3})_2]$
Identification code	5059	3269
Empirical formula	$\text{C}_{83.25}\text{H}_{104.5}\text{Cl}_{2.5}\text{N}_4\text{O}_6\text{V}_2$	$\text{C}_{44}\text{H}_{46}\text{Cu}\text{F}_{12}\text{N}_2\text{O}_2$
Formula weight	1447.71	926.37
Temperature	100(2) K	100(2) K
Wavelength (MoK α)	0.71073 Å	0.71073 Å
Crystal system	Monoclinic	Triclinic
Space group	$\text{P}2_1/\text{n}$, No. 14	P-1
Unit cell dimensions	$a = 23.6897(6)$ Å, $b = 24.5147(7)$ Å, $c = 27.9324(9)$ Å, $\alpha = 90^\circ$ $\beta = 104.534(6)^\circ$ $\gamma = 90^\circ$	$a = 11.426(1)$ Å, $b = 14.197(2)$ Å, $c = 14.726(2)$ Å, $\alpha = 67.95(2)^\circ$ $\beta = 81.28(2)^\circ$ $\gamma = 83.86(2)^\circ$
Volume (Å ³), Z	15704.2(8), 8	2185.2(5), 2
Density (calc.) Mg/m ³	1.225	1.408
Absorption coeff	0.377 mm ⁻¹	0.589 mm ⁻¹
F(000)	6148	954
Crystal size (mm)	0.14 x 0.04 x 0.02	0.36 x 0.16 x 0.15
θ range for data collect.	2.91 to 22.50 deg	2.21 to 26.00
Index range	$-25 \leq h \leq 25$, $-26 \leq k \leq 26$, $-30 \leq l \leq 30$	$-13 \leq h \leq 17$, $-19 \leq k \leq 22$, $-18 \leq l \leq 22$
Reflections collected	114758	17366
Independent reflect.	20469 [R(int) = 0.0777]	8154 [R(int) = 0.0368]
Absorption correction	Not corrected	SADABS
Data/restraints/param.	20469 / 64 / 1798	8146 / 0 / 577
Goodness-of-fit on F ²	1.048	0.994
Final R indices [I > 2 σ (I)]	R1=0.0603, wR2=0.1359	R1=0.0464, wR2=0.1025
R indices (all data)	R1=0.0886, wR2=0.1512	R1=0.0742, wR2=0.1142

	$[\text{Cu}(\text{L}^{2\text{-CF}_3})_2]^0$	$[\text{Cu}(\text{L}^{3,5\text{-F}})_2]^0$
Identification code	4816	3297
Empirical formula	$\text{C}_{44}\text{H}_{51}\text{CuF}_6\text{N}_3\text{O}_2$	$\text{C}_{40}\text{H}_{46}\text{CuF}_4\text{N}_2\text{O}_2$
Formula weight	831.42	726.33
Temperature	100(2) K	100(2) K
Wavelength (MoK α)	0.71073 Å	0.71073 Å
Crystal system	Monoclinic	Monoclinic
Space group	P2 ₁ /n	P2(1)/n
Unit cell dimensions	a = 17.1824(3) Å, b = 11.8651(2) Å, c = 21.0332(5) Å, $\alpha = 90^\circ$ $\beta = 101.501(4)^\circ$ $\gamma = 90^\circ$	a = 5.8867(5) Å, b = 17.533(2) Å, c = 17.854(2) Å, $\alpha = 90.00^\circ$ $\beta = 95.32(2)^\circ$ $\gamma = 90.00^\circ$
Volume (Å ³), Z	4201.96(14), 4	1834.8(3), 2
Density (calc.) Mg/m ³	1.314	1.315
Absorption coeff	0.586 mm ⁻¹	0.652 mm ⁻¹
F(000)	1740	762
Crystal size (mm)	0.40 x 0.28 x 0.20	0.32 x 0.21 x 0.14
θ range for data collect.	2.97 to 30.99 deg	2.29 to 32.50
Index range	-24 \leq h \leq 24, -17 \leq k \leq 17, -30 \leq l \leq 30	-9 \leq h \leq 9, -26 \leq k \leq 26, -27 \leq l \leq 27
Reflections collected	82338	36228
Independent reflect.	13340 [R(int) = 0.0448]	6617 [R(int) = 0.0889]
Absorption correction	Gaussian, Face-indexed	Not measured
Data/restraints/param.	13340/ 0 / 518	6610 / 0 / 229
Goodness-of-fit on F ²	1.058	0.984
Final R indices [I > 2 σ (I)]	R1=0.0385, wR2=0.0947	R1=0.0409, wR2=0.0870
R indices (all data)	R1=0.0461, wR2=0.0987	R1=0.0861, wR2=0.0991

	$[\text{Cu}(\text{L}^{3,5\text{Cl}})_2]^0$	$[\text{Cu}(\text{L}^{3,5\text{-tBu}})_2]^0$
Identification code	3285	3280
Empirical formula	$\text{C}_{40}\text{H}_{46}\text{Cl}_4\text{CuN}_2\text{O}_2$	$\text{C}_{60}\text{H}_{92}\text{CuN}_2\text{O}_3$
Formula weight	992.13	952.90
Temperature	100(2) K	100(2) K
Wavelength (MoK α)	0.71073 Å	0.71073 Å
Crystal system	Monoclinic	Triclinic
Space group	$P2_1/c$	P-1
Unit cell dimensions	a = 12.1419(8) Å, b = 10.2848(6) Å, c = 15.3145(10) Å, $\alpha = 90^\circ$ $\beta = 92.543(4)^\circ$ $\gamma = 90^\circ$	a = 9.5092(7) Å, b = 16.365(1) Å, c = 19.024(1) Å, $\alpha = 83.078(3)^\circ$ $\beta = 79.902(3)^\circ$ $\gamma = 79.567(3)^\circ$
Volume (Å ³), Z	1910.5(2), 2	2854.2(4), 2
Density (calc.) Mg/m ³	1.377	1.109
Absorption coeff	0.888 mm ⁻¹	0.425 mm ⁻¹
F(000)	826	1038
Crystal size (mm)	0.33 x 0.22 x 0.16	0.30 x 0.19 x 0.14
θ range for data collect.	2.39 to 27.50 deg	1.75 to 23.27
Index range	-15 \leq h \leq 18, -14 \leq k \leq 14, -18 \leq l \leq 23	-10 \leq h \leq 10, -18 \leq k \leq 15, -19 \leq l \leq 21
Reflections collected	15776	19197
Independent reflect.	4265 [R(int) = 0.0498]	8051 [R(int) = 0.0378]
Absorption correction	Gaussian, Face-indexed	SADABS
Data/restraints/param.	4249 / 0 / 229	8044 / 0 / 624
Goodness-of-fit on F ²	1.012	0.957
Final R indices [I > 2 σ (I)]	R1=0.0380, wR2=0.0809	R1=0.0391, wR2=0.0910
R indices (all data)	R1=0.0719, wR2=0.0919	R1=0.0644, wR2=0.1097

	$[\text{V}_2\text{O}_2(\text{L}_{\text{cat}}^{\text{CH}_2\text{OH}})_2]^0$	$[\text{Mn}_3(\text{L}_{\text{SQ}}^{\text{CH}_2\text{OH}})_2(\text{L}_{\text{Cat}}^{\text{CH}_2\text{OH}})(\text{L}_{\text{BQ}}^{\text{CH}_2\text{OH}})\text{Cl}]^0$
Identification code	5236	5167
Empirical formula	$\text{C}_{42}\text{H}_{52}\text{N}_2\text{O}_6\text{V}_2$	$\text{C}_{88}\text{H}_{110}\text{Cl Mn}_3\text{ N}_6\text{O}_8$
Formula weight	782.74	1580.9
Temperature	100(2) K	100(2) K
Wavelength (MoK α)	0.71073 Å	0.71073 Å
Crystal system	Monoclinic	Triclinic
Space group	$\text{P}2_1/\text{c}$, No. 14	P-1, No. 2
Unit cell dimensions	a = 11.3171(5) Å, b = 9.7889(4) Å, c = 17.9384(8) Å, $\alpha = 90^\circ$ $\beta = 100.349(4)^\circ$ $\gamma = 90^\circ$	a = 16.1719(8) Å, b = 16.1921(9) Å, c = 16.7326(5) Å, $\alpha = 103.201(6)^\circ$ $\beta = 92.060(6)^\circ$ $\gamma = 97.692(6)^\circ$
Volume (Å ³), Z	1954.92(15), 2	4217.03(15), 2
Density (calc.) Mg/m ³	1.330	1.244
Absorption coeff	0.527 mm ⁻¹	0.531 mm ⁻¹
F(000)	824	1672
Crystal size (mm)	0.07 x 0.02 x 0.02	0.10 x 0.06 x 0.02
θ range for data collect.	3.11 to 29.00 deg	3.33 to 24.00
Index range	-15 \leq h \leq 15, -13 \leq k \leq 12, -24 \leq l \leq 24	-18 \leq h \leq 18, -18 \leq k \leq 18, -19 \leq l \leq 18
Reflections collected	27955	32092
Independent reflect.	5185 [R(int) = 0.0570]	12983 [R(int) = 0.0789]
Absorption correction	None	None
Data/restraints/param.	5185/ 31 / 251	12983 / 39 / 1015
Goodness-of-fit on F ²	1.033	1.073
Final R indices [I $>$ 2 σ (I)]	R1=0.0476, wR2=0.1035	R1=0.0687, wR2=0.1448
R indices (all data)	R1=0.0742, wR2=0.1161	R1=0.0717, wR2=0.1327

	$[\text{Cu}_4(\text{L}_{\text{SQ}}^{\text{CH}_2\text{OH}})_4]^0$	$[\text{Mn}(\text{L}_{\text{SQ}}^{\text{COOH}})(\text{L}_{\text{Cat}}^{\text{COOH}})][\text{HNEt}_3]$
Identification code	4936	4903
Empirical formula	$\text{C}_{87.5}\text{H}_{109.5}\text{Cl}_1\text{N}_{4.5}\text{O}_8\text{Cu}_4$	$\text{C}_{48}\text{H}_{64}\text{Mn}\text{N}_3\text{O}_6$
Formula weight	1655.92	683.96
Temperature	100(2) K	100(2) K
Wavelength (MoK α)	0.71073 Å	1.54178 Å
Crystal system	Monoclinic	Monoclinic
Space group	$P2_1/n$	$P2_1/c$, No. 14
Unit cell dimensions	$a = 16.3153(5)$ Å, $b = 29.2224(8)$ Å, $c = 17.7048(5)$ Å, $\alpha = 90^\circ$ $\beta = 100.281(5)^\circ$ $\gamma = 90^\circ$	$a = 9.6003(6)$ Å, $b = 10.2524(6)$ Å, $c = 44.910(3)$ Å, $\alpha = 90^\circ$ $\beta = 92.29(1)^\circ$ $\gamma = 90^\circ$
Volume (Å ³), Z	8305.6(4), 4	4416.8(5), 4
Density (calc.) Mg/m ³	1.324	1.254
Absorption coeff	1.100 mm ⁻¹	2.835 mm ⁻¹
F(000)	3480	1784
Crystal size (mm)	0.37 x 0.33 x 0.22	0.14 x 0.06 x 0.03
θ range for data collect.	2.94 to 30.98 deg	3.94 to 69.16
Index range	$-23 \leq h \leq 23$, $-32 \leq k \leq 42$, $-25 \leq l \leq 25$	$-11 \leq h \leq 8$, $-12 \leq k \leq 12$, $-49 \leq l \leq 53$
Reflections collected	96664	27457
Independent reflect.	24851 [R(int) = 0.0325]	8029 [R(int) = 0.0460]
Absorption correction	Gaussian, face-indexed	SADABS, 2004/1
Data/restraints/param.	24851 / 10 / 1025	8029 / 144 / 561
Goodness-of-fit on F ²	1.038	1.266
Final R indices [I > 2 σ (I)]	R1=0.0505, wR2=0.1210	R1=0.0872, wR2=0.1975
R indices (all data)	R1=0.0717, wR2=0.1327	R1=0.0901, wR2=0.1991

	$[\text{Mn}(\text{L}_{\text{SQ}}^{\text{COOH}})(\text{L}_{\text{Cat}}^{\text{COOH}})][\text{HNEt}_3]$
Identification code	5079
Empirical formula	$\text{C}_{48}\text{H}_{64}\text{MnN}_3\text{O}_6$
Formula weight	683.96
Temperature	293(2) K
Wavelength (MoK α)	0.71073 Å
Crystal system	Monoclinic
Space group	P2 ₁ /c, No. 14
Unit cell dimensions	a = 9.706(2) Å, b = 10.323(2) Å, c = 45.132(6) Å, $\alpha = 90^\circ$ $\beta = 92.03(2)^\circ$ $\gamma = 90^\circ$
Volume (Å ³), Z	4419.2(14), 4
Density (calc.) Mg/m ³	1.226
Absorption coeff	0.342 mm ⁻¹
F(000)	1784
Crystal size (mm)	0.09 x 0.05 x 0.03
θ range for data collect.	2.91 to 22.50
Index range	-10 ≤ h ≤ 10, -10 ≤ k ≤ 11, -48 ≤ l ≤ 48
Reflections collected	20414
Independent reflect.	5834 [R(int) = 0.0562]
Absorption correction	None
Data/restraints/param.	5834 / 145 / 563
Goodness-of-fit on F ²	1.047
Final R indices [I > 2σ(I)]	R1=0.0537, wR2=0.1254
R indices (all data)	R1=0.0773, wR2=0.1389

(2) Magnetochemical data

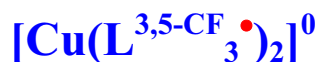
MW = 651.5 gm/mol, $\chi_{\text{dia}} = -416.60 \times 10^{-6} \text{ cm}^3 \text{ mol}^{-1}$
 m = 32.67 mg, H = 1.000 T

No	T(K)	$\chi \cdot T_{\text{exp}}$	$\chi \cdot T_{\text{calc}}$	μ_{exp}	μ_{calc}
1	1.961	0.32519	0.40885	1.61267	1.80826
2	5.008	0.41422	0.42588	1.8201	1.84554
3	9.996	0.42852	0.43127	1.85125	1.85718
4	14.994	0.43541	0.43492	1.86607	1.86502
5	20.004	0.44022	0.43832	1.87636	1.8723
6	30	0.44779	0.44492	1.89241	1.88634
7	40.003	0.45515	0.45146	1.90792	1.90014
8	50.012	0.46139	0.45805	1.92094	1.91382
9	60.021	0.46744	0.46493	1.93349	1.92738
10	70.054	0.47319	0.47258	1.94536	1.94088
11	80.07	0.4796	0.48157	1.95848	1.95426
12	90.077	0.48546	0.49244	1.9704	1.96757
13	100.13	0.49115	0.50569	1.98193	1.98091
14	110.1	0.49664	0.52134	1.99297	1.99419
15	120.12	0.50234	0.5396	2.00438	2.00768
16	130.16	0.50844	0.56028	2.0165	2.02147
17	140.18	0.5152	0.58304	2.02987	2.03564
18	150.19	0.52264	0.60756	2.04446	2.05033
19	160.2	0.53126	0.63352	2.06127	2.06569
20	170.21	0.54035	0.66055	2.07881	2.08183
21	180.22	0.55054	0.68832	2.09834	2.09884
22	190.22	0.56108	0.71652	2.11832	2.11675
23	200.24	0.57237	0.74496	2.13952	2.13565
24	210.23	0.58421	0.77328	2.16154	2.15546
25	220.24	0.59606	0.80146	2.18335	2.17625
26	230.26	0.6087	0.8293	2.20638	2.19795
27	240.25	0.62093	0.85659	2.22843	2.22043
28	250.27	0.63344	0.88341	2.25078	2.24373
29	260.27	0.64661	0.90956	2.27405	2.26766
30	270.24	0.65926	0.93497	2.29618	2.29211
31	280.23	0.67146	0.95975	2.31734	2.31709
32	290.15	0.68506	0.98365	2.34069	2.34228



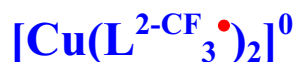
MW = 680.0 gm/mol, $\chi_{\text{dia}} = -430.0 \times 10^{-6} \text{ cm}^3 \text{ mol}^{-1}$
 m = 24.58 mg , H = 1.000 T

No	T(K)	$\chi \cdot T_{\text{exp}}$	$\chi \cdot T_{\text{calc}}$	μ_{exp}	μ_{calc}
1	2,001	1,50058	2,50601	3,46425	4,47683
2	5,106	2,928	2,90361	4,8391	4,81891
3	9,999	3,25025	2,97159	4,87499	4,87499
4	15,001	3,26307	2,98545	4,88635	4,88635
5	20	3,23313	2,99034	4,89035	4,89035
6	29,991	3,17456	2,99385	4,89322	4,89322
7	40,002	3,13172	2,99509	4,89423	4,89423
8	50,005	3,10279	2,99566	4,8947	4,8947
9	60,033	3,08006	2,99598	4,89496	4,89496
10	70,049	3,06439	2,99617	4,89511	4,89511
11	80,076	3,05473	2,9963	4,89522	4,89522
12	90,093	3,04735	2,99638	4,89528	4,89528
13	100,11	3,03948	2,99645	4,89534	4,89534
14	110,12	3,03307	2,9965	4,89538	4,89538
15	120,1	3,02678	2,99654	4,89541	4,89541
16	130,16	3,02069	2,99658	4,89545	4,89545
17	140,18	3,01512	2,99662	4,89548	4,89548
18	150,19	3,01149	2,99667	4,89552	4,89552
19	160,2	3,00535	2,99675	4,90261	4,89559
20	170,21	3,00354	2,99687	4,90113	4,89568
21	180,23	2,99914	2,99704	4,89754	4,89582
22	190,23	2,99606	2,99729	4,89502	4,89603
23	200,23	2,99416	2,99765	4,89347	4,89632
24	210,24	2,99096	2,99812	4,89085	4,8967
25	220,22	2,99022	2,99875	4,89025	4,89722
26	230,25	2,98853	2,99955	4,88887	4,89787
27	240,24	2,98702	3,00055	4,88763	4,89869
28	250,27	2,98684	3,00178	4,88748	4,89969
29	260,24	2,98475	3,00325	4,88577	4,90089
30	270,26	2,98634	3,00499	4,88708	4,90231
31	280,15	2,98637	3,007	4,8871	4,90395
32	290,24	2,98619	3,00935	4,88695	4,90587



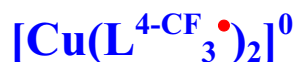
MW = 925.5 gm/mol, $\chi_{\text{dia}} = -535.0 \times 10^{-6} \text{ cm}^3 \text{ mol}^{-1}$
 m = 50.24 mg , H = 1.000 T

No	T(K)	$\chi \cdot T_{\text{exp}}$	$\chi \cdot T_{\text{calc}}$	μ_{exp}	μ_{calc}
1	2,003	0,30958	0,40083	1,57373	1,79071
2	5,004	0,41022	0,41465	1,81156	1,82132
3	9,999	0,41522	0,41672	1,82257	1,82586
4	15	0,41592	0,41711	1,82412	1,82671
5	20,002	0,41642	0,41724	1,82519	1,82701
6	30	0,41679	0,41734	1,82601	1,82722
7	40,001	0,41751	0,41738	1,82759	1,8273
8	50,007	0,41799	0,41739	1,82864	1,82733
9	60,022	0,41783	0,4174	1,82828	1,82735
10	70,046	0,41845	0,41741	1,82964	1,82736
11	80,068	0,41911	0,41742	1,83109	1,82739
12	90,081	0,4193	0,41745	1,83149	1,82745
13	100,11	0,41983	0,41753	1,83265	1,82763
14	110,09	0,41973	0,41771	1,83243	1,82802
15	120,15	0,42027	0,41805	1,83363	1,82877
16	130,18	0,42031	0,41864	1,83371	1,83006
17	140,18	0,42083	0,41955	1,83485	1,83205
18	150,19	0,42168	0,42087	1,8367	1,83493
19	160,2	0,42333	0,42268	1,84028	1,83886
20	170,21	0,42645	0,42504	1,84705	1,84399
21	180,15	0,42967	0,42798	1,85401	1,85036
22	190,23	0,43431	0,4316	1,86399	1,85818
23	200,24	0,43951	0,43586	1,87513	1,86733
24	210,24	0,44466	0,44078	1,88607	1,87783
25	220,26	0,45118	0,44636	1,89985	1,88968
26	230,25	0,45393	0,45255	1,90563	1,90273
27	240,26	0,46409	0,45934	1,92684	1,91695
28	250,26	0,46176	0,46667	1,92199	1,9322
29	260,26	0,47708	0,47451	1,95362	1,94836
30	270,26	0,48133	0,4828	1,96231	1,96531
31	280,24	0,48817	0,49147	1,9762	1,98287
32	290,26	0,49727	0,50052	1,99453	2,00105



MW = 789.5 gm/mol, $\chi_{\text{dia}} = -413.0 \times 10^{-6} \text{ cm}^3 \text{ mol}^{-1}$
 m = 19.57 mg, H = 1.000 T

No	T(K)	$\chi \cdot T_{\text{exp}}$	$\chi \cdot T_{\text{calc}}$	μ_{exp}	μ_{calc}
1	2	0,08409	0,36165	0,82005	1,70068
2	4,978	0,12467	0,37288	0,99854	1,7269
3	10,053	0,19102	0,37459	1,23601	1,73084
4	15,033	0,23736	0,37489	1,37779	1,73155
5	20,007	0,26834	0,375	1,46495	1,7318
6	30,002	0,30473	0,37508	1,56113	1,73198
7	40	0,32521	0,37511	1,61273	1,73204
8	50,003	0,33907	0,37512	1,64672	1,73207
9	60,036	0,34968	0,37513	1,67229	1,73209
10	70,05	0,35801	0,37514	1,69209	1,73211
11	80,069	0,36464	0,37516	1,70771	1,73216
12	90,054	0,3695	0,37523	1,71905	1,73231
13	100,11	0,37366	0,37539	1,72869	1,73269
14	110,13	0,37633	0,37573	1,73486	1,73348
15	120,15	0,37849	0,37635	1,73982	1,7349
16	130,17	0,38031	0,37734	1,744	1,73719
17	140,18	0,38277	0,37882	1,74963	1,74059
18	150,2	0,38556	0,38088	1,75601	1,74532
19	160,2	0,38909	0,3836	1,76403	1,75154
20	170,21	0,3932	0,38705	1,77331	1,75938
21	180,16	0,39733	0,39122	1,78262	1,76884
22	190,22	0,4025	0,39621	1,79416	1,7801
23	200,23	0,4079	0,40196	1,80615	1,79295
24	210,25	0,41378	0,40845	1,81913	1,80738
25	220,2	0,41994	0,4156	1,83263	1,82313
26	230,24	0,42684	0,42347	1,84762	1,84031
27	240,25	0,43355	0,43191	1,86208	1,85857
28	250,26	0,4405	0,44089	1,87695	1,87778
29	260,25	0,44801	0,45032	1,89289	1,89774
30	270,27	0,45611	0,46016	1,90992	1,91838
31	280,24	0,46455	0,47029	1,9275	1,93937
32	290,24	0,47447	0,4807	1,94798	1,96073



MW = 789.5 gm/mol, $\chi_{\text{dia}} = -413.0 \times 10^{-6} \text{ cm}^3 \text{ mol}^{-1}$
 m = 30.59 mg , H = 1.000 T

No	T(K)	$\chi \cdot T_{\text{exp}}$	$\chi \cdot T_{\text{calc}}$	μ_{exp}	μ_{calc}
1	2,002	0,26705	0,40094	1,46143	1,79068
2	5,013	0,44438	0,41479	1,82521	1,82134
3	9,999	0,51852	0,41685	1,82364	1,82586
4	15	0,48625	0,41723	1,8272	1,82671
5	19,999	0,41631	0,41737	1,82468	1,82701
6	29,995	0,41686	0,41747	1,82588	1,82722
7	39,998	0,41734	0,4175	1,82694	1,82729
8	50,007	0,41724	0,41752	1,82672	1,82733
9	60,035	0,41707	0,41752	1,82635	1,82735
10	70,059	0,41691	0,41753	1,82599	1,82736
11	80,075	0,41711	0,41754	1,82643	1,82738
12	90,099	0,41725	0,41757	1,82675	1,82745
13	100,13	0,41729	0,41766	1,82684	1,82763
14	110,16	0,41734	0,41784	1,82694	1,82803
15	120,17	0,4177	0,41818	1,82774	1,82878
16	130,17	0,41779	0,41877	1,82791	1,83007
17	140,12	0,41836	0,41968	1,82917	1,83205
18	150,2	0,4195	0,42101	1,83167	1,83496
19	160,21	0,42095	0,42282	1,83482	1,8389
20	170,21	0,4233	0,42519	1,83993	1,84404
21	180,22	0,42606	0,42816	1,84593	1,85047
22	190,23	0,42969	0,43177	1,85377	1,85826
23	200,22	0,43407	0,43604	1,8632	1,86741
24	210,25	0,43935	0,44098	1,87449	1,87797
25	220,24	0,44543	0,44655	1,88742	1,88979
26	230,23	0,45221	0,45275	1,90173	1,90286
27	240,25	0,4593	0,45956	1,91659	1,91712
28	250,26	0,46694	0,46691	1,93246	1,9324
29	260,26	0,47509	0,47476	1,94924	1,94858
30	270,25	0,48412	0,48306	1,96768	1,96553
31	280,07	0,49302	0,4916	1,98569	1,98283
32	290,25	0,50252	0,5008	2,00473	2,0013



MW = 1550 gm/mol, $\chi_{\text{dia}} = -913.0 \times 10^{-6} \text{ cm}^3 \text{ mol}^{-1}$

m = 39.54 mg, H = 1.000 T

No	T(K)	$\chi \cdot T_{\text{exp}}$	$\chi \cdot T_{\text{calc}}$	μ_{exp}	μ_{calc}
1	2	0,05913	0,08	0,68768	0,79988
2	5,04	0,07441	0,08	0,77144	0,79988
3	10,03	0,12091	0,0869	0,98337	0,83366
4	15,04	0,22632	0,148	1,34536	1,08795
5	20	0,35677	0,284	1,68917	1,50709
6	30	0,64184	0,649	2,26565	2,27825
7	40	0,93607	0,9879	2,73611	2,81084
8	50,01	1,21688	1,2722	3,11963	3,18975
9	60,03	1,46795	1,5132	3,42638	3,47878
10	70,04	1,6844	1,7196	3,6703	3,70846
11	80,07	1,87221	1,8975	3,86952	3,89556
12	90,1	2,03224	2,0508	4,0315	4,04987
13	100,11	2,17024	2,1827	4,16613	4,17808
14	110,15	2,29007	2,2973	4,27961	4,28636
15	120,16	2,39428	2,3968	4,37589	4,3782
16	130,16	2,48441	2,4837	4,4575	4,45686
17	140,18	2,56498	2,5602	4,5292	4,52498
18	150,2	2,63544	2,6279	4,59099	4,58441
19	160,2	2,69967	2,688	4,64659	4,63654
20	170,21	2,75503	2,7417	4,69399	4,68262
21	180,21	2,80482	2,79	4,73622	4,72369
22	190,23	2,84947	2,8335	4,77377	4,76037
23	200,22	2,88919	2,8729	4,80693	4,79336
24	210,23	2,92653	2,9088	4,83789	4,82321
25	220,23	2,95708	2,9416	4,86307	4,85033
26	230,26	2,98671	2,9717	4,88738	4,87508
27	240,26	3,01069	2,9993	4,90696	4,89767
28	250,26	3,03252	3,0248	4,92472	4,91844
29	260,25	3,05209	3,0483	4,94058	4,93751
30	270,25	3,06801	3,0702	4,95345	4,95522
31	280,26	3,08345	3,0906	4,9659	4,97165
32	290,24	3,10146	3,1095	4,98038	4,98683



MW = 1536.0 gm/mol, $\chi_{\text{dia}} = -200.0 \times 10^{-6} \text{ cm}^3 \text{ mol}^{-1}$
 m = 36.35 mg , H = 1.000 T

No	T(K)	$\chi \cdot T_{\text{exp}}$	$\chi \cdot T_{\text{calc}}$	μ_{exp}	μ_{calc}
1	2,001	4,757	5,22842	6,16802	6,46643
2	4,996	8,71285	8,70844	8,34756	8,34545
3	10,012	10,1567	10,0795	9,01272	8,9784
4	15,024	10,0934	10,263	8,98459	9,05976
5	20,004	9,96596	10,1385	8,92769	9,00464
6	30,002	9,66814	9,72195	8,79328	8,81772
7	40,001	9,39417	9,35972	8,66779	8,65189
8	50,012	9,16127	9,08581	8,55967	8,52435
9	60,025	8,9609	8,87973	8,46555	8,42712
10	70,051	8,79655	8,72134	8,38756	8,35163
11	80,086	8,67369	8,59676	8,32878	8,29176
12	90,093	8,56999	8,49694	8,27884	8,24348
13	100,08	8,47064	8,4153	8,23071	8,20378
14	110,12	8,39395	8,34694	8,19337	8,17039
15	120,13	8,32024	8,28935	8,15732	8,14216
16	130,16	8,26226	8,23999	8,12884	8,11788
17	140,18	8,20387	8,19735	8,10007	8,09685
18	150,19	8,16035	8,16015	8,07856	8,07846
19	160,2	8,11648	8,1274	8,05681	8,06223
20	170,21	8,07841	8,09835	8,0379	8,04781
21	180,23	8,04513	8,07238	8,02132	8,03489
22	190,15	8,00447	8,04928	8,00103	8,02339
23	200,24	7,98283	8,02806	7,9902	8,01281
24	210,24	7,9556	8,00898	7,97656	8,00328
25	220,24	7,93338	7,99158	7,96542	7,99458
26	230,25	7,91564	7,97565	7,95651	7,98661
27	240,24	7,89489	7,96103	7,94607	7,97929
28	250,28	7,88504	7,9475	7,94111	7,9725
29	260,24	7,86756	7,93508	7,93231	7,96627
30	270,26	7,8495	7,92349	7,9232	7,96045
31	280,26	7,83878	7,91274	7,91778	7,95505
32	290,25	7,8286	7,90272	7,91264	7,95001



MW = 833 gm/mol, $\chi_{\text{dia}} = -231.0 \times 10^{-6} \text{ cm}^3 \text{ mol}^{-1}$
 m = 24.15 mg, H = 1.000 T

No	T(K)	$\chi \cdot T_{\text{exp}}$	$\chi \cdot T_{\text{calc}}$	μ_{exp}	μ_{calc}
1	1.96	0.31579	0.40892	1.58921	1.80843
2	5.092	0.70218	0.80402	2.36975	2.53579
3	10.164	0.91161	0.93583	2.70012	2.73575
4	15.05	0.94587	0.96288	2.7504	2.77501
5	20.005	0.96049	0.97275	2.77157	2.78921
6	30	0.97332	0.97984	2.79003	2.79934
7	40	0.98113	0.98228	2.8012	2.80284
8	50.011	0.98687	0.98341	2.80937	2.80444
9	60.027	0.98953	0.98401	2.81315	2.8053
10	70.051	0.99128	0.98438	2.81565	2.80582
11	80.046	0.99473	0.98461	2.82054	2.80616
12	90.089	0.99618	0.98477	2.82259	2.80639
13	100.13	0.99748	0.98489	2.82443	2.80655
14	110.14	0.9976	0.98497	2.82461	2.80667
15	120.16	0.99831	0.98504	2.82561	2.80676
16	130.16	0.9974	0.98509	2.82431	2.80684
17	140.18	0.99729	0.98513	2.82417	2.80689
18	150.13	0.99573	0.98516	2.82195	2.80694
19	160.19	0.99591	0.98519	2.82221	2.80697
20	170.22	0.99477	0.98521	2.8206	2.807
21	180.22	0.99376	0.98523	2.81916	2.80703
22	190.22	0.99238	0.98524	2.8172	2.80705
23	200.24	0.99129	0.98525	2.81566	2.80707
24	210.24	0.99064	0.98526	2.81474	2.80709
25	220.25	0.98967	0.98528	2.81336	2.8071
26	230.25	0.98825	0.98528	2.81134	2.80711
27	240.26	0.98674	0.98529	2.80919	2.80712
28	250.23	0.98668	0.9853	2.80911	2.80713
29	260.27	0.98437	0.9853	2.80581	2.80714
30	270.26	0.98286	0.98531	2.80365	2.80715
31	280.15	0.98176	0.98531	2.80209	2.80716
32	290.25	0.98357	0.98532	2.80468	2.80716